# **Experimental Dynamic Substructuring Using Nonlinear Modal Joint Models**

by

## **Daniel Robert Roettgen**

A dissertation submitted in partial fulfillment of the requirements for the degree of

Doctor of Philosophy

(Engineering Mechanics)

at the

University of Wisconsin - Madison

2016

Date of final oral examination: 12/6/2016

This dissertation is approved by the following members of the Final Oral Committee:

Matthew S. Allen, Associate Professor, Engineering Physics

**Daniel C. Kammer**, Professor, Engineering Physics

Michael E. Plesha, Professor Emeritus, Engineering Physics

Melih Eriten, Assistant Professor, Mechanical Engineering

Randall L. Mayes, Senior Technical Staff Member, Sandia National Labs

#### **Abstract**

Component mode synthesis is a branch of dynamic substructuring in which the subcomponents of an assembled structure are represented by the projection of the physical system onto a reduced basis consisting of the generalized modes for each subcomponent. These reduced models are used to compute the dynamics of a built-up structure. Linear component mode synthesis has been used for decades in order to predict the response of an assembly by combining several subcomponent models. These subcomponent models take many forms, as such, component mode synthesis techniques typically differ in which types of component modes are chosen to represent the dynamics of each subcomponent. Many component mode forms have been developed in order to reduce the complexity of the system away from the interface of subcomponents, and preserve the motion and forces at the connection between them. Traditionally, component mode synthesis techniques connect the linear dynamics of subcomponents by imposing compatibility at a selection of interface degrees of freedom. As such, these techniques are well suited for predicting the linear response of a linear system. This dissertation extends linear component mode synthesis techniques using nonlinear subcomponent models and has contributed to this research field in two ways.

The first contribution is a novel technique to identify and quantify the modal nonlinear dynamics of a structure. This dissertation provides a methodology for developing a model of the nonlinear dynamics for weakly nonlinear subcomponents. In a weakly nonlinear structure, the mode shapes of the structure are not dependant on amplitude and there is negligible coupling between any given pair of modes. Experimental evidence has shown that bolted assemblies often contain weak nonlinearities where the damping and frequency of a single harmonic are dependent on vibration amplitude. This dissertation uses a weakly nonlinear framework to represent a structure as a series of weakly nonlinear modes, where each mode can be treated as a single degree of freedom oscillator which include the nonlinear dynamics of the mode. This dissertation provides a methodology to identify these nonlinear modal models from

experimental measurements. This allows a substructure model to be reduced by its linear modes, but still accounts for the nonlinearity that may be present due to internal joints.

The second contribution is the use of these nonlinear modal models to generate dynamic substructuring predictions. This dissertation uses the Transmission Simulator method to perform experimental substructuring predictions. The method allows the interface between two subcomponents to be contained in an experimental model, which helps to preserve the boundary conditions of the joint. This dissertation utilizes weakly nonlinear modal models to represent this experimental subcomponent containing the nonlinear joint dynamics. Linear and nonlinear subcomponent models are then assembled using a primal formulation to impose compatibility at the interface between components and predict the nonlinear response of the assembled structure. This technique is readily applied to two simulated experimental systems. For each system investigated, the nonlinear modal models were used to obtain highly accurate substructuring predictions for assembled structures. Because all of these examples are completed on numerical models of the system, they do not account for experimental error or noise that would be present in a physical experiment. However, the simulations do prove that substructuring is a viable prediction method as long as the structure remains in the micro-slip regime

The accuracy of the simulated experimental substructuring examples led to the extension of this technique using physical hardware. The proposed nonlinear modal modeling framework is finally applied to using experimental measurements on a laboratory structure. Nonlinear modal models are extracted from experimental measurements and used to predict the response of a modified assembly. These predictions are compared to a truth test performed on the modified structure and proved to be extraordinarily accurate. This is the first application of the proposed techniques to experimental hardware. This confirmed, that by using the Transmission Simulator method, the nonlinearities of a weakly nonlinear system can be modeled at the subcomponent level and then used to compute nonlinear response predictions of an assembled structure.

## Acknowledgements

I would like to show appreciation to many mentors, instructors, and colleagues who made this research possible. First, I would like to thank my advisor, Professor Matt Allen, who has provided insight, guidance and patience during my time as his student. From him, I have learned many valuable lessons about engineering dynamics and he has been an excellent professional and personal role model.

I would also like to thank my Ph.D committee for taking the time to review this dissertation and provide feedback as this research was pursued. I'd like to extend a special thanks to Randall Mayes for this expertise and feedback as I studied in the area of structural dynamics. His guidance was instrumental in the development of this work and myself as I pursued my degree. I would also like to thank him and his colleagues at Sandia National Labs for arranging for me to work in their laboratories while I pursued my degree..

Support for this research was provided by the Sandia National Labs. Sandia National Laboratories is a multi-program laboratory managed and operated by Sandia Corporation, a wholly owned subsidiary of Lockheed Martin Corporation, for the U.S. Department of Energy's National Nuclear Security Administration under contract DE-AC04-94AL85000.

While pursing my doctorate, I have met many talented colleagues both within and outside of my research area. These people have helped make my time as a student and research as enjoyable as possible. Many of these colleagues are likely to become life long friends as I continue to research beyond my degree. Finally, I would like to thank my family and loved ones for all their support during my time as a student. I am very grateful for the endless support provided by my wife, Lilly, and look forward to sharing a lifetime of learning with my son, Grayson.

## **Abbreviations and Nomenclature**

#### **Abbreviations**

BRB Brake-Reuss Beam

CB Craig-Bampton

CMS Component Mode Synthesis

CMIF Complex Modal Indicator Function

CPB Cylinder-Plate-Beam

DOF Degree of Freedom

FBS Frequency Based Substructuring

FFT Fast Fourier Transform

FRF Frequency Response Function

MAC Modal Assurance Criterion

MCFS Modal Constraints for Fixture and Subsystem

NOMAD Nonlinear Mechanics and Dynamics

NLROM Nonlinear Reduced Order Model

RFS Restoring Force Surface

SDOF Single Degree of Freedom

SMAC Synthesize Modes and Correlate

TS Transmission Simulator

#### Nomenclature

**B** Boolean constraint matrix

 $\overline{B}$  modal constraint matrix

 $c_1, c_2$  quadratic and cubic damping coefficients

D dissipation

 $F_i$  general joint force

 $F_R$  Smallwood model joint force

 $F_s$  Iwan joint slip force

**H** FRF matrix

I identity matrix

 $K_0$  Iwan joint low level stiffness

 $K_R$  Smallwood model low amplitude stiffness

 $K_T$  Iwan joint stiffness

 $K_{\infty}$  Iwan joint high level stiffness

 $k_1$ ,  $k_2$  quadratic and cubic stiffness coefficients

L synthesizing matrix

M, C, K mass, damping and stiffness matrices

 $\overline{\mathbf{M}}$ ,  $\overline{\mathbf{C}}$ ,  $\overline{\mathbf{K}}$  synthesized mass, damping and stiffness matrices

 $\mathbf{q}, \dot{\mathbf{q}}, \ddot{\mathbf{q}}$  subcomponent modal displacement, velocity, and acceleration

r Smallwood model power-law dissipation factor

*u* joint displacement

w weighting vector

 $\mathbf{x}, \dot{\mathbf{x}}, \ddot{\mathbf{x}}$  physical displacement, velocity, and acceleration

 $\beta$  Iwan joint stiffness ratio factor

 $\zeta$  viscous damping ratio

 $\eta, \dot{\eta}, \ddot{\eta}$  assembled modal displacement, velocity, and acceleration

 $\rho(\phi)$  kernel for joint characterization

 $\chi$  Iwan joint power-law dissipation factor

 $\Phi$  mode shape matrix

 $\phi_{\text{max}}$  maximum slider state for macro-slip

 $\overline{\Psi}$  SMAC filter weighting vector

 $\psi_r(t)$  Hilbert envelope

 $\psi_i(t)$  Hilbert unwrapped phase

 $\omega_n$  natural frequency

 $\omega_d$  damped natural frequency

## **Contents**

A	bstra	act	i
A	ckno	owledgements	iii
A	bbre	eviations and Nomenclature	iv
C	onte	ents	vi
1	Ir	ntroduction	1
	1.1	Motivation	1
	1.2	Background - Traditional Component Mode Synthesis	4
	1.3	Background - Transmission Simulator Method	8
	1.4	Background - Joint Models	12
	1.5	Background - Nonlinear Substructuring	17
	1.6	Scope of the Dissertation	18
2	L	inear Transmission Simulator Method	21
	2.1	Introduction	21
	2.2	Ampair 600 Wind Turbine Test Bed	21
	2.	.2.1 Experimental Set-up	23
	2.	.2.2 Truth Assembly Results	26
	2.	.2.3 Subcomponent Test Results	28
	2.	.2.4 Substructuring Methodology	30
	2.	.2.5 Substructuring Predictions	31
	2.	.2.6 Possible Sources of Error	34
	2.	.2.7 Ampair Wind Turbine Remarks	36
	2.3	Cylinder-Plate-Beam System	37

	2.	3.1	Introduction	37
	2.	3.2	Experiment	38
	2.	3.3	Transmission Simulator Model	40
	2.3.4		Substructuring Methodology	42
	2.	3.5	Substructuring Predictions	43
	2.4	Remarl	ζS	46
3	N	onlinear	Modal Modeling	47
	3.1	Introdu	ction	47
	3.2	Couple	d Catalytic Converter System	48
	3.	2.1	Nonlinear Model Characterization - Theory	48
	3.	2.2	Experimental System - Coupled Catalytic Converters	54
	3.	2.3	Initial Screening – ZEFFT	60
	3.	2.4	Nonlinear Parameter Identification	63
	3.	2.5	Catalytic Converter Example Remarks	74
	3.3	Cylinde	er-Plate-Beam System	75
	3.	3.1	Introduction	75
	3.	3.2	Experimental Set-up	77
	3.	3.3	Preliminary Modal Results	78
	3.	3.4	Signal Processing	78
	3.	3.5	Nonlinear Models	80
	3	3.3.5.1	Modal Iwan Model	80
	3	3.3.5.2	Restoring Force Surface	82
	3.	3.6	Results and Observations	85

3.4 Remarks		90
4 Nonlinear Mo	dal Substructuring: Simulated Experiments	91
4.1 Introduction	1	91
4.2 Theoretical	Development	94
4.2.1 Iwa	n Joint	97
4.3 Spring-Mas	s System Application	97
4.3.1 Est	imating Modal Iwan Models for Substructure A	98
4.3.2 Sub	estructuring Predictions	102
4.4 Brake-Reus	s Beam Application	105
4.4.1 Sub	estructure C - Standard Brake Reuss Beam Model & Identification	106
4.4.2 Sub	estructure A and D: Standard and Modified Half-Beam	110
4.4.3 Noi	nlinear Modal Substructuring Results	111
4.5 Remarks		120
5 Nonlinear Mo	dal Substructuring: Experimental Demonstration	122
5.1 Introduction	1	122
5.2 Background	l and Theory	124
5.2.1 Noi	nlinear Component Mode Synthesis	124
5.2.2 Noi	nlinear Modal Model Identification	128
5.3 Experiment	al System - Brake-Reuss Beam System	130
5.4 Nonlinear S	ubstructuring Results	142
5.5 Remarks		149
6 Conclusions		151
6.1 Nonlinear N	Modal Modeling Techniques	151

6.2	Simulated Experimental Nonlinear Modal Substructuring	152
6.3	Experimental-Analytical Nonlinear Modal Substructuring	153
7 Future Work		
Appen	157	
Appen	160	

## 1 Introduction

#### 1.1 Motivation

It is commonplace for complicated engineering structures to consist of smaller subcomponents designed by individual engineers or different companies who are each responsible for the design and analysis of separate subcomponents. This individual component approach allows a design engineer to truly focus on a specific piece of hardware and on the essential details to complete a time critical project. This approach is essential for the design of complicated systems as it would be impossible for one person or team to master the entire system and find the time to design each part. While a design engineer may be responsible for the detailed design of an individual part, it is also important that the engineer understand the role of their component in an assembly-level response. Predicting the assembly-level response can be quite difficult when the design of neighboring components is handled by an outside vendor as these components may have unknown material properties or complicated geometry. One method to account for these neighboring subcomponents is to predict the assembled structure's response using experimental-analytical substructuring.

Experimental-analytical substructuring allows one to connect an experimental model of one subcomponent to an analytically derived model, created in a finite element program, for a neighboring subcomponent. This process can decrease the cost of analysis as more expensive simulations and tests on large assemblies can be avoided when the dynamic model of the full system can be assembled via a series of finite element or test based models on smaller, simpler subcomponents.

Substructuring is a natural form of reduced order modeling since the subcomponent models that are used (both, experimental and analytical) are typically reduced to include only the most critical features. These reduced subcomponents are coupled to predict the response for the assembled structure. While one could name countless examples where experimental-analytical substructuring would be beneficial, this section shall focus on the following example in order to simplify the discussion. This

example can be observed in the aircraft engine industry where the manufacturing and design of the aft engine casing may be completed by an outside vendor. In this example, the structure is divided into two subcomponents as shown in Fig. 1.

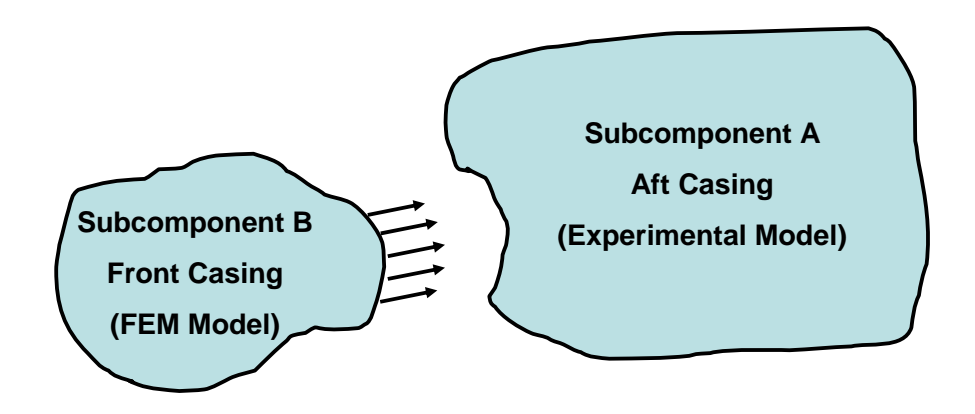


Figure 1. Substructuring Schematic

Subcomponent B is the front casing of a jet engine assembly, containing the fan and compressor module. This can be represented by a finite element model created by a design engineer or hardware owner. Subcomponent A is the aft casing for the same jet engine assembly, which contains the combustor and turbine modules. These casings may be owned by different design teams, but the overall motion of the jet engine is very important to assure that alignment is maintained as the engine is loaded dynamically. Engine alignment and straightness is essential to the performance of a jet engine as it can have a direct impact on the blade tip clearances between the rotating blades and the engine casing. By using experimental-analytical substructuring, it is possible to determine what resonances might exist and whether the resulting response levels will be too large causing an individual casing structure to fail. Here, the aft casing could be represented by an experimental model provided by a modal test engineer. Experimental-analytical substructuring can be used to couple this experimental model to a high-fidelity finite element model of the front case and generate a prediction of the assembled system response. This could allow the engineer designing the front casing to make adjustments to the front casing model and

understand the effects of those changes on the assembled structure. Figure 2 shows an example jet engine casing configuration.



Figure 2. FJ44-1AP Jet Engine at AirVenture Oshkosh

Interfaces in built-up structures are responsible for a large portion of the damping in the assembly [1, 2]. Friction in these jointed surfaces is often a large source of nonlinear damping in structures. Recent works [3, 4] have shown that linear models in jointed structures can overpredict response levels by a factor of 2-3. Many of these jointed structures are weakly nonlinear, meaning the modes of the structure remain uncoupled and the corresponding mode shapes do not change significantly at higher amplitudes. As seen in Fig. 2, the assembled engine casing contains several joints, between the front and aft casings and with the bolted on engine accessories. In this work these nonlinearities are defined using nonlinear modal models, meaning that the nonlinearity of the system is described on a mode-by-mode basis. This method is only applicable to weakly nonlinear structures in the absence of closely spaced natural frequencies.

Current experimental-analytical substructuring techniques are an effective tool for predicting the linear response of an assembled system but do not account for the nonlinearity introduced by the joints between subcomponents. In this dissertation, a novel approach is developed to include joint nonlinearities in experimental-analytical substructuring predictions. This begins by using current experimental-

analytical substructuring tools to predict linear system response. The subcomponent hardware is then probed experimentally to identify reduced nonlinear models to represent each subcomponent. These nonlinear subcomponent models enable one to predict the nonlinear system level response of the built-up structure. Novel contributions to this thesis include:

- Experimental evidence that the modal Iwan nonlinear framework is applicable to realistic joints, as shown on two example systems in Chapter 3
- The first simulation of experimental-analytical modal substructuring using a nonlinear modal model framework. These results demonstrate that nonlinear substructuring techniques work for a system whose discrete joints are modeled as Iwan elements. This content is discussed in Chapter 4
- Highly accurate experimental-analytical substructuring predictions using test and finite element derived models. This shows that it is feasible to test a laboratory structure accurately enough to perform substructuring and obtain high-quality predictions, as discussed in Chapter 5

Dynamic substructuring techniques and nonlinear subcomponent models will be used extensively in this dissertation. To lay the foundation for this, traditional component mode synthesis theory and techniques are reviewed in detail in Section 1.2. While the benefits of interface loading techniques are reviewed in Section 1.3. Finally, a brief review of nonlinear joint models and nonlinear substructuring is presented in Sections 1.4 and 1.5.

## 1.2 Background - Traditional Component Mode Synthesis

Experimental dynamic substructuring methods can be grouped into two categories. The first, Frequency-Based Substructuring (FBS), operates on the frequency response functions (FRFs) of the subcomponents to predict the response (i.e. the FRFs) of the assembled system. These FBS methods are sometimes referred to as impedance coupling [5-7], or admittance modeling [8, 9]. The second category operates on the subcomponent equations of motion and is often called Modal Substructuring or

Component Mode Synthesis (CMS) [10-12]. A recent review of both FBS and CMS methods was presented by de Klerk et al. in [13]. CMS is generally understood as a connection of subcomponents based on the projection of the physical system onto a reduced basis consisting of the generalized modes of the subcomponents.

In the literature, most methods of CMS differ in which types of component modes are chosen to reduce each subcomponent. One popular dynamic substructuring techniques uses a selection of fixed-interface degrees of freedom and a statically determined solution on the interior of the subcomponent. This was first presented by Hurty [14, 15] and later Craig-Bampton improved the technique in [16] using a different method of computing the model. Other reduction methods quickly populated the field including the Guyan static condensation methods [17]. A few component mode representations use the free-interface modes and attachment modes of a subcomponent [18, 19]. When these modes are used in CMS, it is considered the Craig-Chang method [18, 20]. Note, the dual Craig-Bampton method [21] uses these same free-interface modes and differs only in the way which constraints are enforced between subcomponents. These methods all reduce the system away from the interface but augment the basis in order to preserve loads and dynamics at the interface.

The Craig-Bampton method [16] retains every node at the interfaces between subcomponents. In structures with large interfaces this can be quite cumbersome. Craig and Chang first proposed interface reduction in [22]. Castanier et al. looked at using characteristics constraint modes to further reduce each component in [23] with good success. They reduced the interface by performing a secondary eigenvalue analysis on the interface partition of the assembled Craig-Bampton matrices. Recently, Hong et al. [24] proposed an alternative method that performs this secondary eigenvalue analysis at the subcomponent level before synthesizing the system. The Transmission Simulator (TS) method [25-28] is another method of interface reduction, that is primarily designed for experimental applications. In the TS method the interface of the subcomponent is mass-loaded to preserve the forces that the interface would observe in an assembled structure. This is another methodology to obtain a proper basis that preserves

information at the interface. The TS method and other mass-loading techniques are discussed in further detail in Chapter 1.3.

Typically, the easiest modal basis to obtain for an experimental subcomponent are the free boundary modes of the structure. These free boundary modes can be obtained by testing a structure in a free state, often suspended by bungee cords. To complete component mode synthesis using the free boundary modes each component is represented using modal parameters (i.e. natural frequencies, damping ratios, and mode shapes) and by using the modal transformation to relate physical displacement,  $\mathbf{x}$ , to modal displacement,  $\mathbf{q}$ , written as,

$$\mathbf{x} = \mathbf{\Phi} \,\mathbf{q} \tag{1}$$

Each subcomponent is written as a set of uncoupled equations of motion in modal coordinates,  $\mathbf{q}$ , written for subcomponent A as,

$$\mathbf{I}_{A}\ddot{\mathbf{q}}_{A} + \begin{bmatrix} 2\zeta_{A}\omega_{A} & \mathbf{q}_{A} \end{bmatrix} \dot{\mathbf{q}}_{A} + \begin{bmatrix} \omega_{A}^{2} & \mathbf{q}_{A} \end{bmatrix} \mathbf{q}_{A} = \mathbf{\Phi}_{A}^{T} \mathbf{F}_{A}$$
(2)

The equations of motion for each system can be concatenated into a block matrix form to create an uncoupled set of equations of motions.

$$\begin{bmatrix} \mathbf{I}_{A} & \mathbf{0} \\ \mathbf{0} & \mathbf{I}_{B} \end{bmatrix} \begin{pmatrix} \ddot{\mathbf{q}}_{A} \\ \ddot{\mathbf{q}}_{B} \end{pmatrix} + \begin{bmatrix} 2\zeta_{A}\omega_{A} & 0 \\ \mathbf{0} & 2\zeta_{B}\omega_{B} & 0 \end{bmatrix} \begin{pmatrix} \dot{\mathbf{q}}_{A} \\ \dot{\mathbf{q}}_{B} \end{pmatrix} + \begin{bmatrix} \omega_{A}^{2} & 0 \\ \mathbf{0} & \omega_{B}^{2} & 0 \end{bmatrix} \begin{pmatrix} \mathbf{q}_{A} \\ \mathbf{q}_{B} \end{pmatrix} = \begin{pmatrix} \mathbf{\Phi}_{A}^{T} \mathbf{F}_{A} \\ \mathbf{\Phi}_{B}^{T} \mathbf{F}_{B} \end{pmatrix}$$
(3)

Both subcomponents, A and B, are uncoupled as there are no coupling terms in any of the system matrices. To synthesize these subcomponents, the interface motion can be constrained using a constraint equation in the form of

$$\mathbf{B} \begin{Bmatrix} \mathbf{X}_A \\ \mathbf{X}_B \end{Bmatrix} = \{\mathbf{0}\} \tag{4}$$

where B is typically a Boolean matrix that relates the motion between two degrees of freedom on differing subcomponents. In essence, the shared degrees of freedom between the two subcomponents are set equal to each other. For example, if point  $x_A$  from Subcomponent A, and  $x_B$  from Subcomponent B

have the same motion the  $\bf \it B$  constraint matrix would be equal to  $\begin{bmatrix} 1 & -1 \end{bmatrix}$  as this satisfies the constraint that  $x_A - x_B = 0$ . This holds true if both Subcomponents A and B only contain a single degree of freedom. A similar constraint equation can be written for substructures containing multiple degrees of freedom to construct a complete constraint matrix,  $\bf \it B$ .

To complete modal substructuring, these constraints are cast into the modal domain by using the modal transformation from Eqn. (1). The first two terms of this new constraint matrix can be gathered to formulate a modal constraint matrix,  $\overline{\bf B}$ .

$$\mathbf{B} \begin{bmatrix} \mathbf{\Phi}_{A} & \mathbf{0} \\ \mathbf{0} & \mathbf{\Phi}_{B} \end{bmatrix} \begin{Bmatrix} \mathbf{q}_{A} \\ \mathbf{q}_{B} \end{Bmatrix} = \mathbf{\overline{B}} \begin{Bmatrix} \mathbf{q}_{A} \\ \mathbf{q}_{B} \end{Bmatrix} = \{\mathbf{0}\}$$
 (5)

The next step is to generate a transformation matrix that will transform the set of unconstrained modal coordinates,  $\mathbf{q}$ , from Eqn. (3) to some set of synthesized coordinates,  $\mathbf{\eta}$ , that enforce the constraints from Eqn. (5). To simplify matters, a new set of coordinates is defined that always satisfies these constraints as follows

$$\mathbf{q} = \mathbf{L}\mathbf{\eta} \tag{6}$$

Substituting this into the modal constraint equation yields,

$$\overline{\mathbf{B}}\mathbf{L}\boldsymbol{\eta} = 0 \tag{7}$$

where, for any arbitrary  $\eta$  the transformation matrix, L , must reside in the nullspace of  $\overline{B}$  .

$$\mathbf{L} = null(\mathbf{\bar{B}}) \tag{8}$$

This transformation is then applied to the modal equations of motion, Eqn. (3), to generate the equations of motion of the assembly as predicted by substructuring.

$$\overline{\mathbf{M}}\ddot{\mathbf{\eta}} + \overline{\mathbf{C}}\dot{\mathbf{\eta}} + \overline{\mathbf{K}}\mathbf{\eta} = \mathbf{L}^T\mathbf{\Phi}^T\mathbf{F} \tag{9}$$

$$\overline{\mathbf{M}} = \mathbf{L}^{\mathrm{T}} \begin{bmatrix} \mathbf{I}_{A} & \mathbf{0} \\ \mathbf{0} & \mathbf{I}_{B} \end{bmatrix} \mathbf{L} \tag{10}$$

$$\bar{\mathbf{C}} = \mathbf{L}^{\mathsf{T}} \begin{bmatrix} \begin{bmatrix} 1 & 2\zeta_{A}\omega_{A^{\mathsf{T}}, 1} \end{bmatrix} & \mathbf{0} \\ \mathbf{0} & \begin{bmatrix} 1 & 2\zeta_{B}\omega_{B^{\mathsf{T}}, 1} \end{bmatrix} \end{bmatrix} \mathbf{L}$$
(11)

$$\vec{\mathbf{K}} = \mathbf{L}^{\mathsf{T}} \begin{bmatrix} & \omega_{A}^{2} & \\ & & \\ & \mathbf{0} & \begin{bmatrix} & \omega_{B}^{2} & \\ & & \end{bmatrix} \end{bmatrix} \mathbf{L}$$
 (12)

$$\mathbf{x} = \begin{bmatrix} \mathbf{\Phi}_A & \mathbf{0} \\ \mathbf{0} & \mathbf{\Phi}_B \end{bmatrix} \mathbf{L} \mathbf{\eta} \tag{13}$$

The eigenvalue problem can be solved for these synthesized equations of motion, which results in predictions for the natural frequencies, damping ratios and mode shapes of the built-up assembly. These predictions can be used to determine if a system resonance may cause premature failure for a subcomponent under a specific operating condition. With these predictions one can estimate the built-up system response without ever having to create an analytical model for the experimental subcomponent. In the example of the jet engine casing assembly, the front casing design engineer can now predict the assembly response for the entire jet engine casing, by combining his finite element model for the front casing with an experimental dynamic model for the aft casing.

#### 1.3 Background - Transmission Simulator Method

As mentioned in Section 1.2, most CMS techniques differ based on the component modes used to describe individual subcomponents. It is imperative that the component modes of the individual subcomponents form an adequate basis for the motion of the coupled assembly (Ch. 17, [29]). If this is not the case, the subcomponent models will have a difficult time predicting the motion of the assembly and may even lead to erroneous substructuring predictions. Numerous methods have been proposed to achieve said modal basis. These include the traditional Craig-Bampton [16] and free-interface methods [10, 30] as discussed in Chapter 1.2. Not all of these can be used in an experimental context. For example, the constraint modes required by the Craig-Bampton method are practically impossible to measure experimentally.

One method that is more obtainable, from an experimental viewpoint, is to mass-load the interface by attaching masses to the test article at the interface degrees of freedom (DOF). Mass-loading the interface provides many advantages. When a subcomponent is tested separate from an assembly, there are no forces exerted on the interface DOF. This is the location where the structure will eventually be connected to another component. Hence, the modal basis (called free modes because the boundaries and interface are free) all involve zero loading at the interface. Because of this fact, each subcomponent is required to retain a large number of component modes to accurately predict the motion of the assembly. When masses are attached to the interface they exert forces at the interface in all of the component modes. In addition, it reduces the resonant frequencies, possibly bringing more of the modes down into the testable bandwidth. The idea of mass-loading the interface was first approached by Goldenberg and Shapiro [31]. Later, this was expanded by Kanda et al. in [32] where the masses were instrumented to estimate their dynamics and then the effects of these masses were removed from the system. This created an experimentally derived model that captured the interface effects due to the mass-loading. Chandler and Tinker successfully studied these mass additive methods analytically in [33] on a spacecraft application.

Despite the success of [31-33], the addition of this mass comes with some difficulties. Designing a mass that is large enough to have the desired interface loading while also being rigid in the frequency band of interest can be difficult. Adding this mass may also create a need for increased instrumentation as the rotations and translations of the added mass need to be measured. Also, when a mass is used to load an interface experimentally, the dynamic effects of the mass on the subcomponent must be removed prior to predicting the response of the built-up assembly. This removal process is known as substructure uncoupling [34] which is a less commonly used technique. Substructure uncoupling has been documented when it was used to remove rigid masses from a structure [9, 32, 35], Sjovall and Abrahamson further investigated these uncoupling procedures in [36]. They presented a FBS approach that makes use of the responses away from the connection point to address this.

Recently, Allen et al. have proposed a method termed the Transmission Simulator (TS) Method [25-28]. Their work builds upon past experience removing the effects of a mass-loading fixture, but does so in the modal domain instead of using the frequency response functions. In this method the transmission simulator is a fixture that mass-loads the interface between two subcomponents. A modal test is performed on a subcomponent with the transmission simulator attached which simulates the forces that would be located at the interface in the built-up structure. The effects of this fixture are then subtracted in the substructuring process leaving an experimental model for the original subcomponent but including the dynamics due to loading the interface. Predictions produced with the TS method were shown to give more accurate results for the system studied in [26]. This method was also demonstrated further by Rohe, as discussed in [37] on a few industrial structures.

As such, the scheme presented in Fig. 3 is an improvement over the scheme of Fig. 1 that uses only free modes of the front and aft casings. In Fig. 3, the experimental aft casing model benefits from a more realistic interface condition caused by the mass loading produced by the TS. Note that the TS must be subtracted before finalizing an assembly-level prediction.

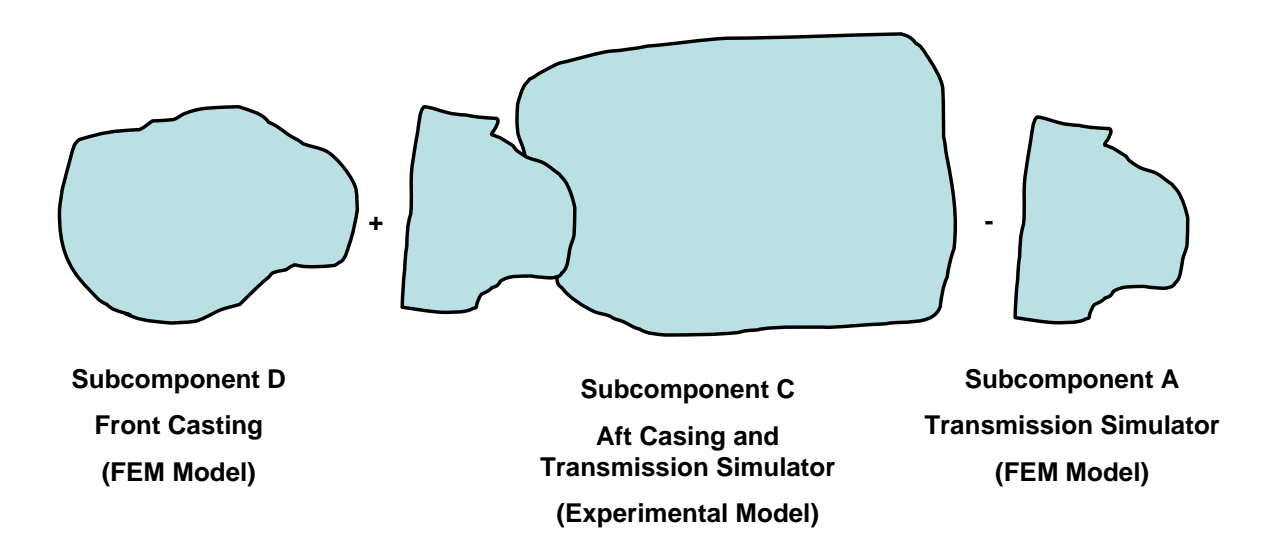


Figure 3. Transmission Simulator Substructuring Schematic

When obtaining an experimental model for Subcomponent C the transmission simulator is already attached. A finite element model of the front casing, Subcomponent D, is to be added to the system, while a negative copy of the transmission simulator will be removed. The DOF for all three subcomponents are concatenated into the block matrix equations of motion from Eqn. (3).

$$\begin{bmatrix}
\mathbf{I}_{C} & \mathbf{0} & \mathbf{0} \\
\mathbf{0} & \mathbf{I}_{D} & \mathbf{0} \\
\mathbf{0} & \mathbf{0} & -\mathbf{I}_{A}
\end{bmatrix}
\begin{bmatrix}
\ddot{\mathbf{\eta}}_{C} \\
\ddot{\mathbf{\eta}}_{D} \\
\ddot{\mathbf{\eta}}_{A}
\end{bmatrix} +
\begin{bmatrix}
\begin{bmatrix}
2\zeta_{C}\omega_{C} \\
\mathbf{0}
\end{bmatrix} & \mathbf{0} & \mathbf{0} \\
\mathbf{0} & \begin{bmatrix}
2\zeta_{D}\omega_{D} \\
\mathbf{0}
\end{bmatrix} & \mathbf{0} \\
\mathbf{0} & -\begin{bmatrix}
2\zeta_{A}\omega_{A} \\
\mathbf{\eta}_{D}
\end{bmatrix} \\
\mathbf{\eta}_{A}
\end{bmatrix} =
\begin{bmatrix}
\dot{\mathbf{\eta}}_{C} \\
\dot{\mathbf{\eta}}_{D} \\
\dot{\mathbf{\eta}}_{A}
\end{bmatrix} +
\begin{bmatrix}
\dot{\mathbf{\eta}}_{C} \\
\dot{\mathbf{\eta}}_{D} \\
\mathbf{\eta}_{D}
\end{bmatrix} +
\begin{bmatrix}
\dot{\mathbf{\eta}}_{C} \\
\mathbf{\eta}_{D} \\
\mathbf{\eta}_{A}
\end{bmatrix} =
\begin{bmatrix}
\dot{\mathbf{\eta}}_{C} \\
\dot{\mathbf{\eta}}_{D} \\
\dot{\mathbf{\eta}}_{A}
\end{bmatrix} +
\begin{bmatrix}
\dot{\mathbf{\eta}}_{C} \\
\dot{\mathbf{\eta}}_{D} \\
\dot{\mathbf{\eta}}_{A}
\end{bmatrix} +
\begin{bmatrix}
\dot{\mathbf{\eta}}_{C} \\
\dot{\mathbf{\eta}}_{D} \\
\dot{\mathbf{\eta}}_{A}
\end{bmatrix} +
\begin{bmatrix}
\dot{\mathbf{\eta}}_{C} \\
\dot{\mathbf{\eta}}_{D} \\
\dot{\mathbf{\eta}}_{D}
\end{bmatrix} +
\begin{bmatrix}
\dot{\mathbf{\eta}}_{C} \\
\dot{\mathbf{\eta}}_{D}
\end{bmatrix} +
\begin{bmatrix}$$

The transmission simulator method not only modifies the equations of motion but the constraint equations as well. Instead of applying strict enforcements of the physical constraints, as in Eqn. (4), the constraints are softened and satisfied in a least-squares sense. This is done by premultiplying the constraints by the pseudo-inverse of the transmission simulator mode shapes partitioned to the interface degrees of freedoms. This constraints the motion of the transmission simulator onto the orthogonal projection of the experimental system. This method is termed the Modal Constraints for Fixture and Subsystem (MCFS) [26], or simply Modal Constraints. The MCFS method brings the traditional CMS constraints, Eqn. (5), into the following softened form.

$$\begin{bmatrix} \mathbf{\Phi}_{A}^{+} & \mathbf{0} \\ \mathbf{0} & \mathbf{\Phi}_{A}^{+} \end{bmatrix} \begin{bmatrix} \mathbf{\Phi}_{C} & 0 & -\mathbf{\Phi}_{A} \\ \mathbf{0} & \mathbf{\Phi}_{D} & -\mathbf{\Phi}_{A} \end{bmatrix} \begin{Bmatrix} \mathbf{\eta}_{C} \\ \mathbf{\eta}_{D} \\ \mathbf{\eta}_{A} \end{Bmatrix} = \mathbf{\overline{B}} \begin{Bmatrix} \mathbf{\eta}_{C} \\ \mathbf{\eta}_{D} \\ \mathbf{\eta}_{A} \end{Bmatrix} = \{ \mathbf{0} \}$$

$$(15)$$

One problem that may arise when subtracting the effects of the transmission simulator occurs when the model of the fixture is not perfect. This could be due to modal truncation or discrepancies between the transmission simulator hardware and model. In some cases, errors in the subtraction can lead to negative mass or stiffness in the resulting predictions. Efforts have been made to diagnose and correct these negative mass and stiffness issues [27, 38].

The TS method is the primary substructuring technique used in this dissertation. Multiple examples of this method are highlighted including a small wind turbine in Chapter 2.2 and an assembly where a cylinder is connected to a round plate on one end through bolted connection in Chapter 2.3. In prior works and in Chapter 2, these methods have been established only for linear systems. This dissertation will extend these concepts to nonlinear systems. In order to accomplish this task, a method for modeling a nonlinear subcomponent and identifying such a nonlinear model from measurements is essential.

#### 1.4 Background - Joint Models

In order to assemble two substructures they must in some way be connected, often through the use of bolted joints. Joints have long been known to be a significant, if not the most significant, source of damping in built up assemblies [1, 2]. They are also frequently the source of nonlinearity in what would otherwise be a linear structure. However, even when joints behave linearly, their linear stiffness and damping properties are difficult to predict. Hence, when updating a finite element model a significant portion of the effort is focused on the joints.

Researchers have put significant effort into the modeling of joints between subcomponents. Often the motion of the joint is described by the slipping of the jointed surfaces. Slip can be better understood by breaking the slip phenomena into two regimes: micro-slip and macro-slip [39]. Micro-slip occurs when the stiffness of the joint remains intact while small slip displacements occur throughout the contact patch causing frictional energy dissipation. In contrast, macro-slip occurs when the stiffness of the joint is compromised. When this happens larger slip displacements are possible as discussed in [39]. There have been many attempts to create models that accurately describe these joint dynamics. In particular, these models seek to replicate the amplitude dependent changes in dissipation and stiffness that have been reported in various experiments and contact mechanics simulations.

Many of the models developed are based on Coulomb friction laws as discussed by Gaul [40] and Berger [41]. The Dohner model was presented in [42] which explored the construction of one-

dimensional joint models using cubic polynomial representations. Smallwood recognized a power law relationship of dissipation in the micro-slip regime and developed models to account for this in [43]. In that work, Smallwood coupled a Ramberg-Osgood plasticity model [44] with assumed Masing behavior [45] to develop a model that exhibits dissipation in the form of,

$$D = 4 \left(\frac{r-1}{r+1}\right) \left(\frac{F_R^2}{K_R}\right) \left(\frac{f_0}{F_R}\right)^{1+r}$$
 (16)

where D is the dissipation,  $F_R$  is a joint-force that separates the region of near-linear behavior from micro-slip,  $K_R$  is the low-amplitude stiffness of the joint, and  $f_0$  is the applied force on the joint model. The constant r is of particular interest as it relates to the power law dissipation slope which Smallwood hoped to capture with his model.

Another popular joint model that is used to simulate friction contains a spring in series with a Coulomb friction damper, which is referred to as a Jenkins element [39]. Iwan used a distribution of Jenkins elements in parallel, see Fig. 4, to model the hysteresis-type behavior of materials [46].

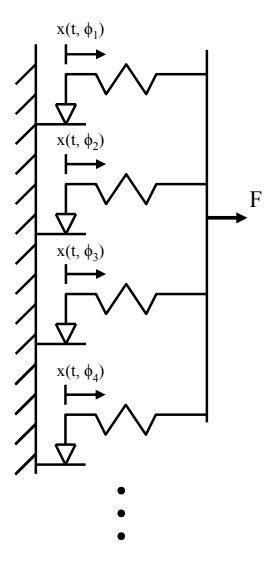


Figure 4. Iwan Element Schematic

In past efforts, Segalman and his colleagues at Sandia National Laboratories, pursued a multiyear project in which models for mechanical joints were derived and calibrated to match experimental force-dissipation measurements [47, 48]. The results showed that the joint parameters can be determined experimentally and implemented numerically into models to replicate the response including the effects of the joints. This greatly increases the cost of the response predictions so model reduction strategies were explored.

The 4-parameter Iwan model [48] establishes a power law dissipation relationship in the microslip regime, similar to that of the Smallwood model, while also adjusting for macro-slip load levels. This model includes several key characteristics of a joint's dynamic response including the joint slip force  $(F_s)$ , the joint stiffness  $(K_T)$ , and power law energy dissipation factors  $(\chi, \beta)$ . The dissipation per cycle is modeled by a 4-parameter Iwan model, and is written as,

$$D = 4F_{s}\phi_{\text{max}} \frac{\left(\frac{x}{\phi_{\text{max}}}\right)^{\chi+3}}{(\chi+3)} \frac{(\chi+1)/(\chi+2)}{\left[\beta + \frac{(\chi+1)}{(\chi+2)}\right]}$$
(17)

where  $\phi_{\text{max}}$  is the displacement at which the sliders shown in Fig. 4 all slip. The four parameters that are used for the Iwan model can be obtained by relating the stiffness and dissipation to the force across the joint model, see Fig. 5.

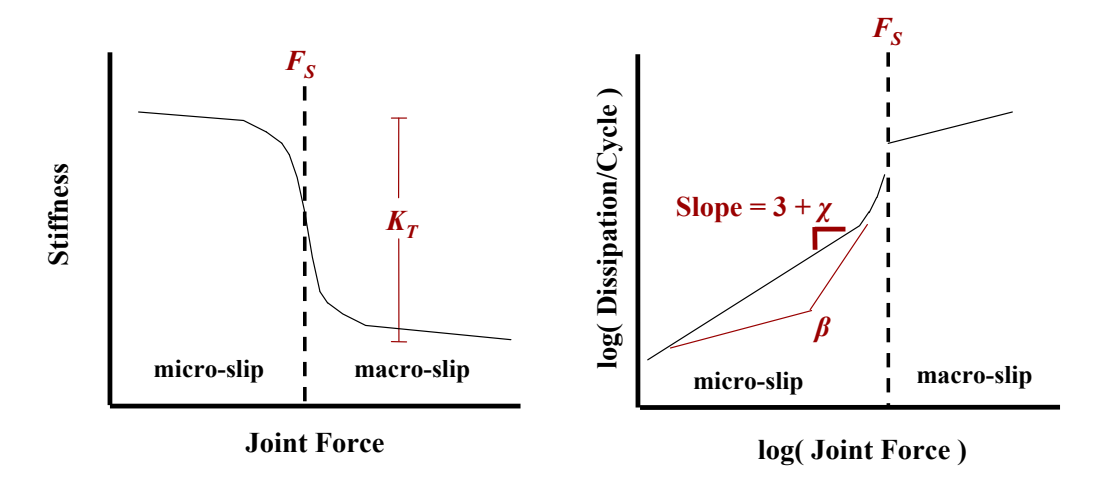


Figure 5. Visual aide for Iwan parameter definitions [39]

Physical joint models are practical for structures that have only a few discrete joints, however this becomes cumbersome when modeling a built-up structure with many joints. This means that in complicated structures one must characterize hundreds of parameters, which can be quite complicated and costly. As seen in Fig. 2, the jet engine casing is assembled through many bolted interfaces as each module is bolted to the assembly axially. Each of these discrete joints is a potential source of nonlinearity and each interface can have hundreds of bolts. To define the physical parameters for each of these joints would be costly and time consuming.

Recent research endeavors have suggested that instead of modeling each joint separately, one can model a complicated structure with a set of uncoupled modes each of which contains a nonlinear dynamic model. Segalman recently proposed to model each mode of a structure as an independent single degree of freedom system with an Iwan joint to represent the joint dynamics [49]. A rigorous theoretical foundation for models with uncoupled modes such as this was developed by Eriten et al. [50], who showed that energy transfer between modes can be negligible in the presence of weak nonlinearity unless their frequencies are close. Using this framework, the nonlinearity of each mode can be modeled individually. Segalman has applied this modal Iwan model approach to a simple spring mass system [51]. Following Segalman's approach each mode of the structure can be fit as a nonlinear model. In the jet engine example, instead of fitting hundreds of physical joints, one could parameterize just a few nonlinear modal joint models to describe the nonlinear behavior of the structure.

In [52], Allen and Deaner expanded the 4-parameter modal Iwan model by adding a viscous damper and linear spring in parallel with the Iwan element, see Fig. 6. This viscous damper accounts for the linear material damping that dominates each mode at very small amplitudes. Recently, Lacayo et al. began to more thoroughly explore the extent to which this modal approximation is accurate [53, 54].

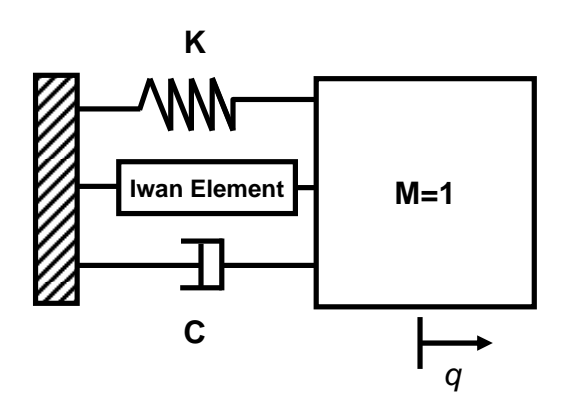


Figure 6. Schematic of SDOF model used for each modal degree of freedom

Allen and Deaner used two tools, the Hilbert transform algorithm developed by Sumali et al. [52, 55] and the Zeroed Early-Time FFT (ZEFFT) algorithm by Mayes and Allen [56], to characterize each mode of a structure. The ZEFFT algorithm is a simple time-frequency decomposition comparable to the short time Fourier transform, or wavelet transform, that allows one to quickly interrogate each mode to detect those modes that exhibit nonlinearity.

Once each mode has been screened and nonlinear modes have been identified, a Hilbert transform analysis can be used to extract the instantaneous frequency and damping of each single-harmonic in the signal. This analysis is only applicable to single-harmonic signals and so the measurement is often bandpass filtered to isolate a single-harmonic. Other researchers have instead employed empirical mode decomposition or other variants [50, 57, 58], but these algorithms are far from straightforward to use and are sometimes ineffective at separating close frequencies so they were not pursued in this work.

Once a single-harmonic signal has been obtained, the Hilbert transform can be computed. The signal is then smoothed by fitting a spline to the amplitude and phase as a function of time. These single-harmonic amplitude and phase fits can be related to the instantaneous frequency and damping of the time signal. Sapsis et al. [59] recently presented another interesting alternative, in which the local maxima of the velocity and displacement were fit to a spline function and then energy measures were derived to extract the instantaneous stiffness and damping.

This dissertation continues the works of Segalman, Allen, and Deaner using Iwan models in the modal framework. Additional model models are identified and utilized using methods such as the restoring force surface methods presented in [60] and summarized in [61]. It is assumed that tested structures are weakly nonlinear and the modes of each structure remain uncoupled. The ability to detect, characterize, and model modal nonlinearities is critical to the success of this research.

#### 1.5 Background - Nonlinear Substructuring

Dynamic substructuring involves enforcing compatibility and equilibrium constraints at the interface between subcomponents. The extension of this synthesis to nonlinear systems is trivial, however the challenge comes in determining the best model form of the nonlinear subcomponents. The model form presented in the previous section is only one of many possibilities that might be used to model a nonlinear subcomponent. This section reviews related literature on other forms that have been used to compute substructuring predictions. A few works [62-64] have extended linear frequency based substructuring into the nonlinear realm using the harmonic balance method. The harmonic balance method is used to compute an effective mass, stiffness and damping for each subcomponent. These subcomponent models are assembled using an iterative procedure to predict the nonlinear response of the assembly. More recently, Krack explored descriptions of individual subcomponents with nonlinear normal modes in [65]. Krack explores many examples of systems where one mode is dominant and nonlinear while others can be treated as linear. These nonlinear subcomponents are analyzed using the "single nonlinear mode method" of Szemplinska-Stupnicka [66] in which only one mode of the system is dominant and nonlinear. They recommend to investigate the nonlinearity of the mode shapes for the subcomponent. If the mode shapes do not change with vibration amplitude, it is reasonable to neglect any nonlinear coupling terms. In essence, this method provides similar findings to the weakly nonlinear assumptions explored in Section 1.4.

Recently, in [67], Kuether et al. developed an approach to couple two geometrically nonlinear simply supported beams. In their work, the component modes of the system were Craig-Bampton

nonlinear reduced order models (CB-NLROMS). These reduced order models retained coupled nonlinear forcing terms in each subcomponent.

Chong and Imregun used variable modal parameters to couple multiple nonlinear substructures, focusing on weakly nonlinear structures in [68-70]. They assume that the mode shape of a single important mode changes with amplitude and all other modes can be assumed to remain linear. In [70], Chong and Imregun begin with a set of assembled equations using a coupled stiffness matrix,  $\mathbf{K}_C$ , while  $\omega_A$  and  $\omega_B$  represents the linear natural frequencies of their respective subcomponents.

$$\begin{bmatrix} \mathbf{I}_{\mathsf{A}} & \mathbf{0} \\ \mathbf{0} & \mathbf{I}_{\mathsf{B}} \end{bmatrix} \begin{pmatrix} \ddot{\mathbf{\eta}}_{\mathsf{A}} \\ \ddot{\mathbf{\eta}}_{\mathsf{B}} \end{pmatrix} + \begin{bmatrix} \mathbf{\Phi}_{\mathsf{A}}^{\mathsf{T}} & \mathbf{0} \\ \mathbf{0} & \mathbf{\Phi}_{\mathsf{B}}^{\mathsf{T}} \end{bmatrix} \mathbf{K}_{\mathsf{C}} \begin{bmatrix} \mathbf{\Phi}_{\mathsf{A}} & \mathbf{0} \\ \mathbf{0} & \mathbf{\Phi}_{\mathsf{B}} \end{bmatrix} + \begin{bmatrix} \begin{bmatrix} \mathbf{\omega}_{\mathsf{A}}^{\mathsf{2}} & \mathbf{0} \\ \mathbf{0} & \begin{bmatrix} \mathbf{\omega}_{\mathsf{B}}^{\mathsf{2}} & \mathbf{0} \\ \mathbf{0} & \begin{bmatrix} \mathbf{\omega}_{\mathsf{B}}^{\mathsf{2}} & \mathbf{0} \end{bmatrix} \end{bmatrix} \begin{pmatrix} \mathbf{\eta}_{\mathsf{A}} \\ \mathbf{\eta}_{\mathsf{B}} \end{pmatrix} = \begin{pmatrix} \mathbf{\Phi}_{\mathsf{A}}^{\mathsf{T}} \mathbf{F}_{\mathsf{A}} \\ \mathbf{\Phi}_{\mathsf{B}}^{\mathsf{T}} \mathbf{F}_{\mathsf{B}} \end{pmatrix}$$
(18)

The eigenvectors and values for this coupled system are calculated. A modal amplitude for the nonlinear jth mode of interest,  $P_j$ , is assumed for the coupled system. Subcomponent modal amplitudes are then computed using the mode shapes and the assumed modal amplitude of the coupled system.

$$\{\mathbf{\eta}\}_{i} = \left[\Phi_{coupled}\right]_{i} \{\mathbf{P}\}_{i} \tag{19}$$

The subcomponent frequencies and mode shapes from Eqn. 18 are then updated based on the computed subcomponent modal amplitude. In this case, the nonlinearity at the subcomponent level is already understood. The eigenvectors and eigenvalues of the updated, coupled equations of motion can now be found. This process is repeated until the assumed modal amplitude is satisfied. In contrast, this dissertation focuses on weakly nonlinear modes where the mode shapes are not amplitude dependent, such as those described as weak nonlinearities in Section 1.4. This dissertation uses this weakly nonlinear modal framework to formulate reduced models for each subcomponent in a substructuring problem.

## 1.6 Scope of the Dissertation

This dissertation extends the traditional transmission simulator method to include nonlinear subcomponents and enables the prediction of nonlinear system response. This approach requires a

technique to identify and validate nonlinear modal models from experiments on realistic jointed structures. These nonlinear modal models capture the amplitude dependent stiffness and damping introduced by joints within an experimental subcomponent. Figure 7 shows an overview of the research presented in this dissertation to generate accurate nonlinear substructuring predictions for jointed structures. The steps boxed in the dashed red line are novel contributions to this research area as previous works only contain linear predictions.

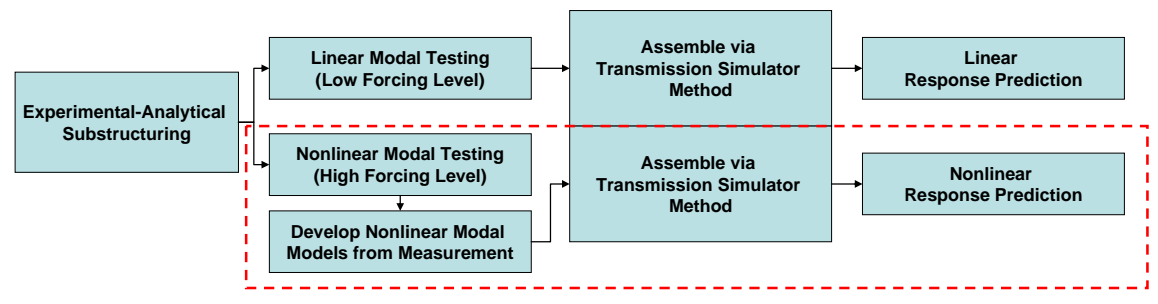


Figure 7. Overview of research presented in dissertation

Starting in Chapter 2, multiple examples of the Transmission Simulator method are completed on assumed linear assemblies. The methods used in Chapter 2 were first developed by Allen et al. in [25-28] and are applied in this dissertation on two jointed structures. First, this method is demonstrated on the Society of Engineering Mechanics dynamic substructuring test bed, the Ampair 600 Wind Turbine [71-73]. The second system in this study is a cylinder with an internal mass packed in foam that is connected to a plate via a continuous interface [74, 75], referred to as the Cylinder-Plate-Beam system. This continuous interface can be particularly challenging to standard CMS techniques and greatly benefits from the strengths of the transmission simulator method. It is important to understand how well linear substructuring techniques work, and know their limitations, before investigating any nonlinear substructuring practices. This provides a backdrop to the nonlinear problem and allows for an understanding of the accuracy of current linear prediction methods.

In Chapter 3, the proposed process of identifying the nonlinear behavior in a jointed structure is presented. This section focuses on two examples; an assembly of catalytic converters [3] and the Cylinder-Plate-Beam system discussed in Chapter 2. The catalytic converters are modeled using a set of

weakly nonlinear modes. These modes are assumed to remain uncoupled and the modal nonlinearity of each mode is described using a 4-parameter modal Iwan model [3]. This is the first rigorous investigation of this approach on a true industrial system.

The first foray into simulated nonlinear modal substructuring is discussed in Chapter 4. This is first completed on a spring-mass system. Next, this approach is used to investigate a numerical model of the Brake-Reuss Beam [76] using the same nonlinear modal framework to predict the motion of the built-up structure. Both of these examples are completed on numerical models of the system and do not account for experimental error or noise that will be present in a real experiment, but the second example does include modal truncation. However, the simulations do prove that substructuring can work as long as the structure remains in the micro-slip regime, and show that a substructure can be modeled effectively using uncoupled nonlinear modal models.

Chapter 5 extends this technique by applying the proposed nonlinear modal substructuring approach to actual hardware, in this case the Brake-Reuss Beam [76]. The experimental system is tested rigorously to obtain information about the subcomponent nonlinearity. Then, using the same nonlinear modal framework, nonlinear modal models for the structure are derived from test data. Finally, these nonlinear subcomponent models are used to obtain predictions for a modified assembly. These predictions are compared to a truth test performed on the modified system. Chapter 6 makes concluding remarks regarding the work presented in this dissertation and Chapter 7 briefly discuses ideas for future work in this research area.

#### 2 Linear Transmission Simulator Method

#### 2.1 Introduction

As discussed in Chapter 1.3, the Transmission Simulator (TS) method is a promising new method for experimental-analytical substructuring. The TS method is very relevant to industrial design problems. This chapter focuses on two examples of the linear Transmission Simulator method. The first example is on a small wind turbine, the Ampair 600 Wind Turbine [72], and is discussed in Chapter 2.2. The goal of this example is to construct predictions for the response of a three-bladed rotor assembly using the results from a single-blade-and-hub experiment. The second system studied in this chapter is a cylinder with an internal mass packed in foam that is connected to a plate via a continuous interface, referred to as the Cylinder-Plate-Beam system. This example is discussed in Chapter 2.3.

It is important to validate and understand the current capabilities of this technique on realistic systems and see how accurate they are compared to a truth test of the assembled structure. These assumed linear case studies are the first step in completing the primary goal of the completed thesis. In order to develop quality nonlinear substructuring predictions, the limitations and capabilities of the linear substructuring must be understood.

#### 2.2 Ampair 600 Wind Turbine Test Bed

The objective for this example is to generate a linear model for the dynamics of the hub and three blade assembly, pictured in Fig. 8 from the Ampair 600 Wind Turbine using the Transmission Simulator method. This model will be compared to a "truth model" that was derived from a modal test of the pictured assembly. The Ampair 600 Wind Turbine system is the benchmark system for the dynamic substructuring committee through the Society of Engineering Mechanics [72] and thus it was a practical choice for this example.

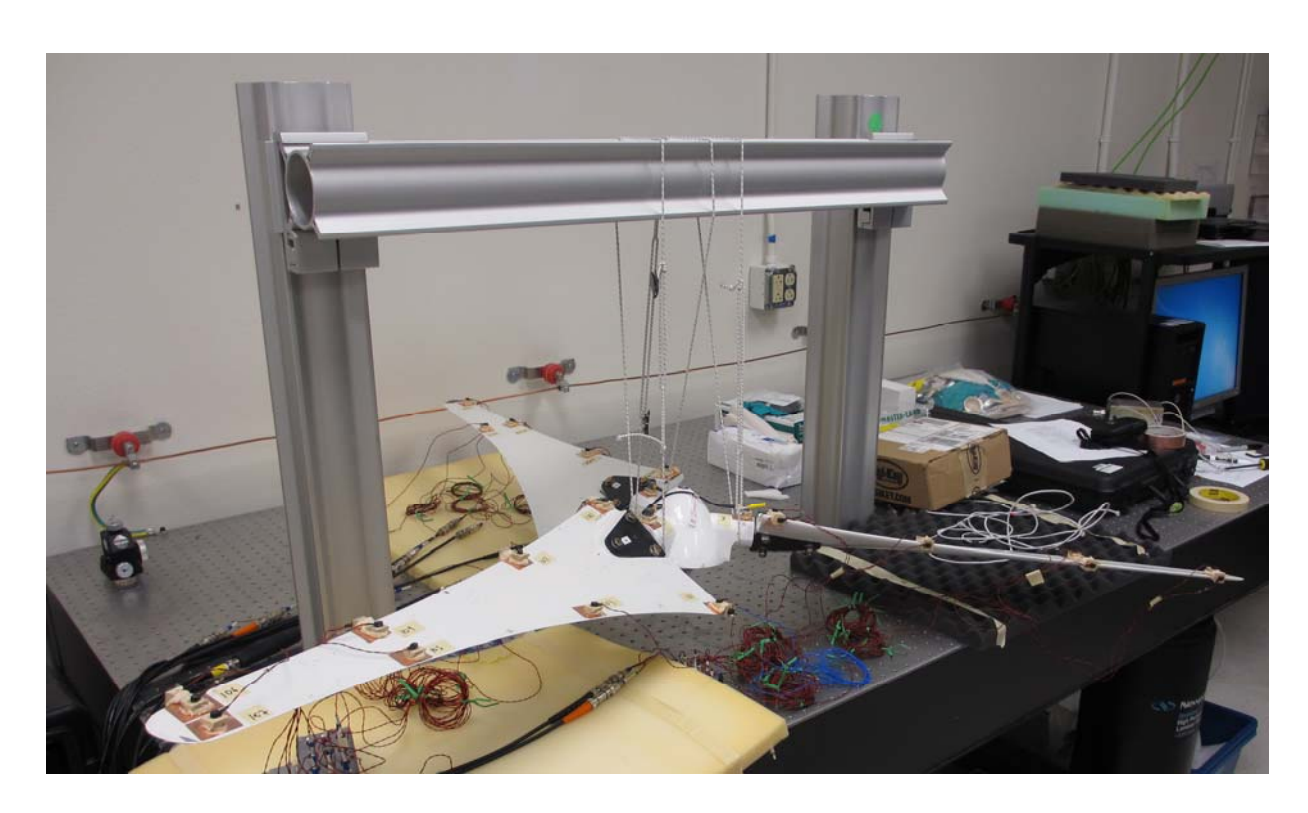


Figure 8. Experimental Set-up for Built-Up Three-Blade-and-Hub Assembly

To begin, a single-blade-and-hub assembly is tested to generate a subcomponent model. This subcomponent model is then replicated and rotated twice. By enforcing constraints, these subcomponent models can be used to develop predictions for the built-up assembly. Here, the hub acts as the transmission simulator, which is ideal as no additional hardware needs to be built in order to provide a fixture for the system. Figure 9 shows the substructuring schematic being used for this example. Three single-blade-and-hub subcomponents are coupled together, with two negative copies of the hub in order to develop accurate predictions.



Figure 9. Transmission Simulator Ampair 600 Wind Turbine Substructuring Schematic

### 2.2.1 Experimental Set-up

Previous tests containing these structures in similar configurations [71, 72, 77] show that the highest frequencies of interest would occur below 175 Hz. Therefore, the test range was set to 200 Hz for the truth model to allow the modes of interest (and a few higher) to be captured. For each test, a PCB 086C05 impact hammer was used to excite each structure's elastic modes. In an attempt to minimize nonlinearities in the system, the output of the hammer was amplified allowing extremely soft taps to be used during testing. The auto spectrum of this input was monitored during testing to ensure quality data was gathered. After completing the testing, modes were extracted from the experimental data using the Synthesize Modes And Correlate (SMAC) algorithm [78].

Tests were performed on two different structures in order to create both a full-assembly "truth" model and a subcomponent, or substructure, model. The first structure tested was the full-assembly, the hub connected to all three blades. Hardware assets were used from Sandia National Laboratories with the serial numbers for Blades A, B, and C being SNL009, SNL008, and SNL007, respectively. The second structure tested, the "substructure", was the turbine hub assembly with just Blade A connected.

Each third of the turbine was given its own Cartesian coordinate system with the x-direction along the blade, y-direction perpendicular to x-direction in the rotation plane, and z-direction along the axis of rotation. The origin of these coordinates systems was defined at a common point on the center of the hub. Figure 10 shows these coordinate systems as they are aligned with each blade.

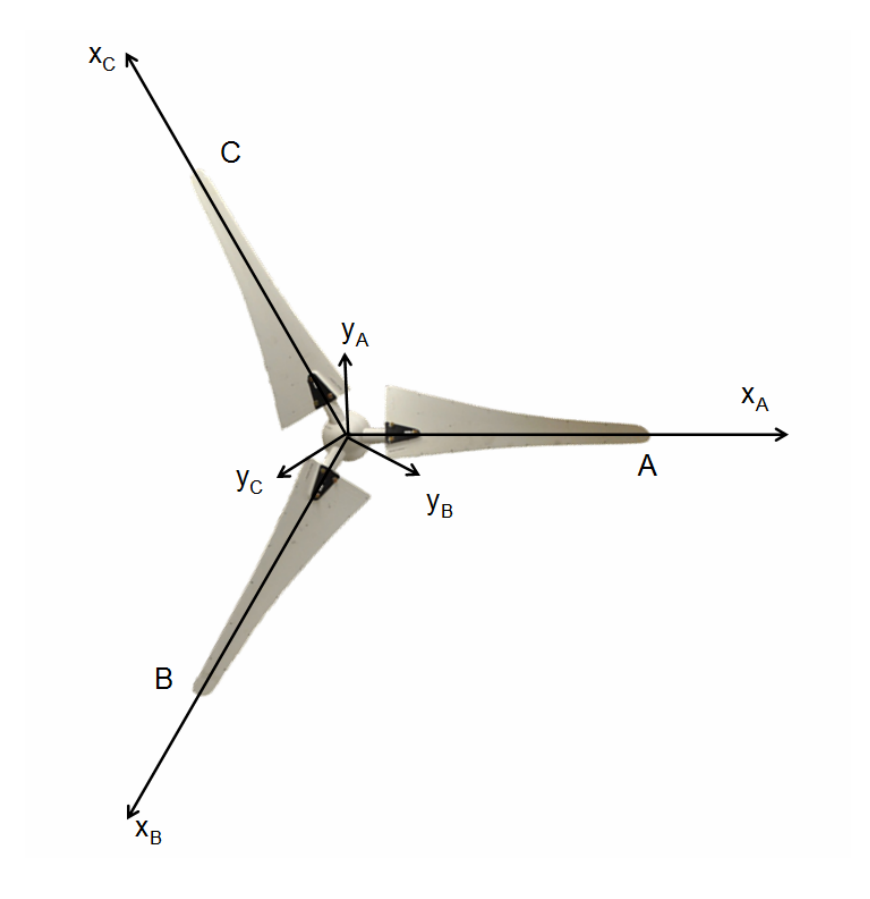


Figure 10. Built-Up Wind Turbine Prediction Coordinate Systems

The built-up assembly was instrumented with 36 single axis accelerometers as well as 3 triaxial accelerometers. The primary blade, Blade A, was instrumented based on previous testing [71, 72, 77] such that all mode shapes up to the third out-of-plane bending mode would be independent. This primary blade was instrumented more heavily than the secondary blades as this instrumentation would remain in place during subcomponent testing. Accelerometer locations and directions are depicted in Fig. 11.

Two uniaxial accelerometers were placed at four locations along the leading edge of each blade. These accelerometers were oriented in the local *y* and *z*-directions for each blade's coordinate system. Accelerometers were also placed along the trailing edge of the blade but mainly oriented in the *z*-direction with one accelerometer placed in the *y*-direction at the trailing edge root of each blade.

The transmission simulator, rotor hub, was instrumented with three triaxial accelerometers with a higher sensitivity. This higher sensitivity was required because hub motion tended to be very small compared to the light flexible blades. These triaxial accelerometers were placed on the branch extending

from the hub associated with each blade. Additionally, one high sensitivity uniaxial accelerometer was placed on the Blade A sector of the hub pointed in the *y*-direction

Blocks were used to align the accelerometers in the local blade displacement coordinate systems with accelerometers on the blade face pointing in the *z*-direction and those on the trailing and leading edge in the *y*-direction. These wood blocks were taken into account when analytically constructing rigid body modes for the different assemblies.

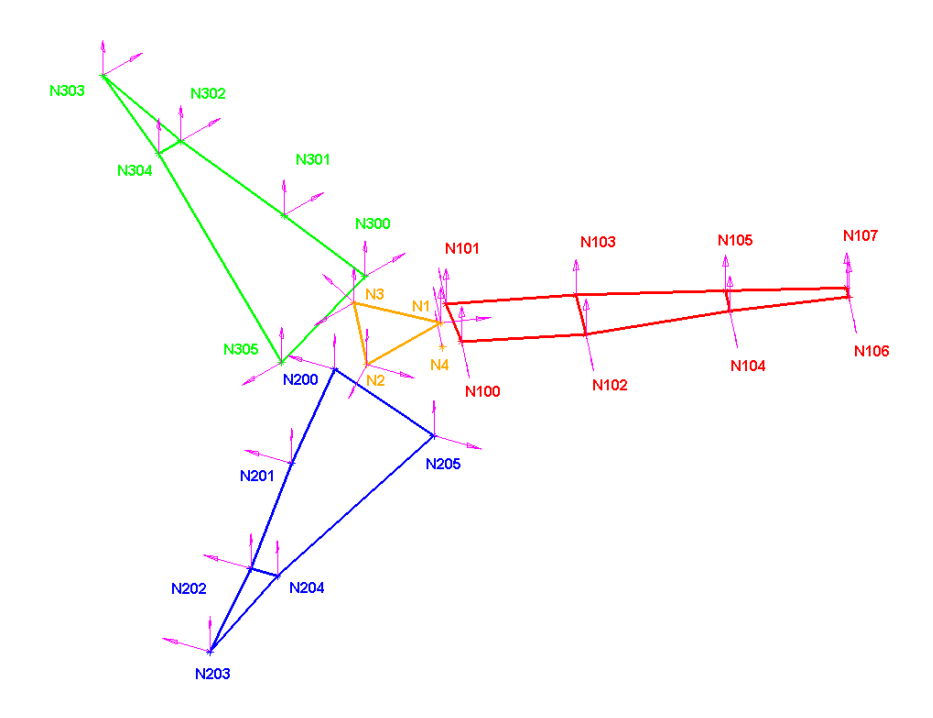


Figure 11. Instrumentation Placement

The built-up assembly was suspended from a rig on an optical table using bungee cords to simulate a free-free condition as seen in Fig. 8. Previous work showed the lowest elastic mode to occur at about 20 Hz. In an effort to minimize error due to the boundary conditions, the bungee cords provided a rigid body bounce mode around 2 Hz. This achieved a desired ratio between the elastic and rigid mode frequencies in order to minimize error due to boundary conditions as discussed in [79].

## 2.2.2 Truth Assembly Results

The suspended structure was excited at several drive points in the usual attempt to find the best location to excite each individual mode. Measurements were gathered from impact forces applied on the blades and on the rotor hub to fully understand the system. The drive points on the rotor hub provided the highest quality results, not because they excited the modes the most, but because they excited the modes well enough and produced FRFs with the most linear characteristics. To create a truth model for the built-up assembly, the measured response from the best driving point was used to calculate the modal parameters for each elastic mode.

Analytical rigid body mode shapes were calculated using the moments of inertia and center of gravity detailed in [71]. With the larger number of accelerometers, and positioning blocks, it was decided that the mass of this instrumentation was not negligible in the calculation of the mass properties, as such, the mass of these objects was accounted for when calculating the mass properties of the system. These updated mass properties are listed in Table 1.

Table 1. Mass properties for built-up assembly

	<b>Entire Rotor</b>
Mass	6.29 kg
$cg_x$	0.00 m
$cg_y$	0.00 m
$cg_z$	-0.0673 m
$I_{xx}$	$0.221 \text{ kg-m}^2$
$I_{yy}$	$0.224 \text{ kg-m}^2$
$I_{zz}$	$0.441 \text{ kg-m}^2$

The analytically generated rigid body modes were combined with nine elastic modes extracted from impact testing, see Table 2. Light hammer excitations were used in an attempt to avoid nonlinearities due to the jointed connection and only excite a linear response in the system. Complex modal indicator functions (CMIFs) are shown for each of the drive points in Fig. 12. No single excitation point was used as a reference for all the modes. Red circles in the figure indicate which modes were

selected from each reference. This truth test is only one realization of truth, since there is variability in individual blades as well as the clearances in the hub brackets holding the blades in place.

Table 2. Extracted and analytically calculated modal parameters for the build up assembly

Mode	Frequency [Hz]	Damping Ratio ζ [%]	Description of Motion	Reference/Source
1	0.00	1.00%	x direction translation	Analytical
2	0.00	1.00%	y direction translation	Analytical
3	0.00	1.00%	z direction translation	Analytical
4	0.00	1.00%	rotation about x	Analytical
5	0.00	1.00%	rotation about y	Analytical
6	0.00	1.00%	rotation about z	Analytical
7	20.56	1.00%	1 <sup>st</sup> Bending, 3 Blades in Phase	1Z
8	27.78	0.98%	1 <sup>st</sup> Bending, Blade C out of Phase	1Z
9	29.03	0.87%	1 <sup>st</sup> Bending, Blade B out of Phase	1Z
10	61.10	1.71%	Edge-wise Mode, Blade C out of phase	4Y
11	64.29	1.27%	Edge-wise Mode, Blade B out of phase	4Y
12	70.68	1.11%	2 <sup>nd</sup> Bending, 3 Blades in Phase	1Z
13	99.40	1.48%	2 <sup>nd</sup> Bending, Blade C out of Phase	3Z
14	102.95	1.08%	2 <sup>nd</sup> Bending, Blade B out of Phase	3Z
15	155.00	1.33%	3 <sup>rd</sup> Bending, 3 Blades in Phase	1Z

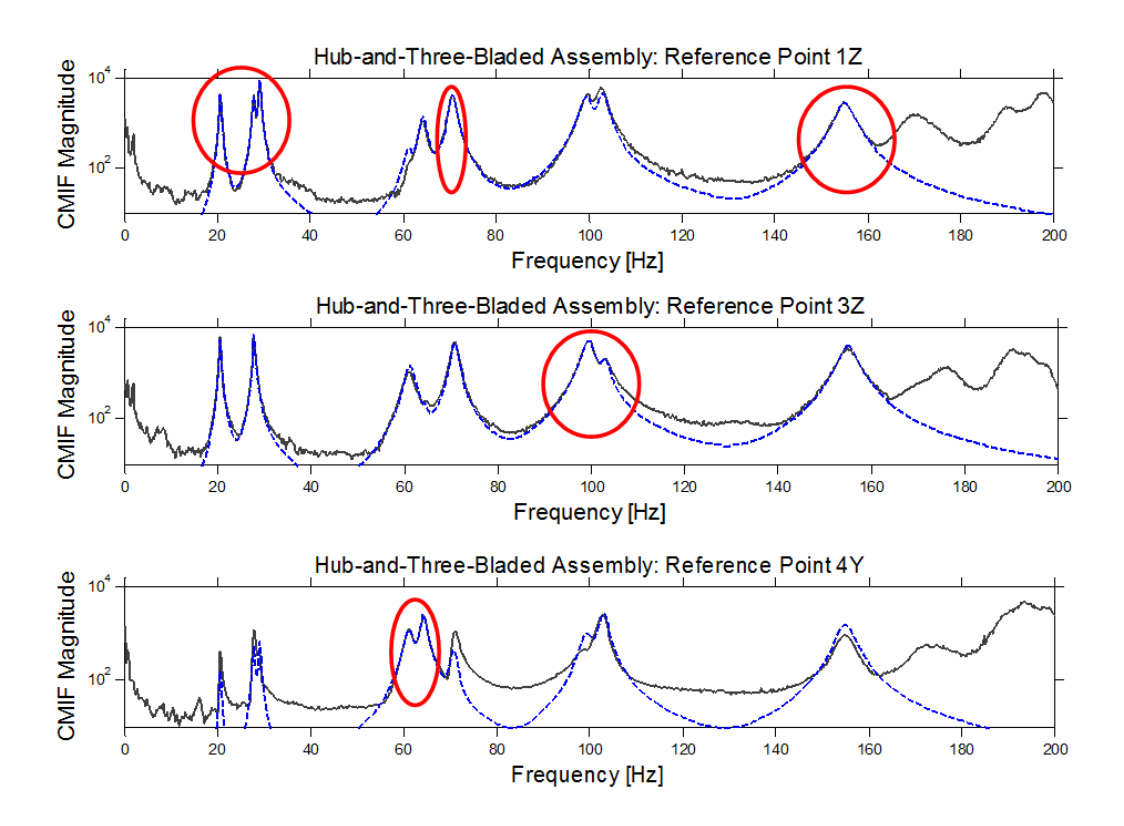


Figure 12. CMIFs for Truth Model (Blue) and Drive Point Measurements (Black)

### 2.2.3 Subcomponent Test Results

The next measurement to be completed was the single-blade-and-hub subcomponent test. Blades B and C were removed from the hub leaving only Blade A connected. The accelerometers on Blade A were not removed to preserve their location relative to the hub-and-three-bladed testing. Blade A was also not disassembled from the hub in order to preserve the joint connection from the assembly level truth test. Measurements were taken up to 200 Hz in order to capture up to the first three out-of-plane bending modes. The test set-up for the subassembly system can be seen in Fig. 13.

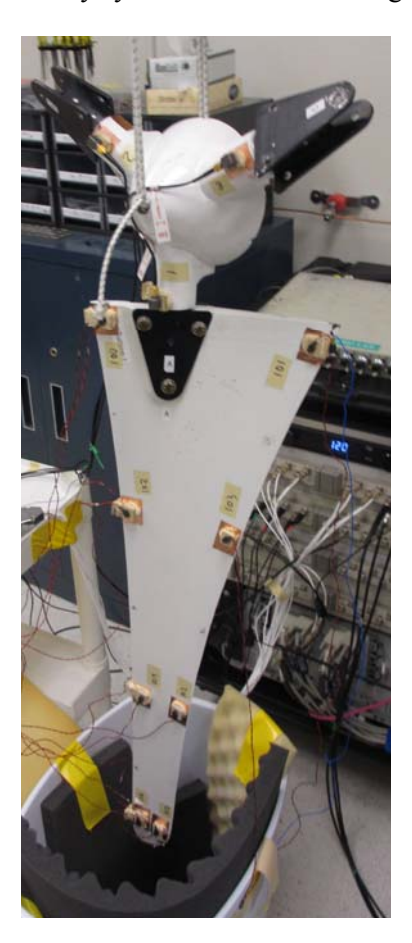


Figure 13. Experimental Set-up for Single-Blade-and-Hub Subassembly

Mass properties of the substructure were calculated using geometry and assumed symmetry properties of the hub-and-three-bladed system. Analytical rigid body modes were again calculated using the mass properties of the system, see Table 3.

Table 3. Mass properties for subassembly

_	<b>Entire Rotor</b>
Mass	4.52 kg
$cg_x$	0.0756 m
$cg_y$	0.0000 m
$cg_z$	-0.0632 m
$I_{xx}$	$0.0252 \text{ kg-m}^2$
$I_{yy}$	$0.0972 \text{ kg-m}^2$
$I_{zz}$	$0.1414 \text{ kg-m}^2$

The subsystem was similarly tested at several drive points in order to determine the excitation locations that provided the best measurement for each of the subsystem's elastic modes. The six analytically generated rigid body modes were combined with five elastic modes extracted from the impact tests, see Table 4. Again, each elastic mode was selected from the strongest responding drive point. CMIFs for those selected drive points can be seen in Fig. 14. Hammer strikes in the z-direction were found to easily excite bending and torsional modes while a y-direction strike was required to excite the blade in edgewise motion. The modes extracted from each reference are circled in red.

Table 4. Extracted and analytically calculated modal parameters for the subassembly

Mode	Frequency [Hz]	Damping Ratio ζ [%]	Description of Motion	Reference/Source
1	0.00	1.00%	x direction translation	Analytical
2	0.00	1.00%	y direction translation	Analytical
3	0.00	1.00%	z direction translation	Analytical
4	0.00	1.00%	Rotation about <i>x</i>	Analytical
5	0.00	1.00%	Rotation about <i>y</i>	Analytical
6	0.00	1.00%	Rotation about z	Analytical
7	29.84	0.91%	1 <sup>st</sup> Bending	3Z
8	86.75	0.92%	2 <sup>nd</sup> Bending	3Z
9	149.82	1.51%	Edgewise Motion	3Z
10	178.25	2.62%	1 <sup>st</sup> Torsion	4Y
11	195.10	1.30%	3 <sup>rd</sup> Bending	3Z

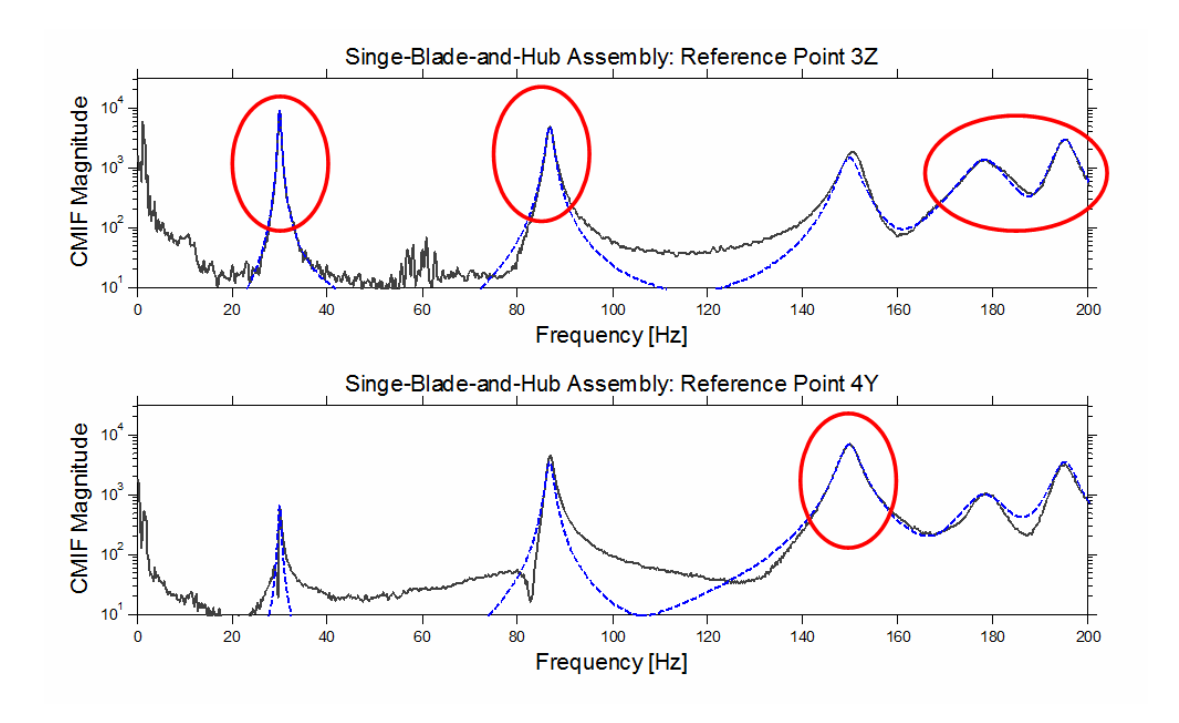


Figure 14. CMIFs for Subcomponent Model (Blue) and Drive Point Measurements (Black)

## 2.2.4 Substructuring Methodology

The transmission simulator method was utilized in order to assemble the three subcomponent systems into an assembled structure. Three copies of the experimental subcomponent model were rotated and added together linking the rotated degrees of freedom associated with the triaxial accelerometers located on the rotor hub (transmission simulator). Two analytical copies of the transmission simulator were subtracted in order to achieve accurate substructuring predictions.

The same rotor hub was used as a transmission simulator in a past experiment and was found to have a first elastic natural frequency above 1200 Hz [71]. This first elastic mode is far beyond the scope of the current test so only the rigid body modes of the transmission simulator were used to couple the systems.

For the following calculations, the subscript A represents the first blade, Blade A, with B, and C, representing the second and third blade respectively; the subscript TS represents the transmission simulator (rotor hub). The modal parameters  $\omega$  and  $\zeta$  represent the natural frequencies and damping

ratios of their respective subsystems and  $\Phi$  represents the associated mode shapes. The subcomponent modal degrees of freedom are denoted by vectors  $\mathbf{q}$ . The modal system of equations for this structure takes form by stacking the three subassemblies with two negative copies of the transmission simulator as shown in Eqn. (20).

$$\begin{bmatrix} \mathbf{I}_{A} & \mathbf{0} & \mathbf{0} & \mathbf{0} \\ \mathbf{0} & \mathbf{I}_{B} & \mathbf{0} & \mathbf{0} \\ \mathbf{0} & \mathbf{0} & \mathbf{I}_{C} & \mathbf{0} \\ \mathbf{0} & \mathbf{0} & \mathbf{0} & -2\mathbf{I}_{TS} \end{bmatrix} \begin{pmatrix} \ddot{\mathbf{q}}_{A} \\ \ddot{\mathbf{q}}_{B} \\ \ddot{\mathbf{q}}_{C} \\ \ddot{\mathbf{q}}_{TS} \end{pmatrix} + \begin{bmatrix} 2\zeta_{A}\omega_{A} & \mathbf{0} & \mathbf{0} & \mathbf{0} \\ \mathbf{0} & 2\zeta_{B}\omega_{B} & \mathbf{0} & \mathbf{0} \\ \mathbf{0} & \mathbf{0} & 2\zeta_{C}\omega_{C} & \mathbf{0} \\ \mathbf{0} & \mathbf{0} & \mathbf{0} & -4\zeta_{TS}\omega_{TS} \end{bmatrix} \begin{pmatrix} \dot{\mathbf{q}}_{A} \\ \dot{\mathbf{q}}_{B} \\ \dot{\mathbf{q}}_{C} \\ \mathbf{0} & \mathbf{0} & \mathbf{0} & \mathbf{0} \\ \mathbf{0} & \mathbf{0} & \mathbf{\omega}_{C}^{2} & \mathbf{0} \\ \mathbf{0} & \mathbf{0} & \mathbf{0} & -2\omega_{TS}^{2} \end{bmatrix} \begin{pmatrix} \mathbf{q}_{A} \\ \mathbf{q}_{B} \\ \mathbf{q}_{C} \\ \mathbf{q}_{TS} \end{pmatrix} = \begin{cases} \mathbf{\Phi}_{A}^{T}\mathbf{F}_{A} \\ \mathbf{\Phi}_{B}^{T}\mathbf{F}_{B} \\ \mathbf{\Phi}_{C}^{T}\mathbf{F}_{C} \\ 2\mathbf{\Phi}_{TS}^{T}\mathbf{F}_{TS} \end{cases}$$

The constraints for this system are the connection points on the transmission simulator. These are nodal locations 1, 2, and 3 from Fig. 11. When coupling the three subassemblies together Node 1 from the Blade A subassembly must be linked to Node 3 from the Blade B subassembly and Node 2 from the Blade C subassembly respectively.

$$\begin{bmatrix} \mathbf{\Phi}_{TS}^{+} & \mathbf{0} & \mathbf{0} \\ \mathbf{0} & \mathbf{\Phi}_{TS}^{+} & \mathbf{0} \\ \mathbf{0} & \mathbf{0} & \mathbf{\Phi}_{TS}^{+} \end{bmatrix} \begin{bmatrix} \mathbf{\Phi}_{A} & \mathbf{0} & \mathbf{0} & -\mathbf{\Phi}_{TS} \\ \mathbf{0} & \mathbf{\Phi}_{B} & \mathbf{0} & -\mathbf{\Phi}_{TS} \\ \mathbf{0} & \mathbf{0} & \mathbf{\Phi}_{C} & -\mathbf{\Phi}_{TS} \end{bmatrix} \begin{bmatrix} \mathbf{q}_{A} \\ \mathbf{q}_{B} \\ \mathbf{q}_{C} \\ \mathbf{q}_{TS} \end{bmatrix} = \begin{bmatrix} \mathbf{0} \\ \mathbf{0} \\ \mathbf{0} \\ \mathbf{0} \end{bmatrix}$$
(21)

Using the methodology detailed in Chapter 1.2, substructuring predictions for the built-up structure were generated by enforcing constrains to connect the individual subcomponents.

#### 2.2.5 Substructuring Predictions

The linear substructuring predictions were compared to the measured linear results as displayed in Table 5. Because some modes of the system were found to be closely spaced these modes had to be correlated based on their Modal Assurance Criterion (MAC) values [80]. This identification was important when looking at the 8<sup>th</sup> and 9<sup>th</sup> substructured modes as well as the 13<sup>th</sup> and 14<sup>th</sup> These modes

could be identified by MAC values as well as visual representation the MAC values and modal parameter comparisons can be seen in Table 5.

Table 5. Substructuring Predictions for the Ampair 600 Wind Turbine

Truth Mode	Frequency [Hz]	Damping Ratio ζ [%]	Predicted Mode	Predicted Frequency [Hz]	Frequency Error [%]	Predicted Damping	Damping Error	MAC
7	20.56	1.00%	7	23.49	14.26%	0.73%	-27.19%	.9912
8	27.78	0.98%	9	28.33	2.00%	0.86%	-12.07%	.7655
9	29.03	0.87%	8	28.03	-3.44%	0.85%	-1.88%	.8808
10	61.10	1.71%	10	66.53	8.91%	0.71%	-58.31%	.9422
11	64.29	1.27%	11	66.67	3.72%	0.71%	-44.03%	.9787
12	70.68	1.11%	12	77.33	9.41%	0.84%	-23.71%	.9402
13	99.40	1.48%	14	96.30	-1.75%	1.00%	-32.17%	.8618
14	102.95	1.08%	13	97.66	-6.45%	0.99%	-8.82%	.8849
15	155.00	1.33%	15	167.26	7.91%	1.29%	-3.05%	.7850

By inspection of Table 5, some trends can be identified. The predictions for first, second, and third in-phase out-of-plane bending modes (7, 12 and 15) are too high in frequency. Three of the four anti-symmetric out of plane bending modes (9, 13 and 14) are low in frequency. The edgewise modes (10 and 11) are high in frequency. These frequencies errors establish a baseline for a linear substructuring prediction.

The substructured damping ratios errors are also displayed in Table 5. Some modes (9 and 15) are quite close in damping while others haves errors as high as 58%. The correlation of modes between the substructured and truth models could be determined either by MAC as seen in Fig. 15 or visual comparison as seen in Figs. 16 and 17. Figure 16 contains the bending modes in an isometric view while Fig. 17 shows the edgewise modes in the *xy*-plane. These error levels are slightly elevated for a typical linear substructuring prediction and possible error sources are discussed in Section 2.2.6.

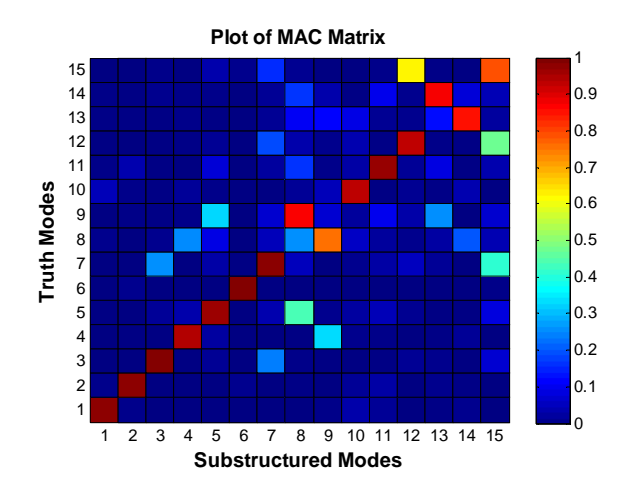


Figure 15. MAC between Truth and Substructuring Predictions

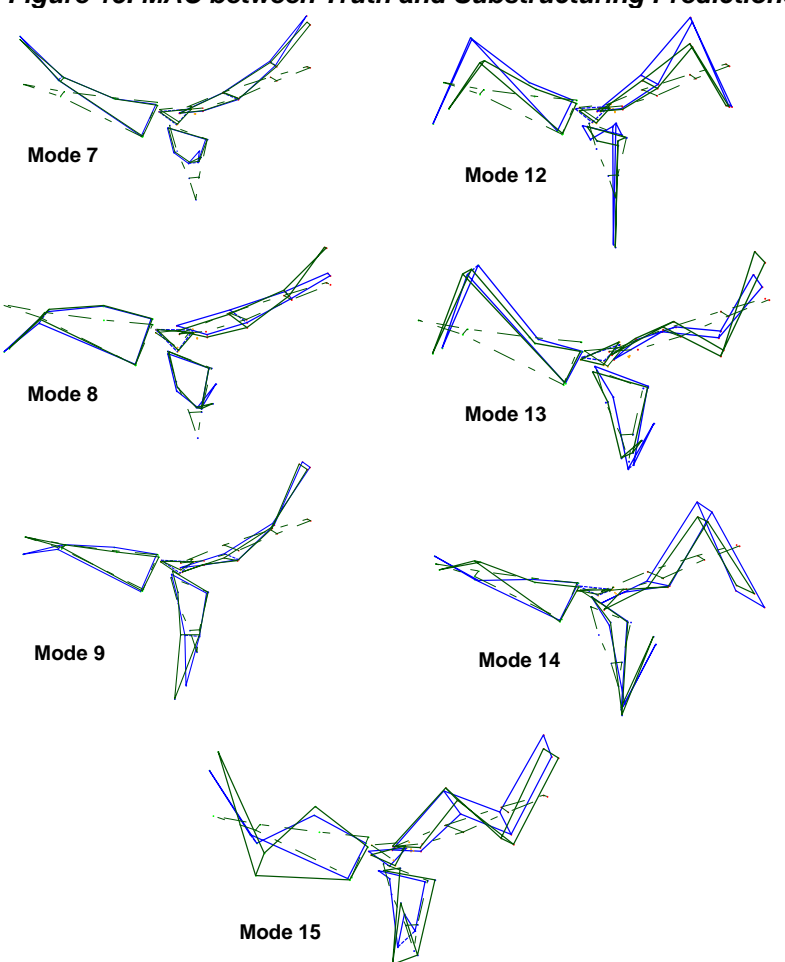


Figure 16. Bending mode shape comparisons (Blue - Substructuring Prediction, Green - Truth Test, Dashed - Undeformed)

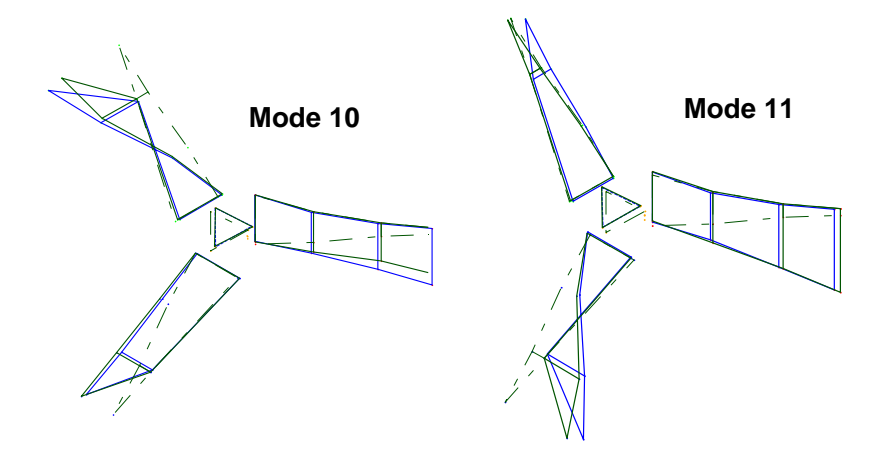


Figure . Edgewise mode shape comparison (Blue - Substructuring Prediction, Green - Truth Test, Dashed - Undeformed)

### 2.2.6 Possible Sources of Error

There were errors of up to 15% in natural frequency, 59% in damping and MAC values as low as 0.7655. Several issues could lead to these errors that could be investigated further with additional study. Some important experimental checks and possible error sources will be mentioned in this section. Modal truncation errors are known to exist but they are not addressed in this exercise.

Previous work [81] has shown that the most important mode shapes to obtain accurately are the rigid body mode shapes. When analytically adding rigid body modes to the experimental data, a check can be performed to ensure the analytically derived rigid body modes are a good match of the system that was tested. In this case, the derived rigid body mode FRF is overlaid with a with the driving point FRF taken from experimental data. Rigid body modes are often hard to extract, but the masslines of these rigid body modes can be compared in such a plot. Figure 18 shows a massline comparison for this substructure. After the rigid body frequency, around 1-2 Hz, the massline magnitude should be similar between the analytical and measured FRFs. If this is not true, the mass properties used to calculate the rigid body modes may be off and could be adjusted to get a better model of the system.

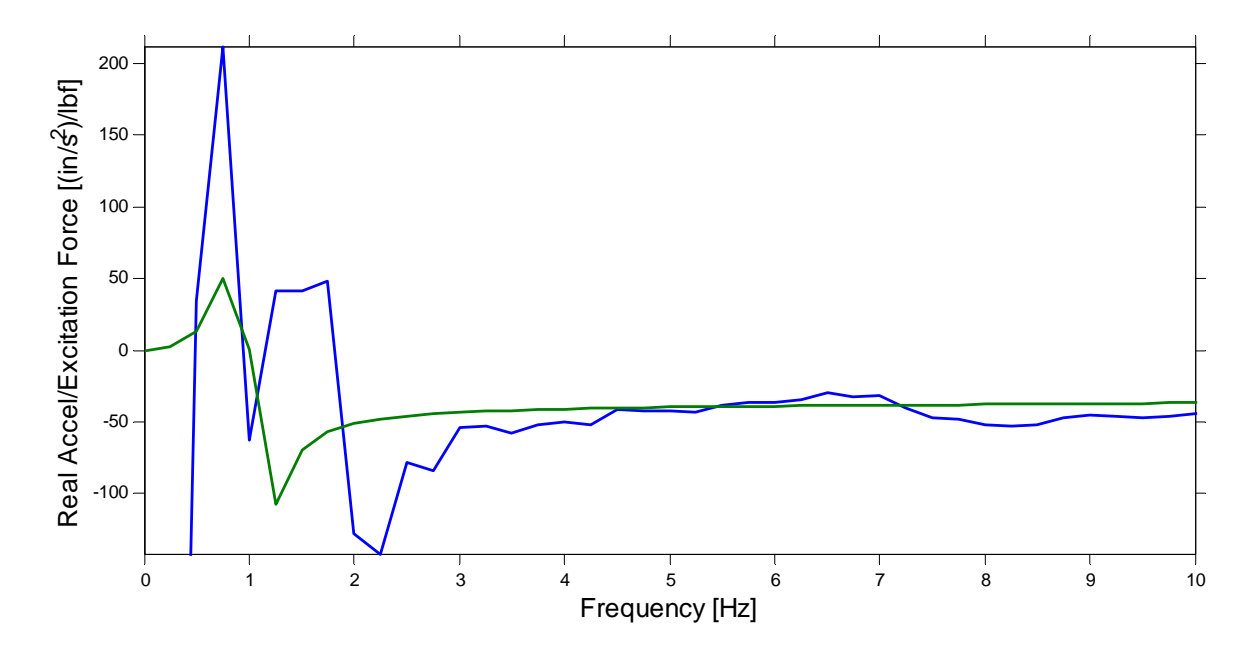


Figure 18. Rigid body massline comparison (Blue - Measured Data, Green - Analytical Model)

Additional best practices were followed when setting up and performing the experiments. Hammer calibration lab reports showed up to 15% variation for hammer measurement sensitivity. To mitigate this large error source, the hammer sensitivity was adjusted using a large block of known mass with a high sensitivity accelerometer attached. The hammer sensitivity was adjusted and checked to within accelerometer specified accuracy.

The accelerometers used on the rotor hub and Blade A were not removed between the testing of the truth assembly and single-blade-and-hub system. Therefore, they are in the same position from test to test. Blades B and C were instrumented individually for the truth test. Small discrepancies were found in the placement of the accelerometers on Blades B and C when compared to those of Blade A. These deviations on the order of one-eighth of an inch could lead to errors when results from Blade A are rotated and assumed to be in the same locations but in the Blade B and C coordinate systems. An additional substructuring exercise was completed using the six degrees of freedom of the center of mass of the hub as the connection degrees of freedom to abate these measurement discrepancies. This method led to a small change in natural frequency (less than 2%).

This example was completed assuming the transmission simulator was completely rigid and therefore only the rigid body modes of the transmission simulator were used. The flanges were mounted on a shaft that extends into a mechanism within the hub. This mechanism was potted, but it was observed that small amounts of flexibility may still be present in the flanges of the hub. Ignoring this flexibility means the transmission simulator model was too stiff and may have led to the increased natural frequencies as seen in modes that strain this potting.

### 2.2.7 Ampair Wind Turbine Remarks

This example used results from a modal test of a single-blade-and-hub substructure to create predications for an assembled structure. This substructure was rotated and linked together generating three blades and three hubs (transmission simulators), thus two of the hubs were analytically removed. The results of this substructuring study were then compared to a truth experiment conducted on the full hub-and-three-bladed assembly. The rigid body modes for these cases were constructed from mass properties.

After substructuring, all elastic modes could be correlated to the truth model either through MACs or using visual shapes. The worst frequency error was about 15% in the first mode. The damping ratios were the most difficult to predict with error as high as 55%. MAC values ranged from 0.77 to 0.99. This example used multiple fully experimental substructures, for the three-blade-and-hub subassemblies, and coupled them together along with negative copies of the rigid transmission simulator. The next example couples an experimental substructure to a finite element model of the transmission simulator, including elastic motion.

### 2.3 Cylinder-Plate-Beam System

#### 2.3.1 Introduction

This section contains another example using the Transmission Simulator method from Chapter 1.3. This example involves the Cylinder-Plate-Beam (CPB) system which consists of a cylinder packed with pressed foam that houses an internal mass. At one end of the cylinder, a plate and beam are attached to the system to simulate the rest of a structure of interest. The cylinder, plate, and beam are made of 6061 T6 aluminum. The cross section of a solid model for this system is shown in Fig. 19.

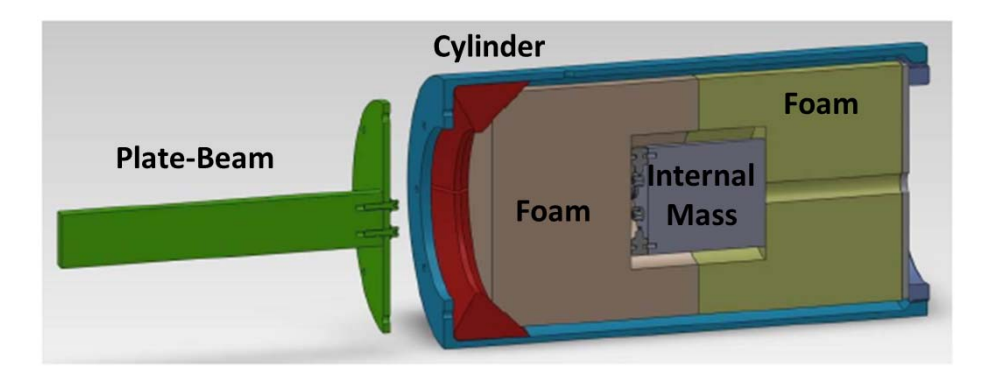


Figure 19. Solid Model of Cylinder-Plate-Beam System

The goal of this study is to estimate a model for the dynamics of the foam and the internal mass. These internals are extremely challenging to model because the foam's material properties are poorly defined and depend nonlinearly on the preload. In addition, the contact conditions between the foam and the rest of the structure are not known.

For this example, the full CPB system is considered Substructure C and is tested in order to deduce an experimental model for the internals components. Both the transmission simulator and Craig-Mayes methods can easily be applied using a finite element model of the transmission simulator, Substructure A, (consisting of the beam, plate and cylinder) leaving an experimental model for the foam and internal mass. To validate this model of the internals, a design modification has been added to the system. This design modification consists of a beam, plate, and cylinder external system but with a mass attached near the end of the beam. This simulates a situation in which the substructure model would be

used to predict the response after the other substructures have been modified. A validation test was completed to check the accuracy of the substructuring predictions. Figure 20 shows the different subcomponents being used in this substructuring example.

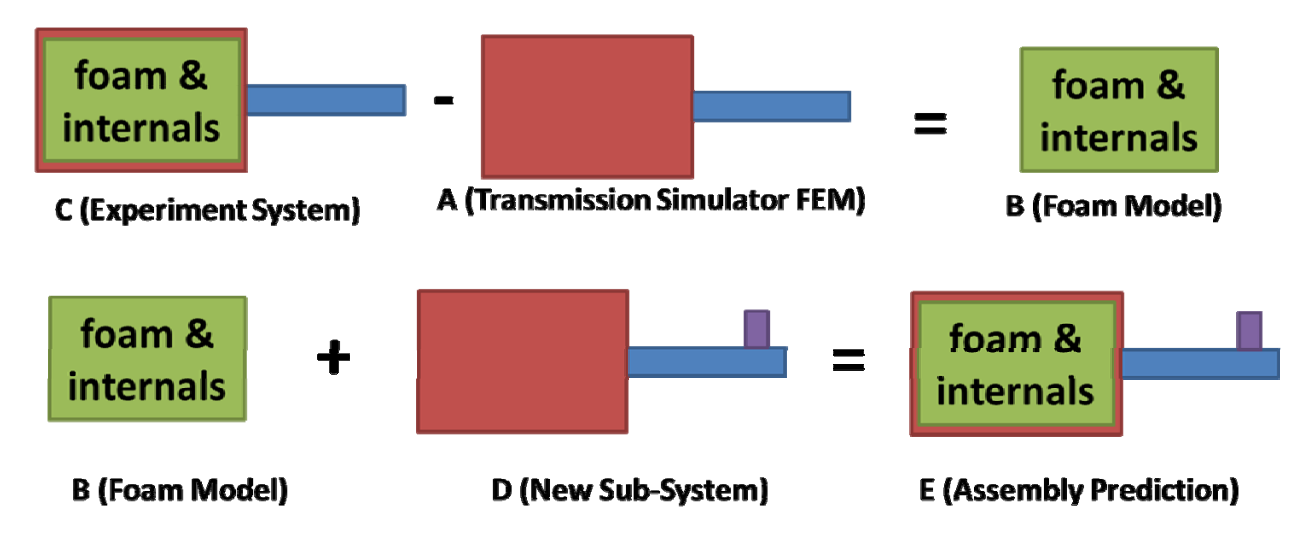


Figure 20. Dynamic Substructuring Schematic for the CPB System

# 2.3.2 Experiment

A modal test was completed for both the CPB system and the mass-loaded truth assembly. The system was instrumented with 18 triaxial accelerometers with sensitivities of 100 mV/g. Fifteen of these accelerometers were placed on the external side of the hardware (twelve on the can at three axial stations with four equally spaced around the circumference at each station and three on the beam). The remaining three triaxial accelerometers were placed on the internal mass, which is packed between the blocks of foam. Figure 21 shows the experimental set up for the CPB system with and without the added mass.

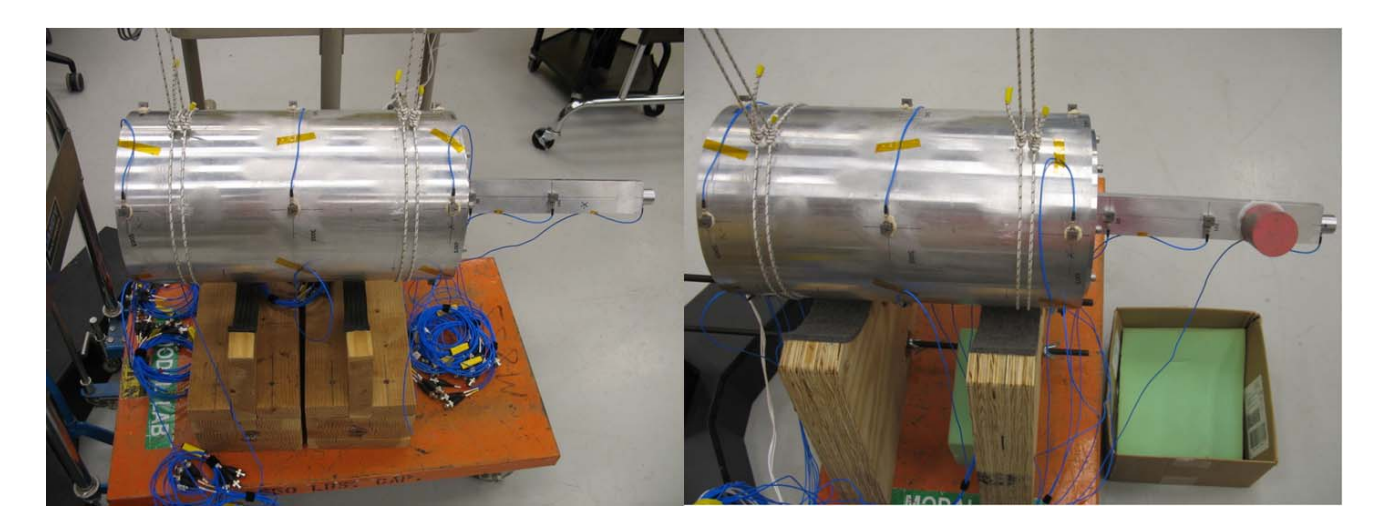


Figure 21. Cylinder-Plate-Beam System Experimental Set-up

The external accelerometers were configured as shown in Fig. 22. These were placed to capture the motion of the CPB system up to 1000 Hertz based on previous experience [75].

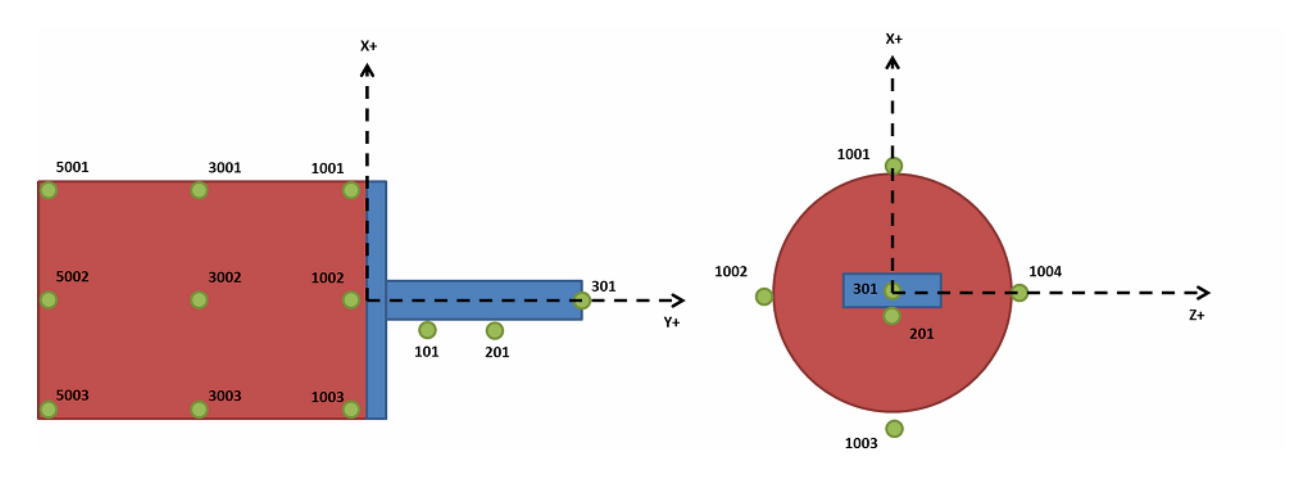


Figure 22. Cylinder-Plate-Beam System Instrumentation Set-up

A series of low level forcing tests were completed in order to avoid any nonlinearities in the system. For each mode, the driving point location at which the system responded most strongly was used to extract the modal parameters using the SMAC algorithm [78]. These driving points are listed in Table 6 in the column labeled "Reference". The information from the linear test on the baseline CPB system is shown in Table 6. Note, the rigid body modes were generated analytically but were checked and compared to the mass lines of the measured frequency response functions.

Table 6. Cylinder-Plate-Beam System low forcing level test results

Mode	Frequency [Hz]	Damning	Reference	Description
1	1	1	NA	Rigid translation in X
2	1	1	NA	Rigid translation in Y
3	1	1	NA	Rigid translation in Z
4	1	1	NA	Rigid rotation about X
5	1	1	NA	Rigid rotation about Y
6	1	1	NA	Rigid rotation about Z
7	116	0.27	5003X+	1st bending in the X-Direction
8	153	0.15	5002Z+	1st bending in the Z-Direction
9	276	2.37	5002Z+	Internals rotation about Y plus translation in Z
10	282	2.08	5003X+	Internals translation in X and Z
11	300	2.26	5002Z+	Off-axis rotation of the internals about Y
12	455	0.32	301Y-	Axial mode, internals and nose out of phase
13	589	2.09	301Y-	Internals rotation about Z
14	634	1.96	5002Z+	Internals rotation about X
15	691	1.28	301Y-	Axial mode, internals and nose in phase
16	742	1.19	3003X_	Suspected foam mode mostly in X
17	761	1.13	3002Z_	Suspected foam mode mostly in Z
18	831	1.00	5002X+	1st Axial torsional mode
19	914	0.79	3002Z+	(2,0) ovaling on-axis
20	964	0.22	5003X+	2nd Bending in the X-Direction

#### 2.3.3 Transmission Simulator Model

A finite element model of the cylinder-plate-beam was constructed and is shown in Fig. 23. The three-dimensional solid structure was modeled by brick type higher order 20-node solid elements with quadratic displacement behavior. The CPB finite element model is comprised of a beam, plate, washer, cylinder and ring, see Fig. 23. The model was constructed as a single linear structure by merging the adjacent nodes at the contact points between each component. The element properties of all of the components except the washers are set as 6061 T6 Aluminum, with the material properties listed in Table 7. Fifteen nodes were selected as the sensor positions and the mesh was constructed such that these corresponded precisely to the actual accelerometer locations.

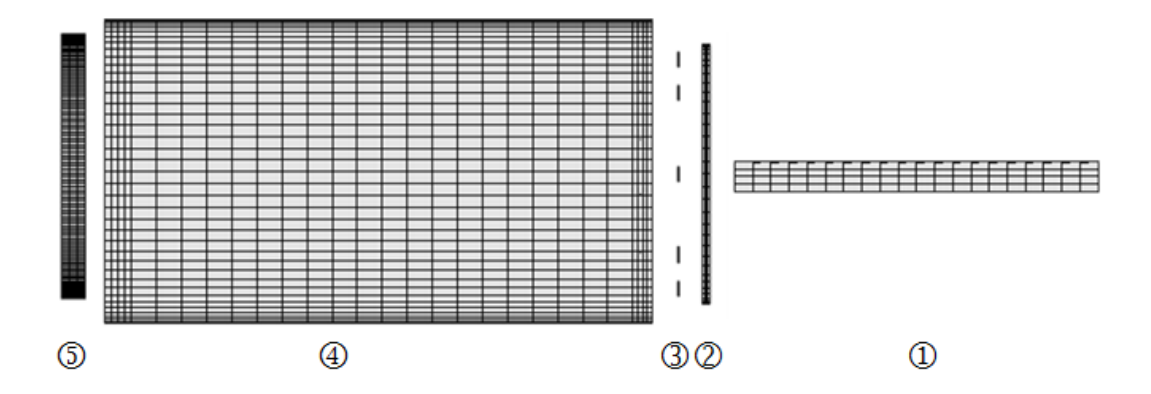


Figure 23. Configuration of CPB for Finite Element Mode: 1 - Beam, 2 - Plate, 3 - Washers, 4 - Cylinder, 5 - Ring

To validate the FE model, the natural frequencies of the Cylinder-Plate-Beam system were examined. Table 8 shows the first eleven elastic frequencies of CPB model with the retaining ring on the far left removed. These were compared to the measured natural frequencies of the actual hardware, from a test that was performed before the foam and retaining ring had been installed [75].

Table 7. Cylinder-Plate-Beam System low forcing level test results

Component	Material	Properties
Beam	6061 T6 Aluminum	$E = 1.0 \text{ x } 10^7 \text{ psi}, v = 0.33, \rho = 0.09775 \text{ lb/in}^3$
Plate	6061 T6 Aluminum	$E = 1.0 \text{ x } 10^7 \text{ psi}, v = 0.33, \rho = 0.09775 \text{ lb/in}^3$
Washer	Steel	$E = 1.0 \text{ x } 10^7 \text{ psi}, v = 0.29, \rho = 0.28000 \text{ lb/in}^3$
Cylinder	6061 T6 Aluminum	$E = 1.0 \text{ x } 10^7 \text{ psi}, v = 0.33, \rho = 0.09775 \text{ lb/in}^3$
Ring	6061 T6 Aluminum	$E = 1.0 \times 10^7 \text{ psi}, v = 0.33, \rho = 0.09775 \text{ lb/in}^3$

Table 8. Elastic modal frequencies of the Cylinder-Plate-Beam

Mode	Test Frequency [Hz]	FEM Frequency [Hz]	Error [%]
1	134.2	133.83	-0.28
2	171.2	171.30	0.06
3	430.0	435.15	1.20
4	511.2	497.42	-2.70
5	975.7	954.60	-2.16
6	1027	1038.14	1.08
7	1312	1301.33	-0.81
8	1528	1535.62	0.50
9	1637	1589.17	-2.92
10	1801	1846.45	2.52
11	1833	1859.75	1.46

The additional mass attached at the end of the beam was modeled with 20 node hex elements. The nodes in this mesh did not naturally align with those in the beam mesh, so the two substructures were connected using the multi-point constraint method.

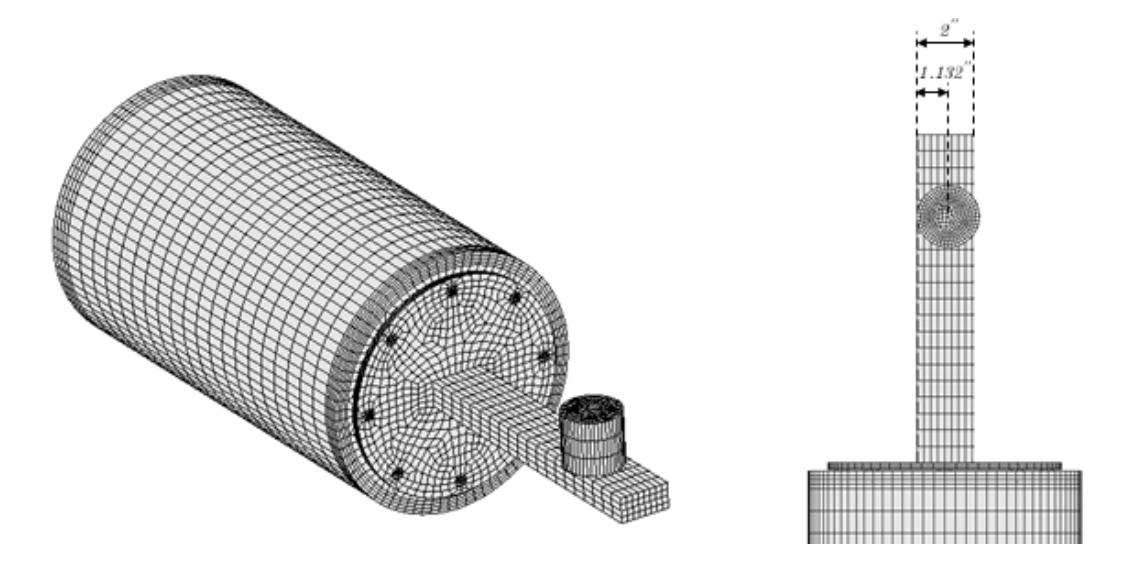


Figure 24. Cylinder-Plate-Beam FEM Model with Additional Mass

# 2.3.4 Substructuring Methodology

Recall from Fig. 20, the first step in this experimental-analytical substructuring prediction process is to generate an experimental model of the foam and internal mass (Subsystem B). This model can then be coupled with the finite element model containing the additional mass (Subsystem D) mentioned in Chapter 2.3.3. This process is done through two means.

The first is the standard transmission simulator method which was used to complete the previous example on the Ampair 600 Wind Turbine. In this case, the metal cylinder, plate, and beam act as the transmission simulator and thus all accelerometers placed on these objects are considered connection degrees of freedom. The system modal equations of motion can be written in terms of the subscripts C (the experimental system), D (the mass loaded finite element model), and TS (the finite element model of the transmission simulator).

$$\begin{bmatrix} \mathbf{I}_{C} & \mathbf{0} & \mathbf{0} \\ \mathbf{0} & \mathbf{I}_{D} & \mathbf{0} \\ \mathbf{0} & \mathbf{0} & -\mathbf{I}_{TS} \end{bmatrix} \begin{pmatrix} \ddot{\mathbf{q}}_{C} \\ \ddot{\mathbf{q}}_{D} \\ \ddot{\mathbf{q}}_{TS} \end{pmatrix} + \begin{bmatrix} 2\zeta_{C}\omega_{C} & \mathbf{0} & \mathbf{0} \\ \mathbf{0} & 2\zeta_{D}\omega_{D} & \mathbf{0} \\ \mathbf{0} & \mathbf{0} & -2\zeta_{TS}\omega_{TS} \end{bmatrix} \begin{pmatrix} \dot{\mathbf{q}}_{C} \\ \dot{\mathbf{q}}_{D} \\ \dot{\mathbf{q}}_{TS} \end{pmatrix} + \begin{pmatrix} \mathbf{0} & \mathbf{0} \\ \mathbf{0} & \omega_{D}^{2} & \mathbf{0} \\ \mathbf{0} & \mathbf{0} & -\omega_{TS}^{2} \end{bmatrix} \begin{pmatrix} \mathbf{q}_{C} \\ \mathbf{q}_{D} \\ \mathbf{q}_{TS} \end{pmatrix} = \begin{pmatrix} \mathbf{\Phi}_{C}^{T}\mathbf{F}_{C} \\ \mathbf{\Phi}_{D}^{T}\mathbf{F}_{D} \\ \mathbf{\Phi}_{TS}^{T}\mathbf{F}_{TS} \end{bmatrix}$$

$$(22)$$

The softened constraints equation can be formulated in a similar means to that of the Ampair 600 Wind Turbine example,

$$\begin{bmatrix} \mathbf{\Phi}_{TS}^{+} & \mathbf{0} \\ \mathbf{0} & \mathbf{\Phi}_{TS}^{+} \end{bmatrix} \begin{bmatrix} \mathbf{\Phi}_{C} & \mathbf{0} & -\mathbf{\Phi}_{TS} \\ \mathbf{0} & \mathbf{\Phi}_{D} & -\mathbf{\Phi}_{TS} \end{bmatrix} \begin{bmatrix} \mathbf{q}_{C} \\ \mathbf{q}_{D} \\ \mathbf{q}_{TS} \end{bmatrix} = \begin{bmatrix} \mathbf{0} \\ \mathbf{0} \\ \mathbf{0} \end{bmatrix}$$

$$(23)$$

With these equations of motion and constraints substructured prediction of the dynamics of the validation assembly can be computed using the methodology detailed in Chapter 1.2.

The second means of generating a substructured prediction is by following the Craig-Mayes method. This method is described in detail by Mayes in [82] and was used on the CPB system in [74]. The Craig-Mayes formulation is a methodology to generate a Craig-Bampton representation for the experimental subcomponent model. The resulting form resembles the dynamics of Subsystem C (the experiment) minus Subsystem A (the transmission simulator). The resulting formulation can be easily coupled with a Craig-Bampton finite element model of Subsystem D to estimate the dynamics of the modified structure.

#### 2.3.5 Substructuring Predictions

To complete these substructuring predictions the first 20 free modes up to 970 Hz were used to model Subsystem C. A finite element model of the transmission simulator, the CBP structure without internals, was used to remove the effects of the transmission simulator. From the finite element model of the transmission simulator, ten free normal modes up to 805 Hz were retained with an arbitrarily assigned

damping ratio of 0.5 percent. Subsequently, the dynamics of the modified CBP structure (i.e. with the mass attached, Subsystem D) were added to predict the dynamical behavior of the truth hardware assembly. The predictions are compared to experimental measurements from the truth hardware to evaluate the substructuring accuracy.

From the FE model of the modified CBP, Subsystem D, 13 free normal modes up to 858 Hz were retained and an arbitrary damping ratio of 0.5 percent was assigned. All three structures (experimental system C, transmission simulator A and modified CBP structure D) were connected using modal constraints at the 45 exterior measurement degrees of freedom. Table 9 shows the prediction obtained by the traditional TS method compared to the truth experiment E.

Table 9. Frequencies, damping ratios and MAC values for the Traditional TS Method

	, 40.0,	~~g					
Mode [-]	f <sub>experiment</sub>	f <sub>prediction</sub> [Hz]	f <sub>error</sub>	ζexperiment [-]	ζprediction [-]	ζ <sub>error</sub>	MAC [-]
7	88.33	86.59	-1.96	0.00196	0.00215	9.38	0.9803
8	115.80	115.06	-0.64	0.00163	0.00207	26.83	0.9929
9	275.97	276.11	0.05	0.02468	0.02466	-0.10	0.9006
10	283.32	283.24	-0.03	0.02151	0.02168	0.80	0.9995
11	301.40	301.77	0.12	0.02327	0.0229	-1.61	0.9957
12	346.25	349.76	1.01	0.00291	0.00359	23.47	0.9867
13	584.71	583.2	-0.26	0.02119	0.02135	-0.77	0.9963
14	635.16	634.89	-0.04	0.02037	0.01897	-6.87	0.9948
-	NA	670.72	NA	NA	0.00504	NA	NA
15	688.92	690.36	0.21	0.01515	0.01363	-10.03	0.932
-	NA	717.45	NA	NA	0.00537	NA	NA
16	758.36	NA	NA	0.01131	NA	NA	NA
17	769.71	770.99	0.17	0.01191	0.01201	0.84	0.8827

The modes are well predicted up to the 14th mode at 635 Hz, with relative frequency errors between -1.96% and 1.01%, relative damping errors between -6.87% and 26.83% and MAC values between 0.9006 and 0.9995.

By visualizing the predicted mode shapes with a wire frame model built of the sensor nodes, the modes predicted at 670.72 Hz and at 717.45 Hz could be identified as non-physical, so-called spurious modes. In this case, the traditional TS Method is not able to predict the 16th mode of the truth experiment at 758.36 Hz with the number of modes retained from the transmission simulator and from the

modified CBP structure. The MAC values between the predicted and true experimental modes are shown in Fig. 25, and these values were used to complete the pairing in Table 9.

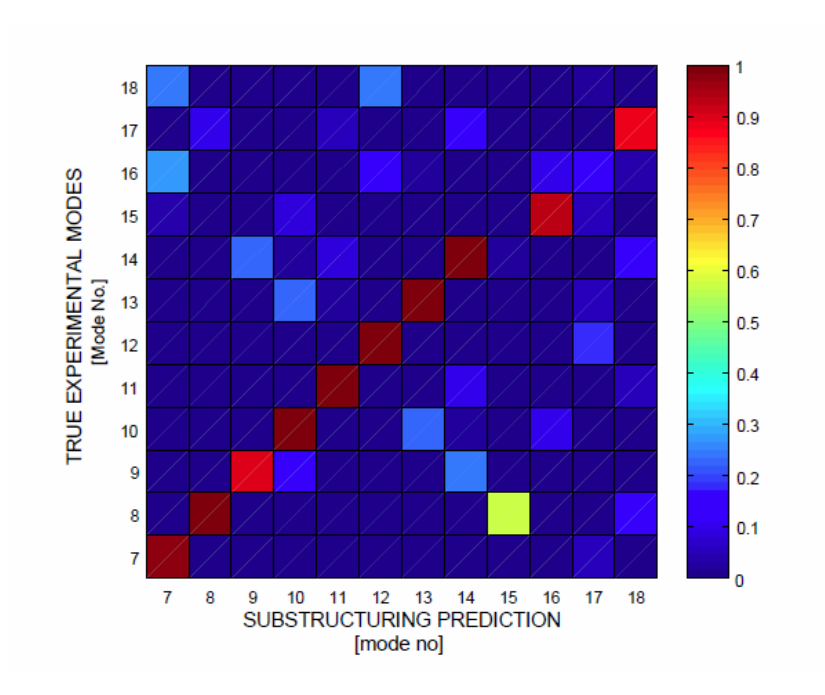


Figure 25. MAC of Traditional TS Predictions versus Truth Test

To complete substructuring with the Craig-Mayes formulation the FE model of the modified CBP was transformed to Craig-Bampton coordinates. Eight fixed-interface normal modes up to 1898 Hz were retained during the transformation. Here, the 45 exterior measurement degrees of freedom were considered as the interface and held fixed. The Craig-Mayes representation resulting from the experiment (Subsystem C) and the transmission simulator (Subsystem A) was connected to the Craig-Bampton representation of the modified CBP structure by primal assembly at the 45 exterior measurement degrees of freedom. Table 10 shows the prediction obtained by the Craig-Mayes method compared to the truth experiment.

Table 10. Frequencies, damping ratios and MAC values for the Craig-Mayes TS Method

Mode [-]	f <sub>experiment</sub> [Hz]	f <sub>prediction</sub> [Hz]	f <sub>error</sub> [%]	Sexperiment	ζprediction [-]	ζ <sub>error</sub> [%]	MAC [-]
7	88.33	89.58	1.42	0.00196	0.00208	5.84	0.9861
8	115.8	115.25	-0.47	0.00163	0.00204	25.14	0.9975
9	275.97	275.83	-0.05	0.02468	0.02459	-0.36	0.8886
10	283.32	282.61	-0.25	0.02151	0.02156	0.23	0.9986

11	301.4	301.48	0.03	0.02327	0.02284	-1.84	0.9966
12	346.25	350.61	1.26	0.00291	0.00343	17.96	0.9897
13	584.71	583.64	-0.18	0.02119	0.02141	1.05	0.9971
14	635.16	634.85	-0.05	0.02037	0.019	-6.69	0.9961
-	NA	679.99	NA	NA	0.00491	NA	NA
15	688.92	691.85	0.43	0.01515	0.01351	10.83	0.9075
-	NA	707.57	NA	NA	0.00574	NA	NA
16	758.36	NA	NA	0.01131	NA	NA	NA
17	769.71	760.69	-1.17	0.01191	0.01125	-5.54	0.8308

The modes are well predicted up to the 14th mode at 635 Hz, with the relative frequency errors ranging from -0.47% to 1.42%, relative damping errors between -6.69% and 25.14% and the MAC values ranging from 0.8886 to 0.9986. Both methods provided nearly identical results.

#### 2.4 Remarks

Though the Ampair example presented in Chapter 2.2 and the Cylinder-Plate-Beam example presented in Chapter 2.3 seem very similar, there are some key differences. The Ampair example consisted of three subsystems coupled together and was completed by removing multiple transmission simulators. In theory multiple transmission simulators could be used, each connecting and replicating the conditions from different subsystem joints. The CPB system was more traditional as the example removed the analytical transmission simulator and then added a design modification back into the system. Here, unlike the Ampair system, the transmission simulator was not considered rigid but included elastic modes as well. Although it is ideal for the TS to be rigid in the frequency bandwidth of interest, sometimes it is not possible for the elastic modes to be designed out of the testing bandwidth. The resulting predictions were quite accurate. The elastic modes retained in the second example seemed to be essential and improved the linear substructuring results, while in the first example this elastic motion was ignored and had slightly higher levels of error. With the linear TS substructuring capability understood, the next step is to understand what nonlinearities may exist in a system experimentally and then determine how those nonlinearities can be represented in a subcomponent model.

# 3 Nonlinear Modal Modeling

#### 3.1 Introduction

As discussed in Chapter 1.4, this dissertation investigates nonlinear modal models and their ability to represent the nonlinear dynamics of jointed structures. Chapter 3 addresses this challenge by testing structures with weakly nonlinear joints and using a recently proposed framework to model the structure as a collection of uncoupled, weakly nonlinear modes or oscillators. Working with uncoupled, weakly nonlinear modes allows these nonlinear joint models to be applied to substructuring predictions. A set of tools is presented that can be used to characterize the nonlinearity in each mode due to the joints in the system.

The approach used here is similar to that which was first used by Deaner et al. in [52] to characterize a beam with a bolted joint. However, this work presents a new means of interpreting the dissipation in the modal Iwan model that allows one to more clearly see how the damping ratio changes with response amplitude while still allowing power law behavior to be identified. Specifically, while previous works [48, 52] characterized the damping in an Iwan model using the energy dissipation per cycle versus velocity amplitude (or force), this work shows that superior information can be obtained by computing the effective damping ratio and displaying it versus log velocity amplitude. Once the damping and stiffness versus amplitude are known, it is possible that the modal Iwan model will not always be the most suited model to reproduce these behaviors. Other models, such as cubic stiffness and damping, may be more suitable in some cases.

This work also builds on the previous works by exploring whether these tools and the modal Iwan modeling framework are effective for a real industrial structure. This structure includes several joints, with bolts tightened to the recommended specifications and with complicated, three-dimensional modal deformations. The effect of the input location is explored in more detail here, presenting strong evidence that the modal Iwan model is valid for a wide range of inputs.

It should be noted that other frameworks have been proposed for modeling structures with joints. Of particular note, is the harmonic balance approach employed in [83] and the associated methods reviewed there and in related works [84]. The harmonic balance approach can be very computationally efficient, especially when seeking to simulate stepped-sine measurements or nonlinear frequency responses. However, some of those gains may be lost when the joint is modeled by an Iwan model with many slider elements, and harmonic balance is, of course, not as useful when impulsive loads are of interest.

This chapter focuses on two examples of experimental nonlinear behavior, screening and modal model development. The first example consists of a pair of bolted catalytic converters. This system is discussed in Chapter 3.2 where experimental measurements are used to fit 4-parameter Iwan modal models. These tools are applied, for the first time, to measurements from an assembly of automotive exhaust system components that contains two interfaces with realistic geometry, gaskets, and bolt torques. The second example is on the Cylinder-Plate-Beam system, discussed previously in Chapter 2.3, and the nonlinear identification of the CPB system is discussed in Chapter 3.3. These measurements are fit to both the 4-parameter modal Iwan models and a Restoring Force Surface model containing cubic stiffness and damping. Understanding and measuring these nonlinear modal models is critical to creating a high quality system level substructuring prediction including the nonlinear joint dynamics.

## 3.2 Coupled Catalytic Converter System

# 3.2.1 Nonlinear Model Characterization - Theory

The first system presented in this chapter is an assembly of automobile catalytic converters. The goal of this example is to show how one can define 4-parameter Iwan modal models to match measured data from an industrial system. This case study begins with a discussion of some of the theory used to generate these Iwan modal models. In order to develop a nonlinear model for a structure, one must first find a means of detecting nonlinearity in measured experimental data. In this work this is done in a two

step process. First, the data is analyzed using the zeroed early-time fast Fourier transform (ZEFFT) [56] to determine which modes exhibit nonlinear behavior. The ZEFFT applies the following window w(t) to the time history x(t), and then the FFT is computed for various truncation times  $t_n$ .

$$w(t) = \begin{cases} 0 & t \le t_n \\ 1 & t > t_n \end{cases} \tag{24}$$

This analysis is quick and simple to perform and by comparing the spectra, FFT(w(t)x(t)), for various truncation times one can discern the type of the nonlinearity by observing how the frequency and shape of the curves change as more and more time signal is zeroed out.

After completing this initial screening process, each mode is isolated to quantify how its frequency and damping change with amplitude. A linear modal test is performed (with the structure excited at very low amplitude) and the mass normalized mode shapes are extracted from a curve fit to the measurements using standard techniques [85]. In previous works [86], a laser vibrometer was used so each response measurement was independent of all others and had to be processed separately. When the structure of interest is sufficiently massive, as is the structure used in this work, one can use accelerometers without adding significant mass or damping (from the cables). As mentioned previously, each mode is assumed to be independent and to be manifest with approximately the same mode shape as in the linear system, so all measurements should be related to one modal response, so the following equation can be solved in a least squares sense to obtain the modal amplitude.

$$\mathbf{\Phi}_r \ddot{\mathbf{q}}_r(t) = \ddot{\mathbf{x}}(t) \tag{25}$$

where  $\Phi_r$  is the *r*th mass-normalized mode vector,  $\ddot{\mathbf{q}}_r(t)$  is the corresponding modal acceleration response and  $\ddot{\mathbf{x}}(t)$  is a vector of accelerations that were measured due to one impact with an instrumented hammer. This method allows multiple hammer strikes to be compared even from different driving point locations. This mode shapes of the structure are assumed to be real and constant which limits this method to weakly nonlinear structures.

The next step in the screening process is to quantify the change in damping with vibration amplitude. As mentioned previously, the Hilbert transform algorithm detailed in [52, 55] is used. First, an 8th order band-pass filter is used to isolate a single harmonic (mode) in the response. Then, the Hilbert transform of the mono-component signal is computed and an 8th order polynomial is fit to the time varying amplitude and phase. In essence, this approach fits the modal response, q(t), to the following functional form, where  $\psi_r(t)$  and  $\psi_i(t)$  are 8th order polynomials in time and are, respectively, the real and imaginary parts of the time varying response model

$$\ddot{q}(t) = e^{\psi_r(t) + i\psi_i(t)} \tag{26}$$

To achieve this, the analytic signal,  $\ddot{Q}(t)$ , is constructed as

$$\ddot{Q}(t) = \ddot{q}(t) + iH(\ddot{q}(t))$$
(27)

where H() denotes the Hilbert transform. The real part,  $\psi_r(t)$ , is fit to the log of the amplitude of the analytic signal,  $\psi_r(t) = \log \left| \ddot{Q}(t) \right|$ , and the imaginary part is fit to its unwrapped phase,  $\psi_i(t) = \arg \left( \ddot{Q}(t) \right)$ .

The phase of the analytic signal gives the oscillation frequency, so the damped natural frequency was defined as its derivative in [52],

$$\omega_d(t) \triangleq \frac{d\psi_i}{dt} \tag{28}$$

which one can readily show gives the desired result for a linear time invariant system. It is convenient to convert the response model from acceleration to velocity for the analysis that follow. The desired velocity response model can be written in a similar form, where the hats denote that this model pertains to velocity rather than acceleration.

$$\dot{q}(t) = e^{\hat{\psi}_r(t) + i\hat{\psi}_i(t)} \tag{29}$$

This can be readily differentiated to obtain the following,

$$\ddot{q}(t) = \left(\frac{d\hat{\psi}_r(t)}{dt} + i\frac{d\hat{\psi}_i(t)}{dt}\right)e^{\hat{\psi}_r(t) + i\hat{\psi}_i(t)}$$
(30)

It is not trivial to relate the velocity and acceleration response models precisely, but if one recognizes that damping is small so that,

$$\left(\frac{d\hat{\psi}_r(t)}{dt} + i\frac{d\hat{\psi}_i(t)}{dt}\right) \approx i\frac{d\hat{\psi}_i(t)}{dt} = i\hat{\omega}_d(t) \tag{31}$$

then one can approximate the acceleration as follows.

$$\ddot{q}(t) \approx i \hat{\omega}_d(t) e^{\hat{\psi}_r(t) + i \hat{\psi}_i(t)}$$
(32)

This reveals that one can take  $\hat{\psi}_r(t) + \mathrm{i}\hat{\psi}_i(t) \cong \psi_r(t) + \mathrm{i}\psi_i(t)$  and estimate the velocity response model by simply dividing the acceleration response model by  $\omega_d(t)$ , exactly as is done for a linear response. Hence, the amplitude of the velocity response will be approximated by the following.

$$\left|\dot{Q}(t)\right| \approx \frac{e^{\psi_r(t)}}{\omega_d(t)}$$
 (33)

If the damping is high, then the approximation in the equation above will introduce some inaccuracy and a more elaborate approach must be developed. However, in the author's experience the decay envelope estimated by the Hilbert transform always exhibits some spurious oscillation, even after smoothing with the polynomial fit, so this approach does not introduce significant uncertainty.

As was done in [52], each mode will be modeled with a single degree of freedom system with a spring, damper, and with the nonlinear joint model represented by the force exerted by the joint as shown in Fig. 26.

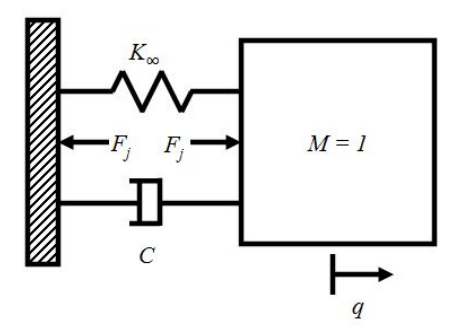


Figure 26. Schematic of SDOF model used for each modal degree of freedom

The force in the joint is given by the following,

$$F_{j}(t) = \int_{0}^{\infty} \rho(\phi) \left[ u(t) - x(t,\phi) \right] d\phi \tag{34}$$

where  $F_j$  is the force in the joint, u is joint displacement,  $\rho$  is a kernel that characterizes the joint and x is a continuum of state variables that evolve as show below

$$\dot{x}(t,\phi) = \begin{cases} \dot{u} & \text{if } ||u - x(t,\phi)|| \\ & \text{and } \dot{u}(u - x(t,\phi)) > 0 \\ 0 & \text{otherwise} \end{cases}$$
 (35)

The form of the kernel,  $\rho(\phi)$ , is discussed in detail in [48] and can be defined by four parameters,  $[F_s, K_T, \chi, \beta]$ ; where  $F_s$  is the joint force required to begin macro-slip,  $K_T$  is the stiffness in the joint,  $\chi$  is related to the exponent in a power law relationship between damping and amplitude in the micro-slip regime and  $\beta$  defines the shape of the dissipation curve near the transition from micro to macro-slip. When this joint model is used in a modal framework, these four parameters define the nonlinear characteristics of each mode in the system and can be obtained from experimental measurements as outlined in [52].  $K_T$  is defined by the change in stiffness as shown in Eqn. (36) where  $\omega_n$  is the natural frequency when the joint is completely stuck and  $\Delta\omega_n$  is the shift in natural frequency when the joint is in macro-slip.

$$K_{T} = \omega_{n}^{2} - (\omega_{n} - \Delta \omega_{n})^{2}$$
(36)

The measurements presented in this work are entirely from the linear or micro-slip regimes, so only those aspects of the modal Iwan model will be reviewed here. At very low amplitudes the nonlinear element acts like a linear spring with no additional damping and the linear viscous damper dominates. In the micro-slip regime the damping becomes nonlinear and the energy dissipated per cycle,  $D_{\text{Micro}}$ , by in the single degree of system in Fig. 26 was shown in [52] to have the following form.

$$D_{\text{Micro}} \approx A_{\text{Iwan}} \left| \dot{Q}(t) \right|^{\chi+3} + 2\zeta_{\nu} \omega_{n} \left( \frac{\pi}{\omega_{d}} \right) \left| \dot{Q}(t) \right|^{2}$$

$$A_{\text{Iwan}} = \frac{4R}{\left( \omega_{d}(t) \right)^{\chi+3} \left( \chi + 3 \right) \left( \chi + 2 \right)}$$
(37)

where R is a function of  $F_s$ ,  $K_T$  and  $\chi$  and was defined in [52]. The second term is the dissipation of a linear viscous damper with damping ratio  $\zeta_v$ . This linear dissipation term is easily derived by recognizing that the power dissipated by a linear viscous damper is given by the product of the modal velocity  $\dot{q}(t)$  and the modal damping force,  $2\zeta_v\omega_n\dot{q}(t)$  and then the term on the right above is readily obtained by assuming that  $\dot{q}(t)$  is harmonic,  $\dot{q}(t) = |\dot{Q}(t)|\sin(\omega_d t)$ , and integrating the power dissipated over one cycle.

One can readily use the response model that was fit to the measurements to estimate the energy dissipated by each modal degree of freedom per cycle. First, note that, although the kinetic energy is oscillatory, its amplitude, here denoted *KE*, is equal to the total energy in the system and is simply,

$$KE = \frac{1}{2} \left| \dot{Q}(t) \right|^2 \approx \frac{1}{2} \left( \frac{e^{\psi_r(t)}}{\omega_d(t)} \right)^2 \tag{38}$$

since the modal mass is unity. The amplitude of the kinetic energy decays slowly (i.e. with the decay envelope of the signal) so the energy dissipated per cycle is readily approximated as the slope of the kinetic energy versus time multiplied by the oscillation period. Hence,

$$D \approx \frac{2\pi}{\omega_d} \frac{dKE}{dt} \tag{39}$$

In [52], this experimentally measured dissipation was fit to the form given by Eqn. (37) to estimate the parameters of the Iwan model, one of the most important being the exponent,  $(\chi+3)$ , of the dissipation versus amplitude. This exponent was estimated by fitting a line to the log dissipation versus log amplitude curve estimated from the Hilbert transform. However, it was subsequently noted that the dissipation versus amplitude curves were difficult to interrogate because, as shown in Eqn. (37), the dissipation increases with the square of velocity amplitude even for a linear system, so the plot shows a slope of two even for a linear system. This is remedied by computing the effective linear damping ratio from the measured dissipation curve. Specifically, using the term on the right in Eqn. (37) as a guide, the measured damping ratio is defined as

$$\zeta_{meas}(t) \triangleq \frac{D}{2\pi \left| \dot{Q}(t) \right|^2} \tag{40}$$

If the system is linear and the damping is purely viscous, then one can obtain a line with  $\zeta_{meas}(t) = \zeta_v / \sqrt{1 - {\zeta_v}^2}$ . The Iwan joint then produces the following damping ratio.

$$\zeta_{\text{Iwan}}(t) \approx \frac{A_{\text{Iwan}}}{2\pi} \left| \dot{Q}(t) \right|^{\chi + 1}$$
(41)

Hence, one can readily estimate the power law exponent and the constant  $A_{Iwan}$  from the damping ratio measured using Eqn. (40).

### 3.2.2 Experimental System - Coupled Catalytic Converters

The proposed approach was applied to a system consisting of a two aft catalytic converters for a Buick LaCrosse (Part Number: 82071258), joined to a thick metal plate as seen in Fig. 27. This same system has also been used to develop linear substructuring techniques, as reported in [86]. The converters were joined to the plate using the same metal gaskets (Part Number: 20893953) that are used in the actual vehicle and assembled with four bolts. The bolts in this assembly were tightened to the recommended 45

N-m torque. The frequency range of interest in these tests was selected to be from 0 to 500 Hertz, which would encompass many of the low frequency modes of the exhaust system.



Figure 27. Photographs of the Catalytic Converter System

The dynamic response of the coupled system was measured using accelerometers placed at seven locations on the center plate and three locations on both converters. A modal test was completed with low level excitation using an impact hammer striking at multiple driving point locations. For each location, a series of five hammer strikes were averaged to minimize noise. Figure 28 shows the layout of these accelerometer and driving point locations for later reference.

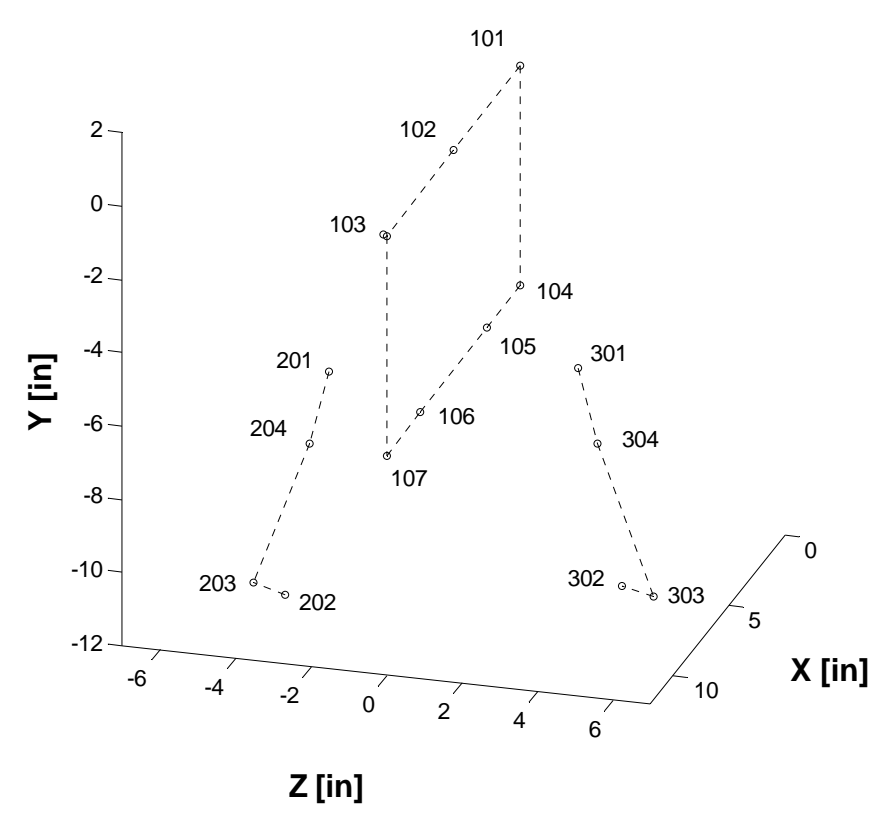


Figure 28. Matlab Generated Visualization of Catalytic Converter System

The measurements acquired in the linear modal tests were used to construct a composite frequency response function (FRF) for each driving point. These composite FRFs are shown in Fig. 29 providing a good indication of which modes are important in the system for each of the driving points. Here, one can observe that modes 1, 2, 3, 4 and 6 are dominated by z-direction motion while mode 5 is more easily excited from the x-direction. After further investigation, the author found modes 3 and 4 to be localized modes where only the heat shields moved significantly. Those modes are disregarded for this study as they do not contribute much to the nonlinear dynamics of the assembly. Linear models for these modes could be readily added to the model if desired.

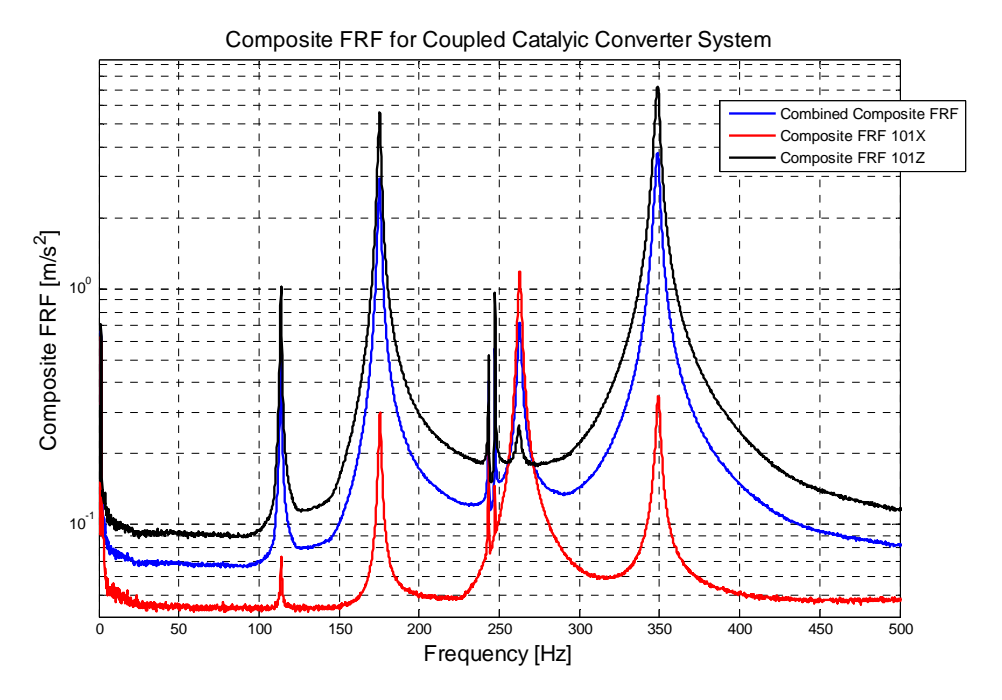


Figure 29. Composite FRF from Various Drive Points for Coupled Catalytic Converter System

Table 11 contains a list of the natural frequencies and damping ratios extracted for each of the modes using the Algorithm of Mode Isolation (AMI), a linear modal parameter identification algorithm that is detailed in [87]. The modes in this frequency range were found to include three bending modes, one torsional mode, and the two modes mentioned previously that are localized to the heat shields.

Table 11: Linear (low amplitude) modal parameters

Modal Index	Natural Frequency [Hz]	Damping Ratio	Deflection Type
1	113.70	0.0030	Bending in Y-direction
2	175.42	0.0043	Bending in X-direction
3	243.41	0.0005	Localized Heat Shield Mode
4	247.38	0.0004	Localized Heat Shield Mode
5	262.71	0.0044	1st Torsion
6	348.68	0.0045	2nd Bending in Y-direction

Mode shapes for the global modes are shown in Figures 30-33. Here, one can visualize the first mode as a bending mode of the system with the catalytic converters out of phase with one another. In the second mode the converters are in phase as the plate rotates. The fifth mode is a torsional mode as the

plate and converters twist about the z-directional axis. The sixth mode is a second bending mode causing the plate to rotate about the other planar x-direction axis.

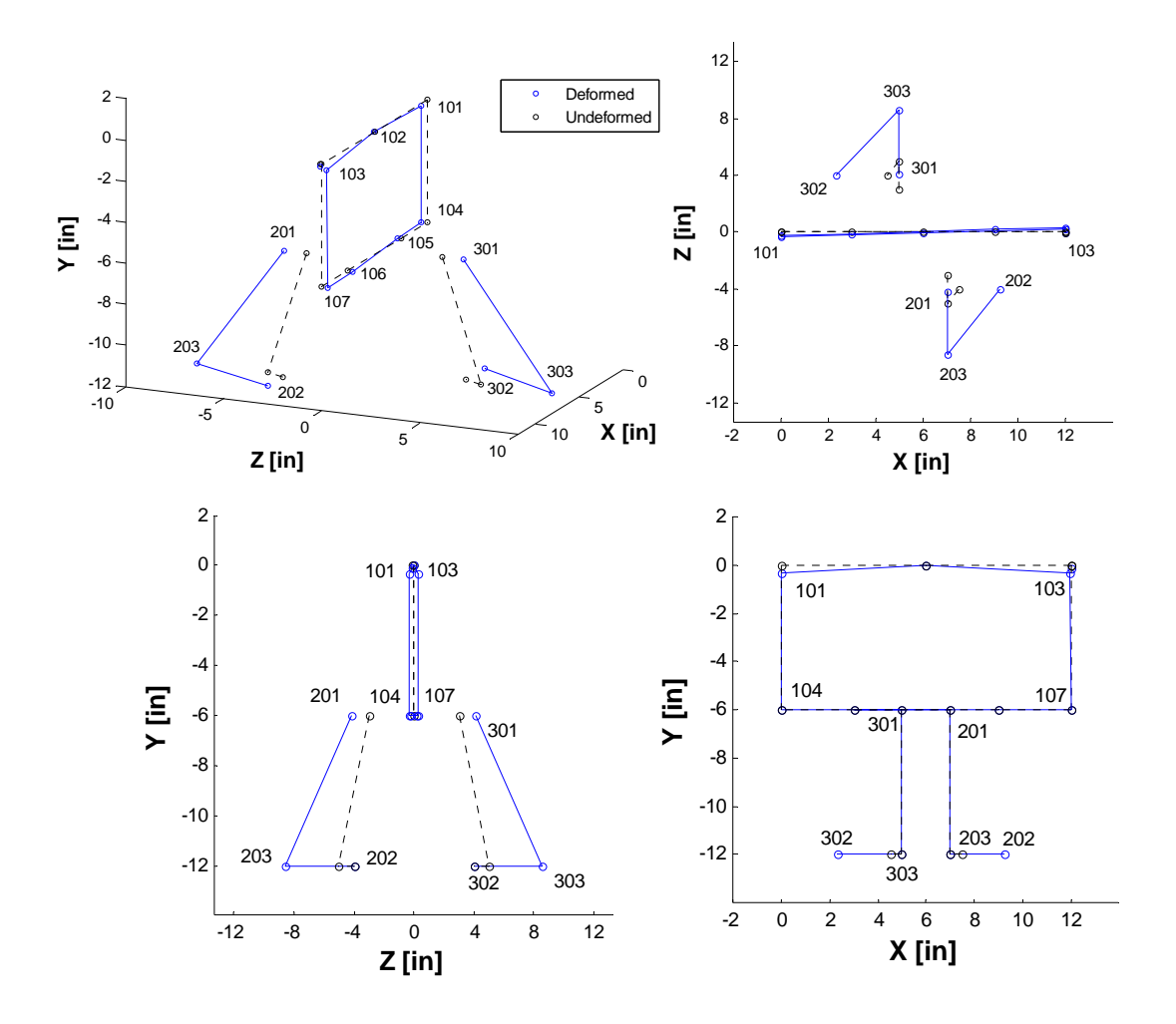


Figure 30. 1<sup>st</sup> Mode Visualization

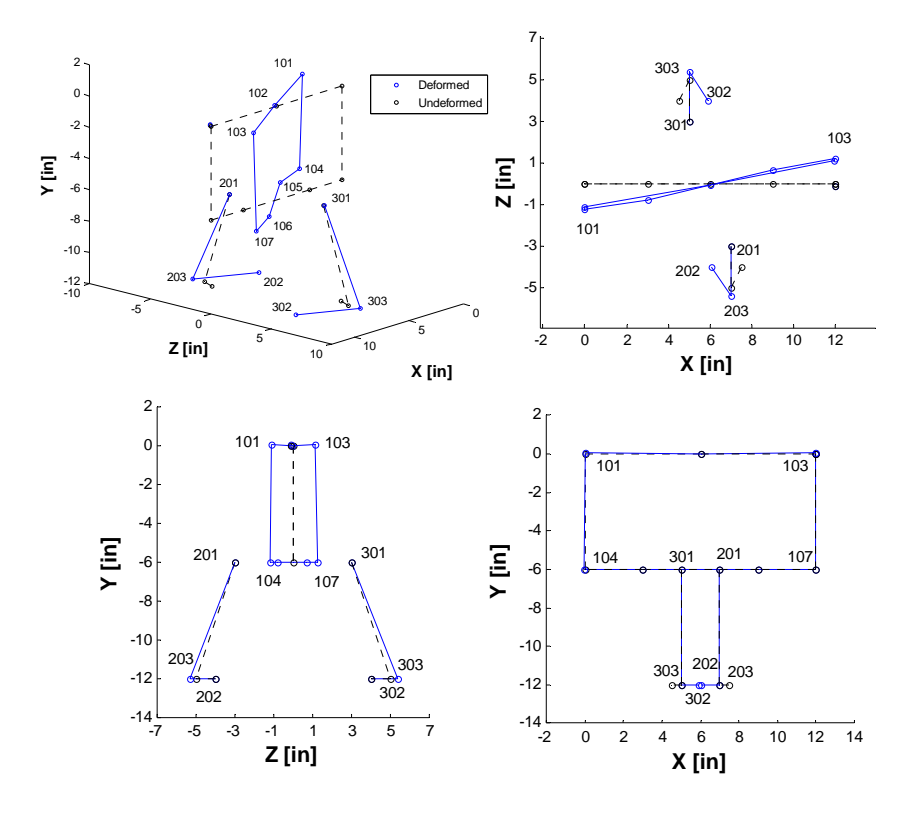


Figure 31. 2<sup>nd</sup> Mode Visualization

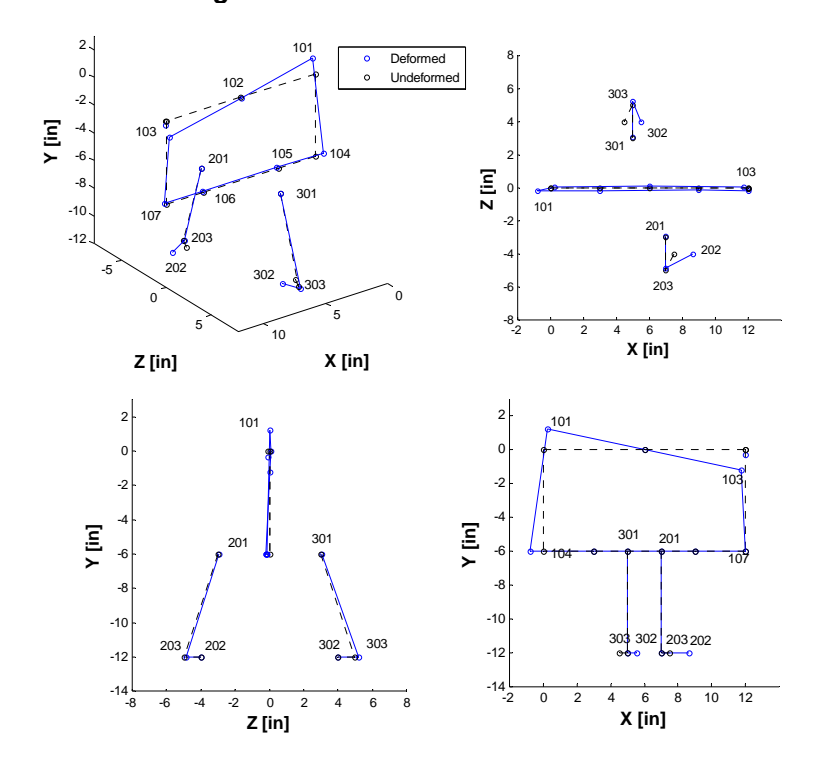


Figure 32. 5<sup>th</sup> Mode Visualization

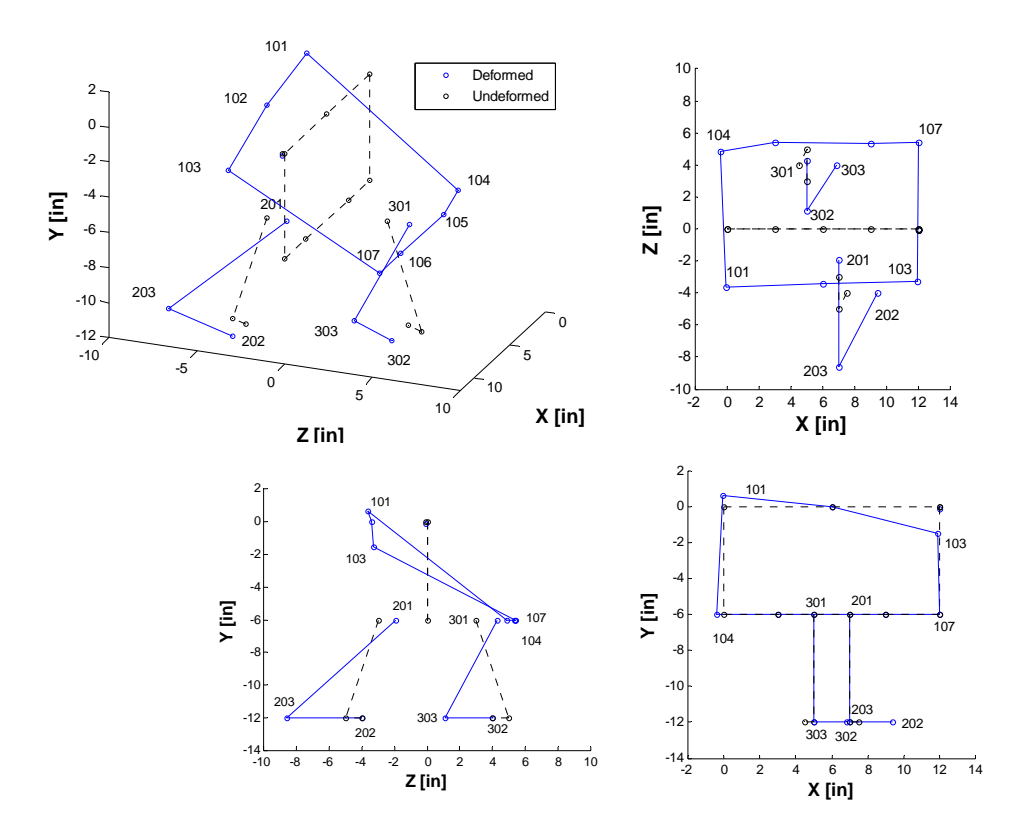


Figure 33. 6th Mode Visualization

# 3.2.3 Initial Screening – ZEFFT

The assembly was first probed using the ZEFFT algorithm, as discussed previously, to deduce whether any modes might behave nonlinearly. The structure was excited in the *z*-direction at point 204, see Fig. 28, with an impulsive force with a peak of 500 Newtons, and the response of Point 303-z was processed with the ZEFFT algorithm. Figure 34 shows the ZEFFT spectra of the assembly at point 303 in the *z*-direction; Fig. 34a shows the spectrum over the whole frequency range of interest; as is usually the case for structures with weak joint nonlinearities such as this, one must zoom in near each harmonic peak to discern any information about the nonlinearity. Fig. 34b shows an enhanced view of the ZEFFT near the first harmonic. The legends give the time  $t_n$ , from Eqn. (24), in milliseconds, at which the zeroed region ended for each curve. The resulting family of spectra show how nonlinear distortions increase as more of the early time (and hence higher amplitude and more nonlinear) parts of the time response are removed from the time history [56].

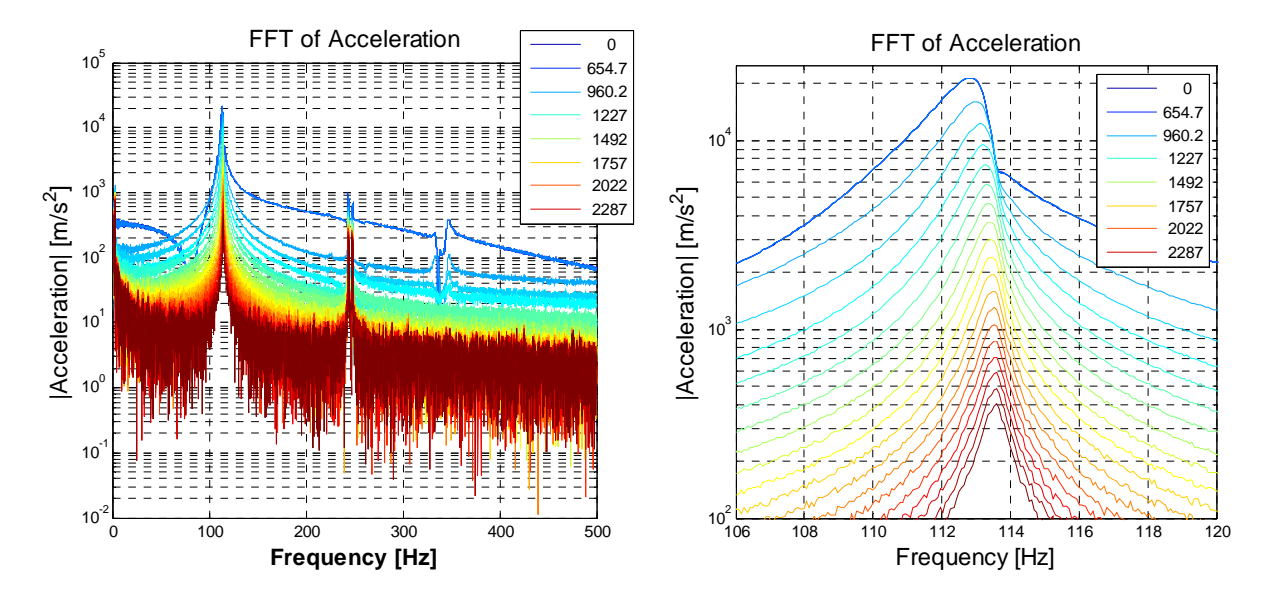


Figure 34. (a) Full ZEFFT spectra (b) Magnified View of ZEFFT spectra near 1st Resonance

The peak in the FFT occurs at a slightly lower frequency in the unzeroed response (denoted "0" in the legend) compared to that when the nonlinear portion of the response has been zeroed out (e.g. "1757 ms" in the legend), revealing that enough nonlinearity is present to cause about a 1.0 Hz (0.8%) shift in frequency. This also identifies the stiffness nonlinearity as a softening nonlinearity. While this frequency shift shows that the stiffness nonlinearity is quite small, this mode exhibited much more significant nonlinearity in damping, as will be elaborated subsequently. It is also worth noting that the shape of the distorted spectrum in the early times in Fig. 34 is similar to what has been seen in other tests and simulations of structures with bolted joints [56, 88].

A similar analysis was performed on the second mode revealing a shift in the natural frequency of 0.4 Hz (0.2%) over the same range of input force. The ZEFFT near the second resonance at point 303 in the z-direction (see Fig. 28), obtained by exciting in the x-direction at point 204 with a peak force of 545 Newtons, is shown in Fig. 35. The magnified view in Fig. 35b also includes a second set of dashed lines that will be explained subsequently. Notice that the ZEFFT does not show any strong evidence of nonlinearity. To check whether the response was indeed linear, the response at a lower amplitude was fit to a linear mode using the AMI algorithm and that fit was then extrapolated to earlier times to show how

the spectrum should have appeared if the mode behaved linearly over this time span. This linear extrapolation is shown on in Fig. 35b with dashed lines, each corresponding to the same value of  $t_n$  as the solid lines from the ZEFFT algorithm. As discussed in [56], extrapolations such as these can often help when it is difficult to detect or make sense of a certain nonlinearity. These results show that the first two modes of the system do exhibit nonlinearity, but the first mode is more strongly excited and shows stronger nonlinearity.

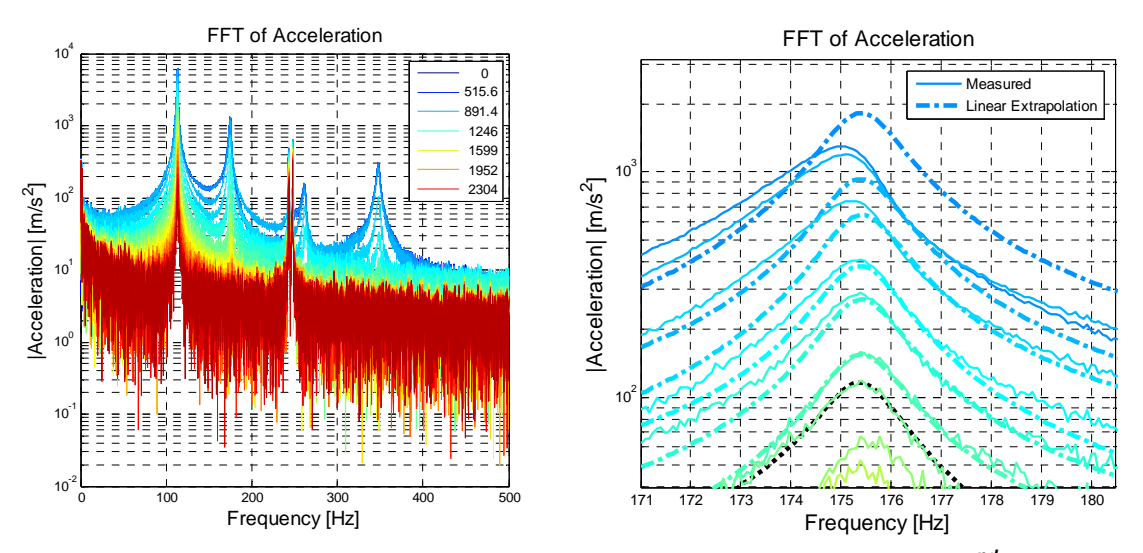


Figure 35. (a) Full ZEFFT spectra (b) Magnified View of ZEFFT spectra near 2<sup>nd</sup> Resonance

The response near the 5<sup>th</sup> and 6<sup>th</sup> modes was also examined as shown in Fig. 36, and while they seem to show traces of nonlinearity, it was negligible in these measurements compared to the first two harmonics. The forcing amplitude rolls off quickly with increasing frequency, so either these modes are less susceptible to the nonlinearity induced by the joint or else the forcing is simply not adequate to excite nonlinearity in these modes. Based on the results of the ZEFFT analysis, the 1<sup>st</sup> and 2<sup>nd</sup> modes were treated as nonlinear and the 5<sup>th</sup> and 6<sup>th</sup> were treated as linear.

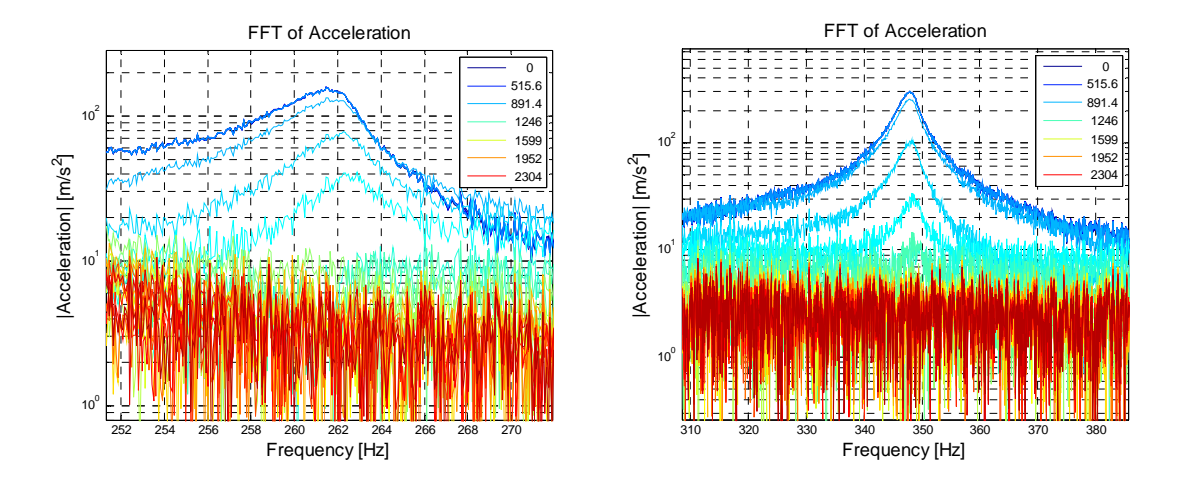


Figure 36. (a) ZEFFT spectra near 5<sup>th</sup> Resonance (b) ZEFFT spectra near 6<sup>th</sup> Resonance

# 3.2.4 Nonlinear Parameter Identification

After this initial screening with the ZEFFTs, the first two modes were characterized in more detail using the Hilbert transform approach discussed previously. Excitations were applied at several different points and at various amplitudes and then for each excitation the response at all of the accelerometers was used in Eqn. (25) to obtain a least squares estimate the modal amplitude  $q_1(t)$ . Figure 37 shows the FFT of an experimental signal both from the modal filter and the band-pass filter. This band-pass filtered signal was the signal used when applying the Hilbert transform.

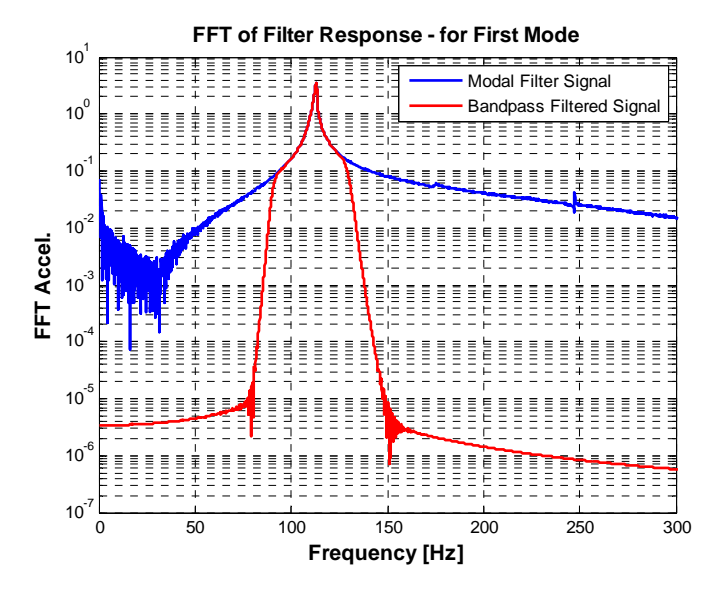


Figure 37. FFT of Filtered Signals

Using the Hilbert transform, this signal was fit over a chosen time window based on the Hilbert amplitude and phase envelopes. As can be seen in Fig. 38 the signal often loses some early time data due to Hilbert transform end effects but the fit amplitude and phase construct a quality representation of the filtered modal acceleration.

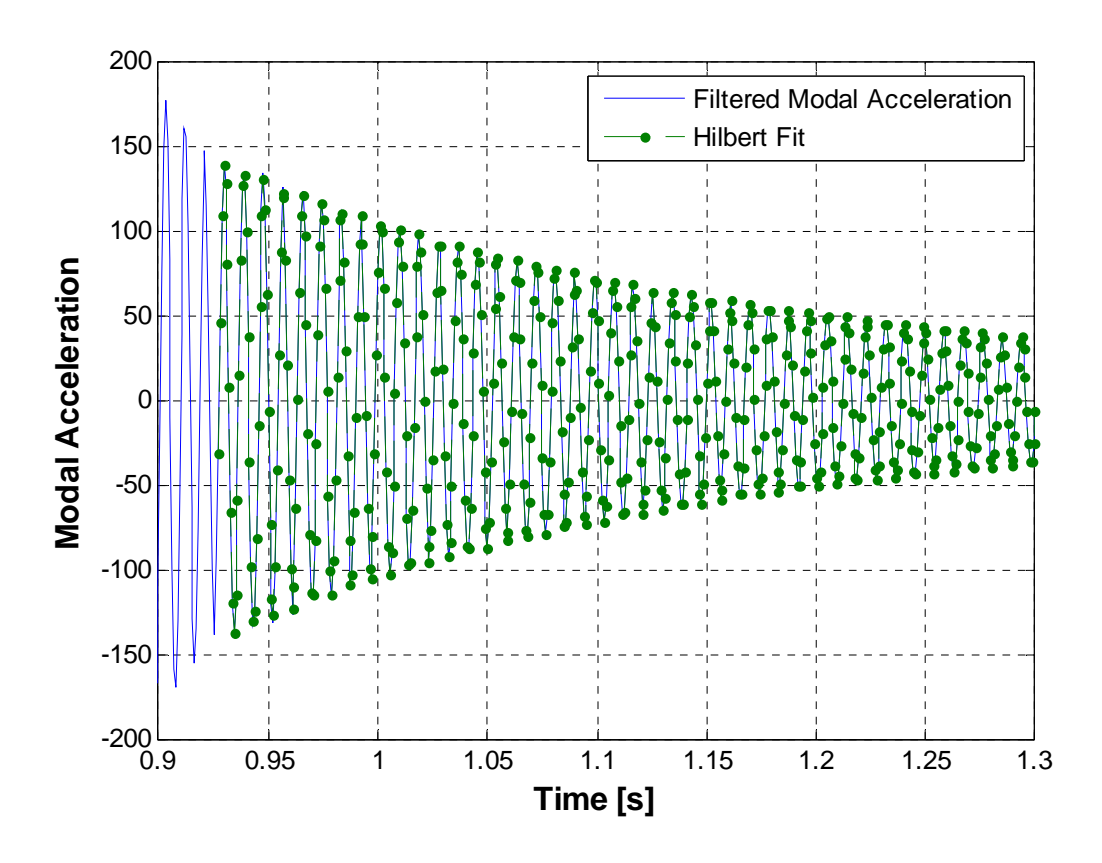


Figure 38. Filtered Modal Acceleration and Hilbert Fit of Signal

These Hilbert fits were then processed as outlined in Chapter 3.2.1 and the resulting measured damping  $\zeta_{meas}(t)$  was plotted against the velocity amplitude,  $|\dot{Q}(t)|$ , as shown in Fig. 39. Polynomials were fit to the analytic Hilbert signal, and while this dramatically reduces noise in the estimated damping, the smoothness of the polynomial fit can also make a spurious measurement appear to be physically meaningful. However, the spurious waviness at the lowest amplitudes is an artifact of the Hilbert transform and should be ignored. At higher amplitudes all of the curves agree remarkably well. All of

the lines of the same colors were taken from the same excitation point but at different force levels. At the point where the curves show the most scatter, which is near an amplitude of 0.020 m/s, the damping ratio ranges from 0.0035 to 0.0037. This represents a variation of about 7% of the average value. The various excitations at different forcing levels and locations all reveal a similar modal damping versus amplitude relationship, especially at high amplitudes where the damping is not constant but shows a power law dependence on amplitude. Each excitation point excites a different combination of the modes, and hence the force across the joint would be different. Nevertheless, these results show that these complicating factors can be ignored and that this mode can be treated as single degree-of-freedom nonlinear system that is uncoupled from the other modes.

Furthermore, the damping at high amplitudes is more than twice that at low amplitudes, so if this nonlinearity is not accounted for one might over predict the response of the structure by more than a factor of two. Additional impulses with even higher forces were applied using a heavy (non-instrumented) rubber mallet and the modal response curves extracted also agreed well with those shown. However, even with those large input forces it was difficult to obtain an estimate of the modal response at much higher amplitudes than those shown, presumably because of edge effects in the Hilbert transform and because the increased damping causes the response to decay more quickly.

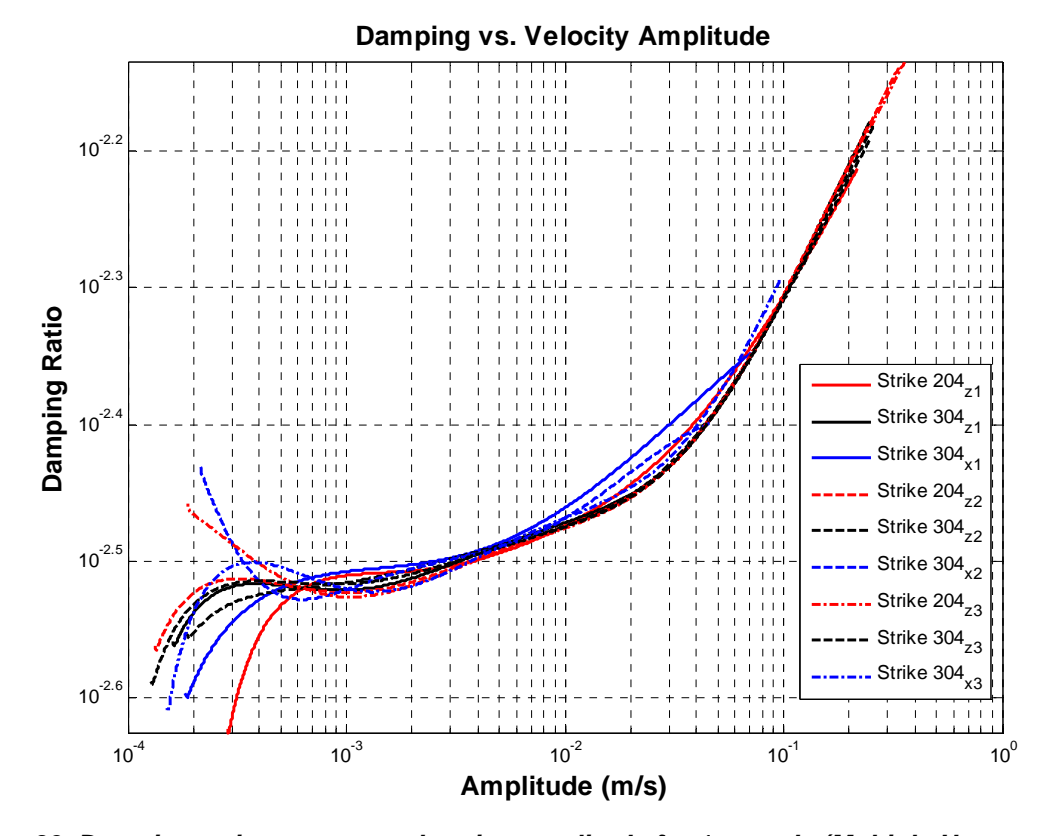


Figure 39. Damping ratio versus acceleration amplitude for 1st mode (Multiple Hammer Strikes)

This analysis was repeated for the second mode as well. Figure 40 shows the measured damping versus amplitude for several different hammer strikes. The Hilbert transform only produced useful data over a relatively small amplitude range for this mode, yet it still shows the damping behavior that is characteristic of an Iwan model in microslip, with the damping increasing with amplitude according to a power law relationship.

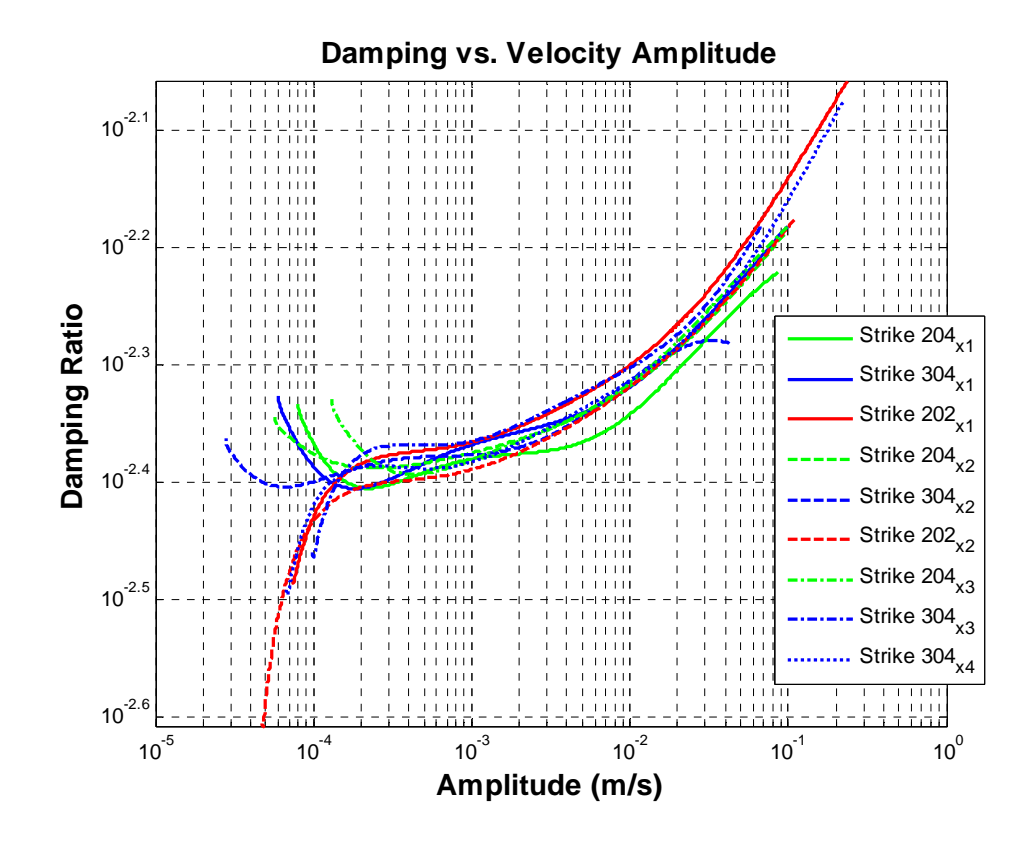


Figure 40. Damping ratio versus acceleration amplitude for 2nd mode (Multiple Hammer Strikes)

A summary of the observed frequency and damping nonlinearities is shown in Table 12. In contrast, the  $5^{th}$  and  $6^{th}$  modes were not excited enough to exhibit nonlinearity and will be modeled as linear.

Table 12: Summary of results for catalytic converter system NA = not applicable (linear mode)

Modal Index	Natural Frequency [Hz]	% Shift in Peak Frequency	Linear Damping Ratio	Maximum Damping Ratio	% Shift in Damping
1	113.70	0.8%	0.0030	0.0072	125.00%
2	175.42	0.2%	0.0043	0.0066	46.67%
5	262.71	NA	0.0044	NA	NA
6	348.68	NA	0.0045	NA	NA

The parameters of a modal Iwan model are estimated from the measurements for the first two elastic modes. There was no obvious evidence of macro-slip in the experimental test; therefore, the slip force can be assumed to be greater than any of the excitations applied experimentally.

$$F_{S} \ge \mathbf{\phi}_{dp} F \tag{42}$$

The joint stiffness is related to the minimum and maximum stiffness that the mode has when the joint goes, respectively, from slipping completely to being perfectly locked. This parameter can be estimated based on the peak frequency shift observed using the ZEFFT algorithm. However, because macro-slip was not observed, one cannot know whether the frequency would shift further if even larger forces were applied.

The  $\chi$ -value can be calculated directly using the slope of the damping versus amplitude curve from Figs. 39 and 40. The  $\chi$ -value was difficult to estimate from Figs. 39 and 40 because the nonlinear Iwan damping was only dominant over part of the measurement. To address this, the linear damping ratio was subtracted from the instantaneous damping in Figs. 39 and 40 to isolate the nonlinear portion of the damping. This was then relatively easy to fit to a power law relationship as shown in Figure 41. For the first mode, the  $\chi$ -value was found to be  $\chi=-0.280$ .

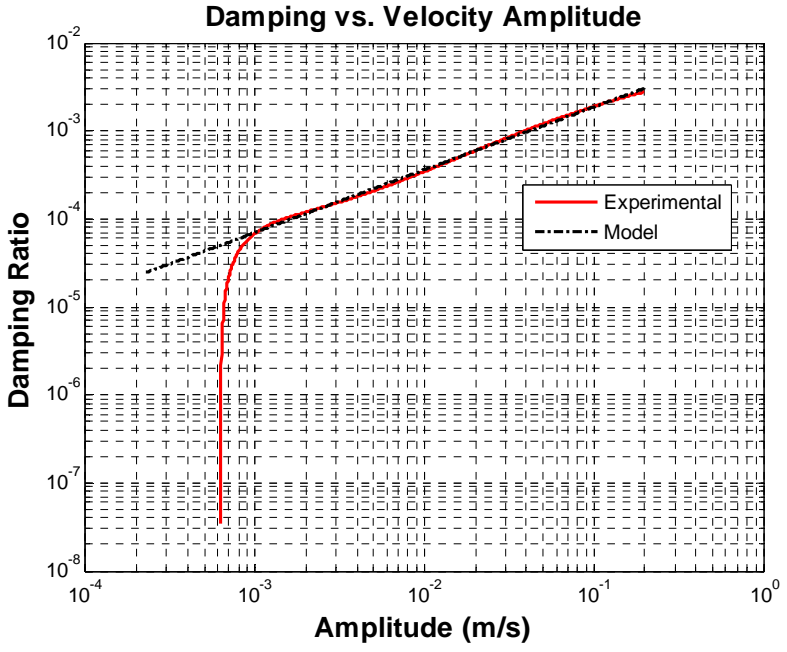


Figure 41. Damping Ratio versus acceleration amplitude for 1st mode after subtracting linear viscous damping of  $\zeta_v$ =0.003.

In principle the parameter  $\beta$  can be found from the y-intercept of the dissipation versus amplitude curve, but in this case this would not be reliable since  $F_S$  and  $K_T$  were not known precisely. Instead  $\beta$  was assumed to be unity and then varied to see whether the results were sensitive to that assumption. These Iwan parameters can then be used to simulate the response of the mode in question to the measured impulse and then to compare the observed damping versus amplitude curves. Alternatively, one can use the approximate expressions derived in [48].

These concepts were used to estimate starting values for the parameters and then they were varied until the damping versus amplitude curve of the modal Iwan model, found by integrating the equation of motion with a Newmark algorithm [89], matched what was measured experimentally. The unknown parameters  $F_s$  and  $K_T$  were varied until the damping and frequency relationships agreed with experimental measurements. Figure 42 shows the damping versus amplitude and Fig. 43 shows the frequency versus velocity amplitude of the modal Iwan model for the first mode. In this comparison, only a single hammer impact was used, and the measured impact force was applied to the modal-Iwan model to obtain a time domain simulation from which the damping versus amplitude and frequency versus time were extracted and which are labeled "Model" in Figs. 42 and 43. The simulation to generate these plots was completed using a forcing time history from a strike at location  $204_{z1}$ , see Fig. 39.

Recall,  $K_T$  is calculated as a function of the natural frequency and the frequency shift using Eqn. (36). It is interesting to note that the Hilbert transform of the simulated response clearly levels off at about  $10^{-4}$  m/s but even for this noise free simulated data the damping estimated by the Hilbert transform eventually shows spurious curvature below  $10^{-6}$  m/s. This was found to be caused by edge effects in the Hilbert transform. The experimentally measured damping shows a strong spurious decrease below  $10^{-3}$  m/s.

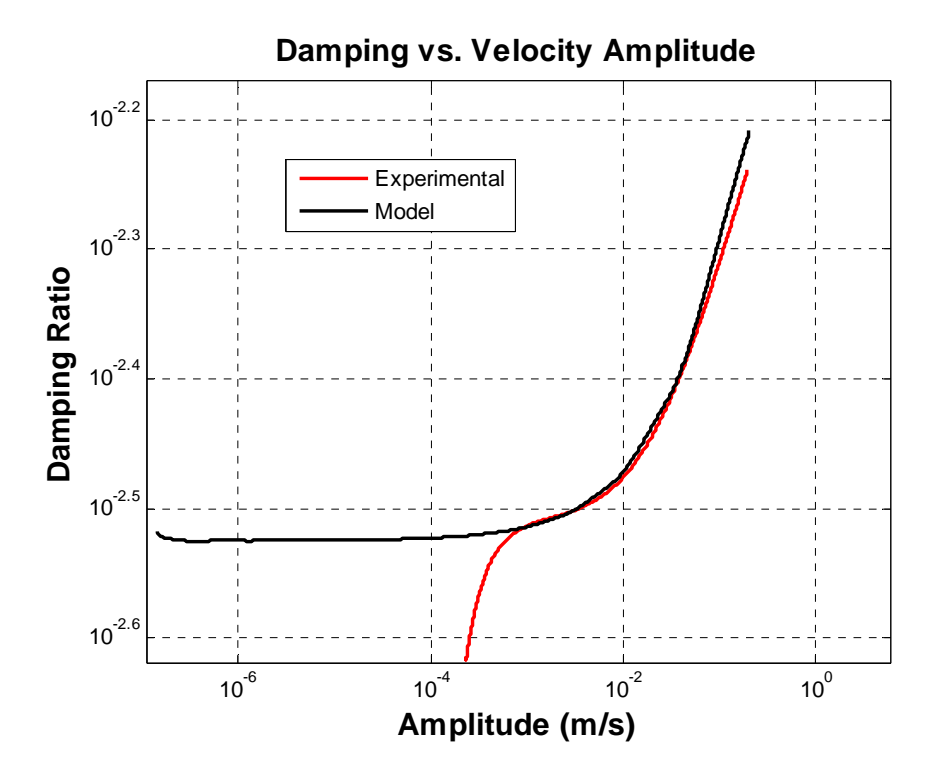


Figure 42. Damping Ratio versus Velocity Amplitude - 1<sup>st</sup> Mode

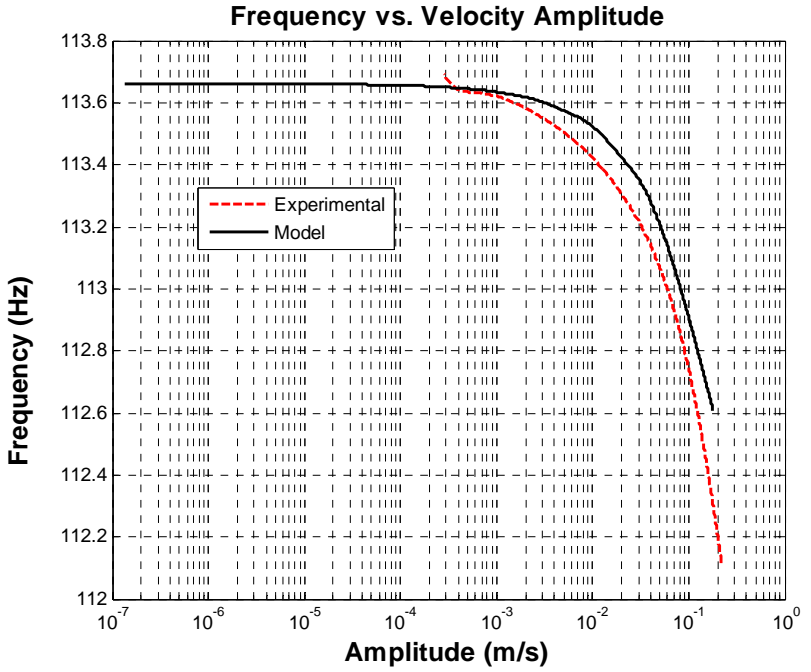


Figure 43. Frequency versus Velocity Amplitude - 1<sup>st</sup> Mode

A similar procedure was used for the  $2^{nd}$  mode resulting in the comparisons shown in Figs. 44 and 45. For this simulation the excitation at point  $304_{x1}$ , see Fig. 40, was used to generate a response.

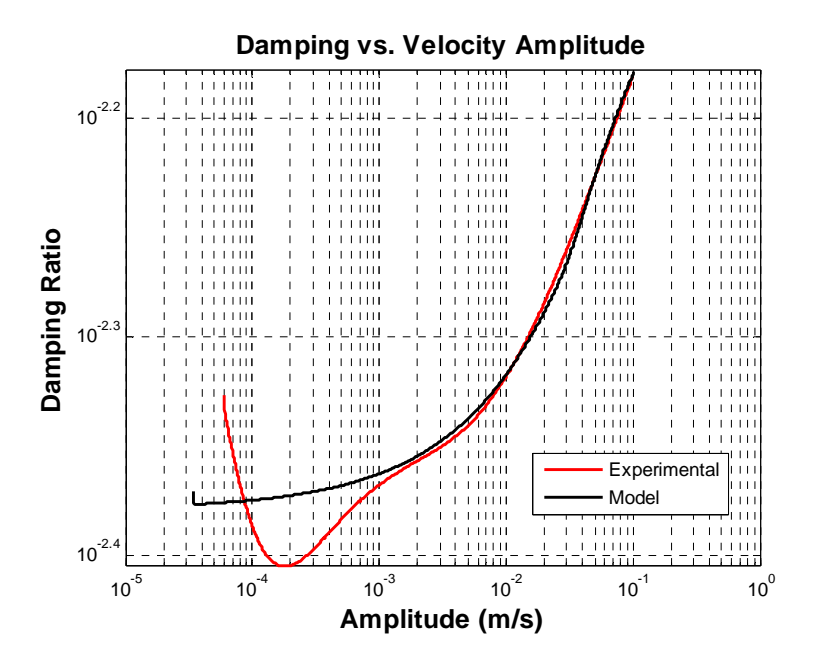


Figure 44. Damping Ratio versus Velocity Amplitude - 2<sup>nd</sup> Mode

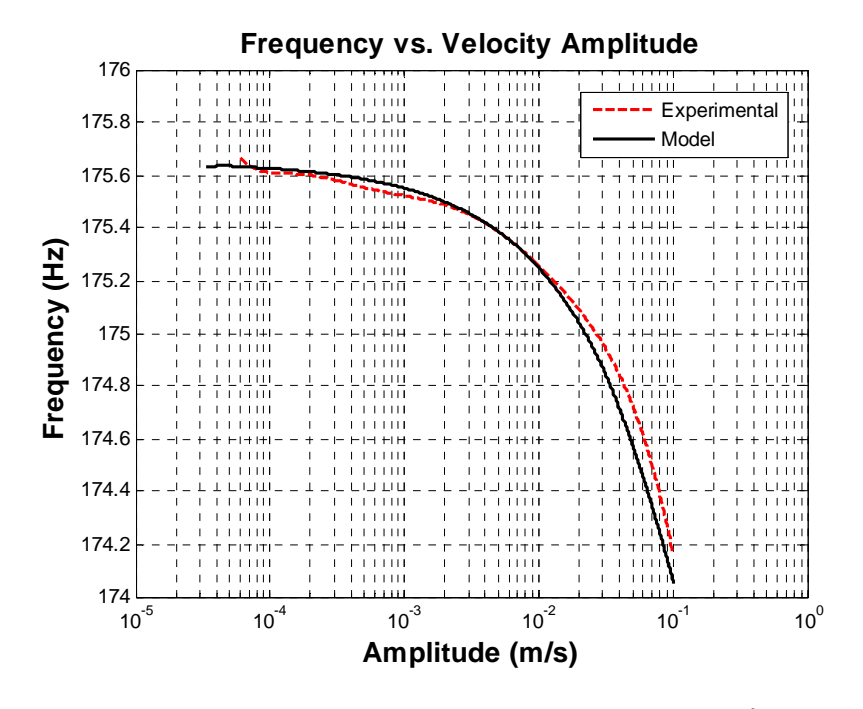


Figure 45. Frequency versus Velocity Amplitude - 2<sup>nd</sup> Mode

Table 13 shows the parameters that were used in simulations of the first two modes.

Table 13: Iwan model parameters for catalytic converter system

Parameter	Simulation Case 1 <sup>st</sup> Mode	Simulation Case 2 <sup>nd</sup> Mode
$F_{s}$ (N)	1200	1000
$\Delta f_n$ (Hz)	40	41
$K_{T}$ (N/m)	295930	501058
β	0.7	0.7
χ	-0.280	-0.400
Linear damping, Linear $\zeta_v$	0.00305	0.0043

The  $\Delta f_n$  values here are much larger than those observed using the ZEFFT algorithm. The amount of energy dissipated in the joint depends on how much load it carries. Hence, for the joint to cause the damping to change by a factor of two as was observed, it must carry significant load and the system experiences a large change in stiffness if the joints slips completely. Even then, this value is reasonable, since the frequency of the first mode would change quite dramatically if the bolts were not present. Indeed, in [52] the joint stiffness in a beam structure was estimated by loosening the bolts until they barely held the parts together and measuring the structure's natural frequencies.

The simulated response of these mode is shown in Figs. 46 and 47 and excellent agreement was found with the measured modal response. The damping decays the signal at a similar rate and the frequency remains lined up throughout the decay even as it changes.

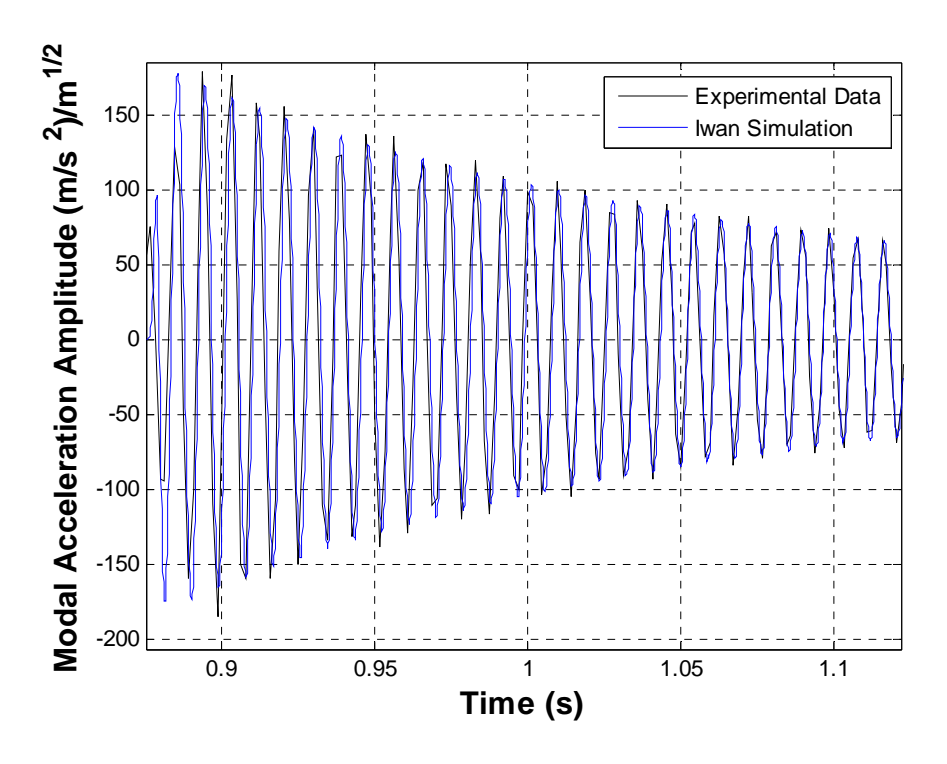


Figure 46. 1st Mode Acceleration Response (Experimental and Iwan Simulation)

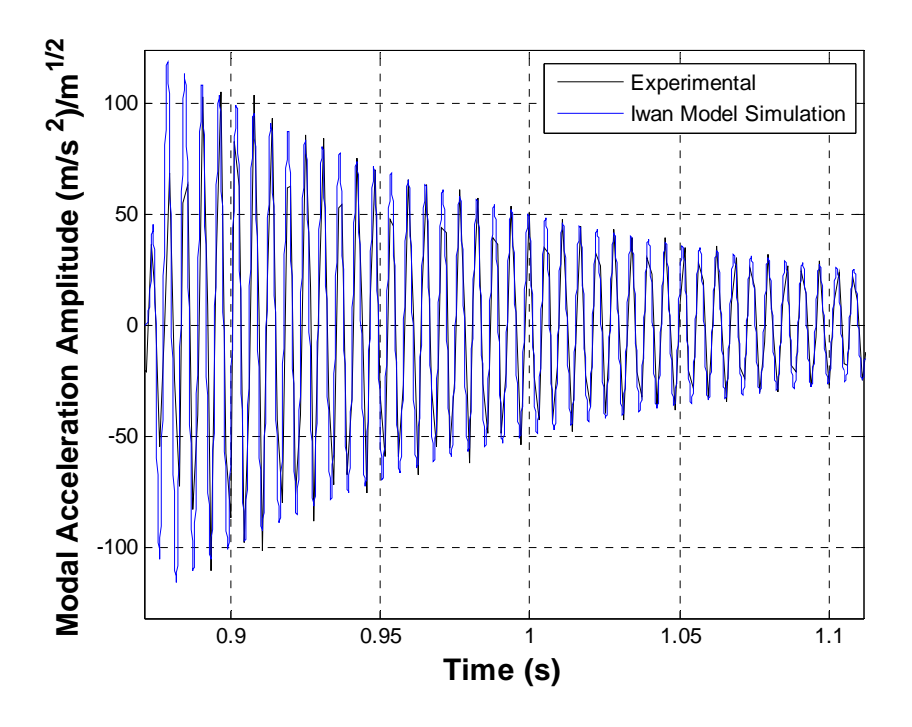


Figure 47. 2nd Resonance Modal Acceleration Response (Experimental and Iwan Simulation)

The two responses that were shown in Fig. 46 and 47 were from two different forces that excite each mode into the nonlinear regime, one could easily apply this procedure to a single force time history and add up all of the modal contributions to see the full response as was done in [52]. This comparison does not add any additional insight because the two modes combine in a complicated way so it was not shown.

# 3.2.5 Catalytic Converter Example Remarks

This work explored the applicability of a modal Iwan model to the first few modes of an assembly structure consisting of actual production exhaust components. The results showed that the ZEFFT was useful in screening modes to determine which modes were most affected by joint nonlinearity. Then, a Hilbert transform analysis was used to quantify the change in damping with response amplitude and then to estimate the parameters of a nonlinear model for each mode. Using these tools, the procedure was relatively fast and could be readily extended to structures with many more modes. All of the modes of the assembly studied were either linear or well described by a modal Iwan model with a viscous damper in parallel to capture low level material damping. It is encouraging that the modal Iwan framework appears to be capable of describing all of these lower modes of this structure, and it was relatively easy to characterize the structure mode-by-mode in this manner. It would have been much more challenging to model each joint as a discrete nonlinearity and then to update a model for the entire structure to try to obtain the behavior that was observed in the measurements, and the resulting model would be more expensive to integrate. The next example is on a system containing many more linear and weakly nonlinear modes.

## 3.3 Cylinder-Plate-Beam System

### 3.3.1 Introduction

As seen in previous example, a large class of structural dynamic system responses are weakly nonlinear in stiffness (a few percent modal frequency change) and significantly nonlinear in damping (hundreds of percent damping ratio change) as a function of amplitude of vibration. Such systems will typically be linear at low level excitation. At higher levels of excitation the resonant frequencies typically decrease slightly and the apparent damping can increase significantly. In [3] damping was observed to increase by a factor of three. Linear models used to simulate the response may over-predict the nonlinear response by tens to hundreds of percent.

This section will explore another weakly nonlinear system the Cylinder-Plate-Beam (CPB) system discussed previously in Chapter 2.3 and pictured in Fig. 19. Consider a frequency response function (FRF) from the hardware used in this work due to a high level and a low level impact as shown in Fig. 48. The test at low force levels produces an FRF whose peak response is a factor of two larger than that from a test at high amplitudes. Occasionally the resonant frequency will go up slightly and the apparent damping will go down with an increase in the amplitude. It is desired to be able to simulate both softening and stiffening behavior. As mentioned previously, Segalman [51] explored the possibility of utilizing a modal Iwan approach to capture spatially distributed nonlinear energy dissipation with a one degree-of-freedom (DOF) analytical model. Segalman showed that a 3DOF system could be modeled as three uncoupled modes using the 4-parameter modal Iwan model. Deaner [88] extended this concept showing that the first several modes of a beam could be modeled as uncoupled and governed by uncoupled nonlinear SDOF systems when he used the modal Iwan model in parallel with a discrete damper.

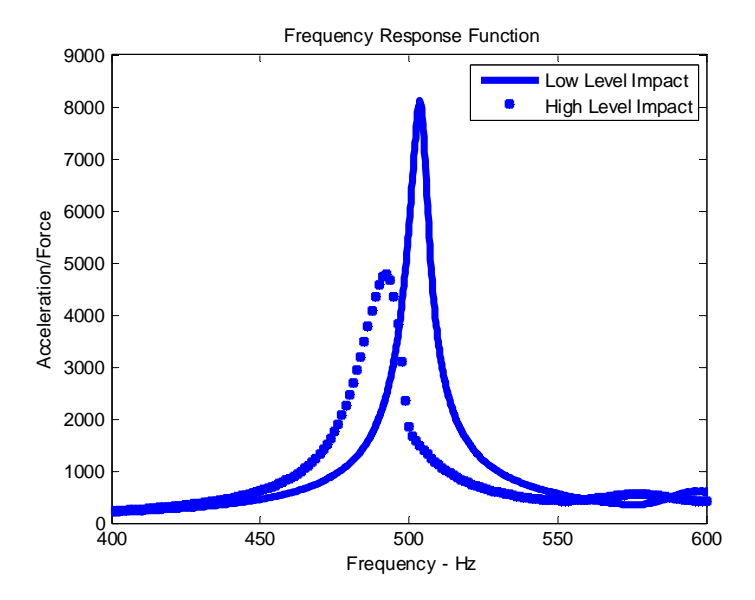


Figure 48. Drive Point FRF magnitude - low level versus high level impact force

The approach used in this example utilizes a weakly nonlinear modal model framework. One assumption for this approach is that superposition of the modal responses can be multiplied by the mode shape matrix to estimate the response at physical DOF. Inherent in this approach is the assumption that the mode shapes do not change with response amplitude, and that the modal DOF do not interact. This approach begins with the standard modal model using a linear spring and damper for each modal mass. The spring and damper are identified in a standard low level modal impact test. It was assumed that nonlinear elements can be connected in parallel with the standard linear elements. A high level impact test on the nonlinear structure provides data for fitting the nonlinear parameters of each model type. Two different nonlinear elements are examined in this section: 1. a 4-parameter Iwan element in parallel with a linear stiffness and damper; and 2. cubic polynomials of stiffness and damping as a function of modal response amplitude. After the elements were identified, a simulated high level structural response was completed to compare with measured data. A key portion of the success of this approach comes from a modal filter that can filter out all the modal responses of the structure except the single mode of interest. The single DOF modal filtered response is used to identify the nonlinear parameters. The Iwan model require that the Hilbert Transform of the modal response be computed as a step in the identification

process. The cubic stiffness/damping model does not have this requirement as it does not rely on the instantaneous damping or frequency but uses the filtered measurement directly in a least squares sense.

# 3.3.2 Experimental Set-up

The experimental set-up used in this work is the same as that shown in Chapter 2.3.2. This hardware is shown in Fig. 21 with the instrumentation layout shown in Fig. 22. The only difference in set-up is that this configuration has no washers in between the plate and the cylinder in this system. This was found to create more nonlinearity in this system, most likely due to the increased contact area. The lack of these washers and reassembling of the system has caused the linear frequencies to shift slightly compared to their measured values from Chapter 2.3.2.

Two series of hammer impact tests were conducted on the hardware described above. The first minimized the nonlinear response by applying low level inputs with peak forces of approximately 23 Newtons at the three locations shown in Table 14. These input degrees of freedom can be observed on Fig. 22 form Chapter 2.3.2. This data was used to extract parameters for the linear modal model of the hardware. The second set of tests excited nonlinearities with inputs at these same locations but with much higher peak forces: 180 and 400 Newton for the radial and axial hits, respectively. The 400 Newton strike was not used for the radial inputs because this force level caused the response to exceed the measurement range of the drive point accelerometers. The high level data was used to first identify which modes were nonlinear and secondly to extract parameters for the nonlinear models.

Table 14: Excitation Information

Input DOF	Description	Low Level Peak Force [N]	High Level Peak Force [N]
301Y-	Axial input at tip of beam	23	400
5002R-	Radial input at aft end of can in the stiff direction of the	23	180
	beam		
5003R-	Radial input at aft end of can in the soft direction of the	23	180
	beam		

# 3.3.3 Preliminary Modal Results

The Synthesize Modes And Correlate (SMAC) program by Mayes and Hensley [78] was used to extract two sets of modal parameters from the low and high level impact data using a real modes approximation in Table 15. Rigid body mode shapes were calculated from solid model mass properties.

Table 15: Linear Modal Parameters - Modes in Green were considered nonlinear

	Low Level Hi		High	High Level		4 %			
Mode	J n	ζ (9/)	$f_n$	ζ (0/)	$\Delta f_n$ (%)	$\frac{\Delta\zeta}{(\%)}$	Reference	Shape Description	
	(Hz)		(Hz)	(70)				at .	
7	119	0.36	116	0.95	-3	167	5003R-	1 <sup>st</sup> beam bend in X	
8	160	0.21	158	0.60	-1	190	5002R-	1 <sup>st</sup> beam bend in Z	
9	276	2.46	273	3.60	-1	46	5002R-	Torsion of internal mass	
10	282	2.10	280	1.92	-1	-9	5003R-	Translation in X of internal mass	
11	302	2.34	298	2.40	-1	3	5002R-	Internal mass off-axis twist	
12	503	0.67	491	1.23	-3	84	301Y-	Axial mode of beam Y	
13	592	2.02	570	2.91	-4	44	301Y-	Rotation of internal mass about Z	
14	635	2.00	630	2.27	-1	14	5002R-	Rotation of internal mass about X	
15	699	1.26	692	1.44	-1	14	301Y-	Axial mode of internal mass Y	
16	734	1.27	732	1.38	0	9	5003R-	Foam mode X	
17	759	1.13	758	1.16	0	3	5002R-	Foam mode Z	

The low level modal parameters were used to create the linear modal model used in the later sections of this report. The high level modal parameters were used to determine which modes should be modeled as nonlinear. Since damping values extracted from measured data can have 10% uncertainty, the heuristic used in this work was that any mode with a damping shift of greater than 30% was declared nonlinear. Modes 7-9, 12, and 13 were thus selected to be modeled as nonlinear.

# 3.3.4 Signal Processing

To develop a nonlinear modal model, the proposed approach requires the structural response be separated into the individual modal responses. This requires some type of filter that can transform multiple sensor measurements into modal coordinates. Once these modal responses are calculated, further processing is required to aid nonlinear parameter identification. The following sections detail this two-step procedure.

A modal filters was used to transform measurements in physical coordinates to modal responses were exercised. A modal filter is desired such that:

$$\overline{\Psi}^T \overline{\mathbf{x}} = \mathbf{q}. \tag{43}$$

where  $\mathbf{q}_i$  is the  $i^{\text{th}}$  modal DOF, column vector  $\overline{\mathbf{x}}$  contains measured responses, and  $\overline{\mathbf{\Psi}}$  is the vector of weights transforming the measured responses to the modal response. The SMAC modal filter [90] operates directly on the FRFs. If one operates on Eqn. (43) in the frequency domain and divides by the input force, then

$$\bar{\mathbf{\Psi}}^T \bar{\mathbf{H}}_x = \mathbf{H}_a \tag{44}$$

where  $\overline{\mathbf{H}}_x$  is now a vector of measured FRFs and  $\mathbf{H}_{q_i}$  is an analytically calculated single DOF (SDOF) FRF with frequency and damping as extracted from the high level impact data. Columns for every frequency line are added to  $\overline{\mathbf{H}}_x$  and  $\mathbf{H}_{q_i}$  creating a matrix of  $\overline{\mathbf{H}}_x$  and a vector of the analytical FRF  $\mathbf{H}_{q_i}$ . Transposing and isolating the modal filter on the left side yields

$$\overline{\Psi} = \overline{\mathbf{H}}_{\mathbf{r}}^{T+} \mathbf{H}_{a}^{T} \tag{45}$$

where the superscript <sup>+</sup> represents the pseudo-inverse. Hence, the SMAC modal filter is obtained with the measured FRFs and an analytical SDOF FRF constructed using the extracted frequency and damping from the high level linear modal parameter extraction. This is different from the spatial filter applied in the Catalytic Converter example which made use of the linear mode shapes rather than the measured FRFs of the system.

Once a single degree of freedom is obtained for each nonlinear mode, damping and frequency are quantified as a function of response amplitude. The procedure for accomplishing this closely follows the work from [52, 91]. In this work, the Hilbert Transform is computed and a cubic polynomial is fit to the time varying amplitude and phase. This follows the same mathematics as Eqns. (26-33).

The nonlinear stiffness and damping from the Hilbert Transform for of each mode can now be evaluated based on changes in damping ratio and frequency with respect to time. The instantaneous damping and frequency can be plotted against velocity and displacement amplitude to bring these parameters into a response based form rather than time based.

It is essential to reduce the signal to a single degree of freedom before completing the above process else the envelope and instantaneous phase will be distorted by interference of other modes. In order to assist the modal filter in eliminating unwanted frequency content, a band-pass filter is applied to the modal response. A forward-backward filter was utilized for this supplemental filter which maintained the timing of the original response signal. A brief sensitivity study was completed to investigate the influences of various passbands on each mode. In this study, passbands were varied from  $\pm 10\%$  of the natural frequency to as high as  $\pm 50\%$ . For each passband and modal response, the time-varying damping and natural frequency were plotted versus time to determine the consequences of narrower/wider passbands. The objective was to determine a passband for each mode that successfully eliminated unwanted frequency content without distorting the measured damping. For this structure a 50% passband was used for all modes which was robust for every mode when using the SMAC modal filter. The passband used in this example is not universal and might need modification for a different system or loading case.

#### 3.3.5 Nonlinear Models

### 3.3.5.1 Modal Iwan Model

As discussed in [52] and earlier in Chapter 3.2.1 each mode can be modeled with a single degree of freedom system as a modal coordinate. Each modal degree of freedom will be linked to ground with a linear spring and damper. In order to capture the nonlinearity in each mode, a 4-parameter Iwan element is added in parallel with the linear spring and damper. Recall the SDOF system diagram from Fig. 26.

Similar to the catalytic converters, in this example the author only obtained measurements in the linear and micro-slip regimes of response. Thus some of the parameters became more difficult to estimate. The stiffness in the joint,  $K_T$ , is defined as the change in stiffness as shown in Eqn. (36).

The parameter  $\chi$  can be determined directly from the damping ratio versus velocity amplitude curve. The value of  $\chi$  defines the power law exponent on the dissipation versus velocity amplitude curve. The linear damping is subtracted prior to fitting  $\chi$  just as was the case for the Catalytic Converter example. As discussed in Chapter 3.2.1 the damping ratio is fit to the form of:

$$\zeta(\dot{q}) = C_{zz} |\dot{q}|^{z+1} \tag{46}$$

where  $C_{zt}$  is calculated as the intercept of the power law fit from

In [48], Segalman defines dissipation in a similar form:

$$Dissipation = R |\dot{q}|^{\chi + 3} \tag{47}$$

In Ginsberg's text [12], the relationship between damping ratio and dissipation can be used to solve for the coefficient R.

$$\zeta = \frac{Dissipation}{m2\pi\omega_d \omega_n |\dot{q}|^{\chi+3}} \to R = C_{zt} 2\pi\omega_d^{\chi+2} \omega_n \tag{48}$$

Based on additional 4-parameter Iwan model definition from [48] one can solve for the remaining unknown parameters  $\beta$  and  $F_s$  using an assumed  $K_T$  along with extracted values for  $\chi$  and R. Using these 4-parameters the joint force can now be calculated and integrated. The identification procedure described above was performed on the nonlinear modes and the results are provided in the table below.

Table 16: Iwan Parameters for Identified Nonlinear Modes

rubic 10: Iwan i ununcters for identifica Nominical Modes									
Mode	χ	β	$F_s$	$K_{T}$	$f_{n,lin}$	$\zeta_{n,lin}$			
7	-0.65	0	245	2.10E+05	119	0.0036			
8	-0.31	0	39	2.91E+05	160	0.0021			
9	-0.22	0	51	9.92E+05	276	0.0246			
12	-0.77	0	52	9.69E+05	503	0.0067			
13	-0.79	0	108	2.24E+06	592	0.0202			

## 3.3.5.2 Restoring Force Surface

This method has been extensively researched and refined with several permutations. Reference [61] contains an extensive synopsis of the past variances and applications of the Restoring Force Surface (RFS) method. Similar to the Iwan model, the version of the RFS model structure adopted for this work is shown in Fig. 49 where the linear elements are in parallel with the nonlinear ones.

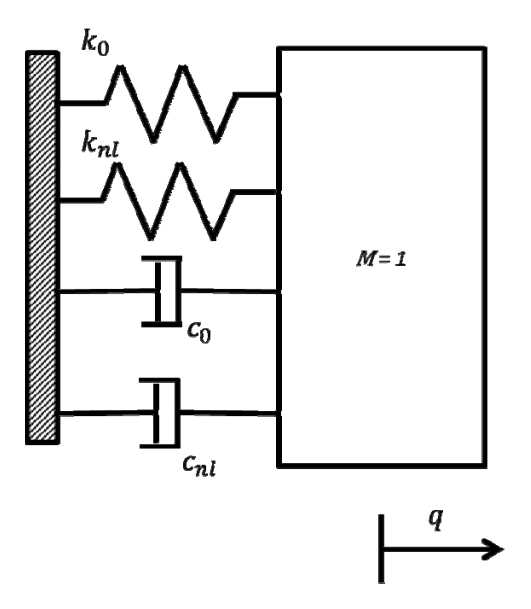


Figure 49. Schematic of SDOF for RFS modal coordinate

The foundation of RFS is in the Newtonian equation of motion:

$$\ddot{\mathbf{q}} + \mathbf{F}_{\cdot \cdot}(\mathbf{q}, \dot{\mathbf{q}}) = \mathbf{F} \tag{49}$$

where  $\mathbf{F}_r(\mathbf{q},\dot{\mathbf{q}})$  represents the damping and stiffness forces (called the restoring forces) and  $\mathbf{F}$  is the excitation force. Assuming the acceleration and excitation force are measured, then at every time instant, the restoring force is also known.  $\mathbf{F}_r$  is written in the following form:

$$\mathbf{F}_{r}(\mathbf{q},\dot{\mathbf{q}}) = c_{0}\dot{\mathbf{q}} + c_{1}|\dot{\mathbf{q}}|\dot{\mathbf{q}} + c_{2}\dot{\mathbf{q}}^{3} + k_{0}\mathbf{q} + k_{1}|\mathbf{q}|\mathbf{q} + k_{2}\mathbf{q}^{3}$$

$$(50)$$

where  $c_1$ ,  $c_2$ ,  $k_1$ , and  $k_2$  are constants. Since  $c_0$  and  $k_0$  are already known from the low level modal tests, Eqn. (50) is rearranged to,

$$\begin{bmatrix} |\dot{\mathbf{q}}|\dot{\mathbf{q}} & \dot{\mathbf{q}}^3 & |\mathbf{q}|\mathbf{q} & \mathbf{q}^3 \end{bmatrix} \begin{bmatrix} c_1 \\ c_2 \\ k_1 \\ k_2 \end{bmatrix} = \mathbf{F} - \ddot{\mathbf{q}} - c_0 \dot{\mathbf{q}} - k_0 \mathbf{q}$$
(51)

or

$$\begin{bmatrix} \mathbf{P} \end{bmatrix} \begin{bmatrix} c_1 \\ c_2 \\ k_1 \\ k_2 \end{bmatrix} = \begin{bmatrix} \mathbf{U} \end{bmatrix} \tag{52}$$

Recall that [P] and [U] are processed measurements and that there is a row for each time sample. The best results were obtained by taking the Fourier transform of each column of [P] and [U] giving,

Note that in order to yield real coefficients,  $\left[P_{\Im}\right]$  must be reconfigured to,

$$[\mathbf{P}_{3}] = \begin{bmatrix} real(\mathbf{P}_{3}) \\ imaginary(\mathbf{P}_{3}) \end{bmatrix}$$
 (54)

and  $[\mathbf{U}_3]$  must be similarly restructured. Pre-multiplying  $[\mathbf{U}_3]$  by the pseudo-inverse of  $[\mathbf{P}_3]$  results in the least squares estimate for nonlinear restoring force coefficients  $c_1$ ,  $c_2$ ,  $k_1$ , and  $k_2$ .

Quality results were obtained by applying a weighting matrix to Eqn. (53) near resonances. If the weighted bandwidth is taken to be  $\pm 5\%$  of the frequency of the resonance, this method gave better parameters than the time domain results from Eqn. (52).

$$\mathbf{W}[\mathbf{P}_{3}] \begin{bmatrix} c_{1} \\ c_{2} \\ k_{1} \\ k_{2} \end{bmatrix} = \mathbf{W}[\mathbf{U}_{3}] \tag{55}$$

where **W** is the block diagonal weighting matrix. For the Restoring Force Surface results in this work this weighted frequency domain approach was utilized with a weight of 100 applied to the narrow resonance bands and 1 elsewhere.

Note that acceleration, velocity, and displacement must all be known (estimated or measured). For this work, acceleration was obtained from the modal filtered measured accelerations and the other two states were estimated by integrating in the frequency domain. The first step was to band-pass filter the modal acceleration as described in Chapter 3.3.4. The velocity and displacement in the frequency domain were then calculated by dividing this acceleration by  $i\omega$  and  $-\omega^2$ , respectively, followed by band-pass filtering using the same filter that was applied to the modal acceleration.

The identification procedure described above was performed on the five nonlinear modes, and the resulting coefficients are provided in Table 17.

Table 17: Restoring Force Surface Coefficients for Identified Nonlinear Modes

Mode	$c_2$	$c_1$	c <sub>0</sub>	$k_2$	$k_1$	$k_{\theta}$
7	-1.36E+03	367	5	1.69E+13	-1.5E+09	5.56E+05
8	-3.77E+03	579	4	1.52E+13	-1.8E+09	1.01E+06
9	-1.94E+05	6.63E+03	85	6.14E+14	-1.5E+10	3.01E+06
12	-5.35E+02	299	42	1.49E+14	-1.9E+10	1.00E+07
13	-3.24E+04	3.33E+03	150	4.42E+15	-1.6E+11	1.38E+07

### 3.3.6 Results and Observations

This section compares the results of each of the nonlinear modal models to the actual nonlinear experimental measurements. First, a discussion of the simulations used to create the analytical modal responses for linear and nonlinear modes is presented followed by a comparison to measured data in physical coordinates. Discussions of features of each method will conclude this section.

The two pseudo-modal models with 17 modes were excited with simulated modal forces corresponding to the measured high level impacts from the three different locations. The modal responses were extended to the physical DOF using the linear mode shape matrix extracted from low level modal tests. These responses were compared against the measured high level data in the plots below. Note that the line labeled "Linear" is the response of a linear model that used the low level linear parameters from Table 15 for all 17 modes.

A representative sample of results are presented. Figure 50 compares the linear model response with the measured data by considering the primary singular value of the complex mode indicator function (CMIF). The CMIF compresses all the responses from all three force impacts into one plot. This plot illustrates that the linear model over-predicts the response from a high level impact; the three main modes of the system (7, 8, and 12) are over-predicted by almost 100%. Additionally, the linear model is slightly too stiff.

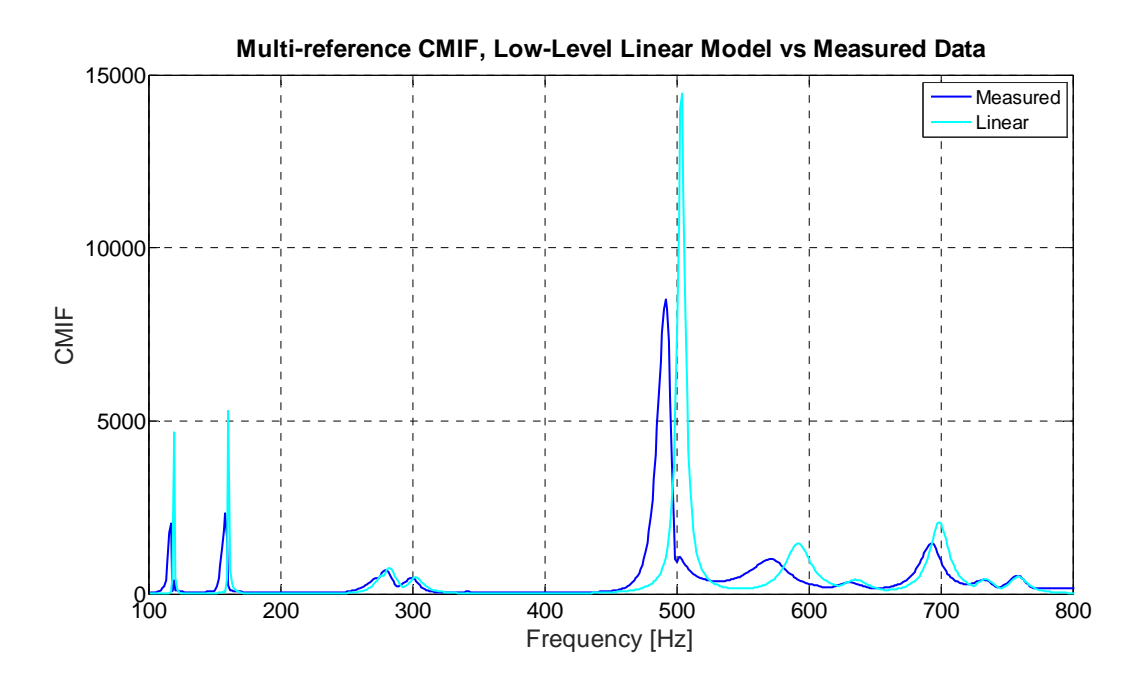


Figure 50. Multi-reference CMIF, linear model prediction versus measured data, max singular value only

Figure 51 shows the primary singular value of the multi-reference CMIF of the high level measured data and the corresponding predictions of both nonlinear models. All models are able to predict the high level test data better than the linear model. Note that for declared linear modes, both model results overlay, an expected result since both pseudo-modal models were the same for the linear modes.

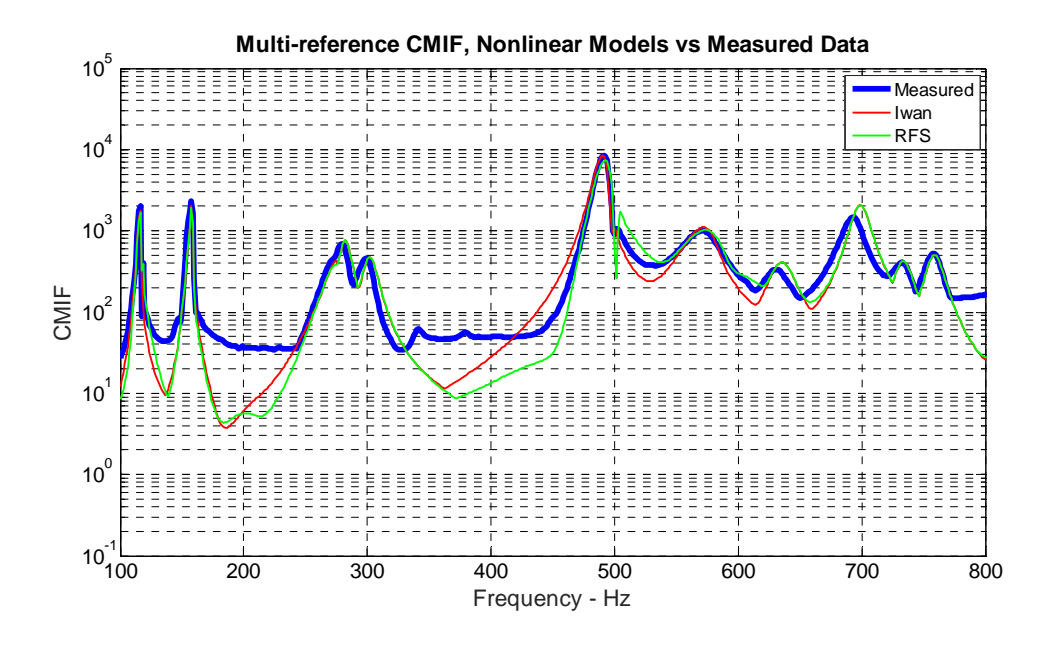


Figure 51. Multi-reference CMIF, nonlinear model versus measured data

The time history plots of Figs. 52-55 reinforce the results from Fig. 51. The drive point response to the axial input is dominated by mode 12. Both models were able to accurately replicate the measured data.

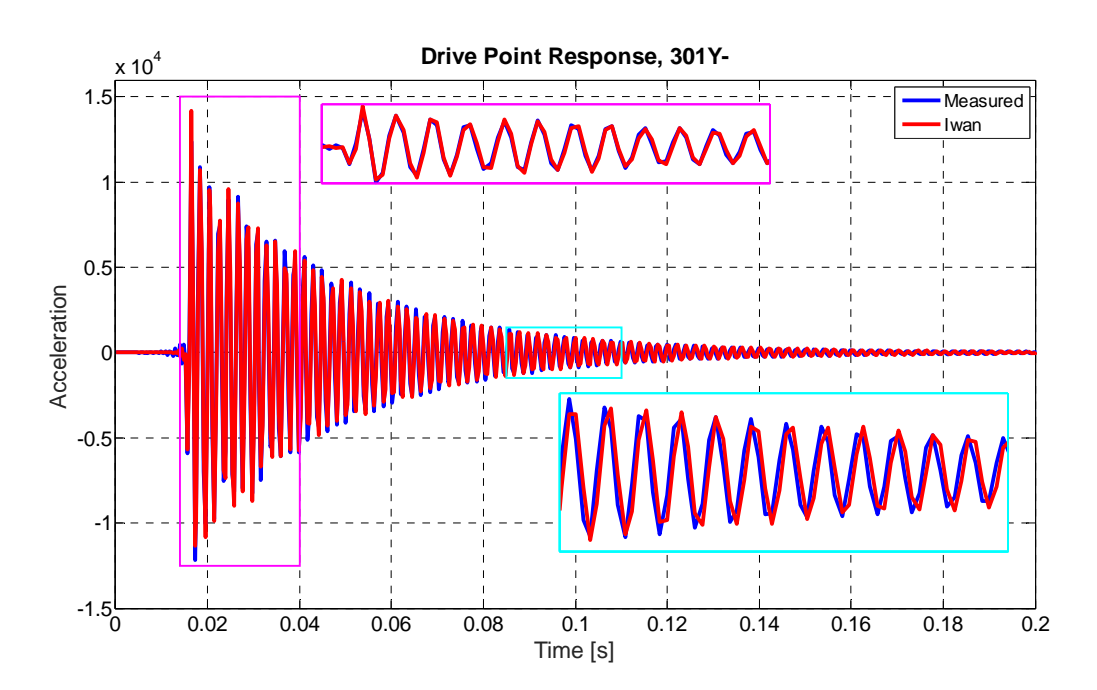


Figure 52. Axial drive point response, Iwan versus measured

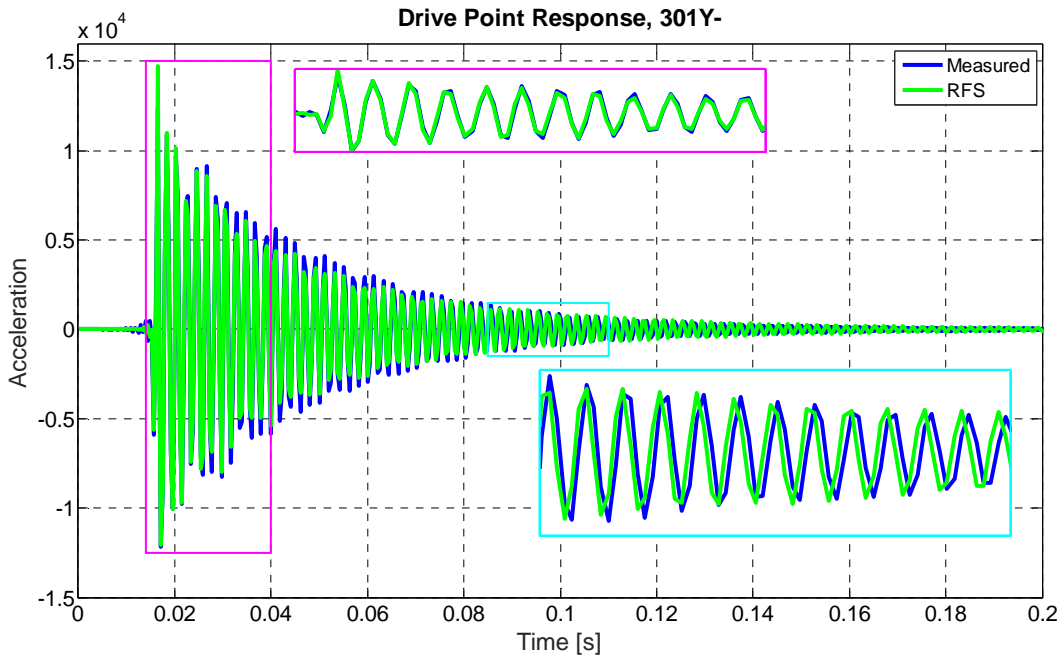


Figure 53. Axial drive point response, RFS versus measured

The Iwan and RFS models comparably predicted the drive point response from the radial input in Figs. 54 and 55. Neither achieved the proper amplitude of the initial acceleration spike, but they simulate the rest of the time history well.

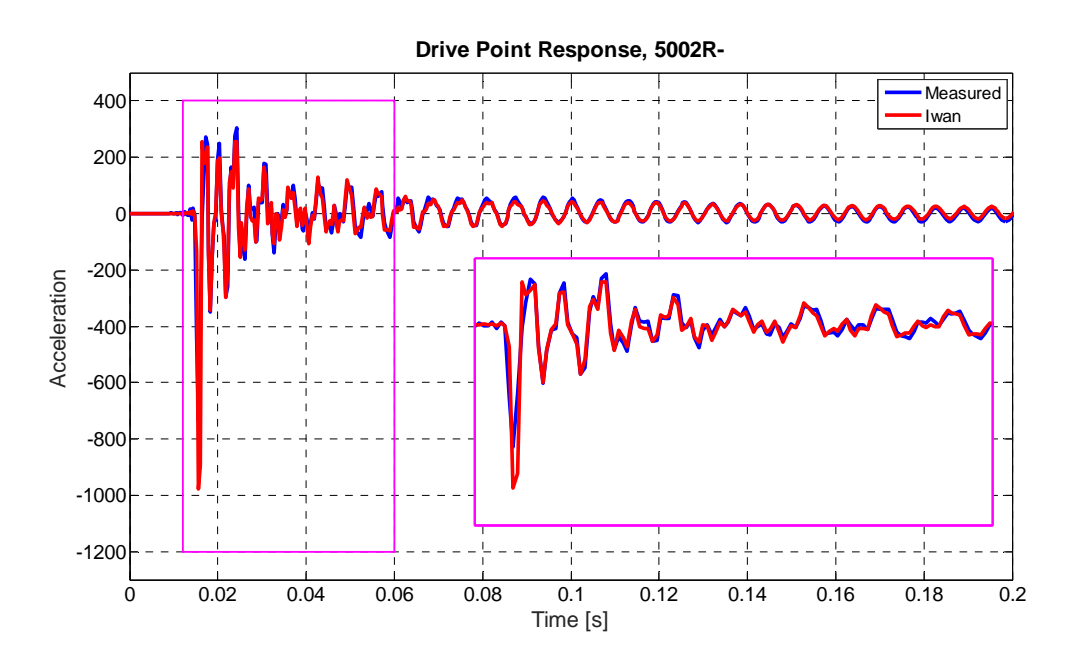


Figure 54. Radial drive point response, Iwan versus measured
Drive Point Response, 5002R-

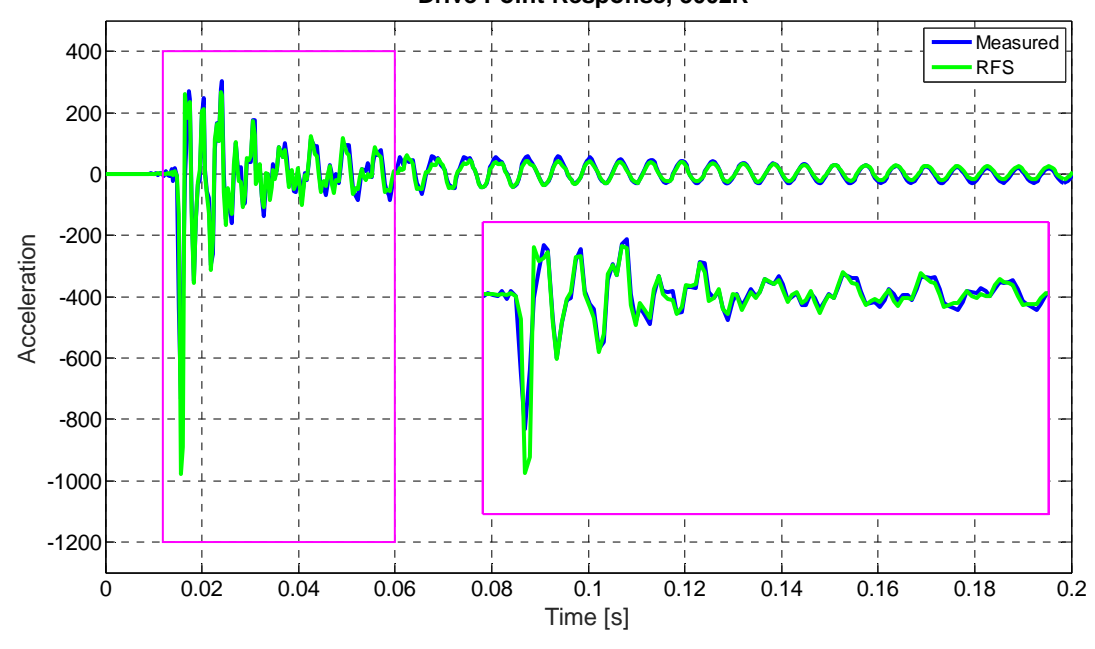


Figure 55. Radial drive point response, RFS versus measured

Although not readily apparent from the figures, it is important to note the significant role of the Hilbert transform in the Iwan model parameterization. While an extremely valuable and versatile tool that provides great qualitative insight into the frequency and damping variation, it can also have adverse effects depending on the characteristics of the data. In the presence of step changes in signal amplitude or frequency, the envelope and instantaneous phase produced by the Hilbert transform will have some overshoot and settling time characteristics [92]. Given that this work utilized impact data which has a large step-like change in amplitude, the envelopes and instantaneous phases extracted from the Hilbert Transform of the measured data were distorted during the initial portion of the response. These errors consequently influenced the polynomial fits for the envelope and instantaneous phase upon which the model depends.

Another aspect worth mentioning is the interplay of the Hilbert transform and the quality of the modal filter. In addition to the transient effects mentioned above, any non-targeted modal peaks that are not adequately attenuated in the modally-filtered response can produce ripples throughout the entire envelope. These ripples influence the polynomial fits to the Hilbert transform and hence the nonlinear parameters of the Iwan model. In extreme cases when the modal filter cannot eliminate a nearby mode (e.g. mode 9), the envelope and instantaneous frequency (and hence the nonlinear parameters) are distorted by the non-suppressed mode. This phenomenon can contribute to an inaccurate prediction. The RFS method can also suffer from non-targeted poorly attenuated modal peaks in the modally-filtered response, but does not rely on the Hilbert Transform, which eliminates effects from the Hilbert distortions as well as the extra steps of calculating and fitting the Hilbert Transform. In addition, the RFS model loses the connection that the Iwan model attempts to keep with the physics of the frictional interface.

Both modeling methods provided satisfactory nonlinear simulations with enough user interaction. For these studies, the Iwan model and the RFS frequency fit model gave similar satisfying simulation results. Six parameters were chosen for each mode for each method to put them on equal footing;

however, the Iwan model never reaches micro-slip so is truly only using 4 of the 6 parameters. A Palmov model [93] may be more appropriate for this comparison.

### 3.4 Remarks

The tools in this chapter present a methodology to screen and find nonlinearities in experimental measurements. This screening process selected a subset of modes on an experimental system that displayed traces of nonlinear behavior. In the first example, an assembly of catalytic converters was tested and a 4-parameter modal Iwan model was used to represent this observed nonlinear behavior with extremely accurate results. On the catalytic converter system only two modes of the system were treated as nonlinear. In contrast, the second example on the Cylinder-Plate-Beam system contained five nonlinear an six linear modes. Again, a 4-parameter modal Iwan model was used to describe the nonlinearity in this system. Additionally, a simpler model was defined representing the nonlinear behavior with cubic stiffness and damping terms added to each modal equation of motion. polynomial model also provided a highly accurate result and bypassed some complications that can arise when using the Hilbert Transform. Despite this advantage, the polynomial model loses the physical meaning of parameters established by the modal Iwan model. Both models provided suitable results to use in a dynamic substructuring prediction. In the remainder of this dissertation, Chapters 4 and 5, 4parameter modal Iwan models are used to capture the nonlinear behavior of simulated and experimental systems. These nonlinear modal models can be used to describe the nonlinear dynamics of an individual subcomponent. These subcomponent models will be used in a component mode synthesis prediction, in order to evaluate how the nonlinear dynamics described in a subcomponent can be used to describe the nonlinearities present in assembled structure.

# 4 Nonlinear Modal Substructuring: Simulated Experiments

#### 4.1 Introduction

This chapter has been submitted as an article to the Journal of Mechanical Systems and Signal Processing [94]. This chapter utilizes the nonlinear modal model identification techniques, as described in Chapter 3, on simulated experimental measurements in order to define a subcomponent model and to perform nonlinear substructuring predictions. This chapter remains unchanged from the original journal submission. As such, some of the content in this chapter is repeated from previous chapters, such as the methodology for fitting a 4-parameter modal Iwan model discussed again in Chapter 4.4.1.

Experimental-analytical substructuring allows one to couple an experimentally derived model of one subcomponent with a finite element model of a different subcomponent. This can be particularity useful when one substructure would be difficult to model; rather than create a finite element model for that component, one can simply perform an experiment to identify a model that captures its dynamics. There are countless compelling industrial applications where experimental-analytical substructuring would be beneficial and most contain interfaces with bolted joints. Interfaces in built-up structures are responsible for a large portion of the damping in the assembly, with bolted joints being the most common source of nonlinearity [1, 2]. Many of these jointed structures are weakly nonlinear, meaning that the mode shapes of the structure do not change significantly as amplitude increases. This work presents an extension of modal substructuring for this class of structure and validates the methodology through simulations. A companion paper applies this methodology to experimental measurements from a real structure.

There are several methods of experimental-analytical substructuring. In [13] de Klerk et al. provide an excellent review of several methods and their history. In essence, substructuring is a process of enforcing constraints at interfaces and assuring that the sum of the reaction forces at an interface is zero. This constraint enforcement is applicable regardless of whether the subcomponents of the structure

are linear or nonlinear. In this work, the transmission simulator method [26, 38, 95] was used to generate dynamic substructuring predictions. This method uses an experimental system that includes a fixture (or transmission simulator) as one subcomponent. This fixture is meant to simulate the boundary conditions of the subcomponent of interest in the assembly.

Recent works have shown that bolted interfaces can cause the damping in a system to increase by a factor of two or more [3, 82, 96], while the effective natural frequency tends to change relatively little. Furthermore, under the conditions outlined in [50] (simplistically that the joint forces and their harmonics are distinct from each modal frequency), the modes of the structure tend to remain uncoupled so that the structure can be modeled accurately using a collection of uncoupled, weakly-nonlinear oscillators [52, 97]. This was confirmed in [3] for an assembly of automotive exhaust components, by exciting the structure at multiple locations and various force levels (in the micro-slip regime). A second investigation, on a cylindrical structure with bolted joints and nonlinear contact between foam and an internal structure, also highlighted the usefulness of this approach [98]. More recently, Krack explored descriptions of individual subcomponents with nonlinear normal modes in [65]. Krack explores many examples of systems where one mode is dominant and nonlinear while others can be treated as linear. While Krack's work focused on a general nonlinear modal modeling framework, which is applicable for a wide range of nonlinear models, this work explores the use of a modal Iwan model to define the nonlinear dynamics of each substructure. A modal Iwan model accurately captures the power-law dependence of damping on amplitude that is frequently observed in experimental measurements as seen in [52, 99-101].

This is not the first work to propose substructuring of nonlinear subcomponents, although relatively little has been published on this topic. A few works [62-64] have extended linear frequency based substructuring into the nonlinear realm using the harmonic balance method. Chong and Imregun [70] used variable modal parameters to couple multiple nonlinear substructures focusing on weakly nonlinear structures. Chong and Imregun used describing functions to specify how the frequency and shape of a mode change with amplitude, however they seem to confuse the tangent stiffness of the system

with the effective stiffness of a single-term harmonic balance model. They employed an iterative approach which was used to solve for the amplitude dependant modal properties of the built-up structure in the frequency domain by updating the equations of motion for each subcomponent. This work also focuses on weakly nonlinear structures, and seeks to obtain predictions across a range of vibration amplitudes, yet modal substructuring is performed in the time domain.

In [26], Allen, Mayes and Bergman presented the transmission simulator (TS) method, one of the features of which is its ability to capture the linear stiffness and damping of the joints between subcomponents. This work extends the TS method to include nonlinearities in subcomponent models. To create a nonlinear model of each subcomponent, this work proposes to use uncoupled single degree-of-freedom (SDOF) oscillators to represent each weakly nonlinear mode in the structure. These subcomponents are then assembled using a primal formulation [13]. Specifically, the set of nonlinear oscillators are assembled using standard finite element assembly techniques. The assembled equation of motion and its Jacobian are then used in a Newmark integration routine to predict the transient response of the assembled structure. The transmission simulator method is especially useful here because it allows one to capture the nonlinearity generated by a bolted joint within a single experimental substructure. This will make it possible to capture the nonlinearities in the system on the subcomponent level and then assemble the subcomponent models to observe how the nonlinear joint forces affect the fully assembled structure.

This chapter is organized as follows; Section 4.2 outlines the approach used, and Section 4.3 validates the proposed techniques on a simple spring-mass system. First, modal models are derived from simulated transient measurements from a 3DOF system. These modal models are then used to predict the response when the 3DOF system is assembled to a linear 2DOF system. Section 4.4 explores the application to a more complicated structure, modeled using finite elements, i.e. the Brake-Reuss Beam [76]. A quasi-static simulation [53] of a Brake-Reuss Beam finite element model is used to obtain a nonlinear modal model for each mode of the beam. Then, using the transmission simulator method, a

linear model of the TS is removed from the system and a modified half-beam structure is added in order to generate predications for a modified Brake-Reuss Beam. This is the first time this methodology has been attempted on a realistic geometry. Conclusions and remarks from both cases are then presented in Section 4.5.

## 4.2 Theoretical Development

In the most general case, the equation of motion for substructure A can be written as follows,

$$\mathbf{M}^{A}\ddot{\mathbf{x}}^{A} + \mathbf{C}^{A}\dot{\mathbf{x}}^{A} + \mathbf{K}^{A}\mathbf{x}^{A} + \sum_{n=1}^{N_{\text{Joints}}^{A}} \mathbf{f}_{J,n}^{A} \left(\mathbf{x}^{A}, \boldsymbol{\phi}_{n}^{A}\right) = \mathbf{f}^{A} \left(t\right)$$
(56)

where  $\mathbf{M}^A$ ,  $\mathbf{C}^A$  and  $\mathbf{K}^A$  are the  $N \times N$  linear mass, damping and stiffness matrices and the nth scalar joint force,  $f_{J,n}^A \left( \mathbf{x}^A, \phi_n^A \right)$  depends on the displacement across the joint, which is typical simply the difference of two displacements,  $\mathbf{x}^A$ , in the system and on its internal slider states  $\phi_n^A$ . The constant vector  $\mathbf{f}_{J,n}^A$  maps each scalar joint force  $f_{J,n}^A$  to the points to which the joint is attached. For example, in the first study that will be discussed later, shown in Fig. 56, the first Iwan joint is between DOF 1 and ground so  $\mathbf{f}_{J,1}^A = \begin{bmatrix} 1 & 0 & 0 \end{bmatrix}^T$  and the third Iwan joint is connected between DOF 2 and 3, so  $\mathbf{f}_{J,3}^A = \begin{bmatrix} 0 & 1 & -1 \end{bmatrix}^T$ . In addition, the displacement across the joint is simply  $x_2 - x_3 = \begin{bmatrix} 0 & 1 & -1 \end{bmatrix} \mathbf{x}^A$ .

When each mode of the substructure is represented as a modal Iwan model, the matrices  $\mathbf{M}$ ,  $\mathbf{C}$  and  $\mathbf{K}$  would be diagonal and the nth joint force would depend on only one modal displacement,  $\mathbf{q}$ , as shown,

$$\mathbf{I}_{A}\ddot{\mathbf{q}}_{A} + \left[ (2\zeta_{A}\omega_{lin,A}) \right] \dot{\mathbf{q}}_{A} + \left[ (\omega_{lin,A}^{2}) \right] \mathbf{q}_{A} + \left\{ \mathbf{F}_{NL,A} \right\} = \boldsymbol{\phi}_{A}^{T} \mathbf{f}_{A}$$

$$\left\{ \mathbf{F}_{NL,A} \right\}^{T} = \left[ F_{NL,1,A}(q_{1,A}) \quad F_{NL,2,A}(q_{2,A}) \quad \cdots \right]^{T}$$
(57)

In the modal domain  $\mathbf{F}_{NL,A}$  now contains a vector of modal forces that are dependant on a single modal degree of freedom, thus at the substructure level the modes remain uncoupled.

A primal formulation [13] is employed to couple the substructures. Without loss of generality, consider the case where substructure *A* will be joined to substructure *B*. The substructures can be coupled by writing constraint equations of the following form,

$$\mathbf{B} \begin{bmatrix} \mathbf{x}^A \\ \mathbf{x}^B \end{bmatrix} = 0 \tag{58}$$

and then eliminating the redundant degrees of freedom using

$$\begin{bmatrix} \mathbf{x}^A \\ \mathbf{x}^B \end{bmatrix} = \mathbf{L}\mathbf{q} \tag{59}$$

$$\mathbf{L} = null(\mathbf{B}) \tag{60}$$

to obtain a set of independent (or unconstrained [12]) coordinates,  $\mathbf{q}$ . The equations of motion for the coupled system then become the following in terms of the coordinates  $\mathbf{q}$ ,

$$\hat{\mathbf{M}}\ddot{\mathbf{q}} + \hat{\mathbf{C}}\dot{\mathbf{q}} + \hat{\mathbf{K}}\mathbf{q} + \mathbf{L}^{T} \begin{bmatrix} \sum_{n=1}^{N_{\text{Joints}}^{A}} \mathbf{f}_{J,n}^{A} f_{J,n}^{A} (\mathbf{x}^{A}, \boldsymbol{\phi}_{n}^{A}) \\ \sum_{n=1}^{N_{\text{Joints}}^{B}} \mathbf{f}_{J,n}^{B} f_{J,n}^{B} (\mathbf{x}^{B}, \boldsymbol{\phi}_{n}^{B}) \end{bmatrix} = \mathbf{L}^{T} \begin{bmatrix} \mathbf{f}^{A}(t) \\ \mathbf{f}^{B}(t) \end{bmatrix}$$
(61)

where

$$\hat{\mathbf{M}} = \mathbf{L}^{\mathrm{T}} \begin{bmatrix} \mathbf{M}^{A} & 0 \\ 0 & \mathbf{M}^{B} \end{bmatrix} \mathbf{L}$$
 (62)

and similarly for  $\hat{\mathbf{C}}$  and  $\hat{\mathbf{K}}$ . Further details can be found in [13] or ([12], Chapter 9).

In order to simulate the response of the assembly, an unconditionally stable Newmark algorithm [89] is used (e.g. with mathematical factors  $\beta_N = 0.25$  and  $\gamma = 0.5$ ). This procedure was first developed by Simmermacher as reported in [99]. A Newton iteration loop is used to adjust the displacement of the joint (and the internal slider states) so that the joint force is in dynamic equilibrium at each time step. Specifically, if the displacement at the *j*th time step is denoted  $\mathbf{q}_j$ , then the residual is defined as,

$$\mathbf{r}_{j} = \hat{\mathbf{M}}\ddot{\mathbf{q}}_{j} + \hat{\mathbf{C}}\dot{\mathbf{q}}_{j} + \hat{\mathbf{K}}\mathbf{q}_{j} + \mathbf{L}^{T} \begin{bmatrix} \sum_{n=1}^{N_{\text{binits}}^{A}} \mathbf{f}_{J,n}^{A} \left( \mathbf{L}\mathbf{q}_{j}, \boldsymbol{\phi}_{n}^{A} \right) \\ \sum_{n=1}^{N_{\text{binits}}} \mathbf{f}_{J,n}^{B} f_{J,n}^{B} \left( \mathbf{L}\mathbf{q}_{j}, \boldsymbol{\phi}_{n}^{B} \right) \end{bmatrix} - \mathbf{L}^{T} \begin{bmatrix} \mathbf{f}^{A} \left( t \right) \\ \mathbf{f}^{B} \left( t \right) \end{bmatrix}$$

$$(63)$$

In order to map the instantaneous joint stiffness, the joint force maps,  $\mathbf{f}_{J,n}^A$ , are assembled into a global vector,

$$\mathbf{f}_{global,n}^{A} = \begin{cases} \mathbf{f}_{J,n}^{A} \\ \mathbf{0} \end{cases} \qquad \mathbf{f}_{global,n}^{B} = \begin{cases} \mathbf{0} \\ \mathbf{f}_{J,n}^{B} \end{cases}$$
 (64)

Then, the Jacobian is written as,

$$\mathbf{J}_{j} = \hat{\mathbf{M}} + \gamma \Delta t \hat{\mathbf{C}} + \beta \left(\Delta t\right)^{2} \left(\hat{\mathbf{K}} + \mathbf{L}^{T} \left[\sum_{n=1}^{N_{\text{Joints}}^{A}} \left(\mathbf{f}_{global,n}^{A}\right) \left(\mathbf{f}_{global,n}^{A}\right)^{T} k_{J,n}^{A} + \sum_{n=1}^{N_{\text{Joints}}} \left(\mathbf{f}_{global,n}^{B}\right) \left(\mathbf{f}_{global,n}^{B}\right)^{T} k_{J,n}^{B}\right] \mathbf{L}\right) (65)$$

where  $k_{J,n}^A$  is the instantaneous joint stiffness for the *n*th joint. The estimate of the acceleration, displacement and velocity at the *j*th time step are updated as follows. For the first iteration the same procedure is used, only with  $\mathbf{r}_j = 0$ .

$$\ddot{\mathbf{q}}_{j,new} = \ddot{\mathbf{q}}_{j} - \mathbf{J}_{j} \mathbf{r}_{j}$$

$$\dot{\mathbf{q}}_{j,new} = \dot{\mathbf{q}}_{j} + \Delta t (1 - \gamma) \ddot{\mathbf{q}}_{j-1} + \gamma \ddot{\mathbf{q}}_{j,new}$$

$$\mathbf{q}_{j,new} = \mathbf{q}_{j} + \Delta t \dot{\mathbf{q}}_{j-1} + \frac{1}{2} (\Delta t)^{2} (1 - 2\beta_{N}) \ddot{\mathbf{q}}_{j-1} + 2\beta_{N} \ddot{\mathbf{q}}_{j,new}$$
(66)

Note that  $\mathbf{L}^{\mathrm{T}} \begin{bmatrix} \mathbf{f}_{J,n}^A \\ \mathbf{0} \end{bmatrix}$  and  $\mathbf{L}^{\mathrm{T}} \begin{bmatrix} \mathbf{f}_{J,n}^A (\mathbf{f}_{J,n}^A)^{\mathrm{T}} & \mathbf{0} \\ \mathbf{0} & \mathbf{0} \end{bmatrix} \mathbf{L}$ , and similarly for substructure B, are simply constant

matrices that map each joint force onto the appropriate degrees of freedom in the assembled system. These matrices, and the assembled system matrices  $\hat{M}$ ,  $\hat{C}$  and  $\hat{K}$  are calculated in advance and only the joint forces and stiffnesses need to be updated in each iteration.

## 4.2.1 Iwan Joint

The preceding discussion is valid for a variety of joint models. In this work the Iwan model is used, so each joint can be characterized by four parameters  $F_s$ ,  $K_T$ ,  $\chi$  and  $\beta$  [48]. The first two parameters describe, respectively, the force at which the joint slips completely (macro-slip) and the stiffness of the joint when all sliders are stuck. The model exhibits energy dissipation per cycle, D, that depends on magnitude of the displacement |x| in a power-law fashion as

$$D = R \left| x \right|^{3+\chi} \tag{67}$$

where R is a constant. By analogy with a linear system, the effective damping ratio  $\zeta$  of an SDOF system with mass m and with an Iwan joint in parallel with a spring of stiffness  $K_0$  is the following,

$$\zeta = D / \left( m 2\pi \omega_d \omega_n \left| x \right|^2 \right) \tag{68}$$

where  $\omega_n^2 = (K_0 + K_T)/m$  and  $\omega_d = \omega_n \sqrt{1 - \zeta^2}$ . These relationships together with a Hilbert transform are used to fit an Iwan model to simulated measurements of each substructure. For further details, see [3, 52].

## 4.3 Spring-Mass System Application

The proposed approach was applied to the system depicted in Fig. 56.

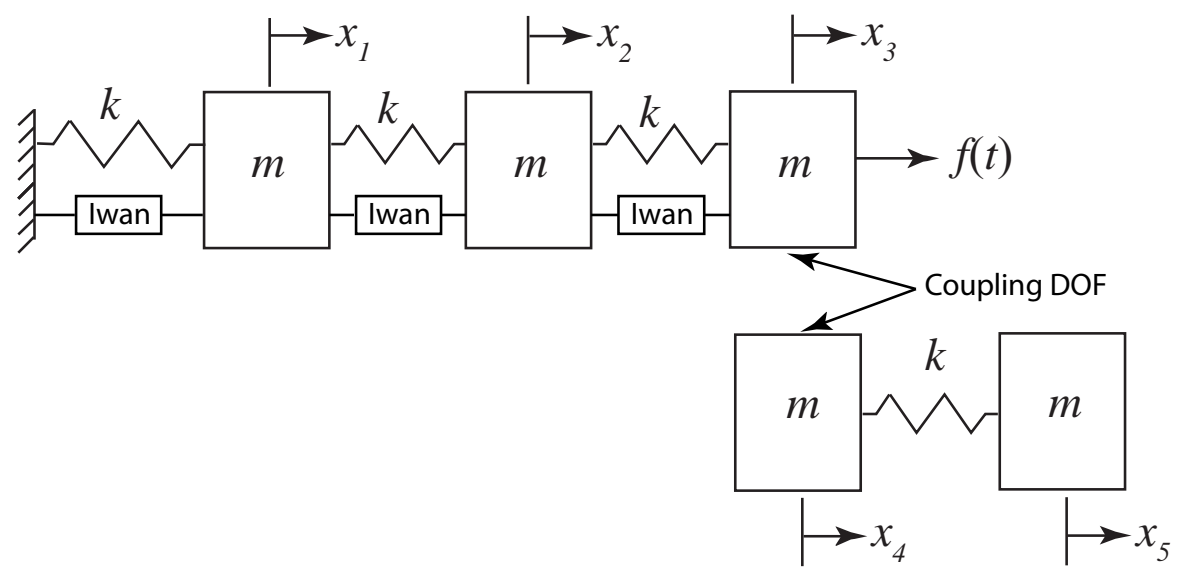


Figure 56. Schematic of the discrete system used to validate the proposed substructuring procedure. (top-left) Substructure A, (bottom-right) Substructure B. Mass and stiffness proportional damping was added to simulate material damping (dashpots not shown).

Substructure A consists of three masses connected by linear springs of stiffness k in parallel with Iwan elements with the parameters shown in Table 18. The other system parameters are m=10 kg, k=5 N/m,  $C^A=0.002(\mathbf{M}^A+\mathbf{K}^A)$ , and  $C^B=0.002\mathbf{K}^B$ . The goal is to simulate a test on Substructure A to determine modal Iwan models for each mode of that substructure, and then to utilize modal substructuring to predict the response of the assembly when the masses are joined as indicated in Fig. 56 with  $x_3=x_4$ .

Table 18. Parameters of Iwan Joints in Substructure A

Iwan Joint	$F_{\mathrm{S}}$	$K_{\mathrm{T}}$	χ	β
$x_1$ – ground	10 N	5 N/m	-0.5	0.1
$x_1-x_2$	1 N	4 N/m	-0.2	0.01
$x_2 - x_3$	100 N	3 N/m	-0.8	1

## 4.3.1 Estimating Modal Iwan Models for Substructure A

The linear mode shapes  $[\phi_1 \ \phi_2 \ \phi_3]$  of Substructure A were assumed to be known (e.g. having been measured from a low-amplitude linear test). Note that in such a test each Iwan joint acts as linear spring with stiffness  $K_T$ . Then, to identify a nonlinear model for Substructure A, an experiment was simulated in which a half-sine impulse with a 0.1 second long period and amplitude of 100 Newtons was

applied to mass 3. The Newmark routine was used to determine the transient response and then the response of each mode was estimated using  $\mathbf{q} = \mathbf{\phi}^{-1}\mathbf{x}$ . Note that the mode matrix used in this calculation corresponds to the linear, low amplitude modes that include the stiffness of the joints. The FFT,  $Q_r(\omega)$ =FFT( $q_r(t)$ ), of each modal response is shown in Figure 57. A weak nonlinearity, as is typical of a structure with bolted joints, is visible near each peak. Each mode only shows frequency content near its peak, suggesting that the modes are not interacting significantly.

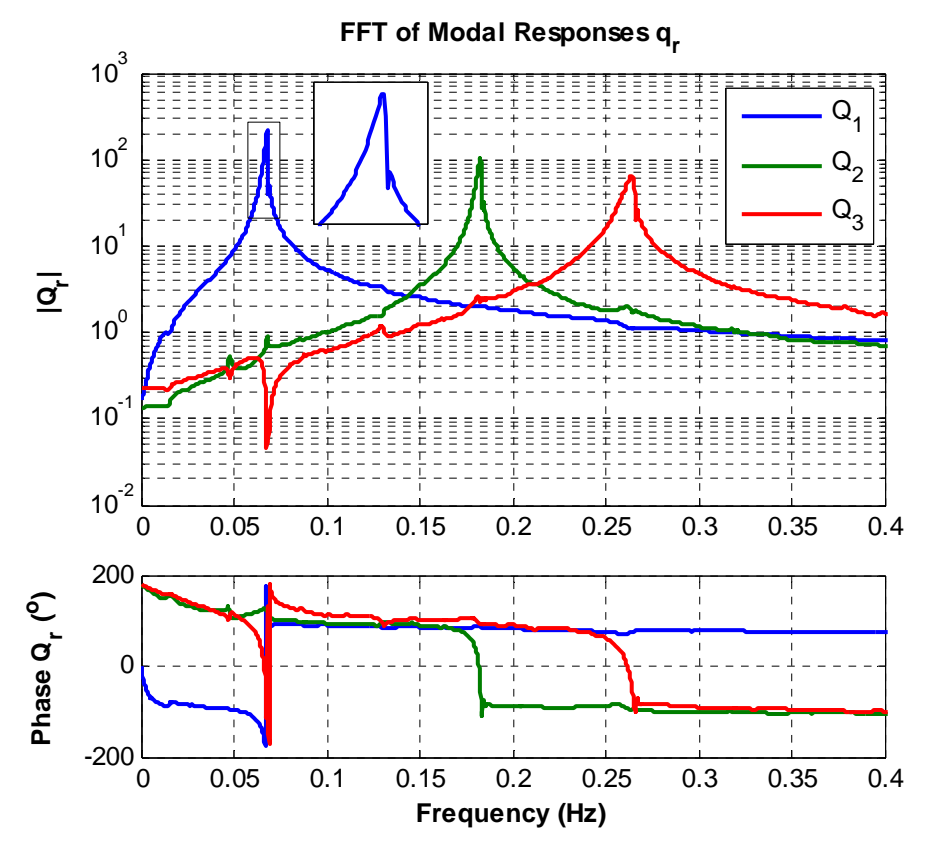


Figure 57. Fast Fourier Transform of the modal response of substructure A.

The simulated measurements were then post processed using the procedure outlined in [100] to identify modal Iwan parameters for each mode. Briefly, each mode's response was band-pass filtered and a smoothed Hilbert transform was used to estimate the instantaneous phase and amplitude as a function of time. The derivative of the phase gives the damped natural frequency,  $\omega_{\rm d} \approx \omega_{\rm n}$ , as a function of time, and the derivative of the amplitude gives  $\zeta(t)\omega_{\rm n}(t)$ , from which the damping can be determined. Then the

frequency and damping were plotted versus amplitude and used to determine the modal Iwan parameters. To assure that the power-law behavior was accurately captured, the low-level material damping  $\zeta_0$  was subtracted from the estimated damping by visually inspecting the damping versus amplitude curve. Then, a line of the following form

$$\zeta(|Q_r|) = R|Q_r|^{\chi+1} \tag{69}$$

where R and  $\chi$  are constants, was fit to the log damping versus log amplitude using least squares. Note, macro-slip was not observed in any of these simulations (and must be avoided for the modal Iwan model to retain its validity). Hence, the joint stiffness cannot be measured and so it was simply assumed to be such that the frequency of each mode shifts by 0.05 Hz in macro-slip. This and the linear natural frequency were then used to find  $K_T$ , and then these values were used to solve for a value of  $F_S$  and  $\beta$  such that the power law strength, R, in the Iwan model was equal to that obtained from the curve fit. In essence, the model used is equivalent to a Palmov model [102], since macro-slip is never activated. In all cases the modal Iwan model was found to fit the measured modal response very well, as illustrated for the first mode in Fig. 58. The modal Iwan parameters obtained for each mode are shown in Table 19.

The modal Iwan model is a SDOF model that could be integrated in response to an applied load (mapped onto the mode of interest) to compute the transient response. For example, the 100 Newton half-sine pulse used to derive the parameters for the first mode was applied to its modal Iwan model and the transient response was computed using the Newmark integrator. The transient response thus computed is compared to the measured modal response  $q_1(t)$  in Fig. 59. While the computed and "measured" responses do eventually go out of phase due to small frequency errors, the simulation captures the amplitude and frequency of the measured response very well over the entire range of response amplitude. Thus, this modal Iwan model can be used with confidence.

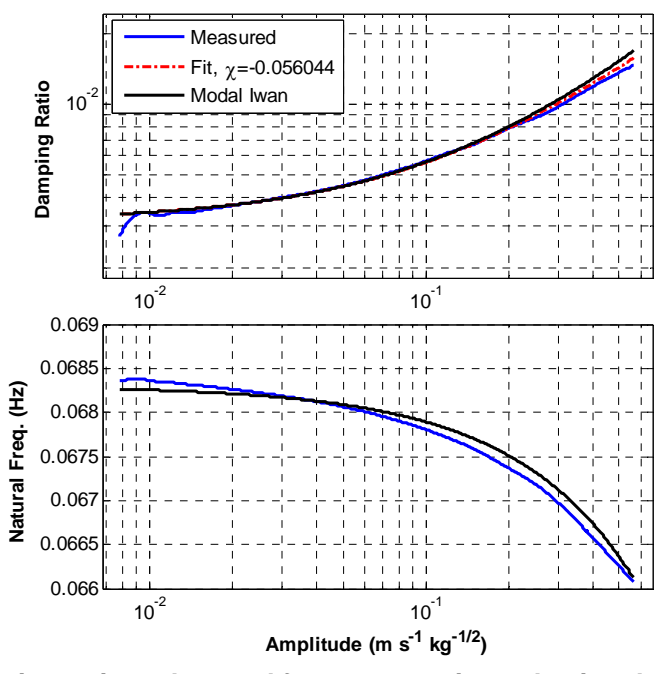


Figure 58. (blue) Damping ratio and natural frequency estimated using the Hilbert transform, and (black) those of a modal Iwan model fit to the measurements. (red dash-dot) Curve fit using eq. (69) to the damping ratio vs. amplitude, which was used to estimate the modal Iwan parameters.

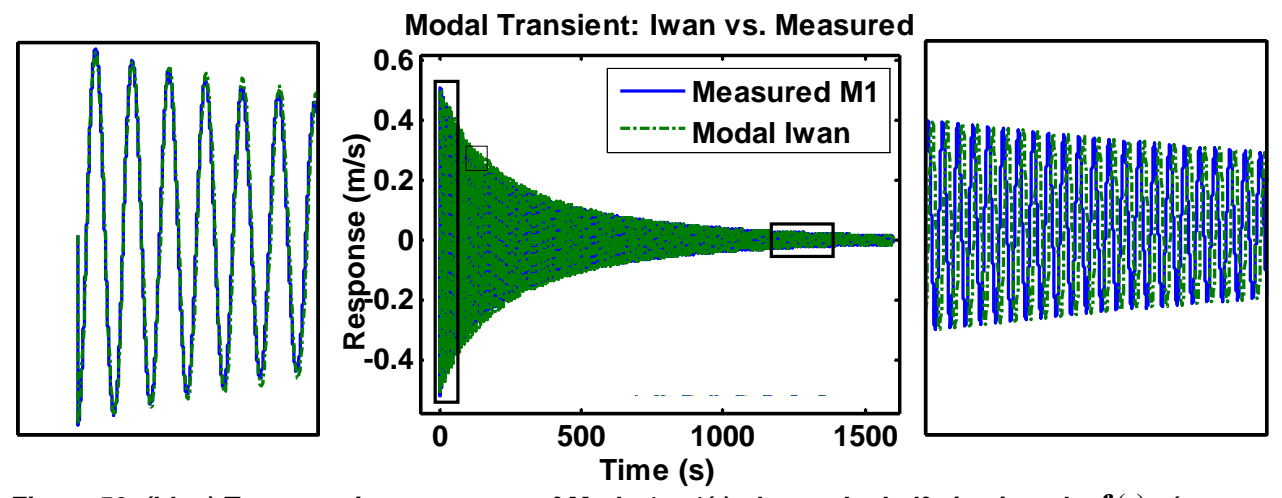


Figure 59. (blue) True transient response of Mode 1, q1(t), due to the half-sine impulse  $\mathbf{f}(t)$ . (green dash-dot) Estimated modal response  $\hat{q}_{_1}(t)$  computed using the modal lwan model and the modal force  $\mathbf{\phi}_{_1}{}^{\mathrm{T}}\mathbf{f}(t)$ .

The same procedure was repeated for the second and third modes and the resulting modal Iwan parameters are shown in Table 19. For reference, the true natural frequencies and damping ratios of the linearized system are  $f_{n0,true}$ =[0.0686, 0.185, 0.269] Hz and  $\zeta_{0,true}$ =[0.00255, 0.001532, 0.001548]. The identification procedure has estimated the frequencies quite accurately, but there are errors of up to 25%

in some of the damping ratios. While these errors could have been reduced by integrating longer time histories and using a finer time step to improve the accuracy of the Newmark integrator, this level of error is probably to be expected in a real experiment so further improvement was not sought.

Table 19. Parameters of modal Iwan models of substructure A, estimated from simulated measurements. The parameters in parenthesis are not fully relevant since the modal Iwan model is only valid if the response is low enough to avoid macro-slip.

	u.o . oop					
Modal Iwan Models (Substructure A)	$(F_{\rm S})$	$(K_{\mathrm{T}})$	χ	β	$f_{ m n0}$	$\zeta_0$
Mode 1	0.886	0.171	-0.023	0.0519	0.0683	0.0032
Mode 2	17.7	0.629	-0.641	0.132	0.184	0.00161
Mode 3	0.508	0.959	-0.564	0.000833	0.268	0.00172

## 4.3.2 Substructuring Predictions

The substructures were assembled and the low-amplitude, linearized modal properties were calculated by solving an eigenvalue problem with the assembled mass and stiffness matrices including the linearized joint stiffnesses. The damping ratios were then calculated using the light damping approximation [12] (preserving the classical real modes) and are compared with the true values in Table 20. Because these modal properties were computed with the joints linearized, they include only the linear viscous damping that was used to represent the material damping and thus there is no effect from friction in the joints. The results show that the frequencies were accurately estimated, but the damping ratios show errors that are of a similar level as the errors in the estimates of the modal damping ratios of Substructure A.

Table 20. Linear natural frequencies and damping ratios of the assembly predicted by substructuring.

Mode	True Freq. $f_0$ (Hz)	Estimated Freq. $f_0$ (Hz)	% Error	True $\zeta_0$	Estimated $\zeta_0$	% Error
1	0.04502	0.044842	-0.40	0.00156	0.001948	24.92
2	0.1287	0.12852	-0.14	0.001185	0.001307	10.31
3	0.17712	0.17629	-0.47	0.001402	0.001465	4.49
4	0.26524	0.26423	-0.38	0.001524	0.00171	12.19

The response of the assembly to a 100 Newton input was then computed, and the responses  $x_1(t)$  and  $x_5(t)$  are shown in Fig. 60. The substructuring predictions agree very well with the true transient response, both in frequency and damping.

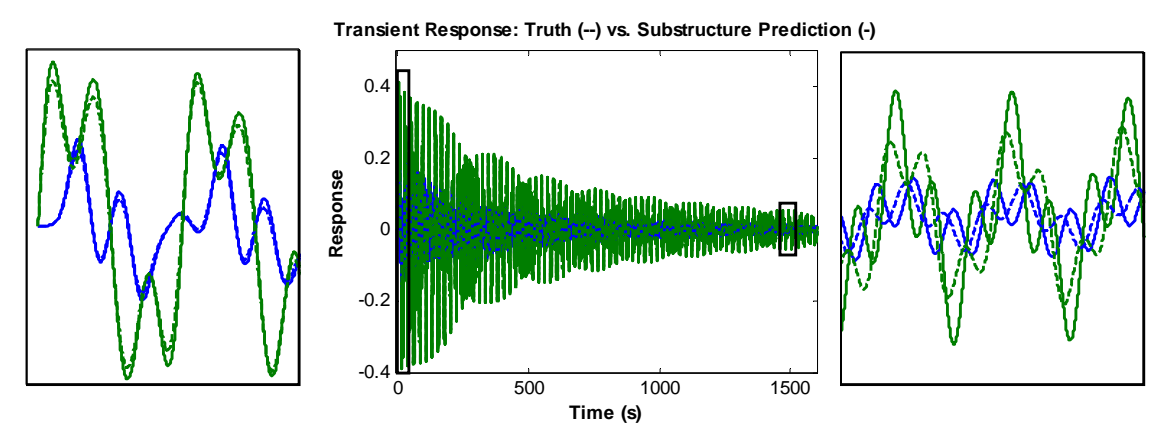


Figure 60. Transient response of the 4DOF assembly to a 100 N impulse. (solid lines) True response, (dashed lines) Substructuring prediction, using the modal lwan model for Substructure A, (blue) x1(t), (green) x5(t). The panes on the left and right show a magnified view near the beginning and end of the response.

Further insight can be gained by considering the FFT of the response, projected onto each linearized mode of the assembly, as shown in Fig. 61. This shows that the substructuring predictions contain the correct frequency content for each mode, including small distortions which cause the modal responses to show slight coupling. The modal responses shown were estimated by multiplying the responses with the inverse of the linear, low-amplitude mode shape matrix.

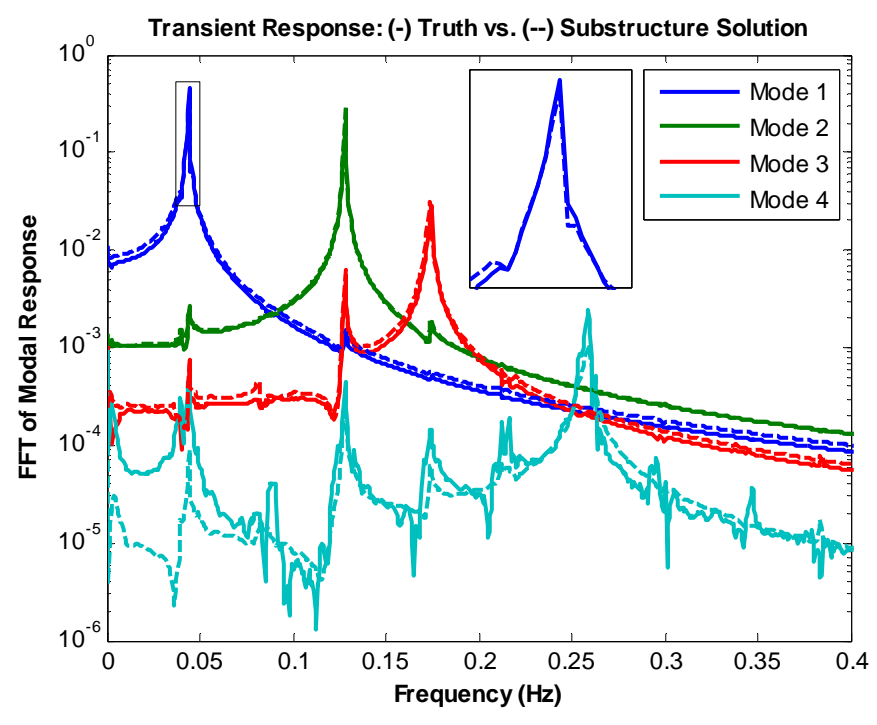


Figure 61. FFT of the transient response of the 4DOF assembly to a 100 Newton impulse. (solid lines) True response of each mode, estimated using  $\mathbf{q} = \mathbf{\phi_0}^{-1}\mathbf{x}$  with the linear (low amplitude) modes, (dashed lines) Substructuring prediction, obtained using a modal Iwan model for each mode of Substructure A.

Most previous research, and industry practice, is based on a linear approximation. Hence, it is also informative to consider how much the predictions shown above improve upon a linear approximation. An example of such a comparison is shown in Fig. 62, for an impulsive input with a 500 Newton amplitude. The linear approximation greatly overestimates the amplitude of the vibration, producing a response whose root mean square (RMS) value is a factor of two larger (+99% error) than the true RMS response. Of course, the level of error incurred by using a linear model depends on the strength of the forcing. For the 100 Newton impulsive input mentioned previously the linear model is in error by only 38%. At higher load levels the errors would be even larger.

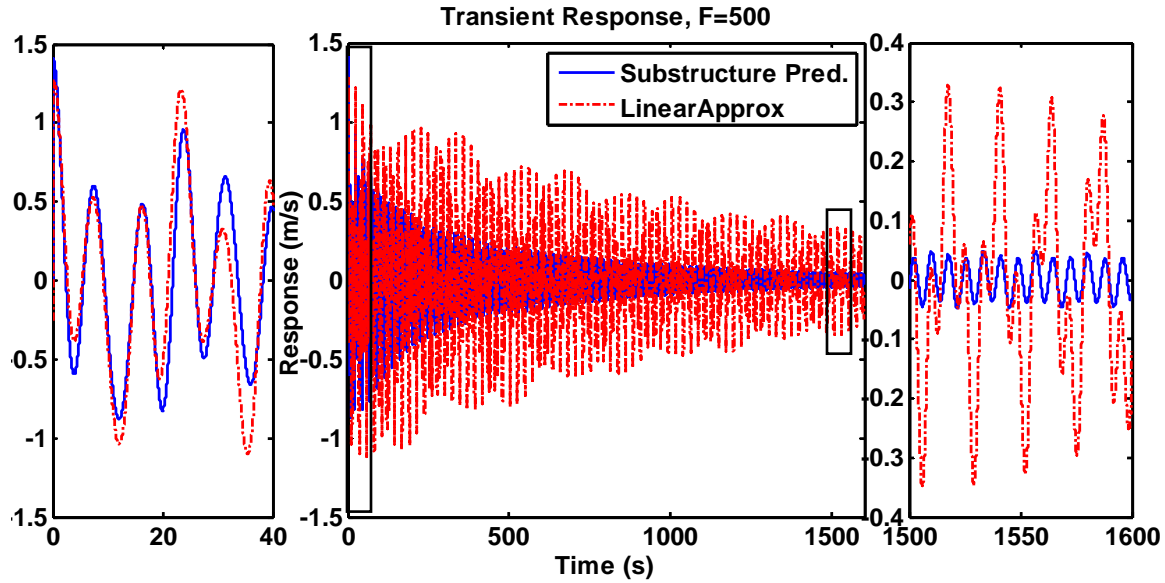


Figure 62. Transient response, x5(t), of the 4DOF assembly to a 500 N impulse. (solid blue) Nonlinear substructuring prediction, (dashed red) Response predicted by linear substructuring.

## 4.4 Brake-Reuss Beam Application

The proposed nonlinear modal substructuring approach provided excellent results for the springmass system discussed in Section 4.3. Next, the authors investigated how well these predictions performed for a more realistic geometry. The system of interest for this section is the Brake-Reuss Beam [76], which consists of a pair of 304 stainless steel half-beams bolted at the center with a lap joint.

Figure 63 shows the subcomponents used in this substructuring example. Substructure C is the standard Brake-Reuss Beam. Substructure A is the transmission simulator for these predictions and is simply half of the Brake-Reuss Beam system. The goal of this study is to create a model of the half-beam subcomponent, Substructure B. This model should include the nonlinear dynamics due to the joint and the loading at the interface.

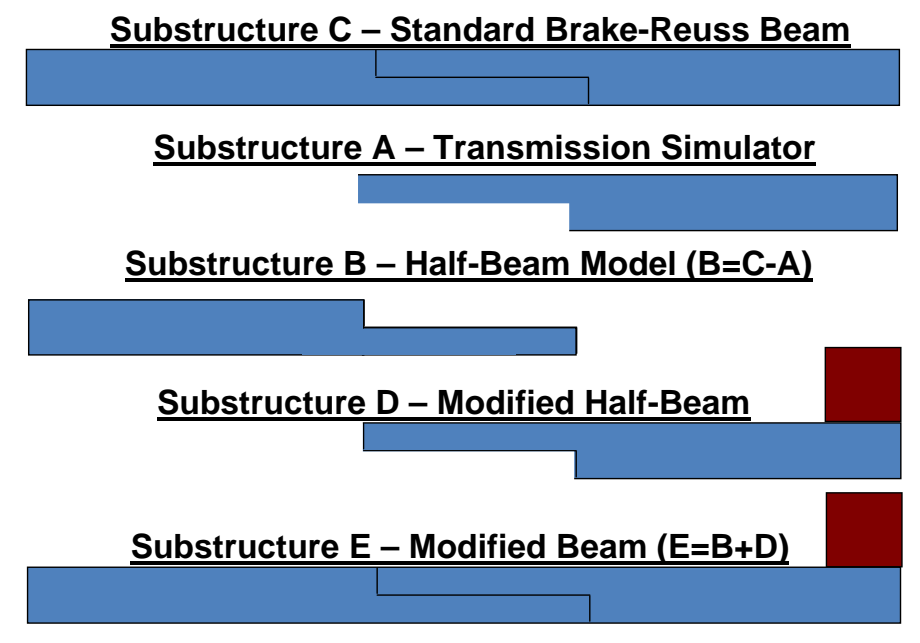


Figure 63. Substructure overview

To complete this task, the transmission simulator method was used to remove the dynamics of Substructure A from Substructure C. In order to validate this experimental-analytical model a modified half-beam, Substructure D, was then attached to the system using a primal formulation [13]. This new modified Brake-Reuss Beam, Substructure E, was then compared to a truth model constructed from the same finite element program. Utilizing finite element models for each substructure allowed the authors to explore several scenarios including sensor selection, modal retention, and prediction quality all in the absence of experimental error.

### 4.4.1 Substructure C - Standard Brake Reuss Beam Model & Identification

In order to simulate substructuring for this system, a finite element model of Substructure C was developed. This model was derived from a model used by Gross et al. in [103]. A solid mesh of the Brake-Reuss Beam system using 22,000 elements is shown in Fig. 64. The half beams of the system were modeled and meshed separately at this stage. A Craig-Bampton (CB) model was extracted from the FEM program retaining 30 fixed interface modes and the 6 interface nodes (36 interface degrees of freedom). These interface nodes are at virtual node locations between the two half beams, see Fig. 65.

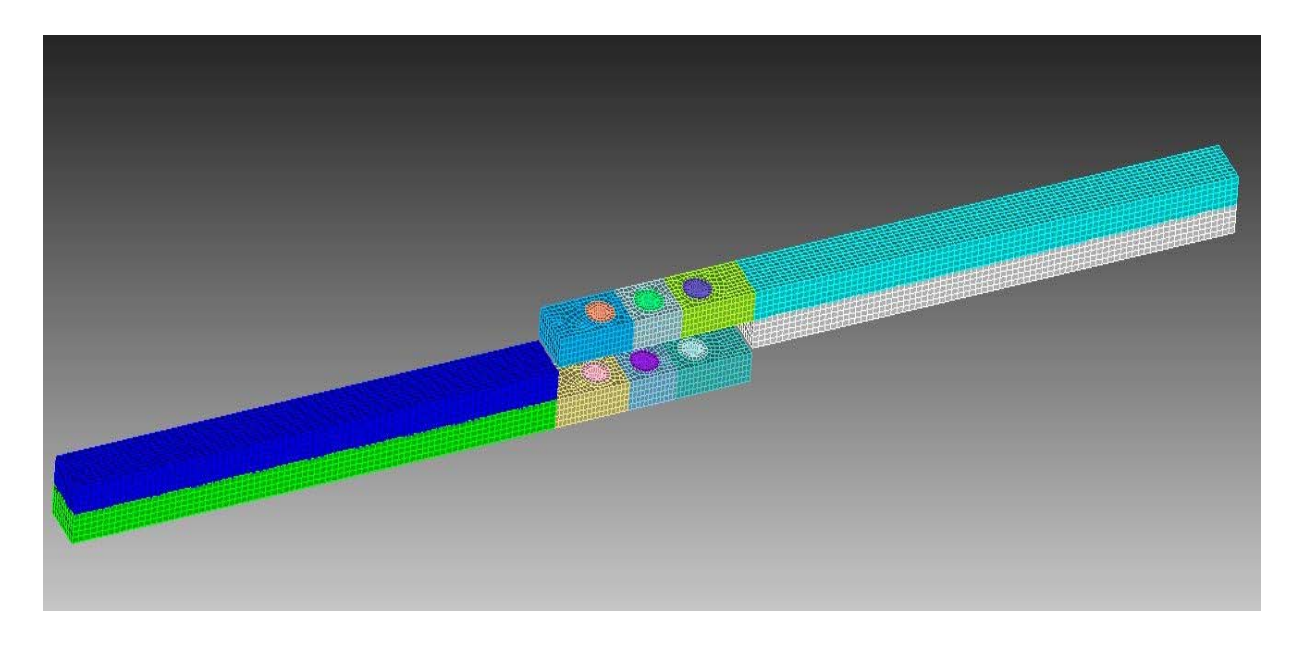


Figure 64. Finite element mesh for Brake-Reuss Beam substructure C

In order to connect the two half beams, the joint surfaces were connected to the interface node using rigid bar elements (e.g. RBE3 in Nastran). These spider-like connections are shown in Fig. 65. Linear springs were added between the pairs of virtual nodes except in the axial direction. Instead of using linear springs, the DOFs in the axial direction were coupled using a 4-parameter Iwan element.

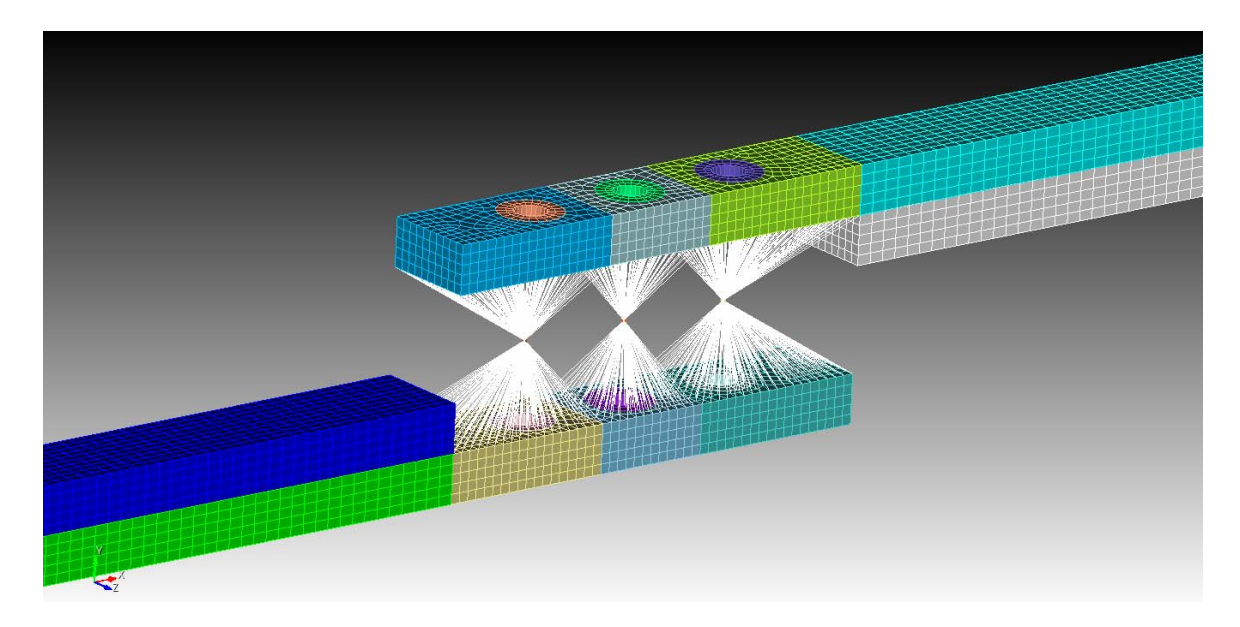


Figure 65. Finite element joint surface spider-patch

In order to assure that the finite element model was a good representation of a real structure, the finite element model and discrete Iwan elements were updated to best match an experimental benchmark

[104], as is discussed further in Appendix A. The Iwan parameters for the three discrete joints are given in Table 21. It is worth noting that, while one could connect each pair of the nodes at the joint surface with a nonlinear element, this would be contrary to the idea of using an Iwan element. The Iwan element internally contains a parallel array of slider elements that are tuned to represent the stiffness and damping of an entire joint. Then, to obtain the linearized, low-amplitude modes the discrete Iwan elements were replaced by springs with the joint's low amplitude stiffness,  $\mathbf{K_0}$ , and the eigenvalue problem was solved to obtain the natural frequencies and mode shapes for Substructure C.

Table 21: System C Discrete Iwan Parameters

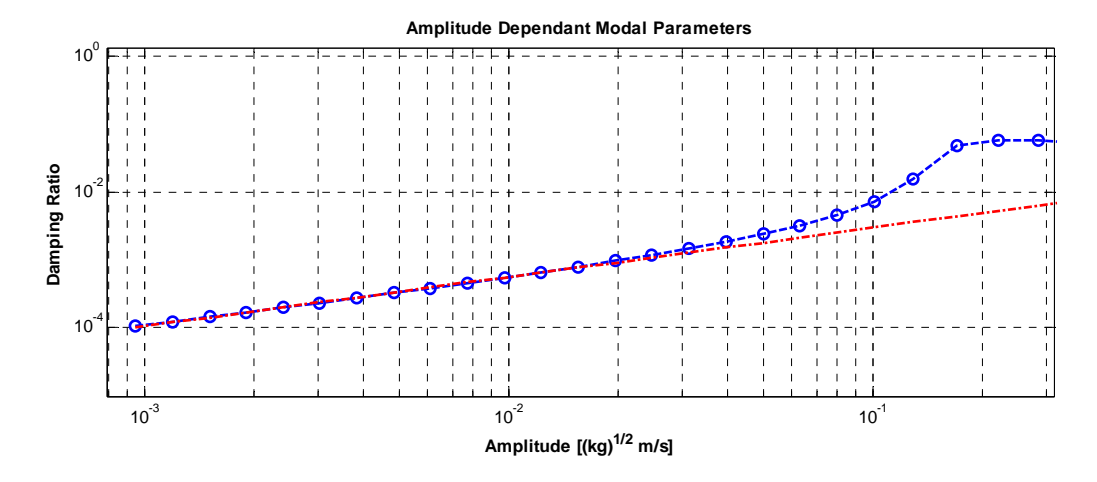
Joint #	$\mathbf{F}_{\mathbf{s}}$	K <sub>T</sub>	β	χ
1	25	2,200,000	-0.35	0.0500
2	10	1,840,000	-0.90	0.0500
3	25	2,200,000	-0.35	0.0500

In order to simulate experimental modal substructuring for this model, simulated "measurements" were needed from which a SDOF nonlinear model could be estimated for each mode. In [53] Allen, Lacayo, and Brake presented an adaptation of the quasi-static algorithm of [105] that statically loads a structure in the shape of a mode to excite one mode of interest. The study in [53] showed that this algorithm accurately estimates the behavior of each mode of a typical structure in a small fraction of the time required to perform a dynamic simulation. The authors used this quasi-static algorithm to obtain the modal damping vs. amplitude and frequency vs. amplitude curves that are needed to estimate the parameters of each modal Iwan model. Each modal model was defined by four parameters,  $[F_s, K_T, \chi, \beta]$  as well as the low level linear damping ratio,  $\zeta_0$  and the stiffness in macro-slip,  $K_\infty$ .

To best fit the dissipation parameter,  $\chi$ , of the micro-slip range of the amplitude dependant damping curve was fit by setting the slope of this curve equal to  $\chi+1$ . The joint stiffness,  $K_T$ , is dependent on the frequency shift observed once the structure is in macro-slip, this can be found directly using the frequency versus amplitude curve from the quasi-static solution, as it provides a simulated measurement in the micro and macro-slip regimes.

$$K_T = K_0 - K_{\infty} = \omega_0^2 - (\omega_0 - \omega_{shift})^2$$
 (70)

The slip force  $F_s$  can be set manually in order to achieve the onset of macro-slip to best match the quasi-static data. In principle, the parameter  $\beta$  can be found from the y-intercept of the dissipation versus amplitude curve. Figure 66 contains an example for the first elastic mode. For this mode the nonlinear modal model is optimized to fit the micro-slip region in both damping and frequency. This model doesn't fit well as the system enters into macro-slip, but here we only intend to model the system in the micro-slip regime, so this is not significant to the predictions presented later.



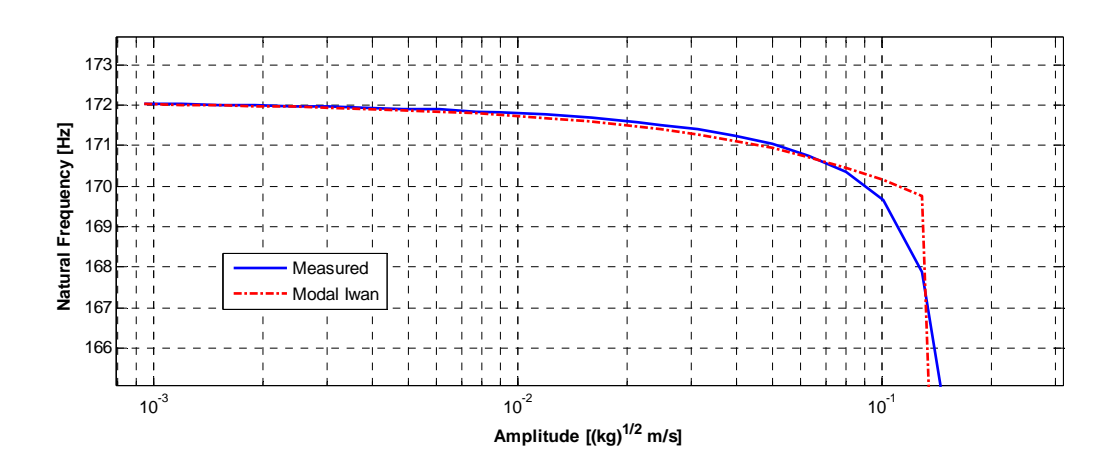


Figure 66. Quasi-Static results and Iwan parameter model fit

Table 22 contains the modal Iwan parameters for the four elastic modes of Substructure C. The numerical model of Substructure C comprises these four nonlinear elastic modes in combination with two rigid modes.

Table 22: Substructure C Numerical FEM Parameters

Modal Index	Natural Frequency [Hz]	Damping Ratio	Linear or Nonlinear	$\mathbf{F}_{\mathbf{s}}$	$\mathbf{K}_{\mathtt{T}}$	β	χ
1	171.26	0.0010	Nonlinear	105	382963	3.24	-0.2291
2	578.28	0.0010	Nonlinear	389	908040	2.01	-0.7108
3	1195.20	0.0010	Nonlinear	225	9,289,100	8.3752	-0.3066
4	1616.10	0.0010	Nonlinear	2,250	82,326,000	33.959	-0.7081

### 4.4.2 Substructure A and D: Standard and Modified Half-Beam

The transmission simulator, A, and the modified half-beam substructure, D, were extracted from the same finite element mesh as Substructure C. The first is a simple half-beam from the Brake-Reuss Beam system. This substructure will act as the transmission simulator, so modal constraints will be used to couple the negative copy of this substructure to the same degrees of freedom on Substructure C. Figure 67 shows the finite element mesh for the transmission simulator.

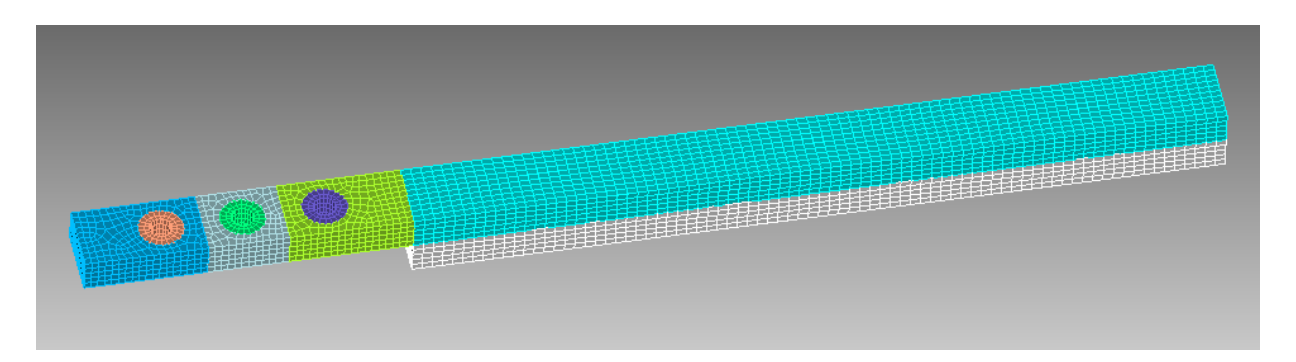


Figure 67. FEM of Substructure A

Recall from Fig. 63, the transmission simulator will be replaced with the modified half-beam in order to evaluate the substructure models. Figure 68 displays the FEM mesh of the modified half-beam. The 0.75 kg mass was connected to the beam using high stiffness springs between each pair of adjoining nodes, simulating glue that would be used in an experiment.

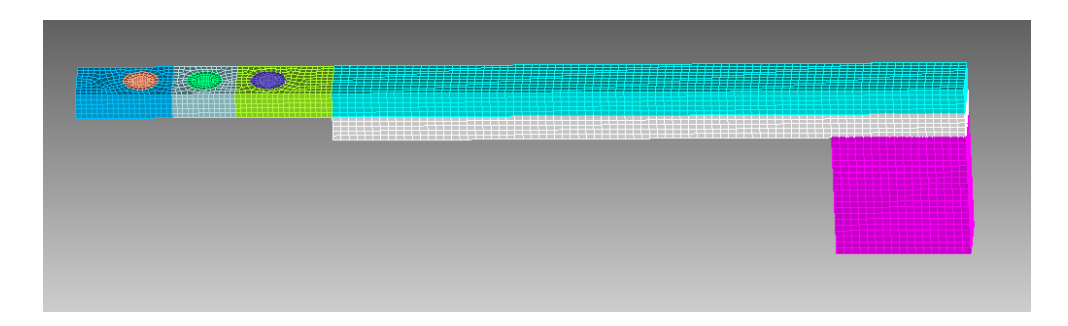


Figure 68. FEM of Substructure D

To verify that Substructures A and D are sufficiently different so that the substructuring problem is not trivial, their linear natural frequencies were compared and the results are shown in Table 23. Each natural frequency shifts by at least 13% (more than one hundred times the width of the peak in the FRF), so the change is judged to be adequate to provide an interesting case study. Material damping of 0.1% was used for each mode in the transmission simulator and modified half-beam.

Table 23: Modified System Frequency Shifts from Linear FEM Model

Modal	Substructure A	Substructure D	%	Substructure C	Substructure E	%
Index	[Hz]	[Hz]	Change	[Hz]	[Hz]	Change
1	623.37	539.12	-13.52%	171.26	151.83	-11.35%
2	1438.72	1134.38	-21.15%	578.28	578.28	-10.85%
3	3033.48	2295.71	-24.32%	1195.20	1195.20	-15.71%
4	4562.07	3930.13	-13.85%	1616.10	1616.10	-6.04%

## **4.4.3** Nonlinear Modal Substructuring Results

Next, the dynamic substructuring equation, Eqn. (61), was used to generate predictions of the modified assembly. In contrast to an experiment where the number of sensors is limited, with the numerical model of Substructure C, it was possible to retain as many nodes as desired in the simulation. The authors selected a reduced set to simulate a detailed yet realistic experiment. Figure 69 shows the retained nodes used in the simulated experimental substructuring.

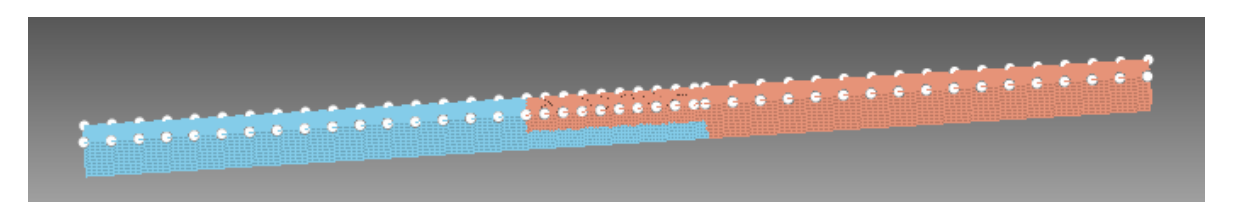


Figure 69. FEM with sensor set location for simulated experiments

The number of modes in each substructure was varied to gain insight into how sensitive the linear substructuring predictions were to the particular modes used for each substructure. Table 24 shows the errors in the linear natural frequencies for several of the combinations evaluated. A few important observations may be made. Cases #4 and #7 show that the error increases significantly if the 4th mode of Substructure A is not included. Cases #9-#11 can be compared to Cae #3 and to observe that additional modes in Substructure C do not improve the quality of the prediction significantly.

Table 24: Mode Convergence Study

	Table 24. Wode Convergence Study						
Case	# Modes in C	# Modes in A	# Modes in D	RMS Frequency % Error	RMS Damping % Error		
1	6	6	6	0.911 %	3.585 %		
2	6	5	6	0.930 %	3.412 %		
3	6	4	6	0.798 %	3.342 %		
4	6	3	6	5.261 %	3.362 %		
5	6	5	5	0.813 %	3.556 %		
6	6	4	4	0.749 %	3.345 %		
7	6	3	3	4.682 %	3.576 %		
8	6	2	2	5.702 %	2.325 %		
9	7	4	6	0.798 %	3.343 %		
10	8	4	6	0.798 %	3.343 %		
11	9	4	6	0.797 %	3.345 %		

The predictions shown in the remainder of this paper are those using the number of modes in Case #3. Table 25 shows the linear frequencies that this substructuring model predicts for the first four elastic modes. For this substructuring example, 6 modes (2 rigid and 4 elastic) were used in each of Substructures C and D; while only 4 modes (2 rigid and 2 elastic) were used for the transmission simulator. In a continuation of this work the authors plan to extend this work to an actual experimental system. With the number of modes selected for the simulated experimental substructuring the frequencies are reasonably accurate, suggesting that modal truncation will not be too severe if at least four elastic modes can be measured.

Each subcomponent (Substructures C, A and D) was assumed to have material damping of 0.1%. In theory, Substructure E should also exhibit material damping behavior in the linear regime of 0.1%.

The substructured predictions for damping are shown in Table 25. The same damping ratios were obtained using a state-space form (i.e. see [12], Ch. 10). In essence Substructure C is being modeled as if it has material damping, but using an equivalent viscous damping matrix, so it should not be too surprising that the predicted damping for Substructure E does not match what one would obtain from a material damping model. In order to avoid focusing on the linear damping when simulating the dynamic response of the FEM later in this work, the damping ratio predicted by substructuring is used in the simulations that follow. This allows the comparison to focus on the nonlinear contribution to the response.

Table 25: Numerical Linear Substructuring Predictions

Elastic Mode #	Full FEM Frequency [Hz]	Substr. Prediction Frequency [Hz]	Natural Frequency % Error	Assembly Material Damping Ratio	Substr. Prediction Damping Ratio	Damping Ratio % Error
1	151.83	148.57	-2.39%	0.001	0.000869	-13.10%
2	515.55	515.37	-1.00%	0.001	0.000975	-2.54%
3	1007.37	1037.12	1.72%	0.001	0.001003	0.28%
4	1518.52	1519.61	0.72%	0.001	0.000991	-0.81%

Now that linear substructuring predictions have been obtained, the nonlinear forces can be added to the assembled equations of motion and a Newmark integrator can be used to predict the nonlinear response of the system. First, the beam was loaded using an impulsive load distributed on the entire structure in the shape of the *j*th mode in the form of:

$$\mathbf{F}_{\mathbf{ext}} = \mathbf{A}\mathbf{M}\boldsymbol{\phi}_{j} \tag{71}$$

where A is a scalar amplitude for the forcing,  $\mathbf{M}$  is the mass matrix of the synthesized system, and  $\boldsymbol{\phi}_j$  is the *j*th mode shape vector. This limits the excitation to mainly the *j*th mode of the assembled structure. The response was then decomposed into the contribution of each mode using a modal filter. A truth FEM was constructed using the same CB model of Substructure C with the transmission simulator, A, replaced with the modified half-beam, D. Note that the parameters of the three discrete Iwan joints were not

altered when A was replaced with D as the discrete joint properties are supposed to be unaffected by the modifications seen in E. The time history from this modal loading case is shown in Fig. 70. The substructuring prediction matches the full truth FEM simulation remarkably well.

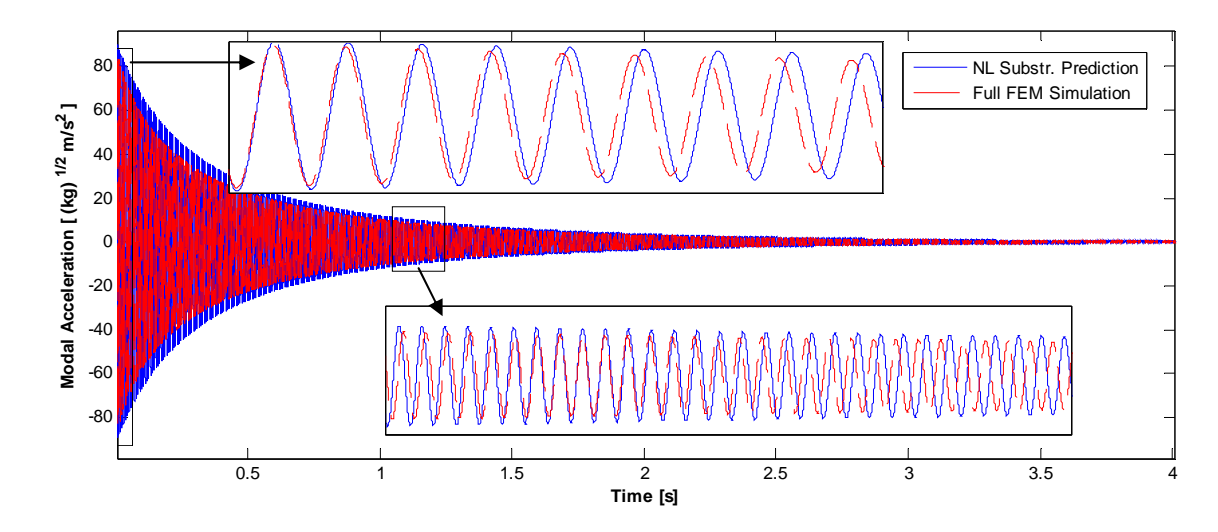


Figure 70. Comparison of true response and substructuring prediction when an impulse is applied that would excite only the 1st Elastic mode of the assembly

A linear prediction of the response to this same force was also simulated using the parameters from Table 25. The maximum modal acceleration amplitude for the first elastic mode due to this modal loading was 83 (kg)<sup>1/2</sup> m/s<sup>2</sup>, while the second mode was 0.08 (kg)<sup>1/2</sup> m/s<sup>2</sup>. As such, the modal loading was successful at only exciting the first mode. Figure 71 shows the time history of the linear prediction and nonlinear prediction for loading case from Eqn. (71). The improvement gained by using a nonlinear prediction is highlighted by observing the difference between these two predictions. Both predictions contain an accurate response early in time but as time advances the linear model does not account for the increased damping due to nonlinearity and quickly over estimates the response. This leads to a large disparity in amplitude even after just half a second.

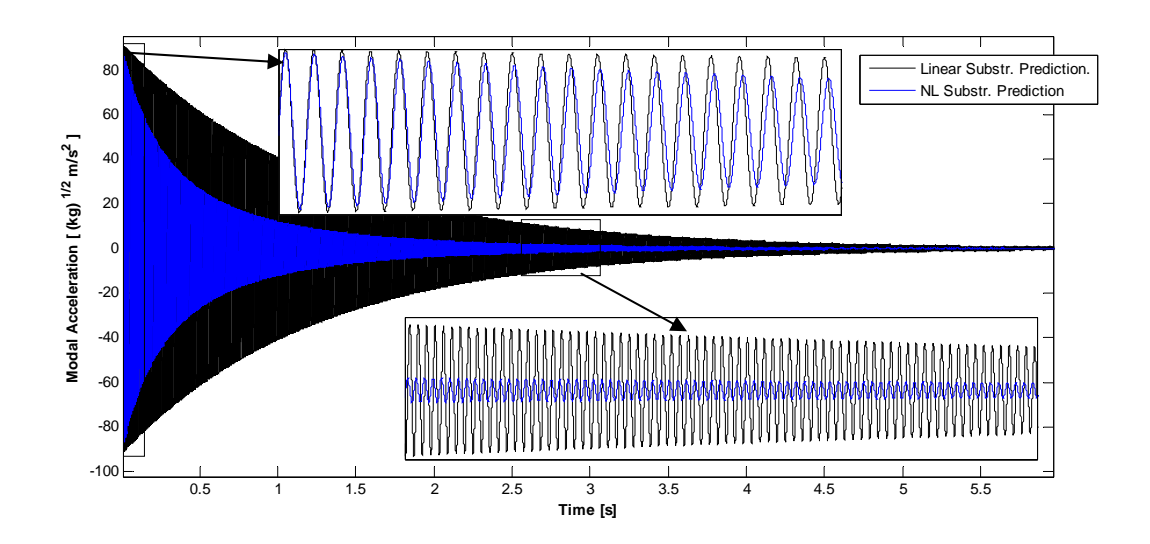


Figure 71. 1st Elastic mode: modal acceleration time history

An impulsive load in the shape of the second elastic mode was also used to excite the numerical model. The time history for this modal loading is shown in Fig. 72. Again, the substructured prediction matched the finite element simulation extraordinarily. This means that the subcomponent nonlinear modal model can be used with good confidence to describe the system nonlinearity.

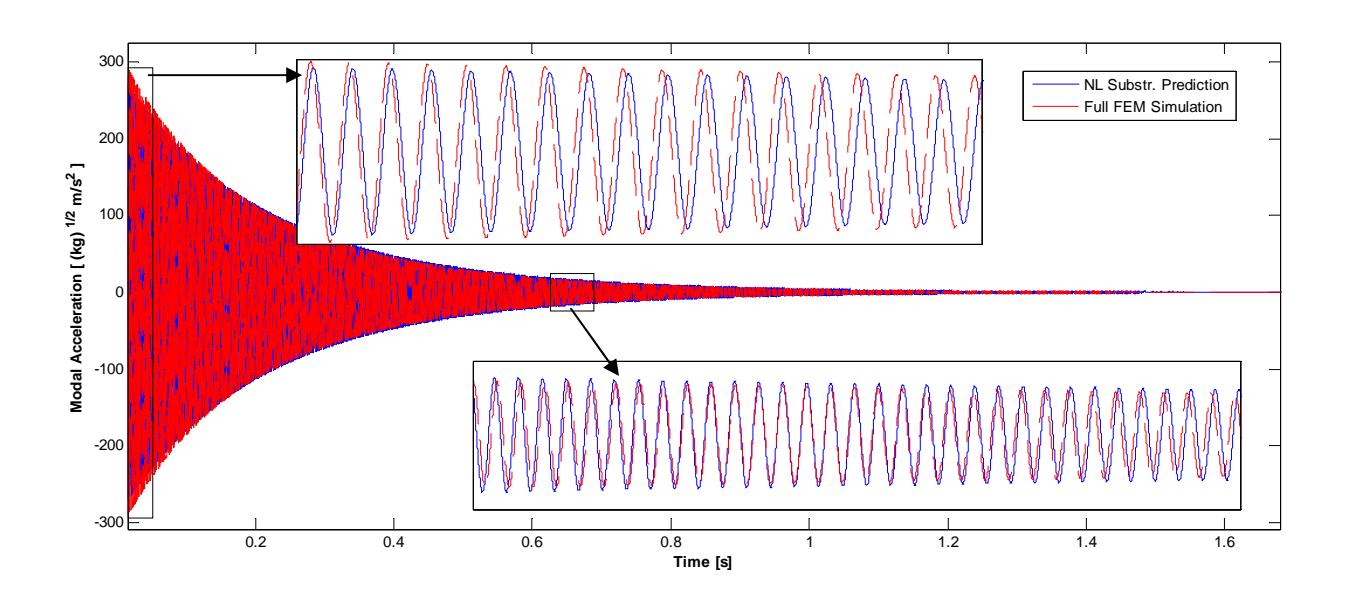


Figure 72. Comparison of true response and substructuring prediction when an impulse is applied that would excite only the 2nd Elastic mode of the assembly

In addition to the time histories, the response predicted by substructuring can be compared to the full finite element simulation by way of the amplitude dependent frequency and damping ratio, as shown in Fig. 73. The frequency is normalized to the linear natural frequency to make the trends visually comparable despite the difference in the linear natural frequencies. Both the frequency and damping correlate well between the prediction and the FEM simulation for the 1<sup>st</sup> elastic mode. In these amplitude dependent curves, small frequency changes are observable (less than 1% shift) but large changes in damping can be seen at high amplitude. As seen in the first mode, the damping ratio increases by a factor of 3.5.

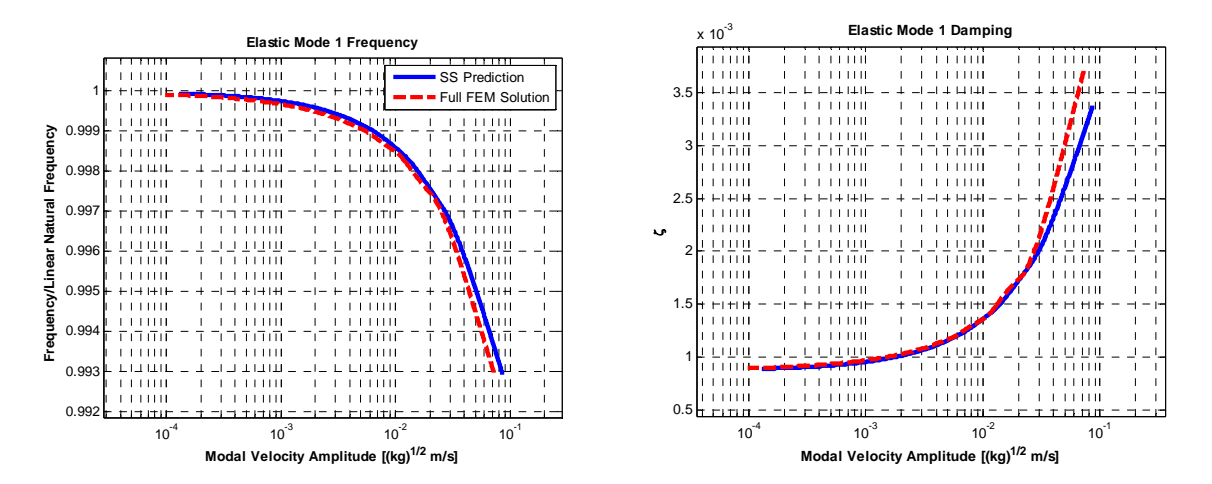


Figure 73. Amplitude dependent frequency and damping under modal loading - 1<sup>st</sup> elastic mode

Using a similar process, the second mode was also found to show clear evidence of nonlinearity, although less than the first mode. The damping ratio of the second mode changed by a little less than a factor of two and the frequency shifted by less than half a percent. This reveals that the second mode acts more linearly than the first mode. It is interesting to note that this was true for the standard Brake-Reuss Beam, Substructure C, as seen in Table 22, where the first mode had a  $\chi$ -value of -0.23 and the second mode had a  $\chi$ -value of -0.71. In a linear system a  $\chi = -1$ , closer to the value found for the 2<sup>nd</sup> bending mode. Overall, the nonlinear simulated experimental substructuring prediction is an excellent estimate of the truth model under modal loadings.

Next, a simulated impulsive load was applied near the center of the beam to excite multiple modes simultaneously. The response of both the Craig-Bampton reduced FEM truth model and substructured system was found due to the same forcing. This reveals how accurate the substructured model might be when an arbitrary force that excites multiple modes is applied. The time histories, once again projected onto the first and second elastic modes, are shown in Figs. 74 and 75. Both modes match the full truth FEM simulation remarkably well with the first elastic mode fitting slightly better than the second. The frequency for both modes is off slightly, but this is to be expected considering the frequency error present in Table 25. This suggests that it is still acceptable to treat each mode of Substructure E as uncoupled even though several modes are simultaneously excited in the response.

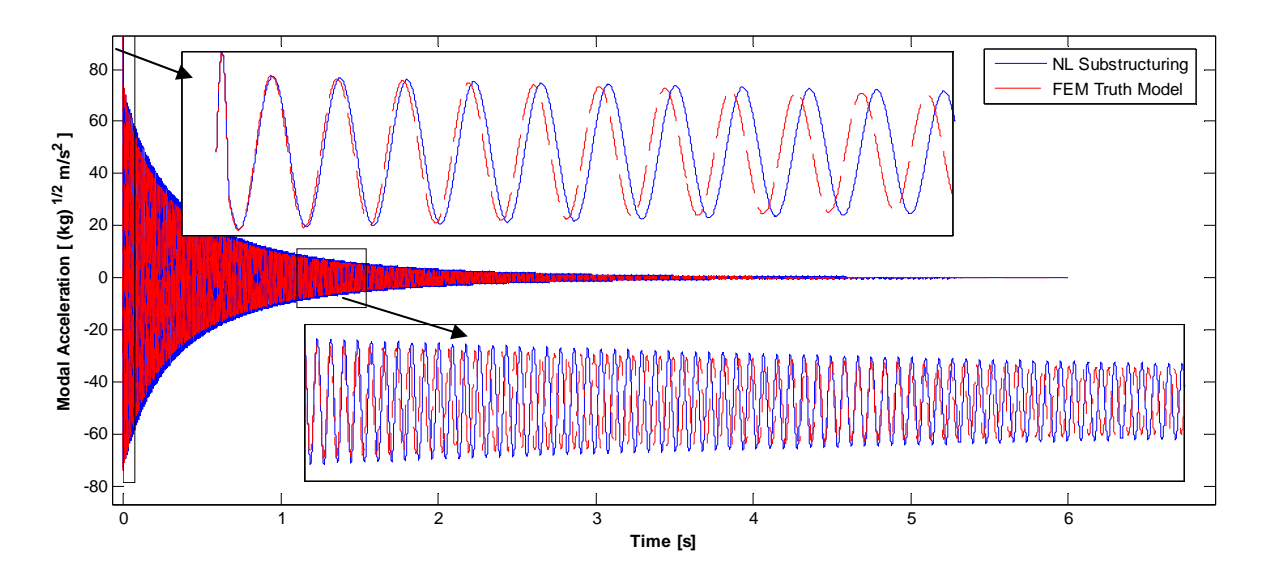


Figure 74. Comparison of true response and substructuring prediction, projected onto the 1<sup>st</sup> elastic mode, when an impulse is applied at midpoint of beam

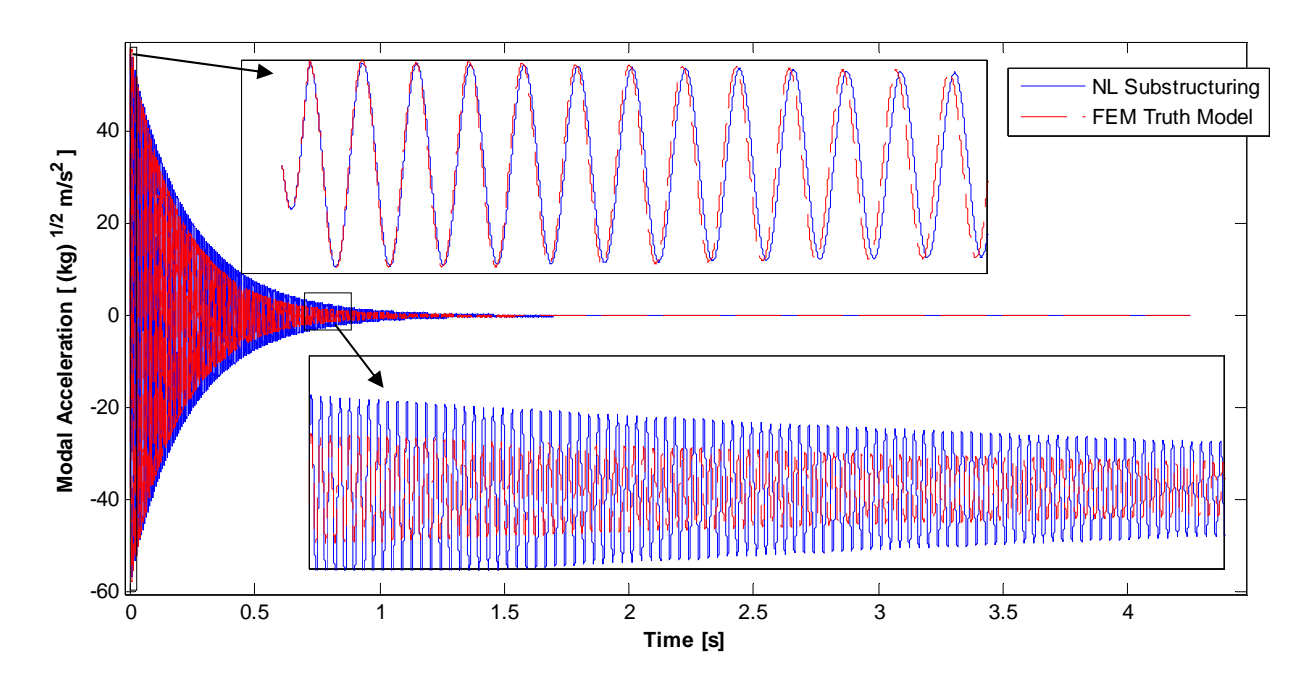


Figure 75. Comparison of true response and substructuring prediction, projected onto the 2<sup>nd</sup> elastic mode, when an impulse is applied at midpoint of beam

To obtain another view of the nonlinear effects these signals can be compared in the frequency domain by observing the drive point FRF for each time signal, as shown in Fig. 76. The peaks created by the nonlinear substructuring prediction and the full FEM simulation correlate well. The same small nonlinear distortion is visible in both the substructuring prediction and the truth model. Both have the same shape expect that one is shifted to the left meaning the only major source of error is due to a frequency shift in the linear substructuring prediction. This reveals that both the substructured prediction and the truth model contain the same nonlinearity but differ by a small shift in linear response.

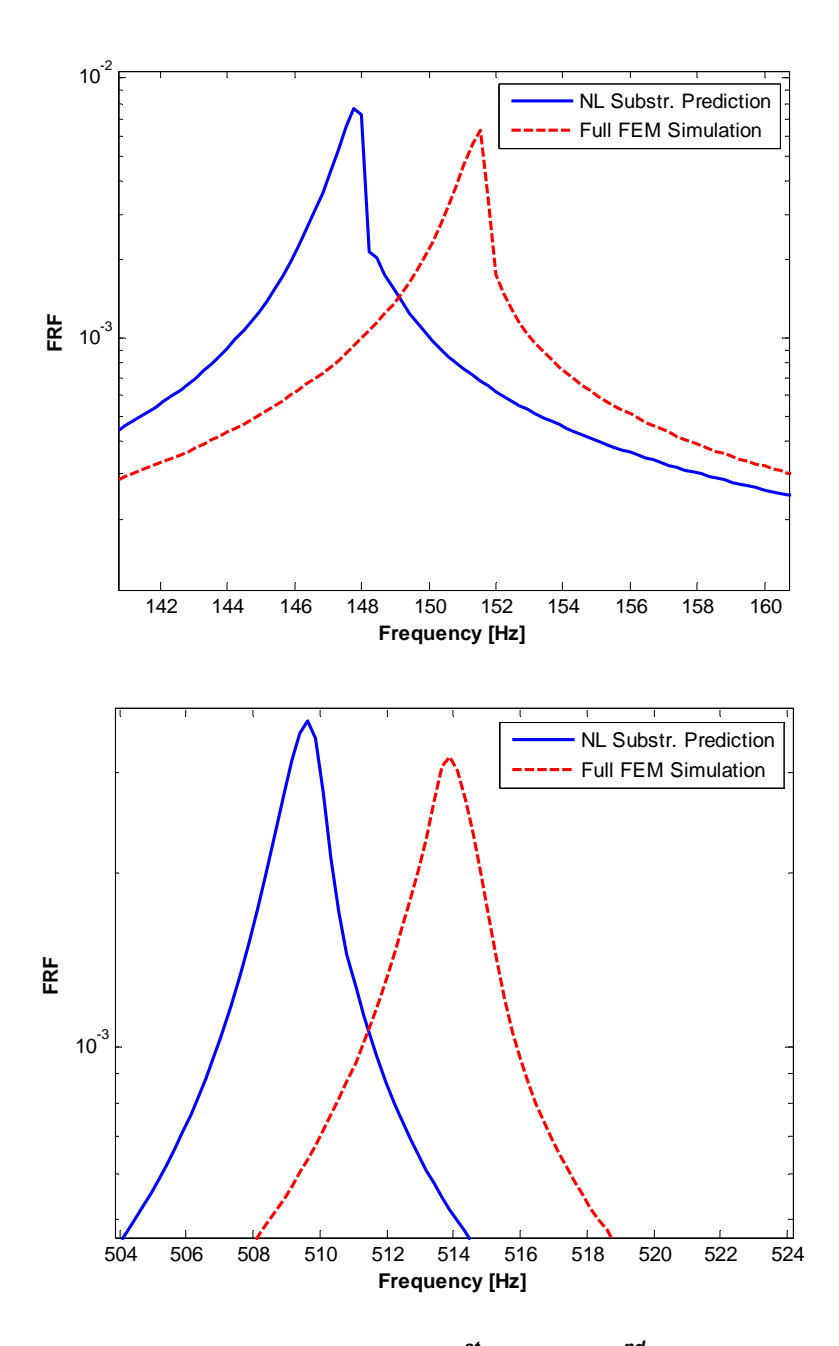


Figure 76. FFT of modal acceleration for 1<sup>st</sup> (top) and 2<sup>nd</sup> (bottom) elastic modes

Ultimately, predictions of physical response on the structure are desired. Figure 77 shows the physical response at the drive point location when the same impulse is applied at the midpoint of the beam. The nonlinear substructuring response is a highly accurate prediction of the full finite element model simulation. A linear substructuring prediction was also completed using the parameters from Table 25 under the same impulsive loading. The three time signals can be compared by calculating a root

mean squared (RMS) value for each signal. The truth model has an RMS value of 11.01 m/s<sup>2</sup> while the nonlinear substructuring prediction has a RMS value of 13.50 m/s<sup>2</sup>. In contrast, the linear model has a RMS value of 19.20 m/s<sup>2</sup>. The nonlinear substructuring model is clearly much more accurate than the linear model.

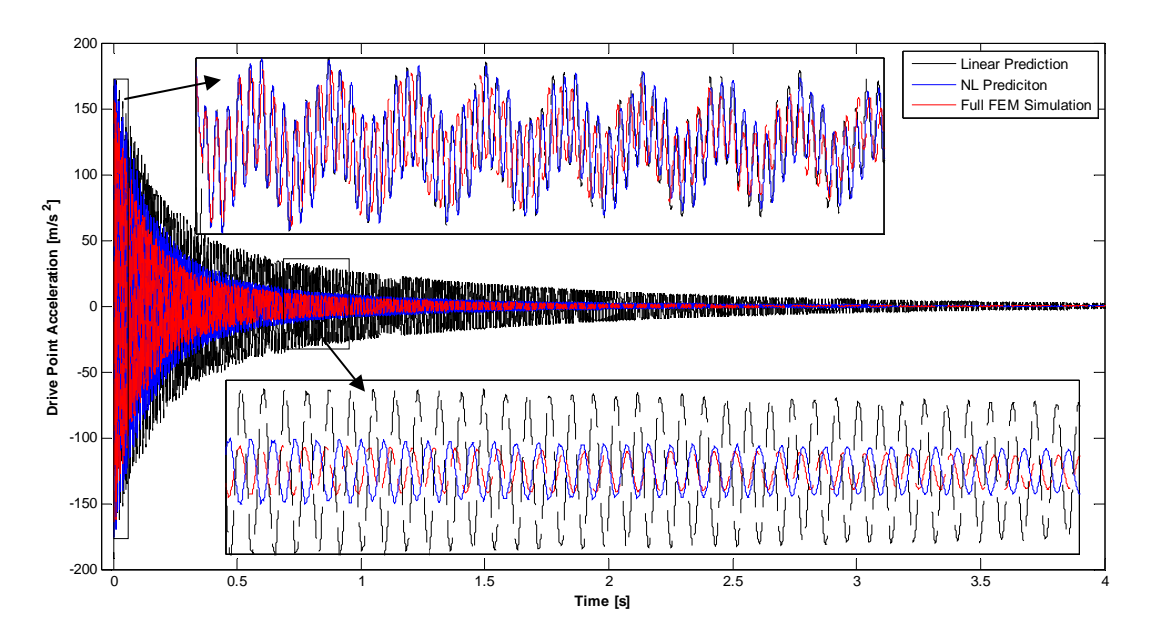


Figure 77. Driving Point Acceleration due to Impulsive Load

While the simple spring-mass model showed that modal substructuring can work with Iwan-type nonlinearities, in that example every mode of each substructure was presumed to be measured. This case has shown that modal substructuring can provide reasonably accurate predictions of the system-level response even when the modes of each substructure are truncated. It appears that this type of analysis should be feasible even if only the first few elastic modes of each substructure can be experimentally obtained.

### 4.5 Remarks

This work has proposed to model a nonlinear substructure with strong damping nonlinearities (and weak stiffness nonlinearity), due to friction at bolted interfaces, using a nonlinear modal framework. The linear modes are assumed to be preserved and to diagonalize the system, so that each mode's

response depends only on its displacement, velocity, and on the slider states used to capture its nonlinearity. These nonlinear modal models were then assembled using standard techniques and the equations of motion of the assembly were integrated using a Newmark integration algorithm.

This method was demonstrated by estimating a modal Iwan model for each mode of a 3DOF spring-mass system from simulated transient response measurements due to an impulsive load. Then these modal Iwan models were used to create a nonlinear model for the substructure that was assembled to a linear 2DOF system. The proposed approach was used to integrate the assembled equations subject to various impulsive loadings, producing estimates of the response that were found to be quite accurate. The accuracy seemed to be primarily limited by the accuracy with which the modal Iwan model could be fit to the simulated measurements.

The approach was also used to generate simulated experimental-analytical substructuring predictions for a more realistic structure, the Brake-Reuss Beam. In this example, each substructure was modeled with a small set of modes, allowing this approach to be tested when modal truncation was significant. One reason this is possible is because the transmission simulator mass-loads the interface improving the modal basis of the subcomponents. If free-free modes were used for each substructure many higher frequency modes would be required. In any event, because the intent of this work is to capture the joint nonlinearity in subcomponent test free-free modes were not really an option for this structure. The predictions for both examples were found to be highly accurate, especially when compared to a standard linear model. A companion paper will further develop this methodology by applying it to actual experimental test data from the Brake-Reuss Beam.

# 5 Nonlinear Modal Substructuring: Experimental Demonstration

### 5.1 Introduction

This chapter has been submitted as an article to the Journal of Mechanical Systems and Signal Processing [106]. This chapter utilizes the nonlinear component mode synthesis techniques, as described in Chapter 4.2 in order to predict the response of a modified nonlinear assembly. Instead of using simulated experiments, see Chapter 4, this work extends these techniques by using nonlinear subcomponent models derived from experimental measurements. This chapter remains unchanged from it's original journal submission. As such, some of the content in this chapter is repeated from previous chapters, mainly the theory presented in Chapter 5.2.

Dynamic substructuring is a method that allows the dynamics of two individual subcomponents to be synthesized in order to predict the response of a built-up structure. A comprehensive review of dynamic substructuring procedures is discussed in [13]. Experimental-analytical substructuring is a special class of dynamic substructuring in which different subcomponents of the system are described by experimental and analytical models. This allows the results of an experimental model to be coupled to that of a high-fidelity finite element model. This is often useful in industry when one of the components is made by an outside vendor or has a difficult geometry to model. The transmission simulator method (TS) [26, 38, 95] is a technique of experimental-analytical substructuring where the experimental subcomponent is mass-loaded with a fixture, or transmission simulator. This fixture is meant to simulate the boundary conditions of the subcomponent of interest in the next level assembly by mass-loading the interface.

When assembling a complicated structure with physical hardware, it is highly likely that bolted joints will be used to in some capacity. The frictional interface of these bolted joint regions generate a large portion of the damping in the built-up assembly and this damping usually changes nonlinearly with excitation amplitude [1, 2]. Jointed structures are often weakly nonlinear; as such, the modes of the

structure remain uncoupled and the mode shapes do not change with higher response or forcing amplitude. Weakly nonlinear subcomponents have been investigated and were found to often have large increases in damping at higher amplitudes with relativity small shifts in frequency [52]. This was shown recently on an industrial system, a bolted pair of catalytic converters [3], and on a complicated cylindrical structure with a continuous interface [98]. In those articles, each mode of a system was treated as an uncoupled nonlinear single degree of freedom oscillator.

This article uses the same weakly nonlinear framework and represents the mass-loaded experimental component with a combination of linear and nonlinear modes. Previous studies using the transmission simulator method on experimental hardware [37, 73, 74] were completed to capture the linear stiffness and damping of the joint. However, in those prior studies the joint nonlinearities caused by high amplitude response were ignored as the systems were tested solely at low forcing levels, which did not illicit these nonlinearities. The transmission simulator method allows one to contain the bolted joint dynamics in an individual experimental subcomponent. By using a nonlinear model for this experimental subcomponent, the nonlinear dynamics due to the joint are added into the built-up assembly prediction.

This work proposes to use nonlinear modal models to represent the mass-loaded experimental subcomponent in an experimental-analytical substructuring prediction. This will be the first application of these nonlinear modal substructuring techniques using measurements from real hardware. The system of interest will be a simple beam structure, the Brake-Reuss Beam [76]. A simulated experimental substructuring prediction of this system was completed in [94]. That study showed that it was possible to obtain an accurate prediction of the response of this system using the transmission simulator method even if only the first few modes could be measured. Previously, nonlinear substructuring has mainly dealt with numerical models as presented in [67, 68] but a few attempts with physical set-ups have seen success in the past [69]. The proposed method differs in solution type and its capability to treat multiple modes as

nonlinear in each subcomponent model. Additional review of nonlinear modal models and substructuring techniques was presented in Part I of this work, [94].

The chapter is organized as follows. Section 5.2 outlines the approach used for substructuring and experimental nonlinear behavior identification. In Section 5.3, the substructuring process for the Brake-Reuss Beam is reviewed and nonlinear modal models for the baseline Brake-Reuss Beam are identified from measured data. The measurements consist of the response of the structure to high level impact tests, and the measurements are post processed to obtain the amplitude dependent stiffness and damping relationships. Nonlinear modal models are then developed using those amplitude dependent relationships. These nonlinear modal models are used to describe subcomponent dynamics and enable the prediction of a nonlinear system level response. This prediction is discussed in detail in Section 5.4, where the results of the substructuring method are compared to measurements from a truth test. Section 5.5 presents some remarks about this new technique and conclusions on this topic.

## 5.2 Background and Theory

To establish the theoretical foundation for the method used here, two items are reviewed. First, the nonlinear substructuring methodology proposed in [94] is reviewed briefly. This explains how multiple substructures can be coupled including nonlinear joint forces to obtain an assembled prediction. Next, the nonlinear modal model identification process from [3] is reviewed. In this work, a 4-parameter modal Iwan model represents the nonlinear forces in each subcomponent.

### **5.2.1** Nonlinear Component Mode Synthesis

This section begins with a discussion on linear dynamic substructuring using the transmission simulator method, then the nonlinear forces are incorporated into the problem as described later. Traditional substructuring is reviewed in [12] and [13], but an overview is provided here for convenience. For a general linear system, each substructure can be written as,

$$\mathbf{M}_{C}\ddot{\mathbf{x}}_{C} + \mathbf{C}_{C}\dot{\mathbf{x}}_{C} + \mathbf{K}_{C}\mathbf{x}_{C} = \mathbf{F}_{C}$$
(72)

where,  $\mathbf{M}_C$ ,  $\mathbf{C}_C$ , and  $\mathbf{K}_C$  are the mass, damping, and stiffness matrices of Substructure C. This work implements modal substructuring, as such, this equation of motion is cast into modal domain by using a modal transformation where the physical displacements,  $\mathbf{x}_C$ , on Substructure C are related to the mode shapes and modal coordinates,  $\mathbf{q}_C$ , of the substructure. This transformation is completed by using the linear mode shape matrix,  $\mathbf{\Phi}_C$ ,

$$\mathbf{x}_C = \mathbf{\Phi}_C \mathbf{q}_C \tag{73}$$

After making this substitution and premultiplying by the transposed mode shape matrix, the equations of motion for the substructure leads to the modal equations of motion presented in Eqn. (74).

$$\mathbf{I}_{C}\ddot{\mathbf{q}}_{C} + \left[ (2\zeta_{C}\omega_{n,C}) \right] \dot{\mathbf{q}}_{C} + \left[ (\omega_{n,C}^{2}) \right] \mathbf{q}_{C} = \mathbf{\Phi}_{C}^{T} \mathbf{F}_{C}$$

$$(74)$$

The transmission simulator method begins by writing the modal equations of motion for each substructure in block diagonal form as shown in Eqn. (75). Note that as shown, Substructure C and D are positive and Substructure A is negative in the block diagonal. This is the typical transmission simulator scenario where one is adding two substructures together and removing the effects of the transmission simulator from the system.

$$\begin{bmatrix}
\mathbf{I}_{C} & \mathbf{0} & \mathbf{0} \\
\mathbf{0} & \mathbf{I}_{D} & \mathbf{0} \\
\mathbf{0} & \mathbf{0} & -\mathbf{I}_{A}
\end{bmatrix}
\begin{bmatrix}
\dot{\mathbf{q}}_{C} \\
\dot{\mathbf{q}}_{D} \\
\dot{\mathbf{q}}_{A}
\end{bmatrix} + \begin{bmatrix}
\langle (2\zeta_{C}\omega_{n,C})_{\backslash} & 0 & 0 \\
0 & \langle (2\zeta_{D}\omega_{n,D})_{\backslash} & 0 \\
0 & 0 & \langle (-2\zeta_{A}\omega_{n,A})_{\backslash}
\end{bmatrix}
\begin{bmatrix}
\dot{\mathbf{q}}_{C} \\
\dot{\mathbf{q}}_{D} \\
\dot{\mathbf{q}}_{A}
\end{bmatrix}$$

$$+ \begin{bmatrix}
\langle (\omega_{n,C}^{2})_{\backslash} & 0 & 0 \\
0 & \langle (\omega_{n,D}^{2})_{\backslash} & 0 \\
0 & 0 & \langle (-\omega_{n,A}^{2})_{\backslash}
\end{bmatrix}
\begin{bmatrix}
\mathbf{q}_{C} \\
\mathbf{q}_{D} \\
\mathbf{q}_{A}
\end{bmatrix} = \begin{bmatrix}
\mathbf{\Phi}_{C}^{T}\mathbf{F}_{C} \\
\mathbf{\Phi}_{D}^{T}\mathbf{F}_{D} \\
\mathbf{\Phi}_{A}^{T}\mathbf{F}_{A}
\end{bmatrix}$$
(75)

Note that each subcomponent in the equations above is uncoupled from the other components.

Additionally, each mode of each substructure is uncoupled from the other modes. In order to complete the

dynamic substructuring process, constraints must be enforced between the individual substructures which can be written as follows,

$$\mathbf{B} \begin{bmatrix} \mathbf{x}_C \\ \mathbf{x}_D \\ \mathbf{x}_A \end{bmatrix} = \mathbf{0} \tag{76}$$

These constraints tie physical degrees of freedom on different substructures to enforce displacement compatibility at the interface between substructures. Here,  $\bf B$ , is a Boolean matrix that defines this compatibility. These constraints can be cast into the modal domain as shown in Eqn. (77), where the two leading matrices can be combined into one matrix,  $\bf \bar B$ ,

$$\mathbf{B} \begin{bmatrix} \boldsymbol{\phi}_{C} & \mathbf{0} & \mathbf{0} \\ \mathbf{0} & \boldsymbol{\phi}_{D} & \mathbf{0} \\ \mathbf{0} & \mathbf{0} & \boldsymbol{\phi}_{A} \end{bmatrix} \begin{bmatrix} \mathbf{q}_{C} \\ \mathbf{q}_{D} \\ \mathbf{q}_{A} \end{bmatrix} = \overline{\mathbf{B}} \begin{bmatrix} \mathbf{q}_{C} \\ \mathbf{q}_{D} \\ \mathbf{q}_{A} \end{bmatrix} = \mathbf{0}$$

$$(77)$$

A new assembled set of coordinates,  $\eta$  , is then defined. This is accomplished by finding a transformation matrix, L , that resides in the nullspace of  $\overline{B}$  .

$$\mathbf{q} = \mathbf{L}\mathbf{\eta} \tag{78}$$

$$\overline{\mathbf{B}}\mathbf{L}\boldsymbol{\eta} = \mathbf{0} \tag{79}$$

$$\mathbf{L} = null(\overline{\mathbf{B}}) \tag{80}$$

This transformation matrix can now be applied to the modal equations of motion, Eqn. (75), to synthesize the system, where,

$$\overline{\mathbf{M}} = \mathbf{L}^{T} \begin{bmatrix} \mathbf{I}_{C} & \mathbf{0} & \mathbf{0} \\ \mathbf{0} & \mathbf{I}_{D} & \mathbf{0} \\ \mathbf{0} & \mathbf{0} & -\mathbf{I}_{A} \end{bmatrix} \mathbf{L}$$
(81)

and similar transformations are made for  $\overline{\boldsymbol{C}}$  and  $\overline{\boldsymbol{K}}$  ,

$$\overline{\mathbf{M}}\ddot{\boldsymbol{\eta}} + \overline{\mathbf{C}}\dot{\boldsymbol{\eta}} + \overline{\mathbf{K}}\boldsymbol{\eta} = \mathbf{L}^{T} \begin{cases} \boldsymbol{\phi}_{C}^{T} \mathbf{F}_{C} \\ \boldsymbol{\phi}_{D}^{T} \mathbf{F}_{D} \\ \boldsymbol{\phi}_{A}^{T} \mathbf{F}_{A} \end{cases}$$
(82)

As mentioned previously, we presume that the nonlinearity in each subcomponent can be captured on a mode-by-mode basis. Thus, the equations of motion for such a substructure could be modified from Eqn. (75), and written as,

$$\mathbf{I}_{C}\ddot{\mathbf{q}}_{C} + \left[ (2\zeta_{C}\omega_{n,C}) \right] \dot{\mathbf{q}}_{C} + \left[ (\omega_{n,C}^{2}) \right] \mathbf{q}_{C} + \left\{ \mathbf{F}_{NL,C} \right\} = \boldsymbol{\phi}_{C}^{T} \mathbf{F}_{C} \\
\left\{ \mathbf{F}_{NL,C} \right\}^{T} = \left[ F_{NL,1,C} (q_{1,C}, \theta_{1,C}) \quad F_{NL,2,C} (q_{2,C}, \theta_{2,C}) \quad \cdots \right]^{T}$$
(83)

where,  $F_{NL,n,C}(q_{n,C},\theta_{n,C})$ , is a force describing the joint nonlinearity of the nth mode and depends only on that mode's amplitude. This nonlinear force could take many forms but in this work it is represented by a 4-parameter modal Iwan model where each mode of the subcomponent is still treated as uncoupled. This limits this methodology to substructuring with weakly nonlinear substructures. As first discussed in [94], these joint forcing terms can be added to the synthesized equations through the same transformation matrix.

$$\overline{\mathbf{M}}\ddot{\boldsymbol{\eta}} + \overline{\mathbf{C}}\dot{\boldsymbol{\eta}} + \overline{\mathbf{K}}\boldsymbol{\eta} + \mathbf{L}^{T} \begin{Bmatrix} \mathbf{F}_{NL,C} \\ \mathbf{F}_{NL,A} \\ \mathbf{F}_{NL,A} \end{Bmatrix} = \mathbf{L}^{T} \begin{Bmatrix} \boldsymbol{\phi}_{C}^{T} \mathbf{F}_{C} \\ \boldsymbol{\phi}_{D}^{T} \mathbf{F}_{D} \\ \boldsymbol{\phi}_{A}^{T} \mathbf{F}_{A} \end{Bmatrix}$$
(84)

Also note that the nonlinear forces themselves depend on the substructure DOF  $\mathbf{q}_C$ ,  $\mathbf{q}_D$  and  $\mathbf{q}_A$ , which are related to  $\mathbf{\eta}$  via Eqn.(78). Each modal DOF remains uncoupled and hence the response of the substructure can be found by integrating each SDOF modal equation of motion independent of the others. However, when assembling the substructures these nonlinear forces are spread to all assembled degrees of freedom via  $\mathbf{L}^T$  and thus the assembled modal DOF are no longer uncoupled in the built-up system. In [94], the authors discussed specifically how to implement these equations, using a 4-parameter modal Iwan model for each mode and using a Newmark algorithm to find the transient response of the assembly. The same process is used here but the nonlinear subcomponent model is now defined by experimental measurements.

## **5.2.2** Nonlinear Modal Model Identification

This section contains a review of the proposed process for experimental detection and characterization of nonlinear modal behavior. The goal of this section is to highlight each step of the process and give insight into the different tools used when investigate the nonlinear modal behavior in an experimental system. A more rigorous explanation for many of these tools is contained in [3].

To begin identifying the nonlinear modal models, the structure is excited with an impulsive load at high and low force levels. The low force level measurement is used to find linear modal parameters as is the common practice in industrial applications. Next, the high load level data is used to screen each mode for nonlinear behavior. Often, in weakly nonlinear structures, very small frequency shifts are observed but, large changes in damping are seen as amplitude increases. These differences are apparent when one compares the modal parameters extracted from a high forcing level impact test with those from a low forcing level. Additionally, comparing the frequency response function of the measured signals can provide insight as to how the response of the system changes at high and low amplitudes. All measurements are related to each modal response, thus the following equation can be solved in a least squares sense to obtain the modal amplitudes from the acceleration measurements,

$$\mathbf{\Phi}\ddot{\mathbf{q}}(t) = \ddot{\mathbf{x}}(t) \tag{85}$$

where  $\Phi$  is the mass-normalized mode shape matrix,  $\ddot{\mathbf{q}}(t)$  represents the corresponding modal responses, and  $\ddot{\mathbf{x}}(t)$  is a vector of accelerations that were measured during a single-impact hammer test. This method allows multiple hammer strikes to be compared even from different driving point locations to assure that the modal response is independent of the driving point location and the force level.

Each mode can be represented as a single degree-of-freedom (SDOF) system as shown in Fig. 78. This SDOF system contains a modal mass which is tied to ground with a linear spring and damper. Also, a nonlinear element representing the joint force is also connected to this mass, which can be used to capture the nonlinear behavior of this mode's response. This nonlinear element could take many forms,

but for this work a 4-parameter Iwan element is used to represent this nonlinear joint force. The original equation of motion can now be written as was described in Eqn. (83).

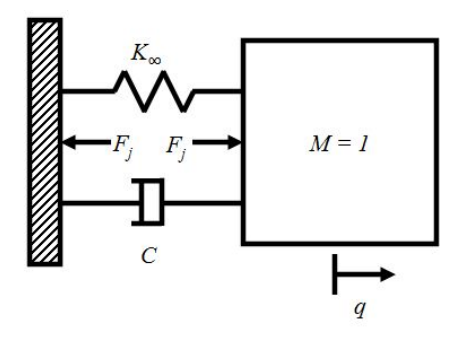


Figure 78. Schematic of SDOF model used for each modal degree of freedom

The next step in the proposed process is to quantify the change in frequency and damping with amplitude. This is accomplished using the Hilbert transform algorithm as detailed in [52, 55]. This approach redefines the modal response, q(t), in the following analytic functional form,

$$\ddot{q}(t) = e^{\psi_r(t) + i\psi_i(t)} \tag{86}$$

where  $\psi_r(t)$  and  $\psi_i(t)$  are a series of splines in time and are, respectively, the real and imaginary parts of the time varying response model. The damped natural frequency can be related to the phase of the analytic signal as was discussed in [52]. Obtaining the damping ratio is covered in detail [3]. The damping ratio relates to both the amplitude and phase of the analytic signal. Based on the derivations mentioned, the modal parameters can be obtained as shown in Eqn. (87). In addition to describing the nonlinear characteristics of the mode, these parameters also allow for the conversion of modal acceleration to modal velocity and displacement.

$$\omega_d(t) \triangleq \frac{d\psi_i}{dt} \qquad -\zeta(t)\omega_n(t) \triangleq \frac{d\psi_r}{dt}$$
 (87)

As mentioned previously, each mode will be modeled with a single degree of freedom system with a spring, damper, and nonlinear joint force which is represented as a 4-parameter Iwan model. This joint force can be written in the following form,

$$F_{j}(t) = \int_{0}^{\infty} \rho(\phi) \left[ u(t) - x(t,\phi) \right] d\phi \tag{88}$$

where  $F_j$  is the force in the joint, u is joint displacement,  $\rho$  is a kernel that characterizes the joint, and x is a continuum of state variables that evolve as,

$$\dot{x}(t,\phi) = \begin{cases} \dot{u} & \text{if } ||u - x(t,\phi)|| \\ & \text{and } \dot{u}(u - x(t,\phi)) > 0 \\ 0 & \text{otherwise} \end{cases}$$
(89)

The form of the kernel,  $\rho(\phi)$ , is discussed in detail in [48] and can be defined by four parameters,  $[F_s, K_T, \chi, \beta]$ , where  $F_s$  is the joint force required to begin macro-slip,  $K_T$  is the stiffness in the joint,  $\chi$  is related to the exponent in the power-law relationship between damping, and amplitude in the micro-slip regime and  $\beta$  defines the shape of the dissipation curve near the transition from micro to macro-slip. When this joint model is used in a modal framework, these four parameters define the nonlinear characteristics of each mode in the system and can be obtained from experimental measurements as outlined in [3, 52]. This identification process is shown for the Brake-Reuss Beam example in Section 5.3.

### 5.3 Experimental System - Brake-Reuss Beam System

The proposed nonlinear substructuring theory provided promising results using simulated experimental models in [94]. In this chapter, the authors validate these theories using experimental models derived from experimental measurements. The system of interest for this study is the Brake-Reuss Beam [76] which consists of a pair of 304 stainless steel half-beams bolted at the center with a lap joint. Figure 96 shows the experimental set-up for the Brake-Reuss Beam system.

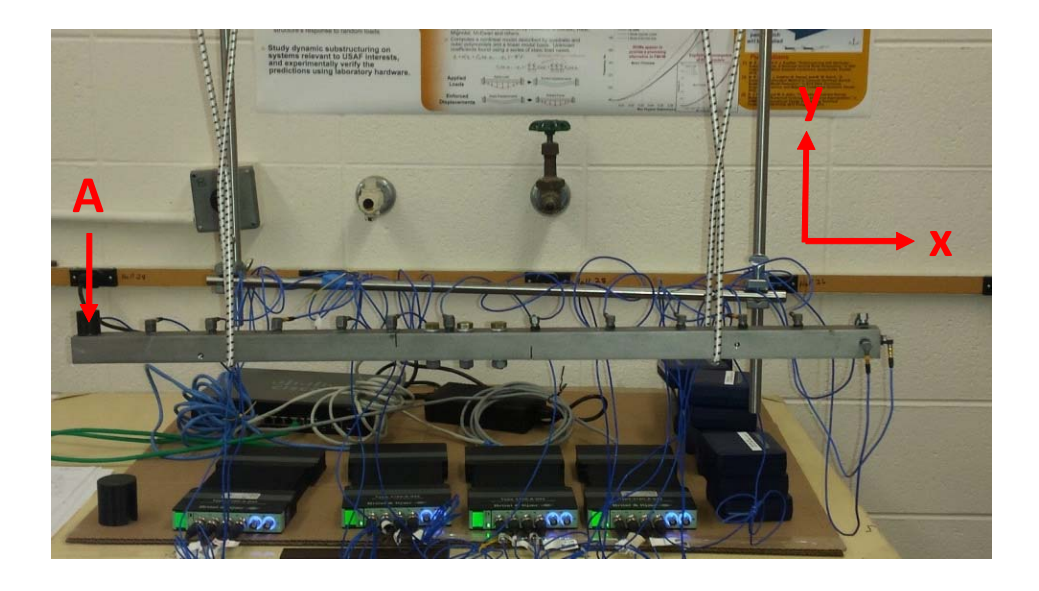


Figure 79. Brake-Reuss Beam Experimental Set-up

Figure 63 shows the three subcomponents and the built-up, modified structure. Substructure C is the standard Brake-Reuss Beam that is represented by an experimental model. Substructure A will be the transmission simulator for these predictions and is simply the right half of the Brake-Reuss Beam system. Substructure D is a design modification; a half-beam with a mass attached to the end. Both Substructures A and D are modeled as FEM models. The details of which are presented in [94]. Finally, the assembly of interest is the modified Brake-Reuss Beam represented by Substructure E. The goal is to predict the dynamics of a modified Brake-Reuss Beam in which the right beam is replaced with a modified structure. This simulates an industrial application where a design modification is made to one part of the assembly such that its dynamics are changed considerably.

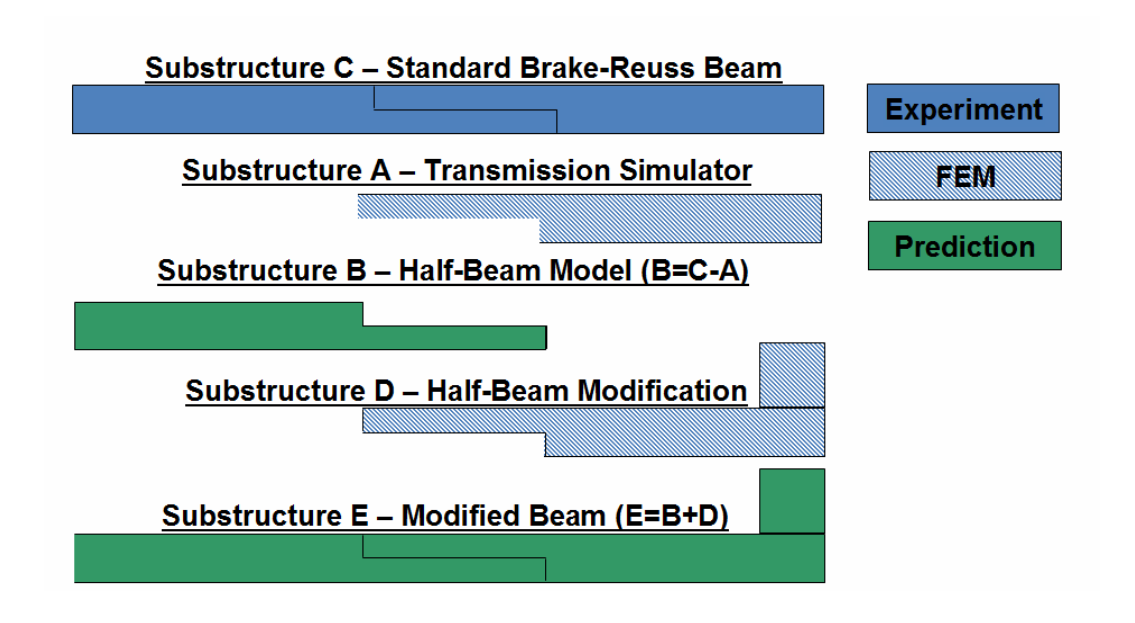


Figure 80. Substructure Overview

This section steps through the process of measuring and defining a nonlinear component model for Substructure C. This experimental model will comprise of a combination of linear and nonlinear modal models. These modal models are derived from measurements of the bolted assembly shown in Fig. 96. The bolts in this assembly were tightened to 10 N-m torque as recommended in [107]. This system has been studied by several groups at the Nonlinear Mechanics and Dynamics (NOMAD) Institute hosted by Sandia National Labs [104, 108]. The beam studied in this work consists of beam halves 1A and 1B from the 2015 NOMAD Institute.

Based on previous experiments [104], the frequency range of interest was obsered to be 0-2000 Hz, where the first few bending modes could be readily obtained. The system was instrumented with 15 low sensitivity (5 mV/g) accelerometers, 13 of these sensors are in the primary direction of interest with 2 off-axis sensors for troubleshooting. Using low level hammer hits on the accelerometer at point A in Fig. 96, the modal parameters of the first four bending modes were extracted from the test specimen. Figure 28 shows the measured bending modes at the measurement points in the y-direction.

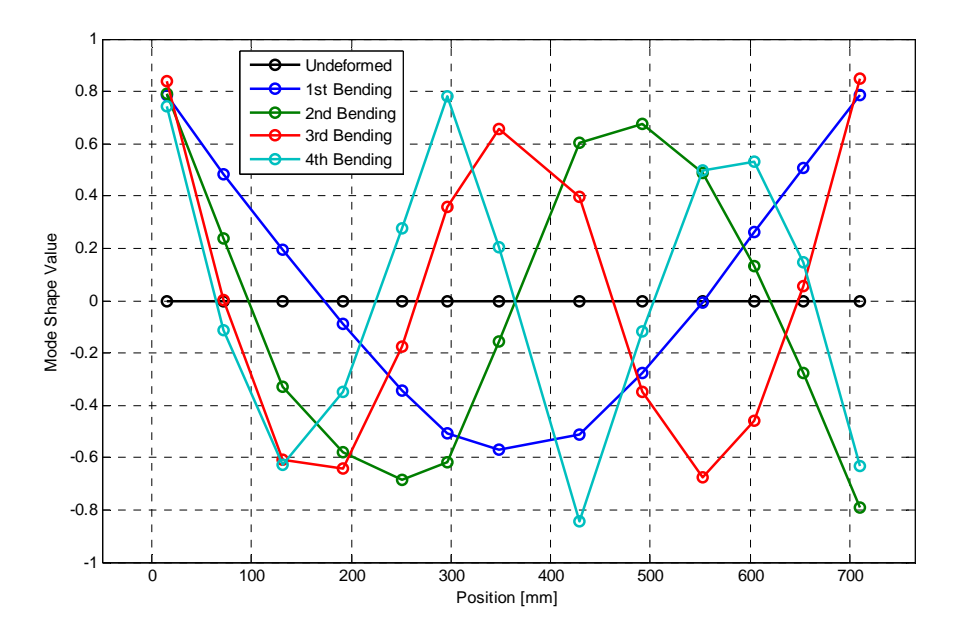


Figure 81. Measured Bending mode shapes of Brake-Reuss Beam, Substructure C

Table 11 contains a list of the natural frequencies and damping ratios extracted for each of the modes using the Algorithm of Mode Isolation (AMI), a linear modal parameter identification algorithm that is detailed in [87]. These parameters establish a linear model of the first four bending modes. Next, the structure was tested at higher impact levels in order to screen the system for nonlinear behavior.

Table 26: Linear (low amplitude) modal parameters of Substructure C

Elastic Mode Index	Natural Frequency [Hz]	Damping Ratio	Deflection Type
1	172.70	0.00095	1 <sup>st</sup> Bending
2	583.26	0.00143	2 <sup>nd</sup> Bending
3	1179.99	0.00376	3 <sup>rd</sup> Bending
4	1645.43	0.00814	4 <sup>th</sup> Bending

The assembly was probed by striking the beam with a impact hammer several times, at various load levels and at various drive points, to deduce whether any modes might behave nonlinearly. By comparing the frequency response function (FRF) for each of these hammer strikes, nonlinear trends in the modal behavior can be observed. Figure 82 shows an example FRF comparison for the 1<sup>st</sup> bending mode. In a linear system all of these curves would overlay as the amplitude of the force and response

would be linearly scaled. Due to the nonlinearities in the Brake-Reuss Beam assembly, increasing the impulsive force results in a slight decrease in the resonant frequency and an increase in the modal damping observed by the decreasing FRF amplitude. These changes are similar to what has been observed in the past when a nonlinear modal model was well suited to fit the response [3].

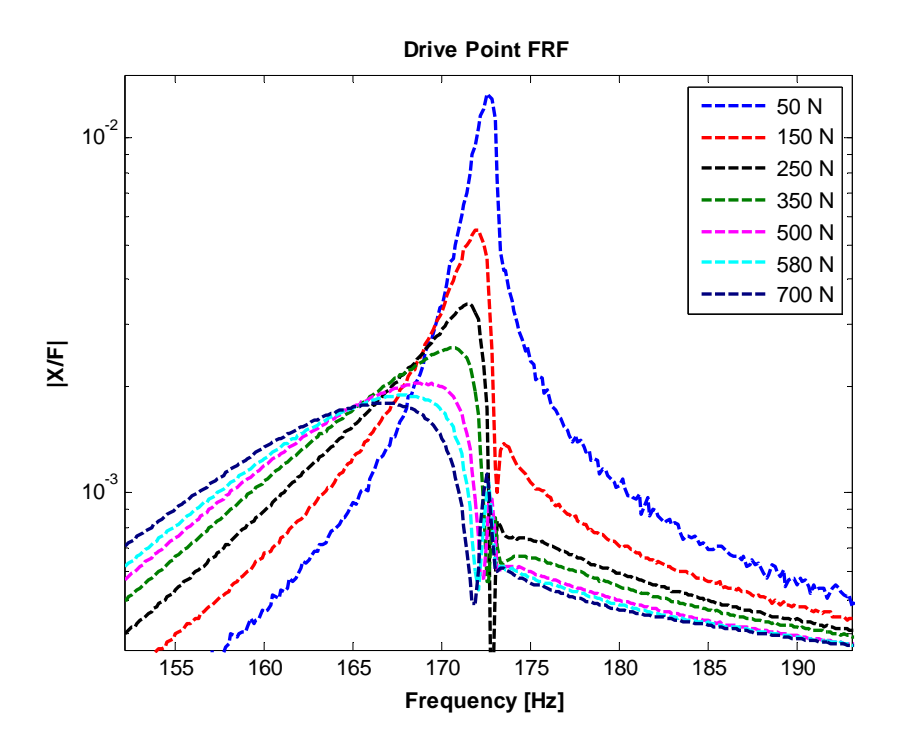


Figure 82. Frequency response function near Mode 1 of Substructure C for various impact for levels

While this frequency shift shows that the stiffness nonlinearity is quite small, this mode exhibited much more significant nonlinearity in damping. A similar analysis was performed on the second elastic mode which also revealed a measurable shift in the natural frequency of over the same range of input force. The third and fourth elastic modes showed much smaller traces of nonlinearity. Hence, it was decided to use linear models for the third and fourth bending modes. A summary of the observed frequency and damping nonlinearities is shown in Table 12. The trends from this table are used solely to screen modes and make sure the results from individually fit nonlinear modal models are reasonable.

Table 27: Summary of Nonlinearity Screening Results for Brake-Reuss Beam Substructure C, NA = not applicable (linear mode)<sup>1</sup>

Elastic Mode	Natural Frequency [Hz]	% Shift in Peak Frequency	Linear Damping Ratio*	Maximum Damping Ratio*	% Shift in Damping
1	172.70	-3.81%	0.00095	0.01060	+1015%
2	583.26	-1.28%	0.00143	0.00625	+337%
3	1179.99	NA	0.00376	NA	NA
4	1645.43	NA	0.00814	NA	NA

Now that the first two modes have been identified as nonlinear, their corresponding amplitude dependent stiffness and damping need to be obtained. A spatial filter was first applied to each of the measured data sets in order to isolate each mode as described in Eqn. (85). This results in a SDOF response for each mode of each test run completed. It is important to properly filter the signals into a single harmonic response because any contamination from closely spaced modes can cause major distortions when the stiffness and damping are fit versus amplitude.

Next, the Hilbert transform was used to obtain an expression in the form of Eqn. (86) for each single-harmonic response. In order to achieve a higher quality fit of frequency and damping, a band-pass filter was applied to the modally filtered signal to ensure the signal was a single harmonic. The envelope and phase of this mirrored signal was then fit to splines with 30 knots.

Using the relationships from Eqn. (87), the fit envelope and phase can be related to the damping and stiffness of the signal. Observing the damping and stiffness versus amplitude yields a relationship from which nonlinear modal model parameters can be formulated. Figures 83 and 84 show an example of this process for the 1st bending mode of the system, where the damped natural frequency and damping ratio are plotted versus time (as returned by the Hilbert transform algorithm) and amplitude (obtained using the amplitude of the signal versus time from the Hilbert transform), respectively.

<sup>&</sup>lt;sup>1</sup> Damping Ratios obtained from Half Power Bandwidth of highest and lowest force level strikes

Note that later in time (lower in amplitude) a frequency is seen near 172.7 Hertz which is the linear frequency from modal testing in Table 11. Early in the time signal (when the modal amplitude is high) the frequency gets as low as 169 Hz, or about a 2% shift in frequency, which is close to what was observed by testing at multiple forcing levels as shown in Fig. 82. Similar comparisons can be seen in the linear damping ratio, which matches the measurement present in Table 11. The nonlinear damping ratio reaches levels much higher than those observed in the simple FRF screening process, most likely due to the half-power bandwidth assumption being used on a nonlinear data set. But this is not surprising since the simple FRF screening process is not expected to accurately estimate the damping because it assumes that the half power bandwidth method extends to a nonlinear system.

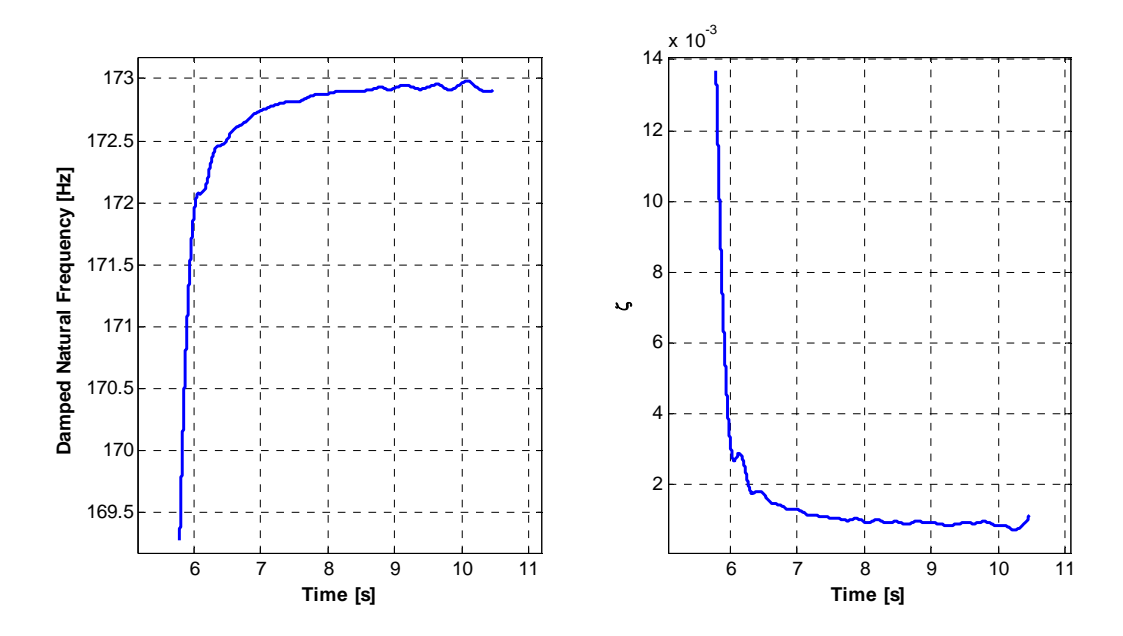


Figure 83. Damped natural frequency and damping ratio for the first mode of Substructure C

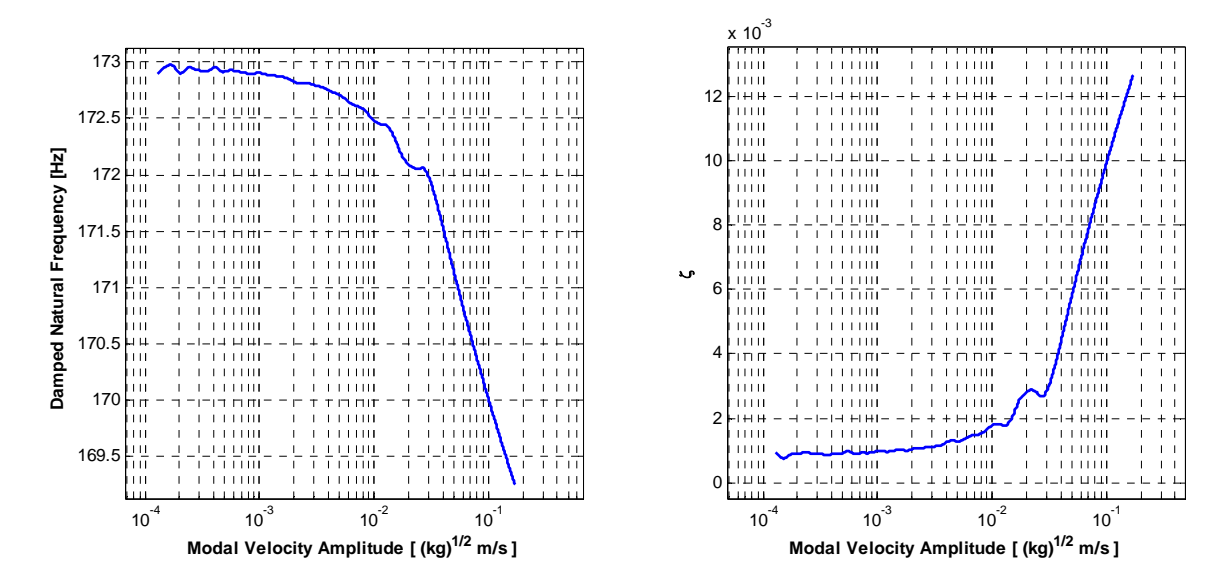


Figure 84. Amplitude dependent stiffness and damping curves for the first mode of the Brake-Reuss Beam, Substructure C

The results shown in Figs. 83 and 84 were extracted from only one of the excitation amplitudes at which tests were performed. The spectra at various load levels are shown in Fig. 82. To ensure that the modes were adequately uncoupled, testing was also conducted from differing drive point locations. For each impact test, a pair of stiffness and damping curves were generated. This ensemble of damped natural frequency and damping ratio curves for each nonlinear mode can be overlaid to see how repeatable these amplitude dependent measurements are. These overlaid curves were used to extract modal Iwan model parameters as shown in Fig. 85.

The modal Iwan model is defined by four parameters,  $[F_s, K_T, \chi, \beta]$ . To fit the dissipation parameter,  $\chi$ , of the Iwan modal model, these amplitude dependent damping curves were fit in a least squares sense. In this figure, the total modal damping in the mode, extracted by the Hilbert transform, is given by the blue curves. Next, the linear contribution was removed from these curves revealing the nonlinear part of the damping in red (i.e. the part that is not linear and viscous). At low amplitudes this can be very noisy, but at higher amplitudes a distinct trend is clear on this log-log scale. The dissipation parameter,  $\chi$ , is then fit to this distinct high amplitude potion of the nonlinear damping curve by setting the slope of this curve equal to  $\chi+1$ . This Iwan fit is shown in black. Finally, to ensure the total modal

damping is well simulated, the linear portion of the damping is added back to the Iwan fit to obtain the total modal damping, shown in green.

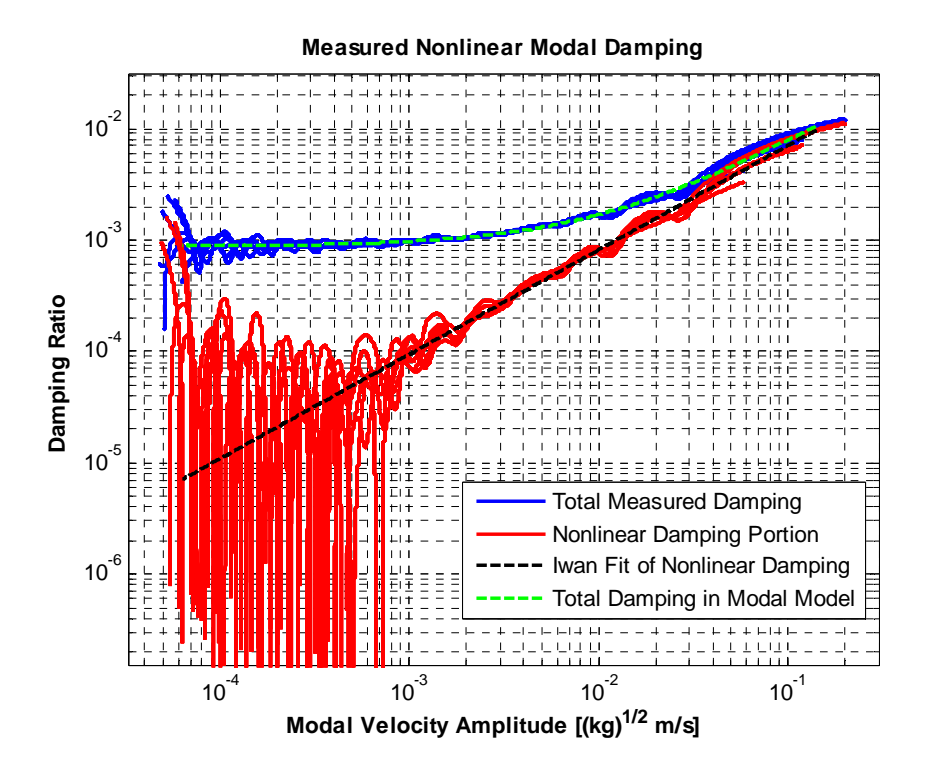


Figure 85. Measured Modal Damping for Mode 1 of Substructure C

The other modal Iwan parameters are more ambiguous, but were selected using engineering judgment and previous testing history. There was no clear evidence of macro-slip in the experimental test; therefore, the slip force can be assumed to be greater than any of the excitations applied experimentally.

$$F_{S} \ge \mathbf{\Phi}_{dp} F \tag{90}$$

The joint stiffness,  $K_T$ , is dependent on the frequency shift observed once the structure is in macro-slip. Because macro-slip wasn't achieved in these tests, this parameter can't be readily estimated. This beam was previously tested by Bonney et al. [104] and their tests included higher amplitude impacts

where the macro-slip frequency for the first mode was observed to be 130 Hz. This was used to estimate  $K_T$  using :

$$K_T = K_0 - K_{\infty} = \omega_0^2 - (\omega_0 - \omega_{shift})^2$$
 (91)

In principle, the parameter  $\beta$  can be found from the y-intercept of the dissipation versus amplitude curve. In this case, this would not be reliable since  $F_s$  and  $K_T$  are not known precisely. Instead,  $\beta$  was assumed to be zero (corresponding to a case where the power law term in the Iwan model is much larger than the macro-slip term) and then varied to see whether the results were sensitive to that assumption.

These concepts were used to estimate starting values for the parameters and then they were varied until the frequency and damping versus amplitude relationships of the modal Iwan model (found by integrating the SDOF equation of motion with the Newmark algorithm [89]) correlated well with what was measured experimentally. Table 13 shows the final parameters that were used in order to model the first and second elastic modes.

Table 28: Modal Iwan parameters identified for the Brake-Reuss Beam, Substructure C

Parameter	1 <sup>st</sup> Bending	2 <sup>nd</sup> Bending	
1 at affected	Mode	Mode	
$F_{s}$	137.72	152.14	
$K_{T}$	484,680	2,668,200	
β	0.26159	0.29688	
χ	-0.049947	-0.41637	

The accuracy of the mode defined by these parameters was initially checked by simulating a SDOF modal response to modal force for each mode and comparing the results to the corresponding measured modal filtered signal. These responses can be compared via their amplitude dependent stiffness and damping for each mode. These curves were extracted from the simulated response using the Hilbert transform as described previously. Figures 86 and 87 show the comparison between the measured and simulated response of each mode. The model obtains good correlation throughout the amplitude range of

interest. A similar process was followed for the second bending mode leading to another nonlinear modal model. All of these figures show an excellent agreement between the model and measured data.

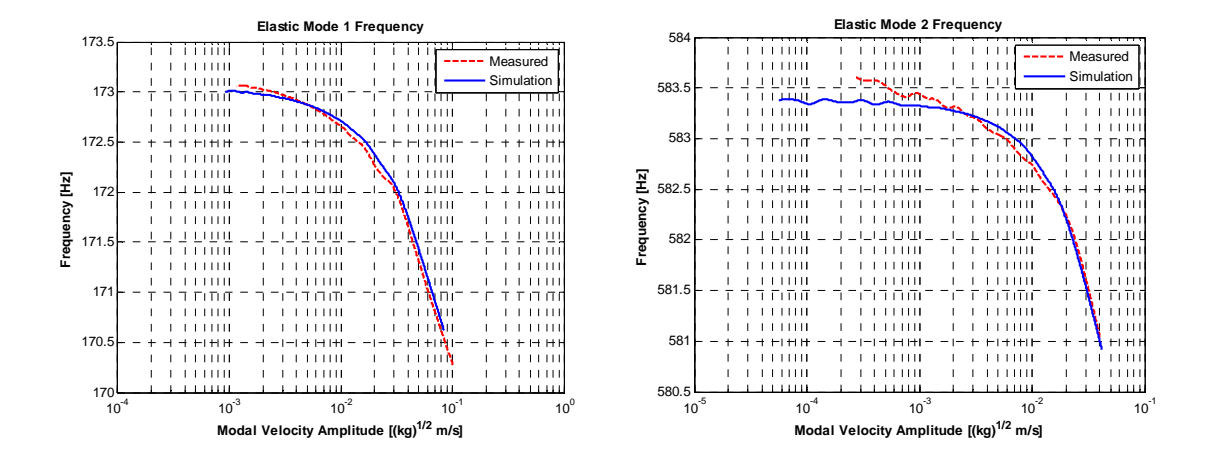


Figure 86. Measured and simulated modal frequency for elastic modes 1 and 2 of Substructure C

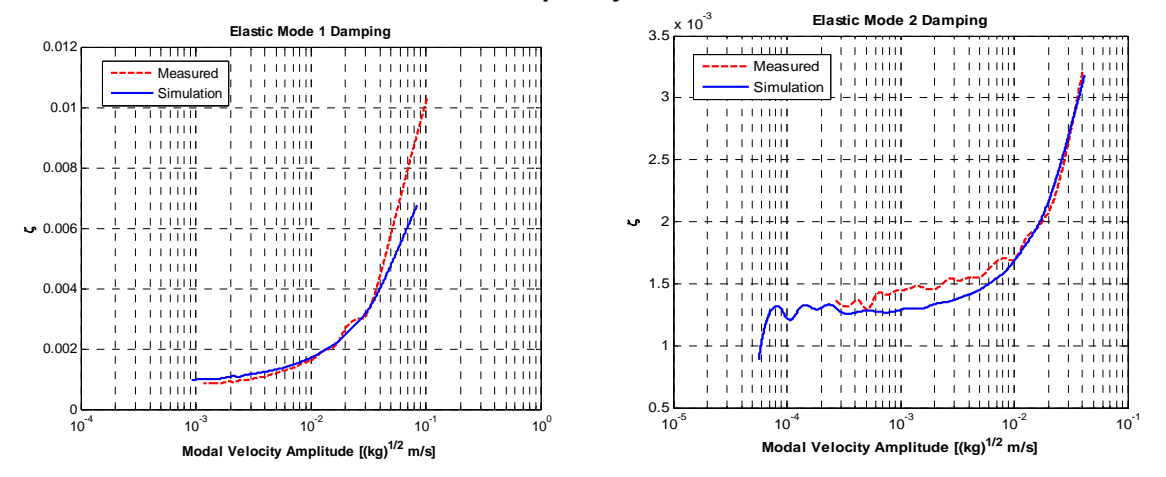


Figure 87. Measured and simulated modal damping for elastic modes 1 and 2 of Substructure C

Figure 88 shows the FFT of the modal acceleration for the simulated response. Enhanced views in Fig. 89 show how well the nonlinear prediction matches the true measurement, especially when compared to that of a linear model. The nonlinear modal model is even able to capture the distortion near the peak in the frequency response function, which is present in the first mode as visible in Fig. 89.

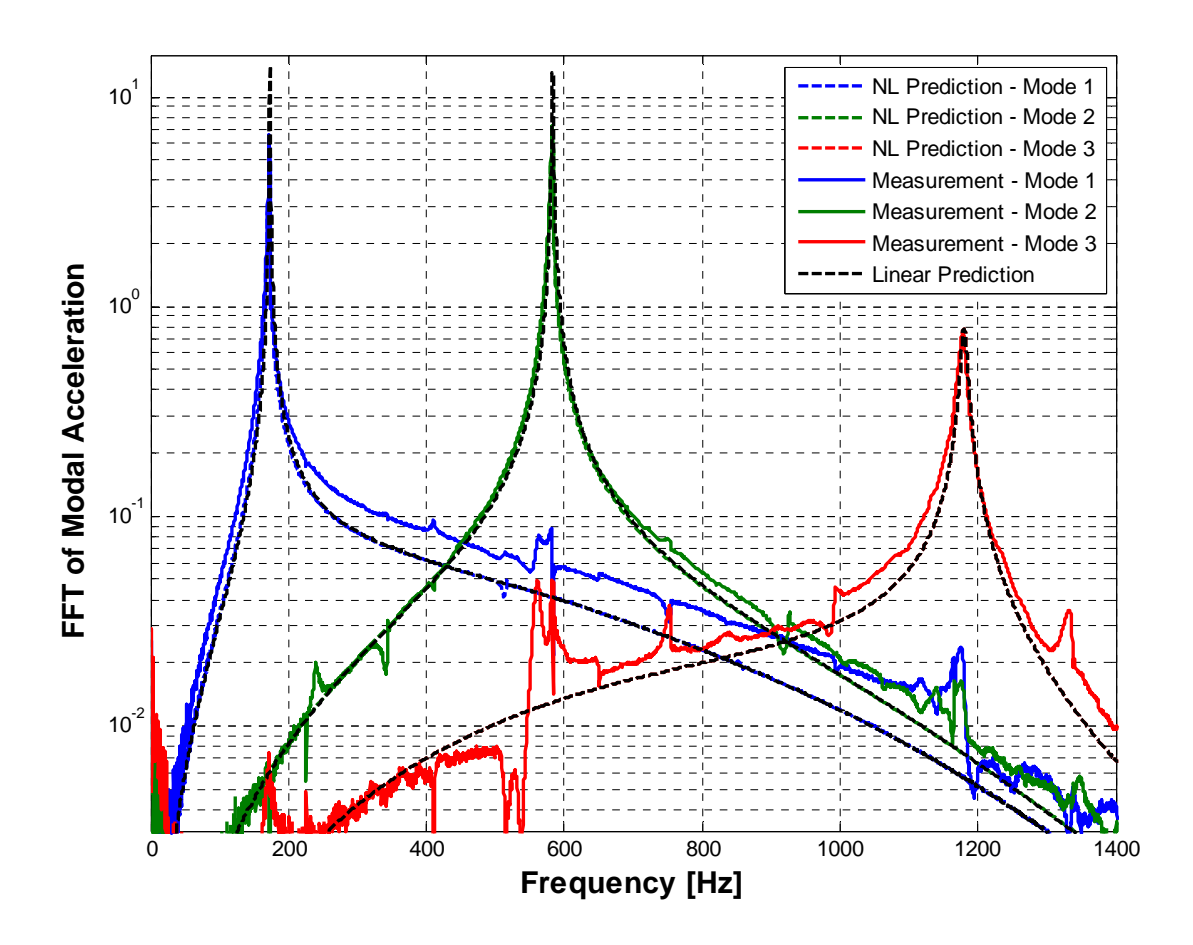


Figure 88. FFT of modal acceleration of Substructure C

These results show that, whether the response is observed in the time or frequency domains, the nonlinear modal model produces an excellent approximation to the measured response. In the next section this nonlinear modal model will be coupled as described in Eqn. (84) to predict the response of the system when the transmission simulator is replaced with a modified substructure

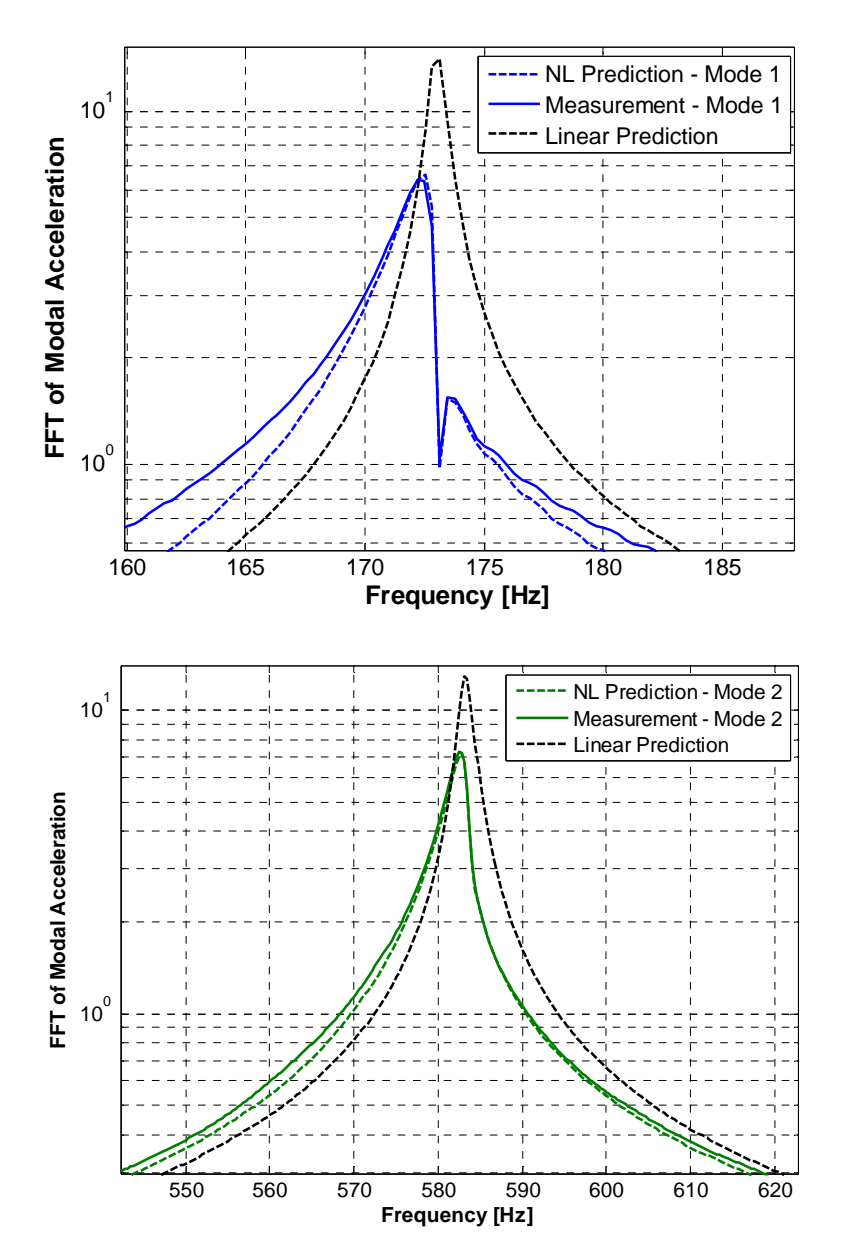


Figure 89. FFT of modal acceleration enhanced view of elastic modes 1 (top) and 2 (bottom) of Substructure C

# 5.4 Nonlinear Substructuring Results

To begin the experimental-analytical substructuring process, a linear substructuring prediction was first completed. The nonlinear forces for each mode were replaced with linear springs corresponding to the completely stuck state, using the low-level stiffness of the system,  $K_0$  (see Eqn. (91)). For this example, six modes each were retained for Substructures C and D, with only four modes in Substructure

A, as was the case in [94]. The predictions of the modal parameters of the first four elastic modes of the assembly are compared with those from the truth test in Table 29. This shows how accurately the linear modal parameters of the assembly are estimated using the transmission simulator method with this set of modes for each component.

Table 29: Experimental-Analytical Linear Substructuring Predictions

Mode #	Linear Truth Test Frequency [Hz]		% Error	Truth ζ	Substr. Prediction $\zeta$	% Error	MAC
1	150.80	153.13	1.54%	0.00194	0.00186	-3.98%	0.999
2	513.69	515.69	0.39%	0.00174	0.00141	-18.84%	0.991
3	994.68	983.23	-1.15%	0.00321	0.00339	5.72%	0.980
4	1507.53	1515.92	0.56%	0.00458	0.00668	45.99%	0.962

In Table 29, the frequency errors are less than 2%. However, one should recall that in the nonlinear testing described in Sec. 5.3 the natural frequencies were only seen to change by 1-3%. Hence, the changes in the natural frequencies due to nonlinearity are not likely to be significant relative to the frequency error that is obtained due to modal truncation. On the other hand, it may be possible to correctly capture the change in each mode frequency with amplitude. The substructuring process has even larger errors when predicting the linear damping ratios of each mode. However, as observed in the screening process, the damping may change by a factor of 2-10 with amplitude and those changes could certainly be significant relative to the error in the prediction of the linear damping.

The MAC values show that the modes correlate between the truth test and the substructured predictions very well. Figure 90 shows the modes shapes of the first two elastic modes. For each of these modes, the prediction matches the experiment very well. Predicted modes are shown using the stuck case,  $K_0$ , for the linear substructure and the undeformed structure is shown as reference.

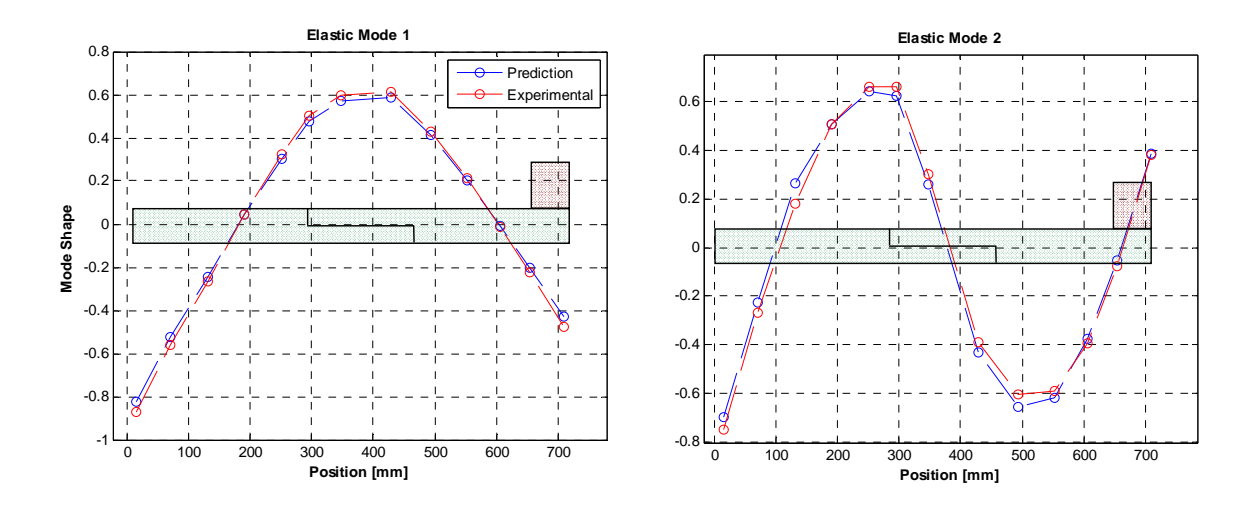


Figure 90. Predicted mode shapes of the modified assembly, Substructure E

The nonlinear forces were then added to the assembled equations of motion and a Newmark integrator was used to predict the nonlinear response to 500 Newton impulsive loading at the end of the beam. Figure 91 compares the response predicted by substructuring with the measured response of the truth model in the frequency domain. The "Linear Measured" curve is a driving point FRF measurement for a low level test case and aims to capture a linear response. The curve shown in red and labeled "500N Measurement" is the measured drive point frequency response due to a high amplitude impulsive loading. The difference between these two measured curves (green and red) gives an indication of the importance of the nonlinearity in the response of the assembled system. The "Linear Substructuring Prediction", in black, is a FRF constructed using the linear modal parameters (see Table 29) found by linear substructuring. Therefore, the shift between the green and black curves illustrates the error in the linear substructuring predictions.

When the nonlinear forces are included in the substructuring prediction, by using a Newmark integrator to simulate Eqn. (84), the impact of the nonlinear modal models becomes clear. Using the linear mode shape matrix, the prediction of the modal coordinate response can be transformed into the physical domain and compared to the measured response. This comparison is completed first by observing the driving point frequency response function. The blue curve represents this nonlinear

substructuring prediction. It is interesting to note that the difference between the blue and the black curves, which represents the difference between a linear an nonlinear substructuring prediction, is very similar to the difference between the green and red curves, which represent the difference between the measured linear and nonlinear response. The frequency of the nonlinear resonant peak is still off by about 1.5%, which is close to the linear frequency error from Table 29, but the shape of the peak and damping levels are much closer to the measured result. This is remarkable as the nonlinear models were fit at a substructure level, yet the predictions at the assembled level capture the measured nonlinearity accurately. Similar results were observed for the second bending mode.

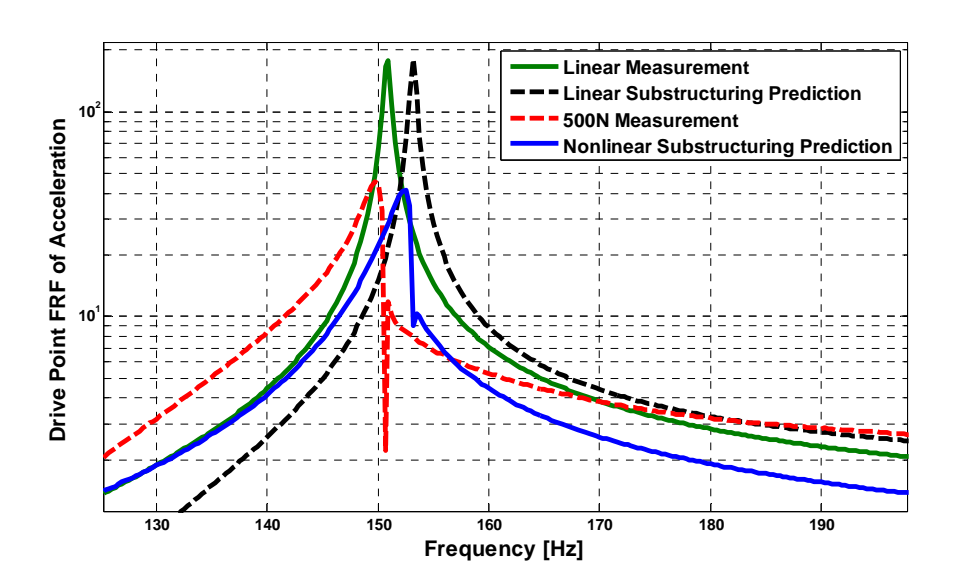


Figure 91. Frequency Domain Comparison: 1st Bending Mode

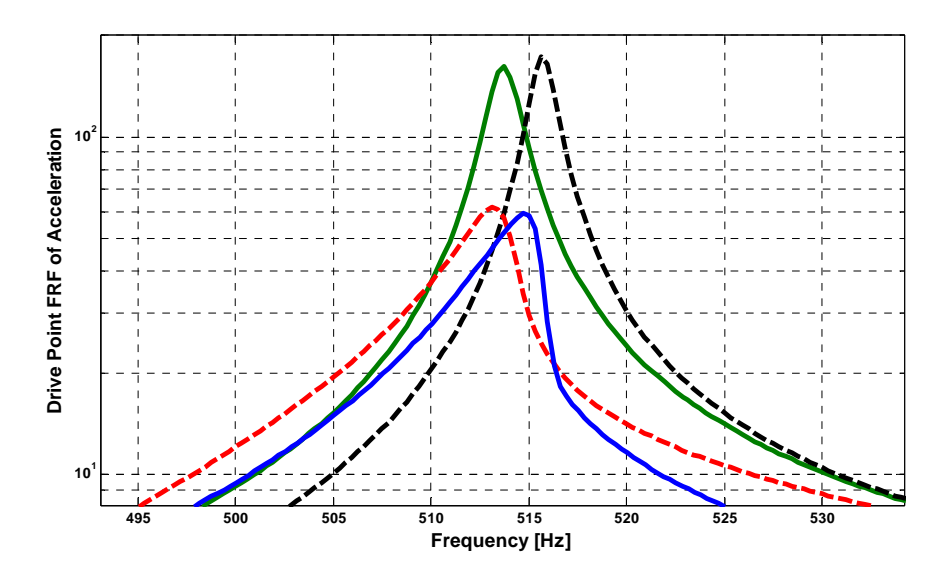


Figure 92. Frequency Domain Comparison: 2nd Bending Mode

Figure 93 shows the drive point acceleration obtained using linear substructuring, the nonlinear substructuring prediction and the measured result. As was the case with the individual modes, all three models correlate well very early in time. However, the linear model contains insufficient damping and becomes inaccurate later in time. The nonlinear prediction has the correct amplitude over the entire time window. The RMS value for the experimental measurement is 35.28 m/s², while the nonlinear prediction has a RMS value of 34.33 m/s². In contrast, the linear modal vastly overpredicts this physical response with an RMS value of 52.56 m/s². One would significantly under predict the fatigue life of the structure if the linear model were used.

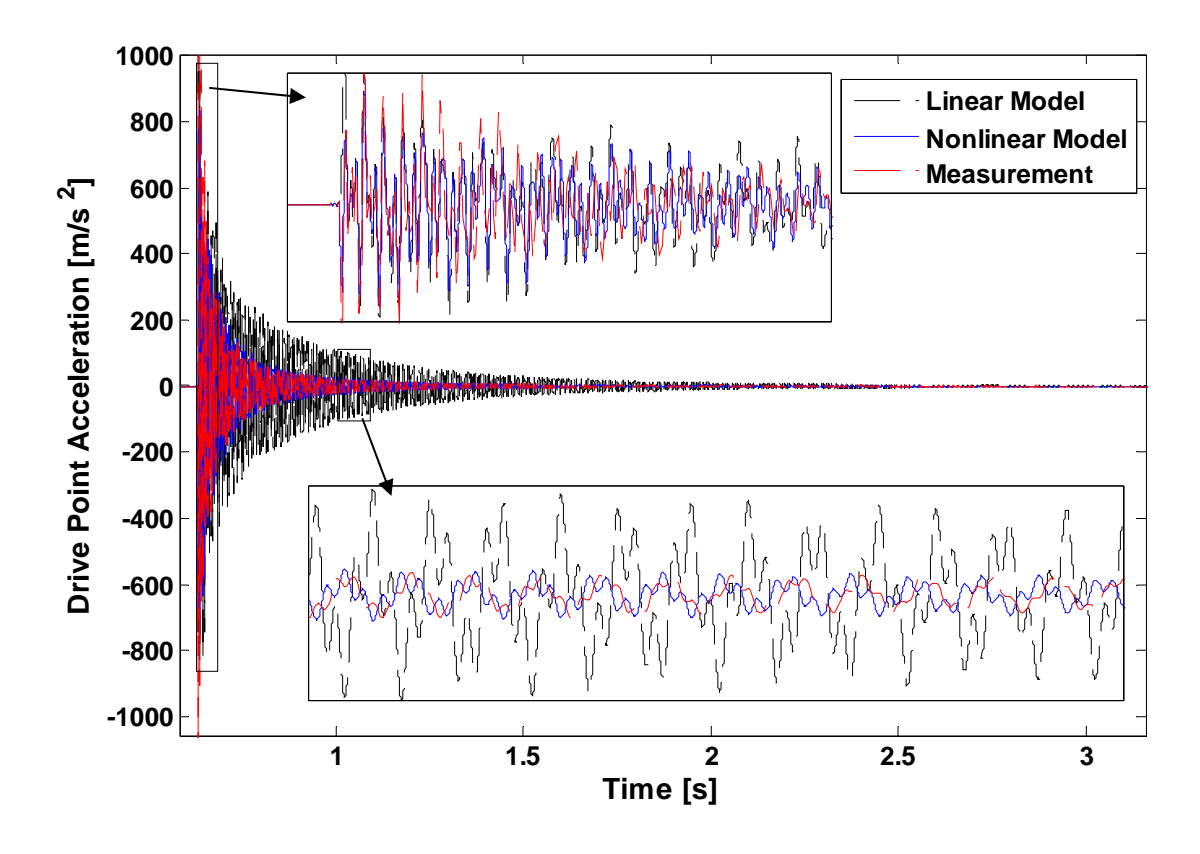


Figure 93. Drive point acceleration for 500N impulsive load with linear model

The predictions are also compared on a mode-by-mode basis. In Fig. 94, the time history of the modal acceleration for the first mode of the modified Brake-Reuss Beam, Substructure E, is shown. Early in time, the linear model, the nonlinear prediction, and the measured data match fairly well. However, the linear model neglects the nonlinear contribution to the modal damping and thus it overestimates the amplitude quickly, by a factor of 5 late in the time history. In contrast, the nonlinear prediction tracks the measured, modally filtered result very well.

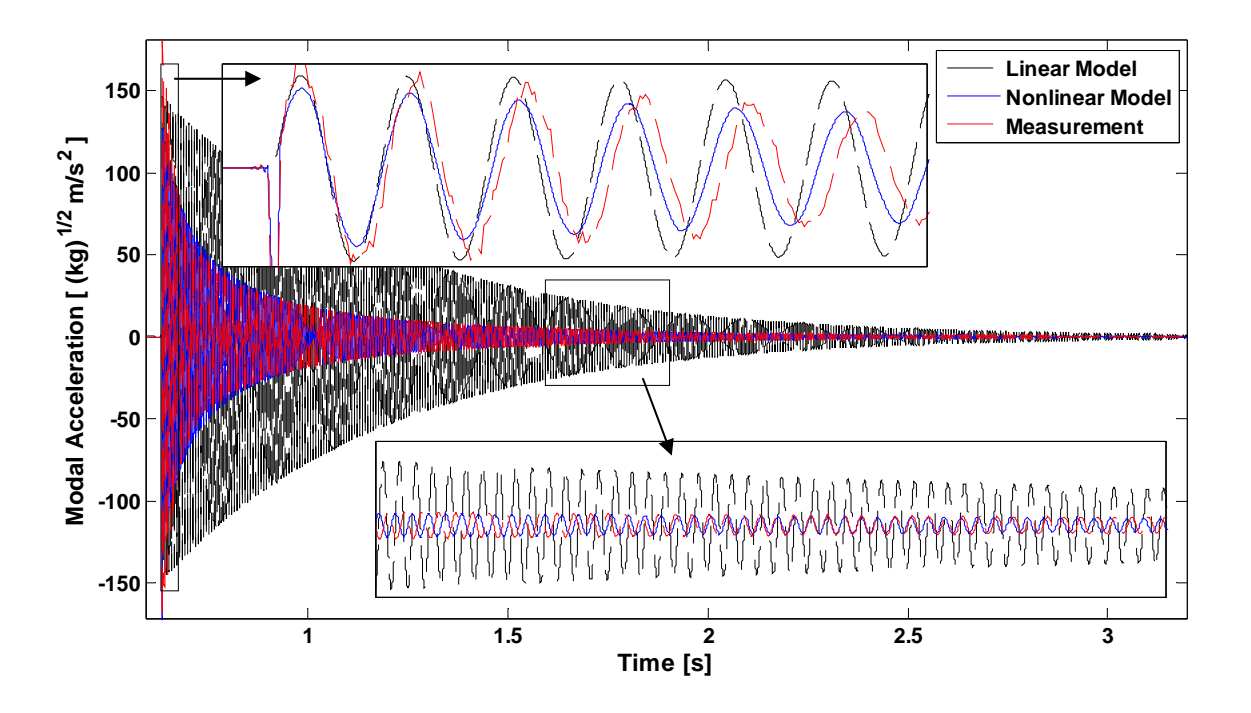


Figure 94. 1st Elastic mode: Modal acceleration time history

Figure 95 shows the amplitude dependent properties of the first and second bending modes of the assembly, Substructure E, obtained using the Hilbert transform. In the damping curve for the first bending mode, at an amplitude of about (0.040 kg<sup>1/2</sup> m/s), the response from the substructuring prediction starts to diverge and under predict the damping when compared to the measured data. This could be due to an error in how the modal Iwan models were fit for Substructure C, but similar effects at high amplitudes have been observed in works by Lacayo et al. [54] so it was suspected this could indicate that modal coupling becomes important at these higher load levels.

Recall from Section 5.3, that these models were fit in a least squares sense over several different impulsive loading cases. These loading cases in general were much smaller than the 500 Newtons impulsive force being applied in this case. Higher force level hits on a substructure may have led to a model that appropriately fits the damping over a larger range of forcing amplitudes. Another possibility is that the system is reaching the onset of macro-slip. Previous studies have shown that nonlinear modal models are accurate only until the onset of macro-slip [54]. If one of the joints is in macro-slip then the

basic assumptions made in the derivation for this method are violated and one would expect erroneous results. Note that for mode 2 the damping seems to match the measured value in the micro-slip region and that the offset in the low level damping region is likely due to inaccuracy in the prediction of the linear damping ratio for this mode.

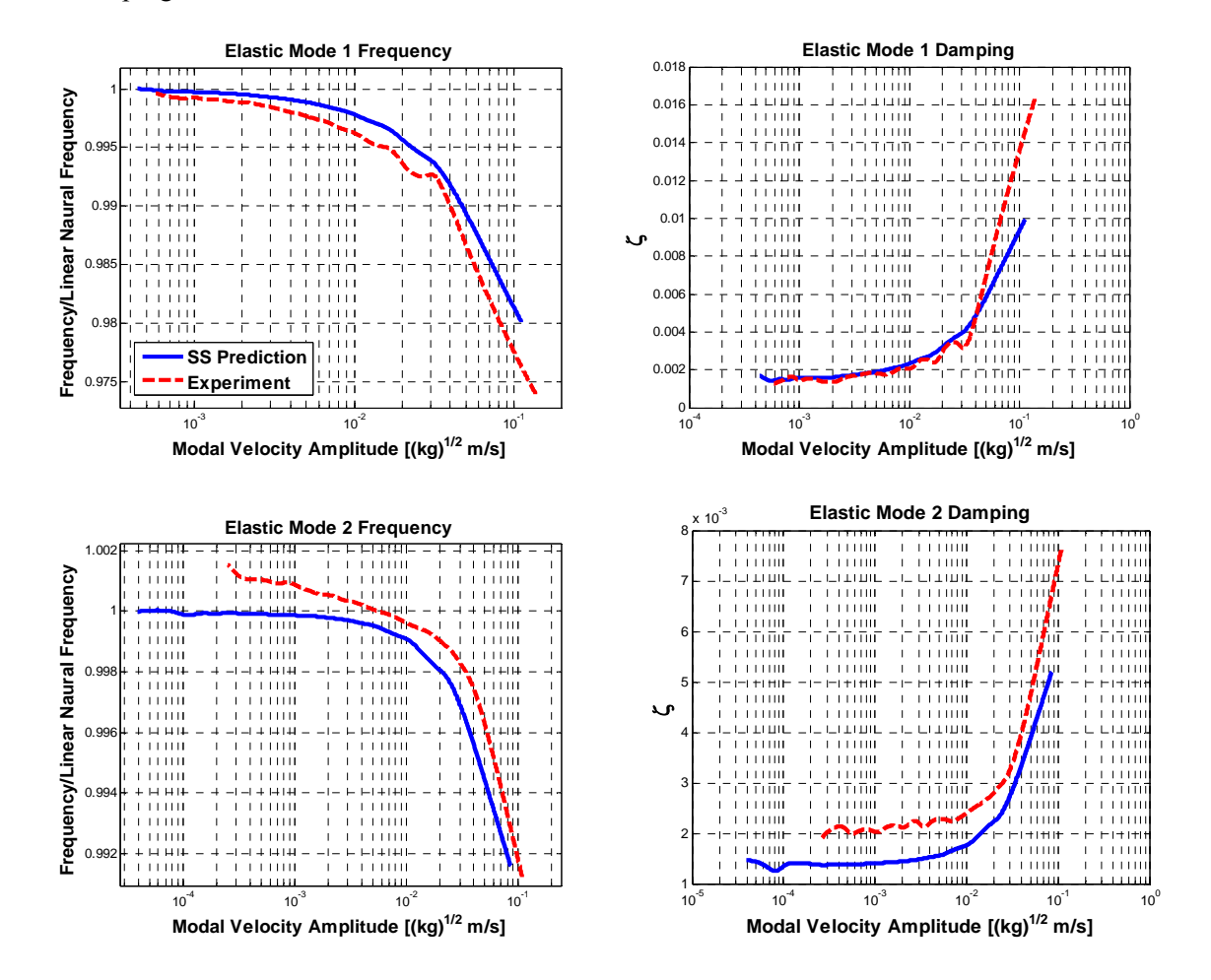


Figure 95. 1st and 2nd Elastic Mode: Amplitude Dependent Stiffness and Damping

#### 5.5 Remarks

This work utilized uncoupled nonlinear modal models to represent a substructure in a dynamic substructuring problem. This was first discussed in [94] using simulated experiments. In this work, true experimental measurement from the Brake-Reuss Beam were used to generate a nonlinear model for one of the subcomponents. These individual components, were then coupled using the Transmission

Simulator method in order to generate a nonlinear model for the assembly. Even though the individual subcomponents are modeled by a set uncoupled, nonlinear single-degree-of-freedom modes, the substructuring process spreads the nonlinearity from the subcomponent modes into the appropriate modes of the assembled system.

The experimental-analytical substructuring predictions obtained here were very promising. Linear frequency errors were low (less than 2%) but damping errors were larger (less than 20%). However, the nonlinearity due to the bolted joint caused the damping to change by factors of 2-10; therefore, even though there were relatively large errors in the linear damping ratio predicted by substructuring the effects of the damping nonlinearity were still captured with reasonable accuracy. The nonlinear substructuring results were quite favorable and showed that the substructuring process is quite effective for this system, whose nonlinearity is dominated by micro-slip. The accuracy of the substructured prediction appears to be tied to the accuracy of the modal model used to describe the nonlinear behavior of the structure subcomponents.

In this work the modal model identified for Substructure C predicted the response of the modified structure, Substructure E, over a wide range of amplitude, although at the largest amplitudes some discrepancies were seen, which have the same character as the discrepancies due to modal coupling that were observed in [53, 54]. Future works should seek to develop a means of modeling this modal coupling, but considering its simplicity, the procedure presented here provides a significant improvement over linear substructuring with only a modest increase in complexity.

## **6** Conclusions

Traditionally, dynamic substructuring techniques connect the linear dynamics of subcomponents by enforcing compatibility at a selection of interface degrees of freedom. This dissertation extends this idea using nonlinear subcomponent models and has contributed to this research field in several ways. First, a novel technique to identify and quantify the modal nonlinear dynamics of a structure was developed. Second, simulated substructuring predictions were obtained on two test systems to verify how accurately the nonlinear subcomponent models could be used to describe the nonlinear dynamics of an assembly truth model. Finally, these methods were applied to experimental data from physical hardware and this technique was validated on an experimental structure, the Brake-Reuss Beam [76]. These contributions are discussed in further detail below.

## **6.1** Nonlinear Modal Modeling Techniques

This dissertation provides a methodology for developing a model of the nonlinear dynamics for weakly nonlinear structures. Experimental evidence has shown that bolted assemblies often contain weak nonlinearities. Recent works have shown that bolted interfaces can cause the energy dissipation in a system to increase by a factor of two or greater [3, 82, 96] while the effective natural frequency tends to change relatively little. As discussed in [106], if the joint forces and their harmonics are distinct from each modal frequency, the modes of the structure tend to remain uncoupled so that the structure can be modeled accurately using a collection of uncoupled, weakly-nonlinear oscillators [52, 97].

In Chapter 3, nonlinear modal models were developed and validated using physical hardware measurements. Two physical systems were tested to validate this modal modeling approach. First, an industrial system of bolted catalytic converters was studied and modal testing was performed. Second, a system consisting of a cylinder attached to a plate via a continuous interface, known as the Cylinder-Plate-Beam, was investigated using similar techniques.

The systems were tested at various forcing amplitudes to screen the hardware for nonlinear behavior. Screening was completed by comparing the frequency response function at different amplitudes in conjunction with the Zeroed Early-Time Fast Fourier Transform [56]. After selecting a set of nonlinear target modes, a spatial filter was applied to the acceleration measurements in order to provide a single degree of freedom (SDOF) response for each harmonic in the measurement. The Hilbert transform [55] was applied to each SDOF response in order to obtain amplitude dependent frequency and damping relationships for each mode of the tested structure. A variation of Segalman's 4-parameter Iwan model [48, 52] was fit to each of the identified nonlinear modes in both systems. The 4-parameter modal Iwan model was able to accurately represent the nonlinear behavior exhibited by weakly nonlinear modes measured from both test structures. Both structures showed high levels of accuracy with an appropriate 4-parameter Iwan model.

Simplified nonlinear modal model forms were obtained for the Cylinder-Plate-Beam system. Specifically, cubic polynomial stiffness and damping terms were obtained using Restoring Force Surface [61] techniques on experimental measurements. The accuracy of these models was comparable to that of the 4-parameter Iwan model. While the parameters for this simplified model are easier to obtain, they do not contain any physical significance and are used as mathematical factors to represent the nonlinear dynamics. These examples illustrate that weakly nonlinear structures can be measured accurately enough to obtain repeatable nonlinear measurements on a mode-by-mode basis and that the modal models were shown to be an accurate representation of the measured motion of the system.

# 6.2 Simulated Experimental Nonlinear Modal Substructuring

This dissertation uses the Transmission Simulator method [26, 38, 95] extensively to perform experimental substructuring predictions. The accuracy and limitations of this method on a linear system were investigated in Chapter 2, while in Chapter 4 a nonlinear modal modeling framework was used to extend these methods to include nonlinear subcomponent models derived from simulated experiments.

These subcomponent models were assembled using a primal formulation [13] to enforce compatibility at the interface between components.

This technique is first demonstrated on a spring-mass system which consists of two subcomponents. The first is a three degree of freedom system with physical Iwan joints used to model the nonlinear dynamics of the subcomponent, while the second subcomponent is a linear two degree of freedom system. The nonlinear modal modeling techniques described in Chapter 3 were applied to the nonlinear subcomponent in order to develop a nonlinear modal model for each harmonic of the system. This nonlinear subcomponent model was coupled with a linear model of the second subcomponent and compared to a truth simulation. The quality of the nonlinear prediction was remarkably accurate, especially when compared to that of a standard linear model.

With the success of the spring-mass system, another simulated experimental model was investigated. A finite element model of a simple bolted beam structure, the Brake-Reuss Beam (BRB) [76], was developed in order to test these methods on a more realistic structure. Nonlinear modal models were developed from simulated results of the BRB model. These nonlinear modal models were used to obtain highly accurate substructuring predictions for a modified structure. Both of these examples were completed on numerical models of the system and do not account for experimental error or noise that would be present in a physical experiment. However, the simulations do prove that substructuring is a useful prediction method as long as the structure remains in the micro-slip regime. In the spring-mass example, every mode of each subcomponent was known. In contrast, the Brake-Reuss Beam example showed that this methodology is applicable even when severe modal truncation is present, such as in physical experiments.

#### 6.3 Experimental-Analytical Nonlinear Modal Substructuring

The accuracy of the simulated experimental substructuring examples led to the extension of this technique using physical hardware. In Chapter 5, the nonlinear modal modeling framework was used to create experimentally derived modal Iwan models for each nonlinear mode in the standard Brake-Reuss

Beam. Testing was completed in the micro-slip regime of joint slipping and verified that each subcomponent was weakly nonlinear in nature. The Transmission Simulator method [26] was used to predict the nonlinear response of a modified Brake-Reuss Beam structure. These predictions are compared to a truth test performed on the modified system. This is the first application of the proposed techniques to experimental hardware and the predicted results were extremely accurate. The nonlinear prediction provided nearly identical root mean squared acceleration, while a standard linear model greatly over predicted the response. This confirmed, that by using the Transmission Simulator method, the nonlinearities of a weakly nonlinear system can be modeled by uncoupled nonlinear modes at the subcomponent level and then used to compute nonlinear response predictions of an assembled structure.

## **7** Future Work

The nonlinear modal modeling framework and substructuring prediction techniques presented in this work may lend themselves to additional investigation. As mentioned extensively in Chapter 3, the proposed nonlinear modal modeling approach only applies to assumed weakly nonlinear structures. This assumption requires the modes of the structure to remain uncoupled regardless of amplitude. Lacayo et al. [53, 54] have begun to research this topic using numerical models of bolted beam structures. Future works should seek to develop a means of modeling this modal coupling as continued research in this topic would help to understand the limitations of this assumption. In particular, understanding the limit of this weakly nonlinear assumption in tested structures can be investigated further.

In order to explore these limitations experimentally, a method to obtain quality measurements at significantly higher modal amplitudes is required. Mayes et al. [109] have begun work using a harmonic excitation that accounts for the nonlinear change in frequency. This harmonic excitation allows one to obtain information about the modal amplitude of each harmonic at much higher levels. Further work developing techniques to excite a weakly nonlinear system at high modal amplitudes would benefit this research in multiple ways. This would allow the limitations of the weakly nonlinear assumption to be bounded, while also providing higher amplitude data to increase the applicable range of the developed nonlinear modal models.

Another area of additional research involves the modal modeling techniques presented in Chapter 3. On the Cylinder-Plate-Beam system, the nonlinear dynamics of the structure were represented by both a 4-parameter modal Iwan model and a cubic polynomial stiffness and damping model. These two techniques could be connected more thoroughly. A new Restoring Force Surface based model could be developed preserving the power-law dissipation relationship established by the Iwan model. Additional studies should be completed to determine the most accurate type of modal model to be used for each structure. The preferred model form could depend on factors such as, structural geometry, mode shape,

and nonlinear behavior type. Ultimately, additional understanding of these nonlinear modal models and the assumptions they require is imperative to further developing a predictive joint model using these modal modeling techniques.

# Appendix A: Update of the Brake-Reuss Beam Finite Element Model

This appendix shows how the Brake-Reuss Beam finite element model was updated to match experimental measurements. The intent was to update the FEM model so that is it reasonably accurate when compared to the real physical system, so that it could be used with confidence to simulate substructuring. To do so, testing was completed on a Brake-Reuss Beam system with the instrumentation shown in Fig. 96.

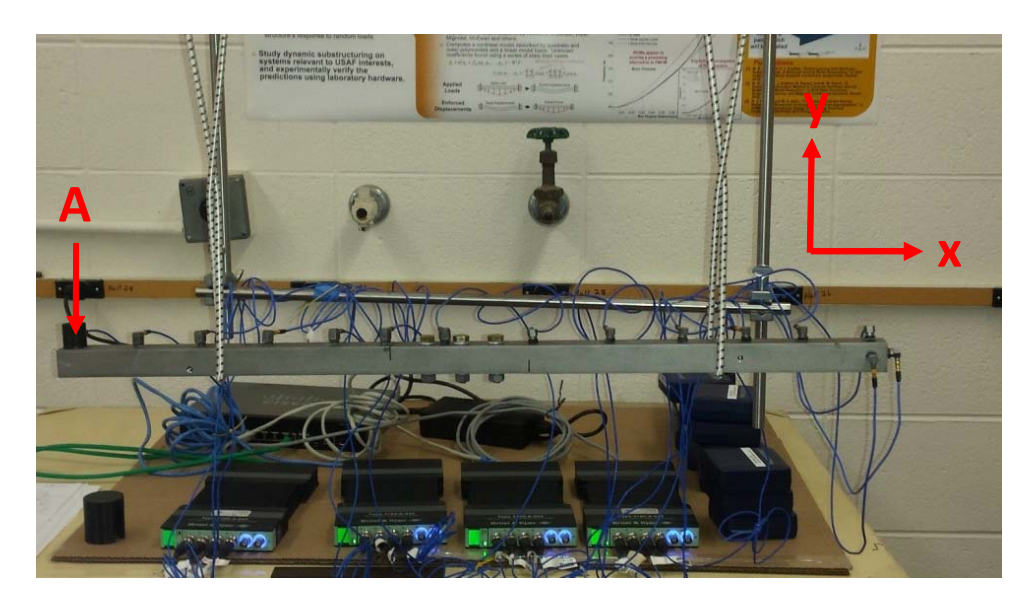


Figure 96. Brake-Reuss Beam experimental set-up

A linear test was completed and comparison of the test and model linear natural frequencies is shown in Table 30. These linear frequencies were used to update the linear springs and modulus of elasticity for the FEM. The model matches very well with frequency errors under 2% and MAC values above 0.98 for all the modes of interest.

Table 30: System C Experimental Parameters

Elastic Modal Index	Experimental Natural Frequency [Hz]	FEM Natural Frequency [Hz]	Frequency % Error	MAC
1	172.70	172.09	-0.35%	0.9994
2	583.26	578.53	-0.81%	0.9975
3	1180.10	1195.20	1.28%	0.9962
4	1645.40	1616.10	-1.78%	0.9897

Figure 97 shows a comparison for the first two elastic modes between the FEM model and the experimentally extracted mode shapes. The mode shapes are similar as expected based on the MAC values present in Table 30.

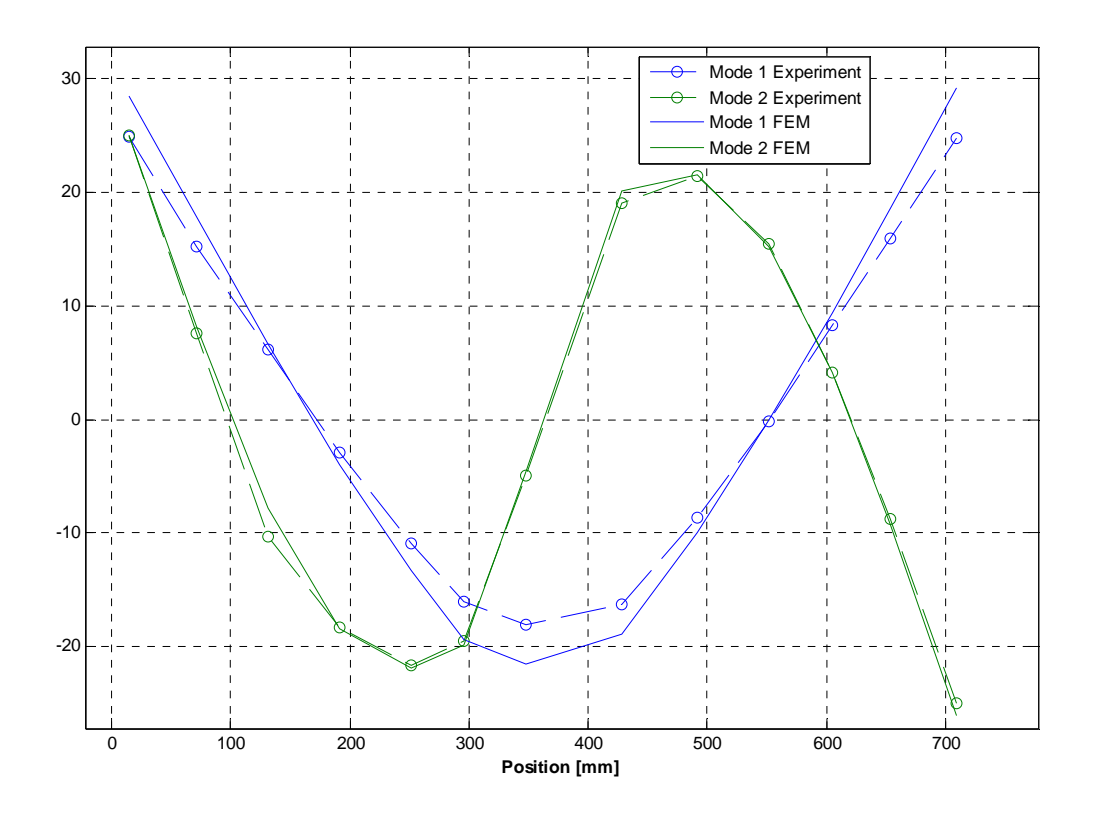


Figure 97. FEM and Experimental Mode Shapes

Testing at higher forcing levels allowed the authors to extract amplitude dependent measurements of frequency and damping. These were obtained using the procedure outlined in [3]. In the FEM model, discrete Iwan elements were used to connect the two half beam structures. Using the quasi-static algorithm from [53] and [105] these Iwan elements were updated to ensure that the nonlinear damping and frequency for the FEM truth model were similar to those observed from the laboratory measurements. Figure 98 shows the results of this quasi-static simulation for the first elastic mode of substructure C compared with experimental results of the system. The system was tested at several drive locations and several forcing levels similar to the testing from [3]. Similar comparisons were made for the second

elastic mode to ensure the modal Iwan parameters selected for the three joints in Substructure C were feasible compared to the real experimental hardware.

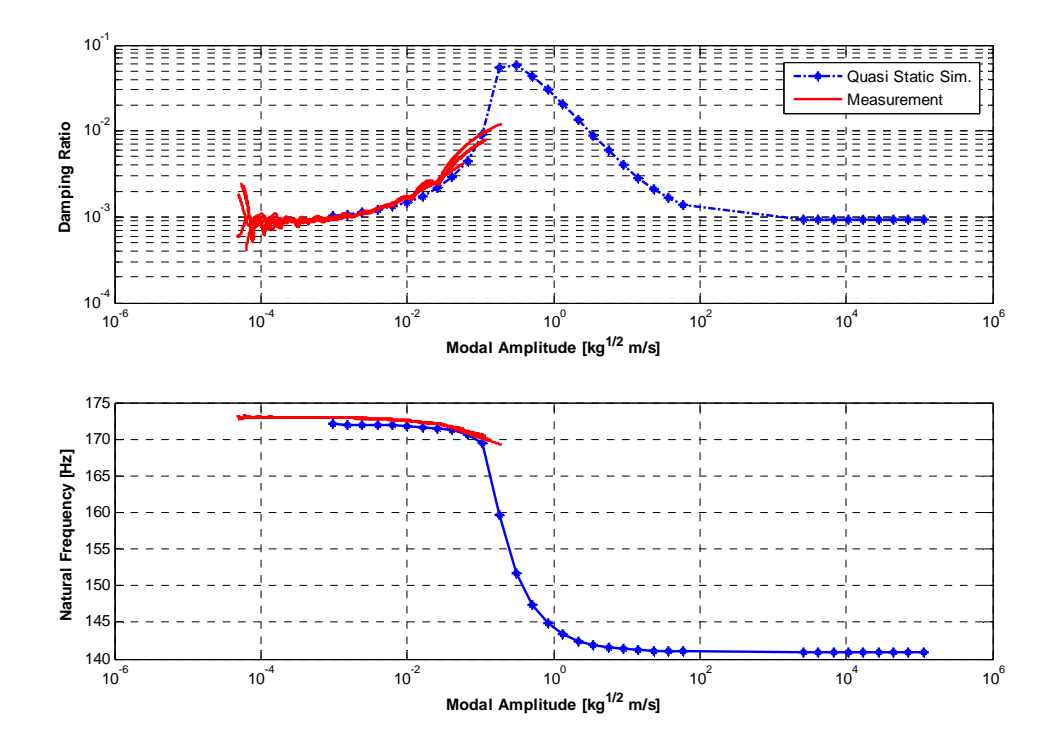


Figure 98. Quasi-Static results for amplitude dependent damping and frequency

# **Appendix B: Publications of PhD work**

# **Journal Papers**

- Roettgen, D. R. and Allen, M. S., "Nonlinear characterization of a bolted, industrial structure using a modal framework," Mechanical Systems and Signal Processing, Vol. 84, Part B, Pages 152-170. dx.doi.org/10.1016/j.ymssp.2015.11.010 [3]
- Allen, M. S., Roettgen, D. R., Kammer, D. C. and Mayes, R. L. "Modal Substructuring using modal
  Iwan models Part I: Simulated Experiments," Mechanical Systems and Signal Processing,
  (Submitted) [94]
- Allen, M. S., Roettgen, D. R., Kammer, D. C., and Mayes, R. L. "Modal Substructuring using modal
  Iwan models Part II: Experimental Demonstration," Mechanical Systems and Signal Processing, (In
  Preparation) [106]

#### **Conference Papers**

- Roettgen, D. R., Allen, M. S., Kammer, D. C., and Mayes, R. L. "Substructruing of a nonlinear beam using a modal Iwan framework. Part II: Nonlinear Modal Substructuring," 35th International Modal Analysis Conference, January 30-February 2, 2017.
- Roettgen, D. R., Allen, M. S., Kammer, D. C., and Mayes, R. L. "Substructruing of a nonlinear beam using a modal Iwan framework. Part I: Nonlinear Modal Model Identification," 35th
   International Modal Analysis Conference, January 30-February 2, 2017.
- Cooper, S. B., et. al. "Effect of Far-Field Structure on Joint Properties", 35th International Modal Analysis Conference, January 30-February 2, 2017.
- Mayes, R. L., Pacini, B. R., and Roettgen, D. R., "A Modal Model to Simulate Typical Structural Dynamic Nonlinearity," 34th International Modal Analysis Conference, January 25-28, 2016
- Allen, M. S., Roettgen, D. R., Kammer, D. C., and Mayes, R. L., "Experimental Modal Substructuring with Nonlinear Modal Iwan Models to Capture Nonlinear Subcomponent Damping"
   34th International Modal Analysis Conference, January 25-28, 2016.

- Roettgen, D. R., Seeger, B., Tai, W.C. et al, "A Comparison of Reduced Order Modeling Techniques
   Used in Dynamic Substructuring," 34th International Modal Analysis Conference, January 25-28,
   2016.
- Roettgen, D. R. and Allen, M. S., "Experimental Dynamics substructured of a Catalytic Converter System using the Transmission Simulator Method," 33<sup>rd</sup> International Modal Analysis Conference, February 2-5, 2015.
- Roettgen, D. R. and Mayes, R. L., "Ampair 600 Wind Turbine 3-Bladed Assembly Substructuring using the Transmission Simulator Method," 33<sup>rd</sup> International Modal Analysis Conference, February 2-5, 2015.
- Allen, M. S., Blecke, J., and Roettgen, D. R., " A Wiki for Sharing Substructuring Methods,
   Measurements and Information," 32nd International Modal Analysis Conference, February 3-6, 2014.

## References

- [1] E. E. Ungar, "The Status of Engineering Knowledge Concerning the Damping of Built-up Structures," *Journal of Sound and Vibration*, vol. 26, pp. 141-154, 1973.
- [2] C. F. Beards, "Damping in Structureal Joints," *The Shock and Vibration Digest*, vol. 24, pp. 3-7, 1992.
- [3] D. R. Roettgen and M. S. Allen, "Nonlinear characterization of a bolted, industrial structure using a modal framework," *Mechanical Systems and Signal Processing*, January 19th 2016.
- [4] R. L. Mayes, *et al.*, "A Modal Model to Simulate Typical Structural Dynamic Nonlinearity," presented at the International Modal Analysis Conference XXXIV, Orlando, FL, 2016.
- [5] M. Imregun, *et al.*, "Structural Modification and Coupling Dynamic Analysis Using Measured FRF Data," presented at the 5th International Modal Analysis Conference (IMAC V), London, England, 1987.
- [6] W. Liu and D. J. Ewins, "Substructure synthesis via elastic media," *Journal of Sound and Vibration*, vol. 257, pp. 361-79, 2002.
- [7] A. P. V. Urgueira, "Dynamic Analysis of Coupled Structures Using Experimental Data," PhD, Imperial College of Science, Technology and Medicine, University of London, London, 1989.
- [8] D. R. Martinez, *et al.*, "Combined Experimental and Analytical Modeling of Shell/Payload Structures," presented at the The Joint ASCE/ASME Mechanics Conference, Albuquerque, NM, 1985.
- [9] T. G. Carne and C. R. Dohrmann, "Improving Experimental Frequency Response Function Matrices for Admittance Modeling," presented at the 24th International Modal Analysis Conference (IMAC XXIV), St. Louis, Missouri, 2006.
- [10] R. H. MacNeal, "A hybrid method of component mode synthesis," *Computers & Structures*, vol. 1, pp. 581-601, 1971.
- [11] D. R. Martinez, *et al.*, "Combined Experimental/Analytical Modeling Using Component Mode Synthesis," presented at the AIAA/ASME/ASCE/AHS Structures, Structural Dynamics & Materials Conference, Palm Springs, CA, USA, 1984.
- [12] J. H. Ginsberg, *Mechanical and Structural Vibrations*, First ed. New York: John Wiley and Sons, 2001.
- [13] D. de Klerk, *et al.*, "General framework for dynamic substructuring: History, review, and classification of techniques," *AIAA Journal*, vol. 46, pp. 1169-1181, 2008.
- [14] W. Hurty, "Dynamic Analysis of Structural Systems Using Component Modes," *AIAA Journal*, vol. 3, pp. 678-685, 1965.
- [15] W. Hurty, "Vibrations of Structural Systems by Component Mode Synthesis," *Journal of Engineering Mechanics/American Society of Civil Engineers*, vol. 86, pp. 51-69, 1960.
- [16] R. R. J. Craig and M. C. C. Bampton, "Coupling of Substructures Using Component Mode Synthesis," *AIAA Journal*, vol. 6, pp. 1313-1319, 1968.
- [17] R. Guyan, "Reudction of Stiffness and Mass Matrices," *AIAA Journal*, vol. 3, p. 380, 1965.
- [18] R. R. Craig Jr and C. J. Chang, "On the use of attachment modes in substructure coupling for dynamics analysis," in *18th Structures, Structural Dynamics and Material Conferen*, San Diego, 1977, pp. 89-99.

- [19] R. M. Hintz, "Analytical Methods in Component Modal Synthesis," *AIAA Journal*, vol. 13, pp. 1007-1016, 1975.
- [20] R. R. Craig Jr and C. J. Chang, "Free-interface methods of substructure coupling for dynamic analysis," *AIAA 14:11*, pp. 1633-1635, 1976.
- [21] D. J. Rixen, "A dual Craig-Bampton method for dynamic substructuring," *Journal of Computational and Applied Mathematics*, vol. 168, pp. 383-391, 2004.
- [22] R. R. J. Craig and C. J. Chang, "Substructure coupling for dynamic analysis and testing," *National Aeronautics and Space Administration*, 1968.
- [23] M. Castanier, *et al.*, "Characteristic Constraint Modes for Component Mode Synthesis," *AIAA Journal*, vol. 39, pp. 1182-1187, 2001.
- [24] S.-W. Hong, et al., "Next-generation parametric reduced-order models," *Mechanical Systems and Signal Processing*, vol. 37, pp. 403-421, 2013.
- [25] M. S. Allen, *et al.*, "Experimental Modal Substructuring to Estimate Fixed-Base Modes from Tests on a Flexible Fixture," *Journal of Sound and Vibration*, vol. 330, pp. 4413-4428, 2011.
- [26] M. S. Allen, *et al.*, "Experimental Modal Substructuring to Couple and Uncouple Substructures with Flexible Fixtures and Multi-point Connections," *Journal of Sound and Vibration*, vol. 329, pp. 4891–4906, 2010.
- [27] R. L. Mayes, *et al.*, "Eliminating Indefinite Mass Matrices with the Transmission Simulator Method of Substructuring," presented at the 30th International Modal Analysis Conference, Jacksonville, Florida, 2012.
- [28] R. L. Mayes and M. Arviso, "Design Studies for the Transmission Simulator Method of Experimental Dynamic Substructuring," presented at the International Seminar on Modal Analysis (ISMA2010), Lueven, Belgium, 2010.
- [29] R. R. Craig Jr and A. J. Kurdila, *Fundamentals of Structural Dynamics*. Hoboken, NJ: John Wiley & Sons, 2006.
- [30] S. Rubin, "Improved component-mode representation for structural dynamic analysis," *AIAA Journal*, vol. 13, pp. 995-1006, 1975.
- [31] S. Goldenberg and M. Shapiro, "A study of modal coupling procedures for the space shuttle," NASA1972.
- [32] H. Kanda, *et al.*, "Structural Dynamic Modification Using Mass Additive Technique," presented at the 4th International Modal Analysis Conference (IMAC IV), Los Angeles, California, 1986.
- [33] K. O. Chandler and M. L. Tinker, "General mass-additive method for component mode synthesis," presented at the AIAA Structures, Structural Dynamics & Materials Conference, Kissimmee, FL, USA, 1997.
- [34] W. D'Ambrogio and A. Fregolent, "Decoupling procedures in the general framework of Frequency Based Substructuring," presented at the 27th International Modal Analysis Conference (IMAC XXVII), Orlando, Florida, 2009.
- [35] C. F. Nelson and C. R. Dohrmann, "Using a modal test to estimate support properties," presented at the 20th International Modal Analysis Conference (IMAC-XX), Los Angeles, CA, United States, 2002.
- [36] P. Sjovall and T. Abrahamsson, "Substructure system identification from coupled system test data," *Mechanical Systems and Signal Processing*, vol. 22, pp. 15-33, 2008.

- [37] D. P. Rohe, "Validation of Experimental-Analytical Substructuring Using the Transmission Simulator Method," M.S., Engineering Physics, University of Wisconsin-Madison, Madison, Wisconsin, 2012.
- [38] M. S. Allen, *et al.*, "Metrics for Diagnosing Negative Mass and Stiffness when Uncoupling Experimental and Analytical Substructures," *Journal of Sound and Vibration*, vol. 331, pp. 5435–5448, 2012.
- [39] D. L. Segalman, *et al.*, "Handbook on Dynamics of Jointed Structures," Sandia National Labs2009.
- [40] L. Gaul and R. Nitsche, "The role of friction in mechanical joints," *Applied Mechanics Reviews*, vol. 52, pp. 93-106, 2001.
- [41] E. J. Berger, "Friction modeling for dynamic system simulation," *Applied Mechanics Reviews*, vol. 55, pp. 535-577, 2002.
- [42] J. L. Dohner, "A reduced order, one dimensional model of joint response," in *SAVIAC*, Washington DC, 2000.
- [43] D. O. Smallwood, *et al.*, "A three parameter constitutive model for a joint which exhibits a power law relationship between energy loss and relative displacement," in *Proceedings of the Shock and Vibration Symposium*, Destin, FL, 2001.
- [44] W. Ramberg and W. R. Osgood, "Description of stress-strain curve by three parameters," *NACA Technical Note No. 902*, 1943.
- [45] G. Masing, "Self-stretching and hardening for brass," in *International Congress of Applied Mechanics*, 1926, pp. 332-335.
- [46] W. D. Iwan, "A distributed-element model for hysteresis and its steady-state dynamic response," *Journal of Applied Mechanics*, vol. 33, p. 893, 1966.
- [47] D. J. Segalman, "An Initial Overview of Iwan Modelling for Mechanical Joints," Sandia National Laboritories, Albuquerque, New Mexico SAND2001-0811, 2001.
- [48] D. J. Segalman, "A Four-Parameter Iwan Model for Lap-Type Joints," *Journal of Applied Mechanics*, vol. 72, pp. 752-760, September 2005.
- [49] D. J. Segalman, "A Modal Approach to Modeling Spatially Distributed Vibration Energy Dissipation," Sandia National Laboratories, Albuquerque, New Mexico and Livermore, California SAND2010-4763, 2010.
- [50] M. Eriten, et al., "Nonlinear system identification of frictional effects in a beam with a bolted joint connection," *Mechanical Systems and Signal Processing*, vol. 39, pp. 245-264, 2013.
- [51] D. J. Segalman, "A Modal Approach to Modeling Spatially Distributed Vibration Energy Dissipation," Sandia National Labs2010.
- [52] B. Deaner, *et al.*, "Application of Viscous and Iwan Modal Damping Models to Experimental Measurements From Bolted Structures," *ASME Journal of Vibrations and Acoustics*, vol. 137, p. 12, 2015.
- [53] R. Lacayo, *et al.*, "Quasi-static Modal Analysis based on Implicit Condensation for Structures with Nonlinear Joints," presented at the International Conference on Noise and Vibration Engineering, Leuven, Belgium, 2016.
- [54] R. Lacayo, *et al.*, "A numerical study on the limitations of modal Iwan models for impulsive excitations," *Submitted to Journal of Sound and Vibration*, 2016.
- [55] M. W. Sracic, *et al.*, "Identifying the modal properties of nonlinear structures using measured free response time histories from a scanning laser Doppler vibrometer,"

- presented at the 30th International Modal Analysis Conference Jacksonville, Florida, 2012.
- [56] M. S. Allen and R. L. Mayes, "Estimating the Degree of Nonlinearity in Transient Responses with Zeroed Early-Time Fast Fourier Transforms," *Mechanical Systems and Signal Processing*, vol. 24, pp. 2049–2064, 2010.
- [57] S. Braun and M. Feldman, "Decomposition of non-stationary signals into varying time scales: Some aspects of the EMD and HVD methods," 2011.
- [58] G. Kerschen, *et al.*, "Toward a fundamental understanding of the Hilbert-Huang transform in nonlinear structural dynamics," *JVC/Journal of Vibration and Control*, vol. 14, pp. 77-105, 2008.
- [59] T. P. Sapsis, *et al.*, "Effective stiffening and damping enhancement of structures with strongly nonlinear local attachments," *Journal of Vibration and Acoustics, Transactions of the ASME*, vol. 134, 2012.
- [60] S. F. Masri and T. K. Caughey, "A Nonparametric Identification Technique for Nonlinear Dynamic Problems," *Journal of Applied Mechanics*, vol. 46, pp. 433-447, 1979.
- [61] G. Kerschen, *et al.*, "Past, present and future of nonlinear system identification in structural dynamics," *Mechanical Systems and Signal Processing*, vol. 20, pp. 505-592, 2006.
- [62] M. D. Cömert and H. N. Ozguven, "A Method for Forced Harmonic Response of Substructures Coupled by Nonlinear Elements," presented at the Proceedings of the 13th International Modal Analysis Conference, Nashville, Tennessee, 1995.
- [63] J. V. Ferreira and D. J. Ewins, "Nonlinear receptance coupling approach based on describing functions," presented at the Proceedings of 14th International Modal Analysis Conference, Dearborn, Michigan, USA, 1996.
- [64] T. Kalaycioglu and H. N. Ozguven, "Harmonic response of large engineering structures with nonlinear modifications," presented at the EURODYN, Leuven, Belgium, 2011.
- [65] M. Krack, *et al.*, "A method for nonlinear modal analysis and synthesis: Application to harmonically forced and self-excited mechanical systems," *Journal of Sound and Vibration*, vol. 332, pp. 6798-6814, 2013.
- [66] W. Szemplinska-Stupnicka, "The modified single mode method in the investigations of the resonant vibrations of non-linear systems.," *Journal of Sound and Vibration*, vol. 63, pp. 475-489, 1979.
- [67] R. J. Kuether, *et al.*, "Modal Substructuring of Geometrically Nonlinear Finite-Element Models," *AIAA Journal*, vol. 54, pp. 691-702, 2016.
- [68] Y. H. Chong and M. Imregun, "Variable modal parameter identification for non-linear MDOF systems. Part I: Formulation and numerical validation," *Shock and Vibration*, vol. 7, pp. 217-227, 2000.
- [69] Y. H. Chong and M. Imregun, "Variable modal parameter identification for non-linear MDOF systems. Part II: Experimental validation and advanced case study," *Shock and Vibration*, vol. 7, pp. 229-240, 2000.
- [70] Y. H. Chong and M. Imregun, "Coupling of non-linear substructures using variable modal parameters," *Mechanical Systems and Signal Processing*, vol. 14, pp. 731-746, 2000
- [71] D. P. Rohe and R. L. Mayes, "Coupling of a Bladed Hub to the Tower of the Ampair 600 Wind Turbine using the Transmission Simulator Method," in *Internaqtional Modal Analysis Conference XXXI*, Garden Grove, CA, 2013.

- [72] R. L. Mayes, "An Introduction to the SEM Substructures Focus Group Test Bed The Ampair 600 Wind Turbine," presented at the International Modal Analysis Conference XXX, Jacksonville, FL, 2012.
- [73] D. R. Roettgen and R. L. Mayes, "Ampair 600 Wind Turbine 3-Bladed Assembly Substructuring using the Transmission Simulator Method," presented at the International Modal Analysis Conference IMAC (XXXIII), Orlando, FL, 2015.
- [74] D. R. Roettgen, *et al.*, "A Comparison of Reduced Order Modeling Techniques Used in Dynamic Substructuring," presented at the International Modal Analysis Conference XXXIV, Orlando, FL, 2016.
- [75] R. L. Mayes and D. P. Rohe, "Coupling experimental and analytical dynamic subsctures using the transmission simulator method," presented at the International Modal Analysis Conference XXXIII, 2013.
- [76] M. R. W. Brake, *et al.*, "Variability and Repeatability of Jointed Structures with Frictional Interfaces," presented at the International Modal Analysis Conference, Orlando, FL, 2014.
- [77] J. Gross, *et al.*, "Model Updating of the Ampair Wind Turbine Substructures," presented at the International Modal Analysis Conference XXXII, Orlando, FL, 2013.
- [78] D. P. Hensley and R. L. Mayes, "Extending SMAC to Multiple Reference FRFs," presented at the 24th International Modal Analysis Conference (IMAC XXIV), St. Louis, Missouri, 2006.
- [79] T. G. Carne, *et al.*, "Support conditions for experimental modal analysis," *Sound and Vibration*, vol. 41, pp. 10-16, 2007.
- [80] M. Rades and D. J. Ewins, "MIFs and MACs in Modal Analysis," presented at the 20th International Modal Analysis Conference (IMAC-20), Los Angeles, CA, 2002.
- [81] D. P. Rohe and M. S. Allen, "Investigation Into the Effect of Mode Shape Errors on Validation Experiments for Experimental-Analytical Substructuring," presented at the Proceedings of the ASME 2012 International Design Engineering Technical Conferences & Computers and Information in Engineering Conference, IDETC/CIE 2012, Chicago, IL, USA, 2012.
- [82] R. L. Mayes, "A Craig-Bampton Experimental Dynamic Substructure using the Transmission Simulator Method," presented at the International Modal Analysis Conference XXXIII, 2015.
- [83] S. Bograd, et al., "Modeling the dynamics of mechanical joints," *Mechanical Systems and Signal Processing*, vol. 25, pp. 2801-2826, 2011.
- [84] D. Suc and K. Willner, "Multiharmonic balance analysis of a jointed friction oscillator," in 6th European Congress on Computational Methods in Applied Sciences and Engineering, ECCOMAS 2012, September 10, 2012 September 14, 2012, Vienna, Austria, 2012, pp. 1907-1914.
- [85] D. J. Ewins, *Modal Testing: Theory, Practice and Application*. Baldock, England: Research Studies Press, 2000.
- [86] D. R. Roettgen, *et al.*, "Feasibility of Describing Joint Nonlinearity in Exhaust Components with Modal Iwan Models," presented at the ASME International Design Engineering Technical Conference, Buffalo, NY, 2014.
- [87] M. S. Allen and J. H. Ginsberg, "A Global, Single-Input-Multi-Output (SIMO) Implementation of The Algorithm of Mode Isolation and Applications to Analytical and

- Experimental Data," *Mechanical Systems and Signal Processing*, vol. 20, pp. 1090–1111, 2006.
- [88] B. Deaner, "Modeling the Nonlinear Damping of Jointed Structures Using Modal Models," M.S., Engineering Physics, University of Wisconsin-Madison, Madison, WI, 2013
- [89] R. D. Cook, et al., Concepts and Applications of Finite Element Analysis, 4th Edition ed. New York: Wiley, 2002.
- [90] R. L. Mayes and D. D. Johansen, "A Modal Parameter Extraction Algorithm using best-fit reciprocal vectors," presented at the 16th International Modal Analysis Conference (IMAC XVI), Santa Barbara, California, 1998.
- [91] M. W. Sracic and M. S. Allen, "Identifying parameters of nonlinear structural dynamic systems using linear time-periodic approximations," presented at the 29th International Modal Analysis Conference (IMAC XXIX), Jacksonville, Florida, 2011.
- [92] M. Feldman, Hilbert Transform Applications in Mechanical Vibration, 2011.
- [93] D. J. Segalman, *et al.*, "Experimental Assessment of Joint-Like Modal Models for Structures"," presented at the International Design Engineering Technical Conferences & Computers and Information in Engineering Conference IDETC/CIE Boston, MA, 2015.
- [94] D. R. Roettgen, *et al.*, "Nonlinear Modal Substructuring using Modal Iwan Models, Part I: Simulated Experiments," *Mechanical Systems and Signal Processing*, vol. TBD, 2017.
- [95] R. L. Mayes, *et al.*, "Correcting indefinite mass matrices due to substructure uncoupling," *Journal of Sound and Vibration*, vol. 332, pp. 5856-5866, 2013.
- [96] C. W. Schwingshackl, *et al.*, "Modeling and validation of the nonlinear dynamic behavior of bolted flange joints," *Journal of Engineering for Gas Turbines and Power*, vol. 135, 2013.
- [97] D. J. Segalman, "A Modal Approach to Modeling Spatially Distributed Vibration Energy Dissipation," Sandia National Laboratories,, Albuquerque, New Mexico2010.
- [98] R. L. Mayes, *et al.*, "A Modal Model to Simulate Typical Structural Dynamic Nonlinearity," presented at the 34th International Modal Analysis Conference (IMAC XXXIV), Orlando, Florida, 2016.
- [99] D. J. Segalman, *et al.*, "Handbook on Dynamics of Jointed Structures," Sandia National Laboratories, Albuquerque, NM 871852009.
- [100] D. R. Roettgen and M. S. Allen, "Nonlinear characterization of a bolted, industrial structure using a modal framework," *Mechanical Systems and Signal Processing*, vol. Submitted June 2015, 2015.
- [101] D. J. Segalman, *et al.*, "Experimental Assessment of Joint-Like Modal Models for Structures," presented at the ASME 2015 International Design Engineering Technical Conferences & Computers and Information in Engineering Conference IDETC/CIE 2015, Boston, MA, 2015.
- [102] V. Palmov, Vibrations of Elasto-Plastic Bodies: Springer, 1998.
- [103] J. Gross, *et al.*, "A Numerical Round Robin for the Prediction of the Dynamics of Jointed Structures," presented at the International Modal Analysis Conference XXXIV, Orlando, FL, 2016.
- [104] M. S. Bonney, *et al.*, "Experimental Determination of Frictional Interface Models," presented at the International Modal Analysis Conference XXXIV, Orlando, FL, 2016.
- [105] H. Festjens, *et al.*, "Nonlinear model order reduction of jointed structures for dynamic analysis," *Journal of Sound and Vibration*, vol. 333, pp. 2100-2113, 2014.

- [106] D. R. Roettgen, *et al.*, "Nonlinear Modal Substructuring using Modal Iwan Models, Part II: Experimental Demonstration," *Mechanical Systems and Signal Processing*, vol. TBD, 2017.
- [107] E. Oberg, *Machinery's Handbook*, 29th ed.: Industrial Press, 2012.
- [108] S. Catalfamo, *et al.*, "Effects of Experimental Methods on the Measurements of a Nonlinear Structure," presented at the International Modal Analysis Conference XXXIV, Orlando, FL, 2016.
- [109] R. L. Mayes, *et al.*, "Nonlinear Finite Element Model Updating, Part I: Experimental Techniques and Nonlinear Modal Model Parameter Extraction " presented at the International Modal Analysis Conference XXXV, Garden Grove, CA., 2017.